



**Marita Alves Cardoso**

**ELETRÓLITOS HÍBRIDOS ORGÂNICOS-  
INORGÂNICOS PARA FACHADAS DE EDIFÍCIOS  
INTELIGENTES**

**LUMINESCENT ORGANIC-INORGANIC HYBRID  
ELECTROLYTES FOR SMART BUILDING GLAZING**



Universidade de Aveiro  
2021

**Marita Alves Cardoso**

**ELETRÓLITOS HÍBRIDOS ORGÂNICOS-  
INORGÂNICOS PARA FACHADAS DE EDIFÍCIOS  
INTELIGENTES**

**LUMINESCENT ORGANIC-INORGANIC HYBRID  
ELECTROLYTES FOR SMART BUILDING GLAZING**



**Marita Alves Cardoso**

## **ELETRÓLITOS HÍBRIDOS ORGÂNICOS- INORGÂNICOS PARA FACHADAS DE EDIFÍCIOS INTELIGENTES**

### **LUMINESCENT ORGANIC-INORGANIC HYBRID ELECTROLYTES FOR SMART BUILDING GLAZING**

Tese apresentada à Universidade de Aveiro para cumprimento dos requisitos necessários à obtenção do grau de Doutor em Ciência e Engenharia de Materiais, realizada sob a orientação científica da Doutora Maria Rute de Amorim e Sá Ferreira André, Professora Associada com Agregação do Departamento de Física da Universidade de Aveiro e da Doutora Verónica Cortés de Zea Bermudez, Professora Catedrática do Departamento de Química da Universidade de Trás-os-Montes e Alto Douro.

Este trabalho foi desenvolvido no âmbito do projeto CICECO-Instituto de Materiais de Aveiro, UIDB/50011/2020 & UIDP/50011/2020, financiado por fundos nacionais através da FCT/MEC e quando aplicável cofinanciado pelo FEDER, no âmbito do Acordo de Parceria PT2020, e cofinanciado pelo FEDER sob o acordo PT2020, Solar-Flex, CENTRO-01-0145-FEDER-030186. A autora agradece o apoio financeiro concedido pela FCT através da bolsa SFRH/BD/118466/2016.



*Aos meus avós que mesmo não estando aqui continuam a ser a minha maior  
inspiração. Aos meus pais e irmão pelo apoio incondicional.*

## **o júri**

presidente

**Prof. Doutor Vasile Staicu**  
Professor Catedrático da Universidade de Aveiro

**Prof. Doutora Maria Manuela Silva Pires Silva**  
Professora Associada com Agregação da Escola de Ciências da Universidade do Minho

**Prof. Doutor Pedro Manuel de Melo Bandeira Tavares**  
Professor Associado do Departamento de Química da Universidade de Trás-os-Montes e Alto Douro

**Prof. Doutor Albano Augusto Cavaleiro Rodrigues de Carvalho**  
Professor Catedrático da Universidade de Coimbra

**Prof. Doutor Joaquim Manuel Vieira**  
Professor Catedrático da Universidade de Aveiro

**Prof. Doutora Maria Rute de Amorim e Sá Ferreira André**  
Professora Associada com Agregação da Universidade de Aveiro

## agradecimentos

A Deus por me guiar e ajudar a seguir em frente.

Gostaria de começar por agradecer às minhas orientadoras Professora Doutora Maria Rute de Amorim e Sá Ferreira André e Professora Doutora Verónica Cortés de Zea Bermudez, sem as quais este trabalho não seria possível. Gostaria de agradecer à Professora Doutora Maria Rute de Amorim e Sá Ferreira André por me ter aceite como aluna de doutoramento e me ter dado a oportunidade de fazer parte de uma equipa de investigação tão ativa e dinâmica como o Phantom-g. Aprendi muito ao longo dos 4 anos em que aqui estive sobre investigação científica, trabalho em equipa e disciplina de trabalho. Agradeço pela disponibilidade e pelas conversas construtivas que me ajudaram a ver as coisas de um outro ponto de vista. Gostaria de agradecer à Professora Doutora Verónica Cortés de Zea Bermudez por mais uma vez me ter aceite como aluna, com quem me iniciei na investigação em 2010 e com quem aprendi imenso ao longo de 10 anos sobre investigação e trabalho científico. Agradeço toda a orientação, conversas construtivas, incentivo pela busca do conhecimento e encorajamento para fazer mais e melhor. Gostaria também de agradecer ao Professor Doutor Luís Dias Carlos pelas discussões científicas.

Aproveito igualmente para agradecer à Professora Doutora Elvira Fortunato e Doutora Sónia Pereira da Universidade Nova de Lisboa pelo fornecimento dos substratos de IZO/WO<sub>3</sub> e NiO/IZO absolutamente essenciais para a construção dos ECDs e para este doutoramento.

Um muito obrigado aos colegas do Phantom-g e do departamento de Química da UTAD, por estarem sempre prontos a ajudar de uma forma espontânea e voluntária. Em particular, agradeço à Doutora Sandra Correia, à Doutora Ana Rita Frias, ao Doutor Carlos Brites e ao Doutor Alexandre Botas do Phantom-g por toda a ajuda, em especial na obtenção dos dados de fotoluminescência. Um muito obrigado também à Doutora Helena Gonçalves da UTAD por toda a ajuda e tratamento de dados dos ECDs bem como nos dados de caracterização térmica e estrutural.

Às minhas amigas Rita e Maria. Obrigada Rita pela boa disposição sempre presente, pelas palavras encorajadoras e por me conheceres tão bem. À Maria agradeço a amizade, apoio, paciência e disponibilidade, mostrando-se uma pessoa incrível e uma verdadeira amiga com um coração enorme.

Finalmente, gostaria de agradecer à minha família, em especial aos meus pais por todo o apoio ao longo do meu percurso académico que acaba aqui, onde foram a constante de tudo. Ao meu irmão Humberto, pelo apoio incondicional e por me mostrar que é sempre possível ultrapassar as dificuldades. Aos meus avós, que mesmo já não estando comigo me mostraram um amor incondicional.

Marita Alves Cardoso

**palavras-chave**

Ionossilicas, líquido iônico, lantanídeos, sol-gel, dispositivos eletrocromicos, camadas luminescentes, concentradores solares luminescentes, edifícios de balanço energético nulo.

**resumo**

Existe uma necessidade global de melhorar a eficiência energética nos edifícios com vista a uma nova geração de edifícios denominados edifícios de balanço energético nulo (ZEBs). Uma das estratégias propostas inclui o desenvolvimento de janelas inteligentes baseadas em dispositivos eletrocromicos (ECDs) acoplados a camadas luminescentes e concentradores solares luminescentes (LSCs). Novos materiais baseados em complexos de íons lantanídeos com elevado rendimento quântico de emissão incorporados em matrizes hospedeiras apropriadas, preparadas pelo método sol-gel, abrem um leque de oportunidades para o desenvolvimento de novos dispositivos com notável desempenho eletro-ótico para janelas de ZEBs. Nesta tese, novos eletrólitos baseados em híbridos orgânicos-inorgânicos dopados com um líquido iônico luminescente permitiram a produção de ECDs com elevada transparência nas regiões espectrais do visível e NIR e, possibilitando o ajuste fino da passagem de luz solar e da energia solar, permitindo operação em três modos (brilhante quente, semi-brilhante quente, e frio escuro). O ECD oferece uma série de recursos extraordinários, em particular alta eficiência e modulação ótica, boa estabilidade, grande eficiência de coloração, excelente memória ótica e capacidade de auto-regeneração após stress mecânico. Além disso, novas ionossilicas funcionalizadas na superfície dopadas com íons lantanídeos ( $\text{Ln}^{3+} = \text{Nd}^{3+}, \text{Eu}^{3+}, \text{Tb}^{3+}, \text{Yb}^{3+}$ ) foram produzidas, caracterizadas e incorporadas em poli(metil metacrilato) produzindo filmes transparentes com auto-absorção desprezável com potencial aplicação em LDS e LSC. Foi observado um aumento absoluto significativo na eficiência quântica externa da célula PV (EQE ~ 32% entre 300-360 nm em relação à célula PV base) demonstrando a aplicabilidade dos materiais desenvolvidos para ZEBs.

**keywords**

Ionosilicas, ionic liquid, lanthanides, sol-gel, electrochromic devices, luminescent down-shifting layers, luminescent solar concentrators, zero-energy buildings.

**abstract**

There is a global need to improve the building energy generation efficiency in the new generation of buildings, so called zero-energy buildings (ZEBs). One strategy includes the development of smart windows based on electrochromic devices (ECDs) coupled to luminescent layers and luminescent solar concentrators (LSCs). New materials based on lanthanide complexes with high quantum efficiency incorporated in appropriate host matrices prepared by sol-gel chemistry opens challenging opportunities for the development of new devices with remarkable electro-optical performance and foreseen application as smart windows for ZEBs. In this thesis, new electrolytes based on organic-inorganic hybrids doped with an ionic liquid allowed the production of ECDs with high visible and NIR transparency and voltage-actuated dual coloration tuning, enabling three-mode operation (bright hot, semi-bright warm, and dark cold). The ECD delivers a number of extraordinary features, in particular high switching efficiency and optical modulation, good cycling stability, large coloration efficiency, excellent optical memory, and unusual self-healing ability following mechanical stress. In addition, new lanthanide ions ( $\text{Ln}^{3+} = \text{Nd}^{3+}, \text{Eu}^{3+}, \text{Tb}^{3+}, \text{Yb}^{3+}$ )-doped surface functionalized ionosilicas (ISs) were produced, characterized and embedded in poly(methyl methacrylate) yielding transparent films with negligible self-absorption with potential to be used LDS layers, and LSC into a single device. The significant absolute increase observed in the PV cell external quantum efficiency (EQE~32% between 300-360 nm relatively to the bare PV cell) supports the applicability of the developed materials for ZEBs.

## Contents

List of Tables .....	ii
List of Figures .....	iii
List of Schemes .....	ix
List of acronyms and abbreviations .....	x
<b>1 - FRAMEWORK AND MOTIVATION.....</b>	<b>1</b>
1.1. Introduction .....	1
1.2. Electrochromic windows.....	7
1.3. Luminescent solar concentrators and down-shifting layers.....	14
1.4. Objectives, innovation and methodologies .....	18
1.5. Organization of the thesis.....	19
<b>2 - FUNDAMENTS AND BACKGROUND.....</b>	<b>21</b>
2.1. Sol-gel method .....	21
2.2. Electrochromic windows: working principles.....	38
2.3. Luminescent solar concentrators and luminescent down-shifting layers: working principles .....	42
<b>3 - LANTHANIDE-BASED IONOSILICAS FOR LUMINESCENT SOLAR CONCENTRATORS AND DOWN-SHIFTING LAYERS.....</b>	<b>45</b>
3.1. Introduction .....	46
3.2. Synthesis.....	47
3.3. Results and discussion.....	52
3.4. Conclusions .....	76
<b>4 - DI-UREASILS FOR ELECTROCHROMIC DEVICES .....</b>	<b>77</b>
4.1. Introduction .....	77
4.2. Synthesis.....	79
4.3. Results and discussion.....	82
4.4. Conclusions .....	93
<b>5 - LUMINESCENT PMMA-BASED SOLID ELECTROLYTE MEMBRANES FOR SMART WINDOWS AIMING ENERGY-EFFICIENT BUILDINGS .....</b>	<b>94</b>
5.1. Introduction .....	94
5.2. Synthesis.....	96
5.3. Results and discussion.....	98
5.4. Conclusions .....	106
<b>6 - GENERAL CONCLUSIONS AND PERSPECTIVES .....</b>	<b>108</b>
Appendix A – Structural and optical characterization.....	110
Appendix B – ECD characterization.....	117
Appendix C – List of publications .....	120
REFERENCES .....	121

## List of Tables

<b>1.1.</b>	Electro-optical parameters of WO <sub>3</sub> -/NiO-based ECDs in the coloured (c) and bleached (b) states. V is applied voltage, t is switching time, T is transmittance, ΔOD is optical density, and CE is coloration efficiency .....	13
<b>1.2.</b>	Figures of merit of illustrative examples of Ln <sup>3+</sup> -based LDS layers applied on different PV cell types, where the absolute power conversion efficiency (PCE) achieved and the percentage increase in PCE (ΔPCE) compared to the bare cell are also presented.....	16
<b>1.3.</b>	Figures of merit of illustrative examples of Ln <sup>3+</sup> -based LSCs applied on different PV cell types.....	17
<b>3.1.</b>	<sup>1</sup> H and <sup>13</sup> C NMR spectroscopic data of [B(TMSP)Im]Cl. Chemical shifts (δ) in ppm .....	54
<b>3.2.</b>	Assignment of the FT-IR vibrational bands of [B(TMSP)Im]Cl.....	56
<b>3.3.</b>	Emission lifetime values, integral overlap ( <i>O</i> , ×10 <sup>19</sup> photons·s <sup>-1</sup> ·m <sup>-2</sup> ), absolute emission quantum yield ( <i>q</i> ), molar extinction coefficient ( <i>ε</i> , ×10 <sup>3</sup> M <sup>-1</sup> ·cm <sup>-1</sup> ) and brightness ( <i>B</i> , M <sup>-1</sup> ·cm <sup>-1</sup> ) of PMMA-Ln-X.....	67
<b>3.4.</b>	Emission lifetime values at low (12 K) and room temperature for IS-Eu and PMMA-Eu-10 excited at 365 and 385 nm, respectively, and monitored at 612 nm.....	69
<b>3.5.</b>	Absolute EQE increase in the UV spectral region for Ln <sup>3+</sup> -based LDS layers for c-Si and dye-sensitized solar cells (DSSCs) .....	73
<b>3.6.</b>	Thickness of the active layer of the LSCs deposited on glass .....	73
<b>3.7.</b>	Quantification of parameters expressed in Equation (3.3) for <i>η<sub>opt</sub></i> calculation .....	74
<b>4.1.</b>	Synthesis procedure of the DUPIL <sub>x</sub> ormolytes .....	81
<b>4.2.</b>	Ionic conductivity of the DUPIL <sub>x</sub> ormolytes .....	86
<b>4.3.</b>	Electro-optical parameters of the a-IZO/WO <sub>3</sub> /DUPIL <sub>60</sub> /NiO/a-IZO ECD. T values are given in % .....	87
<b>5.1.</b>	Electro-optical parameters of ECD@ PISIL and ECD@IS. T values are given in %.....	102
<b>A.1.</b>	Range in wavenumber (cm <sup>-1</sup> ) of various functional groups. <sup>1</sup> .....	111
<b>B.1</b>	Requirements for ECDs. <sup>2,3</sup> .....	118

## List of Figures

<b>1.1.</b>	(A) Representation of the consumption of fossil fuels from 2000 to 2017 and the prediction until 2040. Adapted from <sup>4</sup> . (B) Schematic representation of the energy consumption in Europe, United States, and China in different sectors. (C) Distribution of the residential energy consumption over the different house appliances. Adapted from <sup>5,6</sup> .....	1
<b>1.2.</b>	Three of the United Nations Sustainable Development Goals for 2030. Adapted from <sup>7</sup> .....	2
<b>1.3.</b>	Schematic diagram of an ideal smart window reflecting NIR in (A) warm days and allowing it to enter in (B) cold days, while remaining transparent in the visible region in both climate conditions. <sup>8</sup> .....	3
<b>1.4.</b>	Scheme of the solar irradiation versus established global energy resources. Fossil fuels are expressed with regard to their total reserves, whereas renewable energies are expressed to their yearly potential. From Solar generation 6, adapted from <sup>9</sup> .....	4
<b>1.5.</b>	Schematic representation of a solar cell (A) including a LDS layer and (B) coupled to a LSC. Adapted from <sup>10</sup> . (C) Schematic representation of a window consisting of a triple-insulated glass unit embedding a LSC. Adapted from <sup>11</sup> .....	5
<b>1.6.</b>	Practical examples of LSCs. (A) Photographs of the LSC-based noise barrier site on the left faces North/South, and the barrier on the right faces East/West; (B) Glass to Power company LSC concept; and (C) UbiQD greenhouse scheme with (D) photograph of the LSC films. Adapted from <sup>12</sup> .....	6
<b>1.7.</b>	Proposed scheme for harvesting, conversion, and management of the solar spectrum. In the ECD assembly (top) TCO, EC and IS correspond to the transparent conductive oxide, electrochromic, and ion storage layers, respectively .....	7
<b>1.8.</b>	Scheme illustrating the most important requirements to be fulfilled by PEs. <sup>13</sup> .....	11

<b>1.9.</b>	(A) Photograph of a QD–PMMA-based LSC comprising cadmium selenide/cadmium sulfide (CdSe/CdS) QDs ( $R_0= 1.5$ and $H= 4.2$ nm) illuminated by UV lamp emitting at 365 nm (top) and under ambient illumination (bottom) (scale bar: 5 cm); (B) PMMA-based LSC outdoors on a sunny day; (C) Photograph of a LSC comprising 0.3 wt% zinc sulfide (ZnS)-coated $\text{CuInSe}_x\text{S}_{2-x}$ QDs (LSC dimensions, $12 \times 12 \times 0.3$ cm <sup>3</sup> ) taken with an UV-filtered infrared camera (the LSC is illuminated at 365 nm); (D) Photographs of the luminescent thin film attached on top of c-Si solar cells; (E) Photographs of the LDS layers based on tU5-Eu (tU5 = tri-Ureasil), under 365 nm (scale bars: $10^{-2}$ m), scheme of the solar vehicle with the LDS coating (Right); (F) Solar cells (mc-Si, where mc is multicomponent) coated with different LDS PEVA-based materials. Adapted from <sup>14-19</sup> .....	15
<b>2.1.</b>	Sol–gel processing routes to yield different products .....	24
<b>2.2.</b>	Schematic representation of the (A) hydrolysis and (B) condensation reactions yielding silica using TMOS as precursor compound.....	26
<b>2.3.</b>	(A) Hydrolysis and condensation rates of $\text{Si}(\text{OR})_4$ and (B) structure of the obtained gel, as a function of pH. <sup>20</sup> .....	28
<b>2.4.</b>	(A) Acid- and (B) base-catalysed hydrolysis of silicon alkoxides. Adapted from <sup>21</sup> .....	29
<b>2.5.</b>	(A) Acid- and (B) base-catalysed condensation of silicon alkoxides. Adapted from <sup>21</sup> .....	29
<b>2.6.</b>	Effect of pH on the gel time of a colloidal silica-water system. <sup>22</sup> .....	30
<b>2.7.</b>	Polymerization behaviour of silica describing the sol–gel process. In basic solution the particles grow in size and in acidic solution, or in the presence of coagulating salt, particles aggregate into 3D networks and form gels. Adapted from <sup>23</sup> .....	31
<b>2.8.</b>	Hybrids classification based on the type of molecular interaction: (A) class I and (B) class II. Adapted from <sup>24</sup> .....	33
<b>2.9.</b>	Different types of surface-functionalized ionosilicas. <sup>25</sup> .....	36
<b>2.10.</b>	Synthesis of surface-functionalized ionosilicas via (A) post-synthesis grafting and (B) hydrolysis/cocondensation reactions. <sup>25</sup> .....	37

<b>2.11.</b>	Periodic table of the elements. The coloured boxes refer to the documented transition metals oxides that have cathodic or anodic electrochromism or both. <sup>13</sup> .....	38
<b>2.12.</b>	Schematic representation of an archetypal glass/TCO/WO <sub>3</sub> /electrolyte/NiO/TCO/glass ECD, showing the transport of cations and electrons as a result of applied voltage. ....	41
<b>2.13.</b>	Spectral converters for PV devices and AM1.5G spectrum. (A) Normalized external quantum efficiency for single-junction PV cells with confirmed terrestrial efficiencies measured under the global AM1.5 spectrum (1000 W·m <sup>-2</sup> ) at a cell temperature of 25°C. <sup>26</sup> (B) AM1.5G solar spectral irradiance spectrum. The shadowed areas represent the fraction available for down-conversion (26 %, up to 550 nm), down-shifting (81 %, up to 1100 nm) and up-conversion (16%, in the 1200-2500 nm range) for a c-Si wafer. The fraction absorbed by c-Si is also indicated. <sup>27</sup> Adapted from <sup>12</sup> .....	42
<b>2.14.</b>	Operating principles of luminescence spectral conversion in a: (A) LDS device and (B) LSC. The primary processes and losses occurring are: (1) emission from the optically active centre, (2) Fresnel reflections, (3) surface scattering, (4) waveguide attenuation, (5) transmitted radiation, (6) re-absorption by neighbour centres, (7) non-radiative relaxation, (8) emission within the escape cone, (9) radiation lost through the sides. Adapted from <sup>12</sup> .....	43
<b>3.1.</b>	Schematic representation showing the use of a LDS layer (red colour) acting also as a LSC in combination with PV cells, in which the guided radiation that reaches the edges of the LDS layer is used by edge-mounted PV cells. The inset depicts the chemical composition of the emitting IS-Ln centres .....	47
<b>3.2.</b>	UV/visible absorption spectrum of PMMA .....	49
<b>3.3.</b>	(A) Schematic representation of the chemical structure, and (B) <sup>1</sup> H and (C) <sup>13</sup> C NMR spectra (standardized intensity vs chemical shift) of [B(TMSP)Im]Cl .....	53
<b>3.4.</b>	FT-IR spectra of BIm, CPTMS and [B(TMSP)Im]Cl .....	55

<b>3.5.</b>	Schematic representation of the chemical structure of (A) Na[Ln(tta) <sub>4</sub> ] and (B) [B(TMSP)Im][Ln(tta) <sub>4</sub> ] .....	57
<b>3.6.</b>	FT-IR spectra of tta, Na[Eu(tta) <sub>4</sub> ] and IS-Eu .....	57
<b>3.7.</b>	(A) XRD diffraction patterns of IS-Eu, PMMA-Eu-10 and PMMA-Ln-20 (Ln = Nd <sup>3+</sup> , Eu <sup>3+</sup> , Tb <sup>3+</sup> and Yb <sup>3+</sup> ); (B) POM (crossed polarizers), and (C) TEM images of IS-Eu .....	59
<b>3.8.</b>	ATR/FT-IR spectra of PMMA, IS-Ln, PMMA-Eu-10 and PMMA-Ln-20 (Ln = Nd <sup>3+</sup> , Tb <sup>3+</sup> and Yb <sup>3+</sup> ) .....	60
<b>3.9.</b>	(A) SEM, (B-H) EDS mapping (oxygen – green, carbon – red, nitrogen – orange, europium – dark blue, sulfur – purple, fluorine – cyanide, silicon – yellow) and (I) POM images of PMMA-Eu-10 .....	61
<b>3.10.</b>	TGA (light blue line) and DTGA (red line) curves of IS-Yb .....	62
<b>3.11.</b>	DSC curves of PMMA, IS-Eu and PMMA-Eu-10.....	62
<b>3.12.</b>	Reversible thermal transition of IS-Eu.....	63
<b>3.13.</b>	Water static contact angles of PMMA, IS-Ln, and PMMA-Ln-X.....	63
<b>3.14.</b>	(A) Si absorption spectrum and emission spectra excited at 360-380 nm. The * and ** assign the superimposition between the Eu <sup>3+</sup> <sup>5</sup> D <sub>0</sub> → <sup>7</sup> F <sub>0</sub> , <sup>1</sup> / <sub>1</sub> <sup>5</sup> D <sub>0</sub> → <sup>7</sup> F <sub>2</sub> and the Tb <sup>3+</sup> <sup>5</sup> D <sub>4</sub> → <sup>7</sup> F <sub>4</sub> / <sup>5</sup> D <sub>4</sub> → <sup>7</sup> F <sub>3</sub> transitions, respectively. (B) Excitation spectra monitored at 545 nm/612 nm/978 nm/1062 nm for PMMA-Tb/Eu/Yb/Nd-20. (C) Absorption spectra; the inset shows a magnification of the Nd <sup>3+</sup> related <sup>4</sup> I <sub>9/2</sub> → <sup>4</sup> G <sub>5/2</sub> , <sup>4</sup> G <sub>7/2</sub> .transition.....	64
<b>3.15.</b>	Room temperature emission decay curves for (A) PMMA-Eu-10, (B) PMMA-Eu-20, (C) PMMA-Tb-10, (D) PMMA-Tb-20, (E) PMMA-Yb-10, (F) PMMA-Yb-20, (G) PMMA-Nd-10 and (H) PMMA-Nd-20 excited at 380 nm and monitored at 612 nm (Eu), 544 nm (Tb), 1062 nm (Nd) and 978 nm (Yb). The solid lines represent the best fit (r <sup>2</sup> >0.97) using a single exponential function. The respective residual plots are shown on the right-hand side.....	66
<b>3.16.</b>	(A) Low temperature (12 K) emission spectra excited at 385 nm; the insets show a magnification of the <sup>5</sup> D <sub>0</sub> → <sup>7</sup> F <sub>0</sub> , <sup>5</sup> D <sub>0</sub> → <sup>7</sup> F <sub>1</sub> and <sup>5</sup> D <sub>0</sub> → <sup>7</sup> F <sub>2</sub> transitions and (B) low temperature (12 K) emission decay curves excited at 385 nm and monitored at 612 nm for PMMA-Eu-10 and IS-Eu .....	68

<b>3.17.</b>	(A) Low temperature (12 K) and (B) room temperature excitation spectra of the IS-Eu and of PMMA-Eu-10 and of PMMA-Eu-10 monitored at 613 nm.....	69
<b>3.18.</b>	(A) Low temperature (12 K) and (B) room temperature emission decay curves of IS-Eu and PMMA-Eu-10 excited at 385 nm and monitored at 612 nm. The respective residual plots are shown on the right-hand side ..	70
<b>3.19.</b>	(A) Photograph of the prototype of the combined LDS layer and LSC device under AM1.5G radiation. (B) Total (solid line) and diffuse (dashed line) reflectance of (top) PMMA-Eu-10/20 and (bottom) average curves for different bare PV cells. (C) EQE curves of the bare PV cell, coated PV-1, edge-mounted PV-2 and the curve showing the contribution of both PV devices. (D) V-I curves of the bare PV cell, coated PV-1 and edge-mounted PV-2 .....	71
<b>3.20.</b>	Photographs of the LSCs based on (A,C) PMMA-Eu-20 and (B,D) PMMA-Tb-20 under AM1.5G (top) and UV radiation at 365 nm (bottom).....	74
<b>3.21.</b>	Emission of the LSCs collected at the edges of the LSCs based on (A) PMMA-Tb-20 and (B) PMMA-Eu-20. The emission spectra at the edges of the LSCs spectra were acquired using a spectrometer OceanOptics Maya 2000 Pro coupled with an optical fiber under AM1.5G radiation ...	75
<b>4.1.</b>	Schematic representation of the three-mode modulation of a smart window based on the voltage-actuated a-IZO/a-WO <sub>3</sub> /DUPIL <sub>60</sub> /c-NiO/a-IZO ECD: (A) bright hot mode (0.0 V), (B) semi-bright warm mode (-2.0 V), (C) dark cold mode (-2.5 V), (D) configuration of the ECD .....	79
<b>4.2.</b>	Molecular structures of the (A) [BIm][TfO] PIL and (B) of the non-hydrolyzed d-UPTES(2000) precursor (a+c = 2.5 and b = 40.5).....	80
<b>4.3.</b>	(A) Ultraviolet (UV)-vis spectrum of the DUPIL <sub>60</sub> ormolyte after being washed with water. (B, C) Photographs of the monolith highlighting its transparency and flexibility (scale bar corresponds to 1 cm).....	81
<b>4.4.</b>	(A) XRD patterns and (B) DSC curves of the DUPIL <sub>x</sub> ormolytes with x = 40 (red line), 50 (blue line) and 60 (green line) .....	83

<b>4.5.</b>	(a) SEM, EDS mapping ((b) silicon, (c) carbon, (d) fluorine, (e) nitrogen, (f) oxygen, and (g) sulphur) and (h) POM images of the DUPIL <sub>60</sub> ormolyte (A) as-prepared and (B) washed with water.....	84
<b>4.6.</b>	EDS data for the as-prepared DUPIL <sub>60</sub> ormolyte .....	84
<b>4.7.</b>	(A) Ionic conductivity of the DUPIL <sub>x</sub> ormolytes. The lines drawn are just guides for the eyes. (B) Nyquist plot for the DUPIL <sub>60</sub> ormolyte at different temperatures. The lines drawn are just guides for the eyes .....	85
<b>4.8.</b>	CIE 1976 L*a*b* colour diagram of the ECD: as-deposited state (brown triangle), coloured state at -2.5 V after CA cycling (brown circle), and end of optical memory test (brown square).....	87
<b>4.9.</b>	Left: Transmission spectra of the a-IZO/a-WO <sub>3</sub> /DUPIL <sub>60</sub> /c-NiO/a-IZO ECD in the bleached state (purple line) and in the coloured states upon application of -2.0 V (blue line) and -2.5 V (green line). Right: Photographs of the ECD at variable voltages .....	88
<b>4.10.</b>	Cyclic voltamogram of the a-IZO/a-WO <sub>3</sub> /DUPIL <sub>60</sub> /c-NiO/a-IZO ECD (6 <sup>th</sup> cycle, scan rate 50 mV s <sup>-1</sup> ) .....	88
<b>4.11.</b>	Variation of the current density with voltage steps of ±2.5 V at every 50 s after 500 cycles. Inset: preliminary 30 cycles under the same conditions right after mechanical stress.....	89
<b>4.12.</b>	Coloration efficiency of the bleaching and coloration states at 555 nm as a function of charge density at different cycles .....	90
<b>4.13</b>	Optical memory test of the a-IZO/a-WO <sub>3</sub> /DUPIL <sub>60</sub> /c-NiO/a-IZO ECD ...	91
<b>4.14.</b>	AFM images of the surfaces of (A,B) a-IZO (a-IZO glass plate), (C,D) a-WO <sub>3</sub> (a-WO <sub>3</sub> /a-IZO glass plate) and (E,F) c-NiO (c-NiO/a-IZO glass plate) .....	92
<b>5.1.</b>	Archetypal ECD@PISIL tested. (A) Schematic representation, where IC is PMMA/IS-Eu-1/IS-Nd-19/[BMIm][PF <sub>6</sub> ]-55; (B) as-prepared; (C) coloured state at -2.5 V against a white background; (D) coloured state at -2.5 V against an outside environment background.....	96
<b>5.2.</b>	ATR/FT-IR spectra of PMMA, IS-Eu, IS-Nd and PMMA/IS-Eu-1/IS-Nd-19/[BMIm][PF <sub>6</sub> ]-X monoliths in the (A) 2000-400 cm <sup>-1</sup> and (B) 1760-1680 cm <sup>-1</sup> .....	99

<b>5.3.</b>	DSC curves of the PMMA/IS-Eu-1/IS-Nd-19/[BMIm][PF <sub>6</sub> ]-X monoliths	100
<b>5.4.</b>	Temperature dependence of the ionic conductivity of IS-Eu, [BMIm][PF <sub>6</sub> ] and PMMA/IS-Eu-1/IS-Nd-19/[BMIm][PF <sub>6</sub> ]-X electrolytes. [BMIm][PF <sub>6</sub> ] data from <sup>28</sup>	101
<b>5.5.</b>	(A) Emission spectrum excited at 360 nm and (B) excitation spectra monitored at 612 nm (red line) and 1056 nm (black line) for the PMMA/IS-Eu-1/IS-Nd-19/[BMIm][PF <sub>6</sub> ]-55. The shadowed area represents the AM1.5G photon flux (right y axis)	102
<b>5.6.</b>	Visible-NIR spectra of the ECDs: (A) ECD@PISIL in the as-prepared state (red line), bleached state (light blue line), coloured state after 10 CA cycles ( $\pm 2.5$ V) (dark blue line); and coloured state after 200 CA 200 cycles ( $\pm 2.5$ V) (green line). (B) ECD@IS in the as-prepared state (red line), bleached state (light blue line), coloured state upon application of -2.0 V (dark blue line), bleached state after 50 CA cycles ( $\pm 2.0$ V) (light green line), and coloured state after 50 CA cycles (dark green line)	103
<b>5.7.</b>	CIE 1976 L*a*b* colour diagram of the ECDs. (A) ECD@PISIL: as-deposited state (white circle), and coloured state at -2.5 V after 200 CA cycles (black circle); (B) ECD@IS: as-deposited state (white circle), coloured state at -2.0 V after 50 CA cycles (black circle)	103
<b>5.8.</b>	Variation of the current density of the devices: (A) ECD@PISIL (voltage steps of $\pm 2.5$ V at every 50 s after 200 cycles) and (B) ECD@IS (voltage steps of $\pm 2.0$ V at every 100 s) after 50 cycles	105

## List of Schemes

<b>3.1.</b>	Synthesis of PMMA via free radical addition polymerization	48
<b>3.2.</b>	Syntheses of the IS-Ln ionosilicas	50
<b>3.3.</b>	Syntheses of the composite films/LDS layers/LSC (Ln = Nd <sup>3+</sup> , Eu <sup>3+</sup> , Tb <sup>3+</sup> and Yb <sup>3+</sup> , X= 10, 20 % wt)	52

## List of acronyms and abbreviations

$A_{\text{top}}$  – Top surface area of the LSC

a-IZO – Amorphous indium zinc oxide

AM 1.5G – Air Mass 1.5 Global

$B$  – Brightness

BIm – N-butylimidazole

[BIm][TfO] – N-butylimidazolium trifluoromethanesulfonate

BIPV – Building integrated photovoltaics

[BMIm][PF<sub>6</sub>] – 1-butyl-3-methylimidazolium hexafluorophosphate

BPO – Benzoyl peroxide

[B(TMSP)Im]Cl – 1-butyl-3-[3-(trimethoxysilyl)propyl]imidazolium chloride

$c$  – Speed of light

CA – Chronoamperometry

CE – Coloration efficiency

CIE – Commission Internationale d'Éclairage

CPs – Conductive polymers

CPTMS – (3-chloropropyl)trimethoxysilane

CV – Cycle voltammetry

DCM – Dichloromethane

DSC – Differential scanning calorimetry

$e$  – Electron charge

EC – Electrochromic

ECD – Electrochromic Device

ECW – Electrochromic windows

EDS – Energy-dispersive X-ray spectroscopy

$E_g$  – Band gap

EQE – External quantum efficiency

EtOAc – Ethyl acetate

EtOH – Ethanol

FF – Fill factor of the PV cell

FT-IR – Fourier transform infrared

FTO – Fluorine tin oxide

fwhm – Full-width-at-half-maximum

$h$  – Planck's constant  
HTfO – Trifluoromethanesulfonic acid  
 $I_{sc}$  – Short-circuit current  
IC – Ion conductor  
ICPTES – 3-isocyanatepropyltriethoxysilane  
IEP – Isoelectric point  
IL – Ionic liquid  
ISs – Ionosilicas  
ITO – Indium tin oxide  
IVCT – Intervalence charge transfer  
IZO – Indium zinc oxide  
LDS – Luminescent down-shifting  
 $L_n$  – Lanthanide  
LSC – Luminescent solar concentrators  
MeOH – Methanol  
MM – Methyl methacrylate  
NaOH – Sodium hydroxide  
NaCl – Sodium chloride  
NiO – Nickel oxide  
NIR – Near-infrared  
NMR – Magnetic resonance spectroscopy  
 $O$  – Integral overlap  
OD – Optical density  
ORMOSILs – Organically modified silicates  
 $P$  – Irradiation intensity  
 $P_{out}$  – Output power at the LSC edges  
 $P_{in}$  – Incident optical power  
PAN – Poly(acrylonitrile) (PAN)  
PCE – Power conversion efficiency  
PCL – Poly( $\epsilon$ -caprolactone)  
PE – Polymer electrolytes  
PEDOT – Poly(3,4-ethylenedioxythiophene)  
PEDOT:PSS – Poly(3,4-ethylenedioxythiophene):poly(styrene sulfonate)  
PEG – Poly(ethylene glycol)

PET – Poly(ethylene terephthalate)  
PEVA – Poly(ethylene-co-vinyl acetate)  
PIL – Protic ionic liquid  
PL – Photoluminescence  
PMMA – Poly(methyl methacrylate)  
POE – Poly(oxyethylene)  
POM – Polarized optical microscopy  
PV – Photovoltaic  
PVA – Poly(vinyl alcohol)  
PVB – Poly(vinyl butyral)  
PVC – Poly(vinyl chloride)  
PVDF – Poly(vinylidene fluoride)  
PVS – Poly(vinyl sulfone)  
PZC – Point of zero charge  
Q – Charge density  
QDs – Quantum dots  
RTILs – Room temperature ionic liquids  
SEM – Scanning electron microscopy  
SILCs – Supported ionic liquid catalysts  
SiO<sub>2</sub> – Silicon dioxide  
SPE – Solid polymer electrolytes  
SPM – Spray pyrolysis method  
T – Temperature  
t – Time  
TA – Thermal analysis  
T<sub>b</sub> – Transmittance in the bleached state  
T<sub>c</sub> – Transmittance in the coloured state  
TCO – Transparent conducting oxide  
TEM – Transmission electron microscopy  
TEOS – Tetraethylorthosilane  
T<sub>g</sub> – Glass transition temperature  
TGA, DTGA – Thermogravimetric analysis, Derivative thermogravimetric analysis  
THF – Tetrahydrofuran  
TMOS – Tetramethylorthosilane

tta – 2-thenoyltrifluoroacetate  
WO<sub>3</sub> – Tungsten trioxide  
UV – Ultraviolet  
V<sub>0</sub> – Open-circuit voltage  
VTF – Vogel-Tammann-Fulcher  
XRD – X-ray diffraction  
ZEBs – Zero-energy buildings  
q – Absolute emission quantum yield  
 $\eta_{\text{int}}$  – Internal quantum efficiency  
 $\eta_{\text{opt}}$  – Optical conversion efficiency  
 $\eta_{\text{solar}}$  – PV efficiency relatively to the total solar spectrum  
 $\eta_{\text{PV}}$  – PV efficiency at the LSC emission spectral range  
 $\chi^2$  – Chi-square  
 $\tau$  – Lifetime  
 $\lambda$  – Wavelength  
 $\varepsilon$  – Molar extinction coefficient

1.1.Introduction

Climate change represents one of the biggest threats of our time. The cause lies on use of fossil fuels (coal, oil and gas) for energy production leading to a dramatic increase of carbon dioxide (CO<sub>2</sub>) levels in atmosphere with huge consequences worldwide (e.g. sea level rise, change in the amount and pattern of rainfall).<sup>1,2</sup> Despite the increase in the use of renewable energies, the perspective still points out the essential role of fossil fuels in the coming years, **Figure 1.1A**.

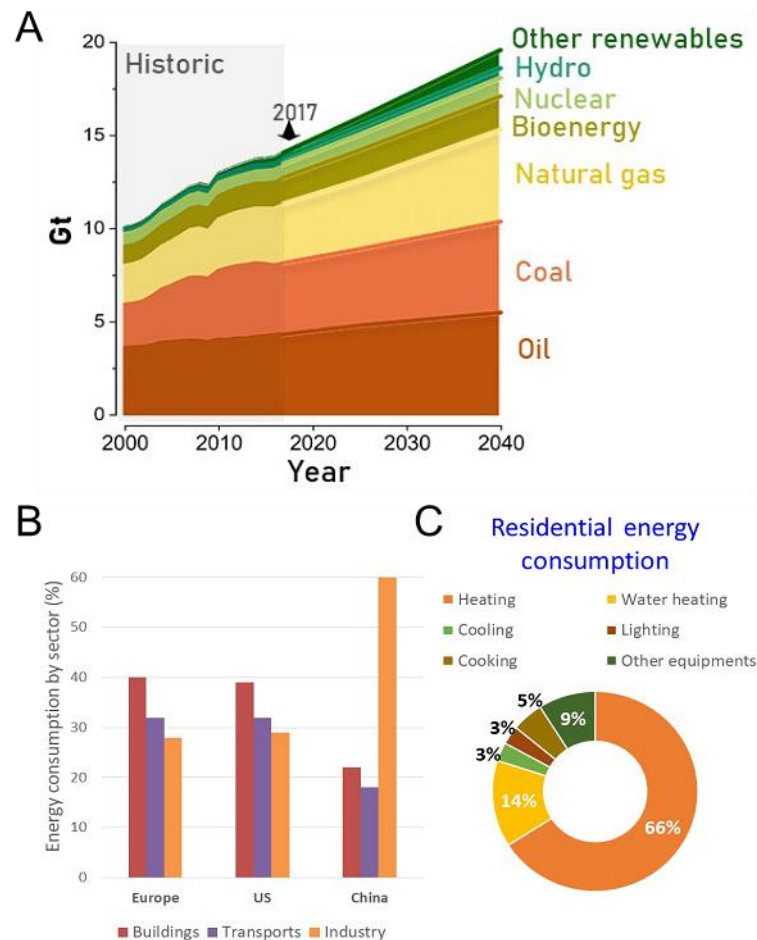


**Figure 1.1.** (A) Representation of the consumption of fossil fuels from 2000 to 2017 and the prediction until 2040. Adapted from <sup>3</sup>. (B) Schematic representation of the energy consumption in Europe, United States, and China in different sectors. (C) Distribution of the residential energy consumption over the different house appliances. Adapted from <sup>4,5</sup>.

Nowadays, the world's energy is mainly consumed by three sectors: buildings, industry, and transportation. The building sector represents 30–40% of the primary energy worldwide. The energy spent in buildings is mainly used for heating, cooling, and lighting (**Figures 1.1B** and **1.1C**). Therefore, reducing building energy consumption can have a beneficial impact on climate.<sup>6</sup> To address this issue, the European Union (EU) has devoted efforts on legislative instruments (2010 Energy Performance of Buildings Directive and the 2012 Energy Efficiency Directive) to promote the energy performance of buildings.<sup>7,8</sup> In 2018, Directive UE 2018/844 replaced the 2010 Energy Performance of Buildings Directive in order to speed up the buildings modernization, given emphasis to building envelope (specially windows) and new technologies allowing the smart and efficient control of the buildings environment. The objective of such strategies is the full decarbonisation of the building sector by 2050.<sup>9</sup> At a global level, the United Nations introduced 17 Sustainable Development Goals for 2030 that intend to be a foundation for a better and more sustainable future.<sup>10</sup> Out of these, Goals 7, 11, and 13 (**Figure 1.2**) aim at making energy more sustainable and accessible to everyone, at rendering cities more inclusive, safe, resilient and sustainable, and at ensuring universal access to affordable, adequate and sustainable housing for all, and thus provide better well-being, safety, less climate change, and more economic progress. For this commitment, new energy efficient technologies are required.



**Figure 1.2.** Three of the United Nations Sustainable Development Goals for 2030. Adapted from <sup>10</sup>.

Fenestration products play an important role in energy saving, since up to 60% of the total energy loss of a building is associated with its windows.<sup>11</sup> Electrochromic devices (ECDs) have emerged as a green technology and have a high potential when applied to windows (smart windows), as they allow tuning the transmission of the solar visible radiation (light) and near-infrared (NIR) radiation (heat) through the application

of a low electric voltage ( $\sim 1\text{-}3\text{ V}$ )<sup>12</sup> (**Figure 1.3**). This sort of technology leads to the curbing of the electric lighting demand, and to the reduction of cooling and heating loads, resulting in a marked decrease of energy consumption in glazed buildings, and providing in parallel more comfort to the building's occupants.<sup>12-14</sup>

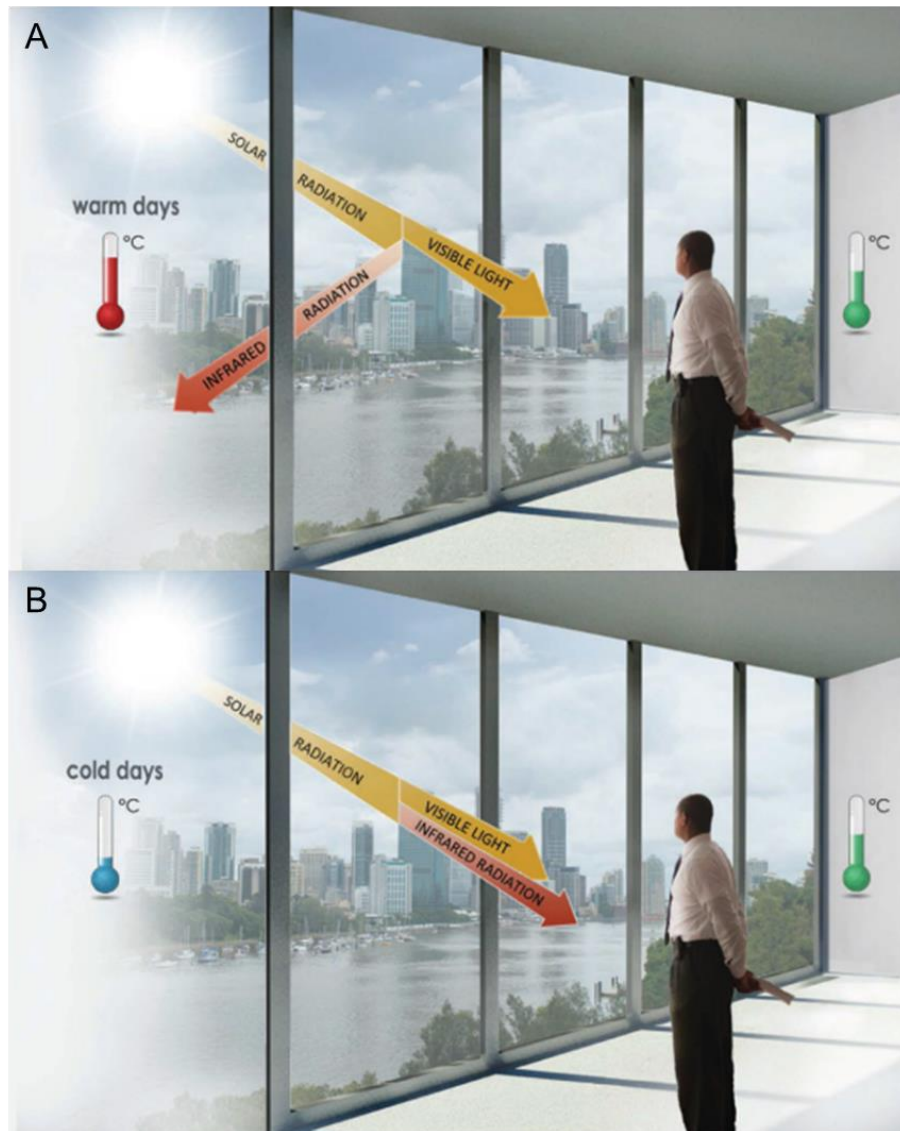


**Figure 1.3.** Schematic diagram of an ideal smart window reflecting NIR in (A) warm days and allowing it to enter in (B) cold days, while remaining transparent in the visible region in both climate conditions.<sup>15</sup>

The smart management of solar radiation has a huge potential compared with other energy sources (**Figure 1.4**). The solar energy that arrives on Earth represents as much as 10 000 times the global energy requirement.<sup>2,16</sup> Photovoltaics (PVs) is an effective way of using that energy by converting solar radiation into electricity and increase the

buildings energy independence with installation of PV modules on roofs and also on building façades.<sup>16</sup>

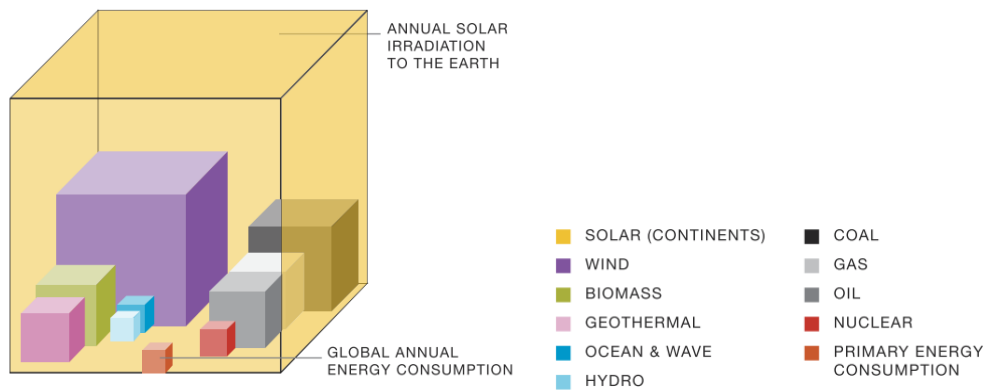


**Figure 1.4.** Scheme of the solar irradiation versus established global energy resources. Fossil fuels are expressed with regard to their total reserves, whereas renewable energies are expressed to their yearly potential. From Solar generation 6, adapted from <sup>16</sup>.

One barrier for PVs building integration is the panels' optimal operation. This is only achieved under uniform direct irradiation, which is not always the case as sunlight is often diffuse and shaded.<sup>17</sup> In addition, for building applications, especially façades and windows, a new approach is necessary to improve aesthetic aspects given the dark and opaque features of PV cells. Building integrated photovoltaics (BIPVs) is a new and rising field that intends to develop energy-efficient buildings by incorporating PV technology into the building structure. To facilitate this integration, emphasis has been given to luminescent down-shifting (LDS) layers and luminescent solar concentrators (LSCs) (**Figure 1.5**). The LDS layers consist of the application of a direct coating on the PV cell surface that: (1) absorbs the incident complementary radiation of the PV cell and re-emits it at a specific wavelength that is refracted to the PV cell; and (2) promotes the reduction of radiation losses on the surface by decreasing reflection and increasing trapping efficiency of the solar radiation.<sup>18</sup> Another interesting approach toward BIPVs is mediated by LSCs that operate similarly under direct and diffuse sunlight conditions.<sup>19</sup> LSCs comprise a transparent matrix incorporating optically active centres that absorb incident radiation and re-emit it at a specific wavelength, which is afterwards transmitted by total internal reflection to PV cells located at the matrix edges.<sup>20,21</sup> **Figure 1.5C** illustrates a window consisting of a triple-insulated glass unit embedding a LSC replacing the inner glass panel.<sup>22</sup>

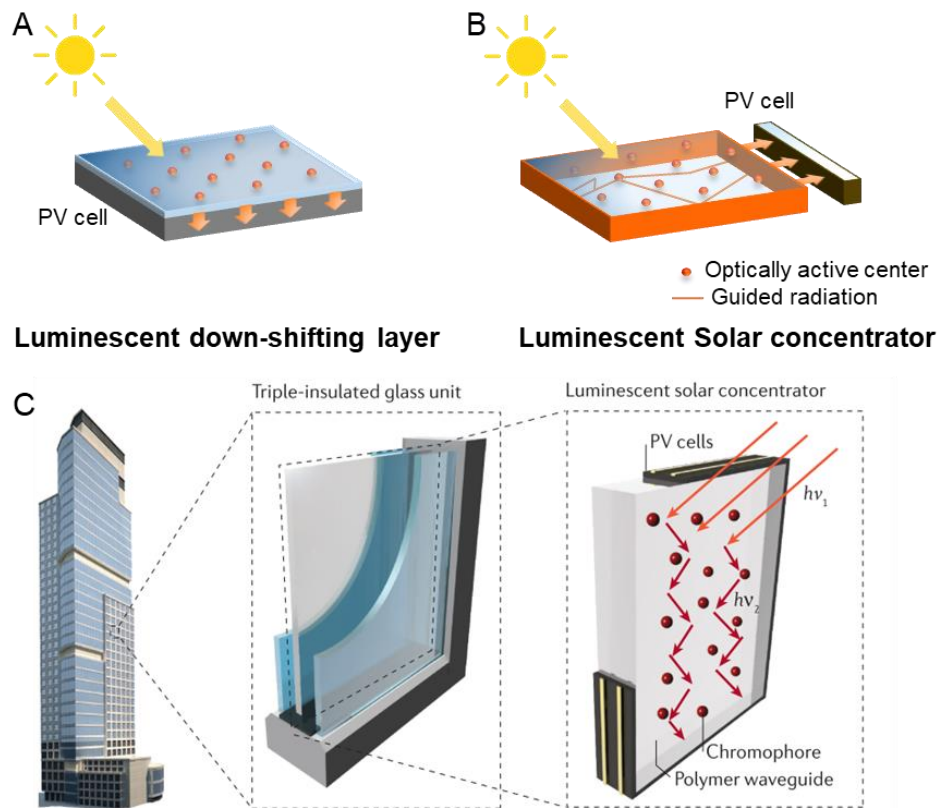


**Figure 1.5.** Schematic representation of a solar cell (A) including a LDS layer and (B) coupled to a LSC. Adapted from <sup>23</sup>. (C) Schematic representation of a window consisting of a triple-insulated glass unit embedding a LSC. Adapted from <sup>22</sup>.

The LDS layers and the LSCs devices are in distinct phases of advancement. For instance, LSCs have found their way to real-world applications from highway sound barriers working as solar energy harvesting units (**Figure 1.6A**) to PV transparent windows (e.g., Glass to Power company,<sup>24</sup> **Figure 1.6B**) and luminescent greenhouses (e.g., UbiQD<sup>25</sup>). The latter example of application is interesting since it takes advantage of the possibility of producing LSC films with tuneable emission colour to selectively filter the sunlight that goes inside the greenhouses. This enables the control of the circadian rhythms of plants or animals, favouring the growth process and maximizing agricultural production (**Figure 1.6C** and **1.6D**).<sup>17</sup>

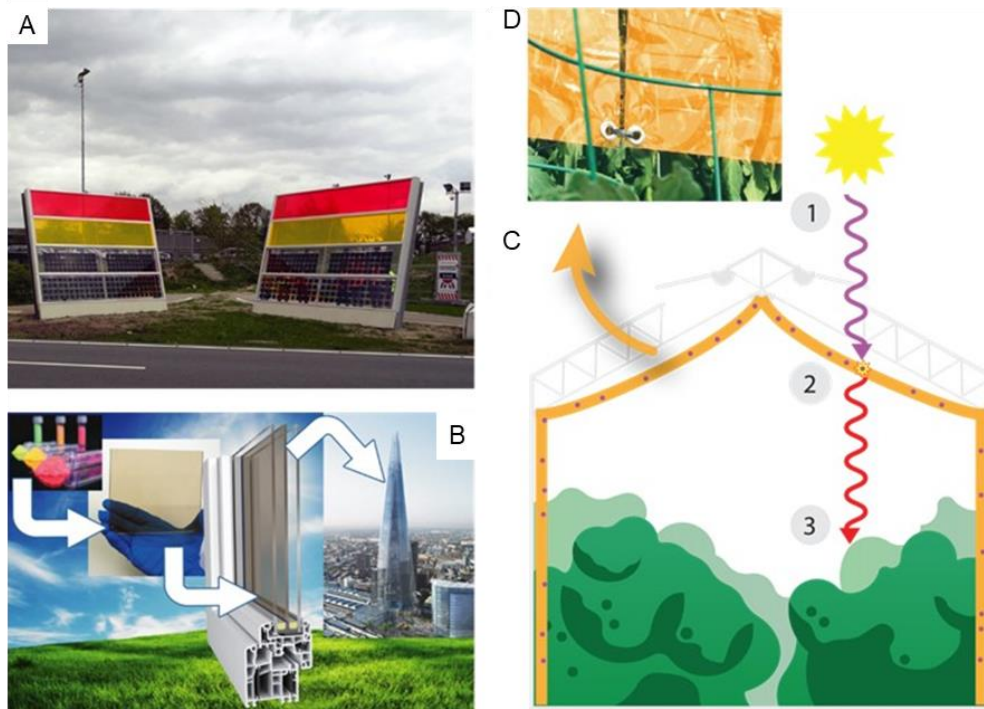


**Figure 1.6.** Practical examples of LSCs. (A) Photographs of the LSC-based noise barrier site on the left faces North/South, and the barrier on the right faces East/West; (B) Glass to Power company LSC concept; and (C) UbiQD greenhouse scheme with (D) photograph of the LSC films. Adapted from <sup>17</sup>.

The combined use of ECDs, LDS layers, and LSCs represent one attractive strategy to reduce the amount of energy consumption in buildings. **Figure 1.7** illustrates the combination of two of these technologies. The underlying concept relies on the use of LSCs that absorb UV radiation and convert it into energy that will be absorbed by the PV cell located at its ends. Then, the energy generated by the PV cell will be used to power the ECD that controls the transmission of visible and NIR radiation hitting the building.<sup>26,27</sup> The judicious choice of the emitting centres in the LSC enables the adjustment of the emission colour, adding aesthetic to the device. Despite the great potential of this multi-device approach, the development of ECD, LDS layers and LSCs faces various challenges, most of which related with the materials used in their design.

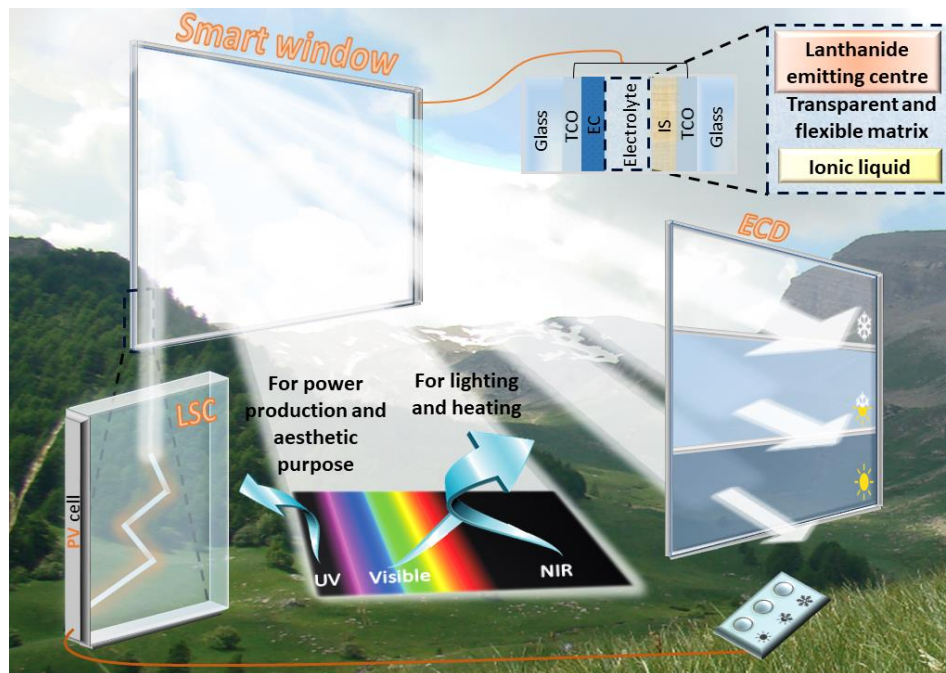


**Figure 1.7.** Proposed scheme for harvesting, conversion, and management of the solar spectrum. In the ECD assembly (top right) TCO, EC and IS correspond to the transparent conductive oxide, electrochromic, and ion storage layers, respectively.

## 1.2. Electrochromic windows

ECDs rely on a specific type of chromism, named electrochromism, a process that causes a reversible change in a compound's colour by application of an electric current.<sup>28</sup> This technology has known several applications for the automotive industry,<sup>29</sup> writing boards,<sup>30</sup> displays, mirrors and lenses.<sup>31</sup> However, smart windows remain as one of the most interesting applications given their potential for ZEBs.<sup>1,12,32–37</sup>

Large area EC windows (ECWs) are a promising “green” technological solution for the fabrication of cheap, smart switchable, and energy-efficient architectural fenestration, offering clear advantages over conventional windows:<sup>38,39</sup> lighting savings due to daylight use and reduced peak cooling loads, better glare control, thermal/visual comfort and outdoors view improvement, free size, design and pattern, and possibility of incorporation into various fenestration design elements without adverse energy and environmental consequences. In addition, ECWs may be used as architecturally and aesthetically appealing dynamic coatings in building façades, and exhibit “memory effect” (zero current consumption after coloration). Research on ECDs remained until recently restricted to non-architectural systems.<sup>11,40,41</sup> In the last few years the focus of

this area has shifted to the production of large scale ECDs for light control in buildings. Flexible ECDs, which may be added as a layer to the existing glass-based windows, eliminating the need for the full replacement of the latter and reducing the cost of current smart windows, will contribute to make EC technology affordable and commercially scalable.<sup>42-44</sup>

The sol-gel process is one of the most attractive methods for the fabrication of ECDs. The "all sol-gel" ECD concept<sup>45,46</sup> led to intense research on organic/inorganic hybrid electrolytes. Ormolytes (organically modified silicate electrolytes) are a valuable alternative to classical polymer electrolytes (PEs), because they can be easily processed into transparent thin films with improved mechanical resistance, chemical/thermal stability, and ionic conductivity.<sup>44</sup>

A typical ECD configuration comprises two external substrates plus a 5-layer assembly including the ion conductor (IC or simply electrolyte) layer sandwiched between the EC and ion storage (IS) layers which are in turn in contact with two TCO layers. In the next sections of the present chapter, the main aspects associated with the substrates, the TCO layers, and the electrolytes that should be taken into consideration in the ECD design will be summarised. The EC layers will be discussed in detail in section 2.2.

### *Substrate features*

The ECD substrates can be made of transparent glass or polymers, such as poly(ethylene terephthalate) (PET),<sup>47-49</sup> poly(vinyl butyral) (PVB),<sup>50</sup> or poly(ethylene-co-vinyl acetate) (PEVA)/PET.<sup>51</sup> Glass substrates are the most widely used (**Figure 1.7top**). The use of polymeric substrates is, however, more appealing, allowing the fabrication of flexible, lighter and cheaper ECDs and especially the addition of the ECD to an already existing window.<sup>52,53</sup> Conductive polymers (CPs) are particularly promising candidates as substrates, with emphasis on poly(3,4-ethylenedioxythiophene) (PEDOT) and poly(3,4-ethylenedioxythiophene):poly(styrene sulfonate) (PEDOT:PSS) that can work simultaneously as EC layer and current collector layer, thus simplifying the device composition.<sup>54-56</sup>

## *TCO features*

The TCOs are used as electrodes when low resistance electrical contacts are required without blocking visible light. The most important intrinsic properties of a TCO material are the band gap and the charge carrier effective mass. The energy band gap of the material should be wide enough so that light (frequencies varying from 1.59 to 3.18 eV) is not absorbed. In addition, high charge carrier mobility is desired.<sup>57</sup> Good properties have been obtained with indium tin oxide (ITO,  $\text{In}_2\text{O}_3:\text{Sn}$ ), indium zinc oxide (IZO,  $\text{In}_2\text{O}_3:\text{Zn}$ ), and fluorine tin oxide (FTO,  $\text{SnO}_2:\text{F}$ ).

ITO, the most widely used n-type TCO, possesses an optical transparency above 80% in the visible spectral region, and a conductivity around  $10^4 \text{ S cm}^{-1}$ . This type of semiconductor must be produced as a thick film (around  $\sim 200 \text{ nm}$  or higher) with low emissivity. As the film thickness is comparable with the wavelengths of visible light, optical effects, such as iridescence, are observed. ITO's optical and electrical properties are directly dependent on the deposition parameters and deposition technologies which are known to yield very different nanostructures.<sup>12,37</sup> Besides ITO, another important TCO is IZO which exhibits low electrical resistivity ( $6 \times 10^{-4} \Omega \text{ cm}$ ), optical transparency above 80% in the visible and NIR regions, and low surface roughness. Moreover, IZO thin films are deposited at low temperatures ( $< 100 \text{ }^\circ\text{C}$ ), a very important characteristic if plastic substrates - that demand low processing temperatures - are used.<sup>58</sup> TCO films, such as ITO and IZO, are extensively used as transparent electrodes in other technologies, such as solar cells and touch panels.<sup>59</sup>

## *Electrolytes' characteristics*

The electrolyte is one important components in the ECD, since it avoids direct electrical contact between the two EC-coated electrodes, but allows the mutual ionic exchanges. Its electronic conductivity must be below  $10^{-12} \text{ S cm}^{-1}$  and its ionic conductivity should range between  $10^{-3}$  and  $10^{-7} \text{ S cm}^{-1}$ , depending on the application.<sup>28</sup> High ionic conductivity provides faster coloration/bleaching, higher transmittance modulation, and shorter switching time. Other characteristics that should also be addressed by electrolytes aiming ECD applications are high transparency, good electrochemical stability, and good compatibility with the anodic and cathodic layers in order to get the ECD to work properly.<sup>12</sup> The electrolyte can be a liquid, a gel, or a solid.<sup>60</sup>

For ECDs, PEs constitute a better option over conventional liquid electrolytes as they present, neither risk of leaking, nor dissolution of the EC and IS layers, that lead to fast device degradation<sup>42</sup>. The electrolyte composition is extremely important as it influences the cycle life of the device. The interfaces between the electrolyte and electrodes dictate the device performance, and the electrochemical stability govern the lifetime of the ECD.<sup>28</sup> The open circuit memory of ECDs is also an important feature for smart window applications, which can hold their electrical charge and optical properties for long periods of time without any energy supply. This effect is directly dependent on the electrical insulation of the electrolyte.<sup>12</sup> Several other requirements should be fulfilled for the successful application of PEs in ECDs, as illustrated in **Figure 1.8**.<sup>12,43,61,62</sup>

PEs consist of salts dissociated in a neutral polymer matrix. In PEs, the charge carriers are single cations, single anions, ion contact pairs, or ionic clusters (or aggregates), depending on the solubility degree (i.e., the extent of ionic association). The ionic environment determines the charge carrier's mobility, as it is dependent on the interaction of the ions with the host polymer and other ions, the nature of the charge carriers, and the flexibility of the polymer chains. Some interpretations have been suggested to explain the ion transfer mechanism in PEs. A hopping mechanism based on the motion of small cations ( $\text{Li}^+$ ,  $\text{Na}^+$ ,  $\text{K}^+$ ) down through channels inside the helical crystalline structure of the archetypal poly(oxyethylene) (POE) host polymer was first proposed.<sup>63</sup> A mechanism based on ion movement associated with the polymer segmental motions via formation and breaking of the coordination bonds between the cations and the host polymer was also proposed.<sup>64</sup> Taking into consideration ion-ion interactions and the different ionic species in PEs, two kinds of ion motion were suggested: (1) ion motion mediated by polymer chain motion, and (2) ion motion from ionic cluster to ionic cluster where polymer chains work as anchoring points.<sup>64</sup>



**Figure 1.8.** Scheme illustrating the most important requirements to be fulfilled by PEs.<sup>12</sup>

PEs can be primarily categorized into solid PEs (SPEs), gel PEs, polyelectrolytes, and composite PEs. The first works reporting the use of polymers as the electrolyte component in ECDs appeared in the early 1980s.<sup>28,65</sup> Some of the most widely used PEs are POE, poly(ethylene glycol) (PEG),<sup>66</sup> poly(vinyl alcohol) (PVA), poly(acrylonitrile) (PAN), poly(methyl methacrylate) (PMMA),<sup>67</sup> poly(vinyl chloride) (PVC), poly(vinyl sulfone) (PVS), and poly(vinylidene fluoride) (PVDF).<sup>66–68</sup> POE has demonstrated high compatibility for a wide range of salts, leading to good film-forming characteristics. Besides, it can be prepared in different sizes and shapes, it is easily synthesized and modified, and is obtained at a low cost. The ionic conductivities range from  $10^{-8}$  to  $10^{-4}$  S  $\text{cm}^{-1}$  at temperatures between 40 and 100 °C, respectively, limiting real-world applications at room temperature. PEs synthesized by the sol-gel method (e.g., POE/siloxane materials), usually known as ormolytes, have been produced and successfully used for ECDs applications, since they can be easily processed into highly transparent, amorphous, thin films with improved mechanical resistance, chemical/thermal stability, and acceptable ionic conductivity.<sup>44,69–74</sup>

Several dopants, such as ionic liquids (ILs) and luminescent centres, can be included in the formulation of PEs to enhance the ECD performance and/or functionality.

ILs are salts with melting points below 100 °C. ILs have been proposed as electrolytes on account of their intrinsically high ionic conductivity ( $10^{-4}$  to  $8 \cdot 10^{-2}$  S  $\text{cm}^{-1}$  at room temperature), wide electrochemical potential window (around 5.7 V with Pt electrodes), and high thermal stability (up to 200-300 °C).<sup>75</sup> The sub-class of room temperature ILs (RTILs) comprises salts with melting point at or below room

temperature, making them liquids at room temperature. RTILs own the same features as ILs, i.e., very low vapour pressures, low flammability, and great versatility in terms of the available design of the constituent ions that allows to modify the properties to meet a particular need in a specific application.<sup>76,77</sup> Not surprisingly, RTILs are often added to PEs to improve their properties, providing new features to ECDs, and ultimately to smart windows.<sup>12</sup>

Salts and complexes of trivalent lanthanide ions ( $\text{Ln}^{3+}$ ) can be also incorporated into the electrolyte to impart optical properties.<sup>78–81</sup> The latter compounds are particularly appealing, since they display unique photoluminescent features, such as narrow emission bands, long emission lifetimes, tuneable emission spectral range (UV/visible/NIR), and high luminescence quantum efficiency. Through the “antenna effect”,  $\text{Ln}^{3+}$ -based complexes can absorb in the UV/visible regions and emit in the visible and NIR spectral regions. Luminescent poly( $\epsilon$ -caprolactone) (PCL)/siloxane-based ormolytes doped with  $\text{Li}^+/\text{Eu}^{3+}$  salts<sup>81</sup>,  $\text{Li}^+/\text{Er}^{3+}$  salts<sup>82</sup>, and  $\text{K}^+$  salt/ $\text{Eu}^{3+}$  complex<sup>82</sup> were successfully tested in ECDs.

A summary of several technical parameters reported in the literature for ECDs comprising the same EC electrodes (tungsten trioxide ( $\text{WO}_3$ ) and nickel oxide ( $\text{NiO}$ )), but different types of electrolytes (hybrid materials,<sup>70,79,83</sup> polymers (e.g., PMMA<sup>84–87</sup> and polysaccharides<sup>88,89</sup>), and ceramics<sup>90–92</sup>) is given in **Table 1.1**. The electrolyte designation in this table follows the nomenclature adopted by the authors in each article.

**Table 1.1.** Electro-optical parameters of WO<sub>3</sub>-/NiO-based ECDs in the coloured (c) and bleached (b) states. V is applied voltage, t is switching time, T is transmittance, ΔOD is optical density, and CE is coloration efficiency.

ECD configuration (electrolyte in bold)	Conductivity (S cm <sup>-1</sup> )	Size (cm <sup>2</sup> )	t <sub>b</sub> /t <sub>c</sub> (sec)	V <sub>c</sub> /V <sub>b</sub> (V)	λ (nm)	T <sub>b</sub> /T <sub>c</sub> (%)	ΔOD	CE <sub>in</sub> (cm <sup>2</sup> C <sup>-1</sup> )	CE <sub>out</sub> (cm <sup>2</sup> C <sup>-1</sup> )	Open circuit memory test	Cycling stability (cycles)	Ref
g a-IZO a-WO <sub>3</sub>   <b>d-U(2000)</b> <sub>60</sub>  NiO a-IZO g	(T= 21°C) 6.3 x 10 <sup>-5</sup>	4.84	50/50	-2.5/3	555 1000	70/6 83/4	1.1 1.3	-12538 -14818	2901 3428	-2.5 V/134 days (11 to 35%) -2.5 V/134 days (T = 9 to 41%)	>500	70
g ITO WO <sub>3</sub>   <b>d-PCL(530)</b>   <b>si<sub>3.8</sub>KEu</b>  NiO ITO g	(T= RT) 1.7 x 10 <sup>-4</sup>	1.47	50/50	-3/3	555	38.7/34.1	0.06	-	126	-	>500	79
g FTO WO <sub>3</sub>   <b>PEO/PEGMA:Li<sup>+</sup></b>  NiO:Li FTO g	-	144	180/180	-2.5/2.5	550 1000	72/42 50/13	-	-	-	14 h (T <sub>rise</sub> < 5%)	-	83
g ITO WO <sub>3</sub>   <b>PSSE</b>  NiO ITO g	-	-	-	-1.6/1.6	555	75/32	-	-	87.8	-	8479	84
p ITO WO <sub>3</sub>   <b>PMMA-PPG-Li<sup>+</sup></b>  NiO ITO p	-	200	200/200	-	555	70/35	-	-	-	-	-	85
g ITO WO <sub>3</sub>   <b>LiTaO<sub>3</sub></b>  NiO ITO	-	-	-	-1.6/0.5	550	91/21	0.64	-	50.4	-	11270 ΔT = 6% of original	90
g/a-IZO/WO <sub>3</sub>   <b>CG<sub>50</sub>Er<sub>40</sub></b>  NiO/a-IZO/g	(T= 20°C) 1.5 x 10 <sup>-4</sup>	4.84	50/50	-3/3	550 1000	52/7 61/11	0.89 0.75	-15902 -13400	3072 2589	-	450	88
g/FTO/a-WO <sub>3</sub>   <b>LiClO<sub>4</sub>+PC+PMMA</b> /a-NiO <sub>360</sub> /FTO/g	-	2.0	11/13†	-2.1/2.1	633	62/6	1.01*	141	-	-	400, ΔT = 100% of original	87
FTO g /NiO/ <b>PADA gel electrolyte</b> /WO <sub>3</sub> /FTO g	(T= 25°C) 1.3 x 10 <sup>-2</sup>	9	7.5/8.5†	-2.3/2.3	660	72/11(1 <sup>st</sup> cycle)	0.82*	78.7	-	1 day (T = 11 to 33%)	-	86
g/FTO/NiO/ <b>GSE</b> /WO <sub>3</sub> /FTO/g	1.04x10 <sup>-4</sup> (13 wt% LiClO <sub>4</sub> ), 2.02x10 <sup>-4</sup> (10 wt% LiCl)	6	60/60	-2/2	600	45/7	0.80	23	-	-	-	89

† calculated; \* calculated values based on T<sub>b</sub>/T<sub>c</sub>; g – glass; p – plastic; RT – room temperature; Si – siloxane;

(a-)IZO – (amorphous) indium zinc oxide; (a-)WO<sub>3</sub> – (amorphous) tungsten trioxide; CG - κ-carrageenan (κ-Cg) + glycerol; dU = di-ureasil hybrid matrix; FTO - Fluorine tin oxide; GSE - Gelatin-based solid electrolyte; ITO - Indium tin oxide; NiO – Nickel oxide; PADA (PC+LiClO<sub>4</sub>+N, N-diethylaminoethylmethacrylate (DEA) + acrylic acid); PC - Propylene carbonate; PEGMA - poly (ethylene glycol methacrylate); PEO - poly(ethylene oxide); PMMA – Poly(methyl methacrylate); PPG - poly(propylene glycol); PSSE - methyl-methacrylate +LiClO<sub>4</sub>+PC.

### 1.3. Luminescent solar concentrators and down-shifting layers

For applications in LDS layers and LSCs, optically active materials with spectral absorption overlapping the AM1.5G spectrum, emission in the visible-to-NIR spectral range (the Si PV cells highest absorption region), and high absolute emission quantum yield in the visible/NIR ( $>0.5$ / $>0.1$ ), are very interesting options. Several studies on LDS layers and LSCs have been reported using different LDS materials, such as quantum dots (QDs),<sup>93–95</sup> organic dyes,<sup>20,94,96,97</sup> and Ln<sup>3+</sup>-based coordination complexes mainly including Eu<sup>3+</sup>.<sup>80,96,98–101</sup> **Figure 1.9** shows examples of LSC (**Figure 1.9A-C**) and LDS (**Figure 1.9D-F**) layers.

Lanthanide-based complexes are particularly attractive candidates, as they present high absorption coefficient and emission from visible to NIR spectral regions,<sup>102</sup> with large ligands-induced Stokes shift.<sup>17</sup> These compounds typically absorb in the UV/blue spectral region, yielding transparent and colourless devices.<sup>93,98,103</sup> Some figures of merit recently reported in the literature for Ln<sup>3+</sup>-based LDS layers and LSCs are presented in **Tables 1.2** and **1.3**, respectively. Relevant parameters, such as the maximum absorbing ( $\lambda_{\text{abs}}$ ) and emission ( $\lambda_{\text{em}}$ ) wavelengths, absolute power conversion efficiency (PCE), percentage increase in PCE ( $\Delta\text{PCE}$ ) compared to the bare cell, external quantum efficiency (EQE) increase and percentage of optical conversion efficiency ( $\eta_{\text{opt}}$ ), are also included. The phosphors designation in these tables follows the nomenclature adopted by the authors in each paper. It can be noticed that the most extensively used substrates (or host materials) are transparent (e.g., PMMA, inorganic crystalline materials, glasses, organically modified silicates (ORMOSILs), and organic paint thinners). Among these, polymeric materials are of particular interest since they can exhibit high transparency in the visible region of the spectrum, acceptable resistance relative to heat and humidity fluctuations, high mechanical strength, and very good host environment for organic dye molecules. In addition they are materials already used in PV industry (e.g., the poly(ethylene-co-vinyl acetate) (PEVA) copolymer is used in wafer-based Si solar cells as entrapment component).

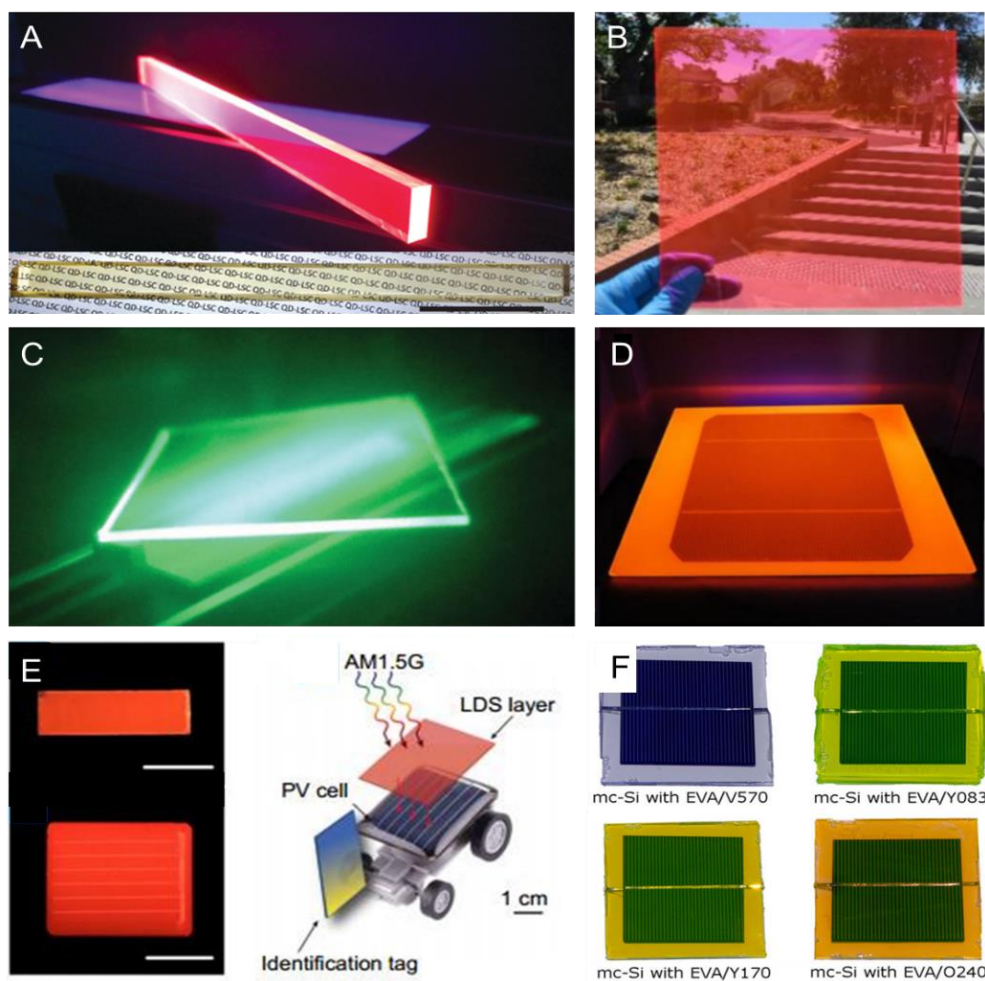


**Figure 1.9.** (A) Photograph of a QD-PMMA-based LSC comprising cadmium selenide/cadmium sulfide (CdSe/CdS) QDs ( $R_0 = 1.5$  and  $H = 4.2$  nm) illuminated by UV lamp emitting at 365 nm (top) and under ambient illumination (bottom) (scale bar: 5 cm); (B) PMMA-based LSC outdoors on a sunny day; (C) Photograph of a LSC comprising 0.3 wt% zinc sulfide (ZnS)-coated  $\text{CuInSe}_x\text{S}_{2-x}$  QDs (LSC dimensions,  $12 \times 12 \times 0.3$  cm<sup>3</sup>) taken with an UV-filtered infrared camera (the LSC is illuminated at 365 nm); (D) Photographs of the luminescent thin film attached on top of c-Si solar cells; (E) Photographs of the LDS layers based on tU5-Eu (tU5 = tri-Ureasil), under 365 nm (scale bars:  $10^{-2}$  m), scheme of the solar vehicle with the LDS coating (Right); (F) Solar cells (mc-Si, where mc is multicomponent) coated with different LDS PEVA-based materials. Adapted from <sup>104–109</sup>.

**Table 1.2.** Figures of merit of illustrative examples of Ln<sup>3+</sup>-based LDS layers applied on different PV cell types, where the absolute power conversion efficiency (PCE) achieved and the percentage increase in PCE ( $\Delta$ PCE) compared to the bare cell are also presented.

Cell	Phosphor	$\lambda_{abs}$ (nm)	$\lambda_{em}$ (nm)	PCE	$\Delta$ PCE (%)	EQE increase (%)	Ref.	
c-Si	d-UPTES(600):TbCl <sub>3</sub> :SA:NaOH	315	543	-	-	27	108	
	t-U(5000)/Eu(tta) <sub>3</sub> ·2H <sub>2</sub> O	365	615	-	-	23		
	[Eu(tta) <sub>3</sub> (tppo) <sub>2</sub> ]/PEVA	365	-	-	8	19	110	
	Eu(tta) <sub>3</sub> (phen)/PEVA	325	-	-	-	17		
	[EuL <sub>3</sub> ]/PEVA	325	615	9.51	6	15		
		[TbL <sub>3</sub> ]/PEVA	325	540	9.42	5	15	100
		[Eu(tta) <sub>3</sub> bpbpy]/PVA	300-400	-	-	-	50	
		Eu-doped phosphor/Ag NP/SiO <sub>2</sub>	-	-	-	-	12	111
			-	-	-	-	8	112
		Eu-doped phosphor/SiO	-	-	-	-	7	113
		-	-	-	-	10	114	
	[Eu(tfc) <sub>3</sub> : EABP] 1:1/PEVA	-	-	-	-	5	115	
	[Eu(tfc) <sub>3</sub> /Eu(dbm) <sub>3</sub> phen]/PVA	-	-	-	-	5	116	
	Ba <sub>2</sub> SiO <sub>4</sub> :Eu <sup>2+</sup>	385	504	15.36	0.23	3	117	
	SiO/Ba <sub>2</sub> SiO <sub>4</sub> :Eu <sup>2+</sup>	350	510	17.7	4	3	118	
	Gd <sub>2</sub> O <sub>2</sub> :Eu <sup>3+</sup>	350	625; 700	12.97	244	-	119	
Cds/CdTe	Eu <sup>3+</sup> , Mn <sup>2+</sup> doped glasses	400	615	17.53	7.14	-	120	
	EuD <sub>4</sub> TEA	350	620	3.41	62	25	121	
DSSC	CaAlSiN <sub>3</sub> :Eu <sup>2+</sup>	460	625	5.0	40		122	
	LaVO <sub>4</sub> /Dy <sup>3+</sup>	-	-	-	-	2	123	
	YVO <sub>4</sub> /Eu <sup>3+</sup>	295	610	7.93	7	-	124	
PSC	ZnGa <sub>2</sub> O <sub>4</sub> :Eu <sup>3+</sup>	400	610	13.8	29	-	125	

SA = salicylic acid; tta<sup>-</sup> = 2-thenyltrifluoroacetate; tppo = triphenylphosphine oxide; PEVA = ethylene-co-vinyl acetate; phen = 1,10-phenanthroline; L = triazole-pyridine-bistetrazolate; bpbpy = 4,5-bis(pinene)-2,2'-bipyridine; PVA = poly(vinyl acetate); Eu(tfc)<sub>3</sub> = tris[3-(trifluoromethylhydroxymethylene)-d-camphorate]europium(III); EABP = 4,40-bis(diethylamino)benzophenone; dbm<sup>-</sup> = dibenzoylmethanate; CdS/CdTe = cadmium sulfide/cadmium telluride, DSSC = dye-sensitized solar cell, EuD<sub>4</sub>TEA = europium(III) tetrakis(dibenzoylmethide) triethyl ammonium; PSC = perovskite solar cell.

**Table 1.3.** Figures of merit of illustrative examples of Ln<sup>3+</sup>-based LSCs applied on different PV cell types.

Cell	Luminophore	$\lambda_{abs}$ (nm)	$\eta_{opt}$ (%)	PCE (%)	Ref.
n.a.	Eu <sup>3+</sup> /bridged silsesquioxane	300-380	12.3		126
	Tb-PVA/PMMA	280-400	8.8		127
	Eu <sup>3+</sup> /bridged silsesquioxane	350	1.7		128
	Eu <sup>3+</sup> /bridged silsesquioxane	270	1.2		129
	Tb <sup>3+</sup> /bridged silsesquioxane	270	1.7		129
	tU(5000)/ Eu(tta) <sub>3</sub> ephen	240-450	9.0	n.a.	130
	CdSe/CdS QDs/PMMA	300-1400	10.2		131
	PbS/CdS QDs/Acrylate	300-1400	6.1		95
	CuInSe <sub>x</sub> S <sub>2-x</sub> /ZnS QDs/PLM	300-1400	3.27		106
	TPE/PMMA	320	13.2		132
	tU(5000)/[Eu(btfa) <sub>3</sub> (MeOH) <sub>2</sub> ]2bpta <sub>2</sub>	290-380	3.2	0.007 <sup>a</sup>	133
	Gd <sub>2</sub> O <sub>2</sub> S:Er, Yb/PMMA	n.a.	8.57	6.93	134
	c-Si	Eu(tta) <sub>3</sub> dpbt/PVB 1.6 wt%,	240-450	n.a.	0.2
Eu(tta) <sub>3</sub> (TPPO) <sub>2</sub> /PMMA		250-400		0.28	136
tU(5000)/SiNc		300-450; 600-850	1.5	n.a.	137
dU(600)/chlorophyl		n.a.	3.70	0.10	138
tU(5000)/Rhodamine 6G		n.a.	1.54	0.009	99
glass container/R-phycoerythrin aqueous solutions		300-550	6.88	0.27	139
gem-pyrene ethane/PMMA		300-1400	n.a.	0.32	140
Perylimide-GLYMO		420-620	18.8	n.a.	141
DCJTb, Pt(TPBP)		300-1400	4.7	6.8	97
M <sub>6</sub> (II)X <sub>12</sub>		300-1400	n.a.	0.44	142
CASN:Eu <sup>2+</sup> /PMMA 0.25 wt%		n.a.	4.90 <sup>b</sup>	5.53	143
LR305/Urethane matrix (LT)		300-1400	2.48	0.49	144

n.a. = information not available. PVA = poly(vinyl alcohol); PMMA = poly(methyl methacrylate); tU = tri-ureasil hybrid matrix; tta<sup>-</sup> = 2-thenoyltrifluoroacetate; ephen = 5,6-epoxy-5,6-dihydro-[1,10]phenanthroline; CdSe = cadmium selenide; CdS = cadmium sulfide; PbS = lead sulphide; PLM = poly(lauryl methacrylate); TPE = tetraphenylethene; btfa<sup>-</sup> = 4,4,4-trifluoro-1-phenyl-1,3-butanedionate; MeOH = methanol; bpta<sup>-</sup> = trans-1,2-bis(4-pyridil) ethane; dpbt = 2-(N,N-diethylanilin-4-yl)-4,6-bis(3,5-dimethylpyrazol-1-yl)-1,3,5-triazine; PVB = poly(vinyl-butylal); TPPO = triphenylphosphine oxide; SiNc = silicon 2,3-naphthalocyanine bis(trihexylsilyloxy); dU = di-ureasil hybrid matrix; GLYMO = (3-glycidoxypopyl)trimethoxysilane; DCJTb = 4-(dicyano-methylene)-2-tert-butyl-6-(1,1,7,7-tetramethyljulolidyl-9-enyl-4H-pyran); TPBP = tetraphenyltetraabenzoporphyrin; M= Mo, W; X = Cl, Br, I; CASN = CaAlSiN<sub>3</sub>; LR305 = Lumogen Red 305; LT = urethane-based crosslinked matrix.

<sup>a</sup> single edge; <sup>b</sup> theoretical

## 1.4. Objectives, innovation and methodologies

In the framework of the survey of the state-of-the art presented above, it is clear that there is a global need to improve the energy efficiency of buildings in terms of solar energy harvesting, generation and management. One of the ways of achieving this goal involves coupling of LDS layers and/or LSCs to PV cells and the latter to ECDs. The combination of lanthanide complexes with high quantum efficiency, appropriate host matrices prepared by sol-gel chemistry, and conducting oxide materials transparent in the visible-NIR regions, opens challenging opportunities for the development of new devices with remarkable electro-optical performance and foreseen application as smart windows for ZEBs.

To address UN Sustainable Development Goals, ECDs, LDS layers and LSCs with judiciously chosen emission in the visible (red, blue and green) and NIR regions will be developed and integrated in device systems comprising commercial PV cells. Given the growing interest demonstrated by architects for the construction of modern colourful buildings, the technology proposed in this thesis has a great potential in terms of aesthetics and social impact on the cities of tomorrow. Keeping in mind the results reported in the literature (**Tables 1.1, 1.2 and 1.3**), the objectives of this thesis were the following.

- To produce novel luminescent electrolytes (IL-doped polymer/siloxane and polymer/ionosilica (IS) hybrid films) with good mechanical properties, high thermal stability, high transparency in the visible region, suitable ionic conductivity, large electrochemical stability window, high quantum efficiency, and red/NIR, blue/NIR, and green/NIR emission.
- To demonstrate the applicability of the new materials developed to fabricate LDS layers and LSCs with emission in the visible and NIR spectral regions to be coupled to commercial Si-based cells.
- To fabricate luminescent ECDs with high-to-very high electrochromic contrast, optical density, and coloration efficiency, fast response time, high stability/durability, long lifetime, and large open circuit memory.

To achieve those objectives innovative methodologies were followed, as detailed next.

- To use dipodal polymer/silica host hybrid structures.
- To use imidazolium-based ISs in which the counter ion is a lanthanide complex anion able to harvest UV radiation and emit with a required colour.
- To add lanthanide complexes and lanthanide complex anions with high quantum efficiency.
- To add distinct lanthanide ions: one ion should emit in the visible region and the other in the visible-to-NIR region.
- To add ILs to increase the electrolyte ionic conductivity and to adjust viscosity.
- To use external visible/NIR-TCO layers.
- To use the materials synthesized first in independent ECDs, LDS layers and LSCs and subsequently integrate the LDS layers and LSCs.
- To use glass substrates.

### 1.5. Organization of the thesis

This thesis is divided into the following six chapters and two Appendices:

- **Chapter 1** describes the motivation and context of this thesis, the summary of the state of the art, the objectives, and the original contribution.
- **Chapter 2** deals with the fundamentals of the sol-gel method, and presents the working principles of the ECDs, LDS layers, and LSCs.
- **Chapter 3** reports the synthesis and characterization of novel lanthanide ( $\text{Nd}^{3+}/\text{Eu}^{3+}/\text{Tb}^{3+}/\text{Yb}^{3+}$ )-doped imidazolium-based ISs embedded in PMMA. These materials were processed as LSCs and LDS layers and their optical performance was characterized. The combination into a single device, using the same optically active material ( $\text{Eu}^{3+}$ -based ISs incorporated into PMMA), resulted in a significant absolute increase in the PV cell EQE of ~32% between 300-360 nm relatively to the bare PV cell, which proves the potential of proposed materials and methodology.
- **Chapter 4** addresses the fabrication of ECDs where the IC is composed of a diureasil hybrid material doped with the IL 1-butylimidazolium trifluoromethanesulfonate ([BIm][TfO]). The combined use of a-IZO, a conducting oxide transparent in the visible and NIR spectral regions, and of the

di-urea cross-linked POE/silica hybrid, obtained by sol–gel chemistry, allowed the production of a glass/a-WO<sub>3</sub>/electrolyte/c-NiO/a-IZO/glass ECD with voltage-actuated coloration tuning, enabling three-mode operation (bright hot, semi-bright warm, and dark cold), and offering several unprecedented electro-optical figures of merit, such as high optical modulation, colossal coloration efficiency, excellent memory effect, and unusual self-healing ability following mechanical stress.

- **Chapter 5** reports the synthesis of a new electrolyte system inspired in the LDS/LSC layer successfully introduced in **Chapter 3**. The new material is composed of PMMA doped with a mixture of Eu<sup>3+</sup>- and Nd<sup>3+</sup>-based ISs, and the IL 1-n-butyl-3-methylimidazolium hexafluorophosphate ([BMIm][PF<sub>6</sub>]). This material was tested in an ECD with a configuration identical to that employed in **Chapter 4**. The ECD delivered a number of interesting features, in particular good cycling stability, high coloration efficiency, and emission in the visible/NIR region. With these encouraging results the foreseen application of the PMMA-based composites doped with the Ln<sup>3+</sup>-based ISs introduced in **Chapter 3** were extended to the field of ECWs. Thus these transparent luminescent materials might operate simultaneously as ECD electrolyte and LDS or LSC layers of windows containing edge-mounted PV cells. This design would guarantee in a single device system energy harvesting, energy generation, and energy management ability.
- **Chapter 6** provides the general conclusions and perspective work.
- **Appendices A** and **B** describe the experimental details concerning the experimental characterization techniques and devices fabrication, respectively. The list of publications resulting from this thesis is presented in **Appendix C**.

#### 2.1.Sol-gel method

The production of new materials that combine different properties is the key to innovative applications. The sol-gel process, a bottom-up chemical method, is extremely attractive, since it allows the synthesis of nanostructured materials whose morphology, molecular structure, and properties can be adjusted through a judicious choice of the process parameters to achieve materials with desired properties. The method versatility relies, not only on the control of the type and concentration of the precursor compounds in the reaction medium leading to products with high homogeneity and purity, but also on the chemical manipulation, since the sol formation makes the control of the structure at the molecular scale possible. Moreover, this process enables the preparation of unique multifunctional organic–inorganic hybrids, such as aerogels, xerogels, ceramics, and powders, at ambient temperature.<sup>145</sup> In the end, materials with the required surface properties, shape, and other physical-chemical features can be obtained for optimized and specific applications.

In this thesis, two types of organic-inorganic hybrid materials were synthesized by the sol-gel process: (1) ISs, a class of organosilicas combining the advantages of silica and ILs; (2) bridged silsesquioxane materials incorporating ILs.

Fundamental features of the sol-gel process and of the above classes of hybrid materials will be addressed in the next subsection.

## *Fundamental features*

The sol-gel synthesis was first reported by the French chemist Jacques-Joseph Ebelmen ca. 175 years ago, when he observed the formation of a transparent material (hydrated silica) as a result of the hydrolysis of esters of silicic acid (or alkoxides).<sup>146,147</sup> Nevertheless, it was not until the 1970s that the synthesis and chemical properties of metal alkoxides were broadly studied.<sup>146</sup> In 1971, with the patenting of the low-bulk density silica production process, involving the hydrolysis of tetraethoxysilane (or tetraethylorthosilane (TEOS)) with cationic surfactants, the basic principles of sol-gel chemistry in the framework of silica gel formation were established. Differing from common glass, that consists of a viscous fluid resulting from silica fusion at high temperature, sol-gel silica is an amorphous, porous material prepared at mild temperature.<sup>148</sup>

In the last three decades, the sol-gel process has become widely used and has found application in several technologically relevant fields, such as glass and ceramics, coating protection, optics, electronics, and solar energy. This interest is mainly due to the clear advantages offered by the sol-gel process for material synthesis, some of which are listed as follows:<sup>148</sup>

- High purity of the precursors;
- High commercial availability of the precursors;
- It requires simple equipment;
- The processing temperature is low when compared with other methods, preventing evaporation losses, contamination, separation, and crystallization of microphases;
- It allows the formation of a “pre”inorganic network in solution;
- “Specific” materials for specific applications may be produced;
- A wide range of materials (ceramics, glass, inorganic oxides, hybrids and composites) may be synthesized;
- It enables the preparation of materials impossible to be produced by other methods (organic-inorganic hybrid materials);
- Nanostructured materials may be produced;
- The morphology and structure of the final materials may be finely tuned by varying certain reaction parameters;
- New crystalline phases from the non-crystalline solids may be formed;

- The products obtained exhibit high chemical, dimensional and thermal stability;
- Possibility of using techniques such as drop-casting, spin-coating and spray-coating.

However, this method also presents some disadvantages:<sup>148</sup>

- The starting compounds are expensive;
- The entire process is too long;
- The production of monoliths is often difficult;
- Difficulties in the chemistry process may arise due to properties control and reproducibility.

The transition from a liquid to a solid elucidates the name of the process (“sol-gel”). A sol consists of a stable colloidal dispersion of particles in a liquid. The particles can be amorphous or crystalline, and possess dense, porous, or polymeric substructures resulting from the aggregation of subcolloidal chemical units. A gel comprises a three-dimensional (3D), porous and continuous network saturated with a liquid phase (“wet gel”).<sup>149</sup>

A typical preparation of sol-gel materials can be summarized in the following steps (**Figure 2.1**). The first step consists of the hydrolysis of silicon alkoxides. This step is followed by condensation reactions which lead to the formation of silica nanoparticles. At this stage and depending on the reaction conditions, these particles can size up to form a sol that can be deposited on a substrate to yield a film (e.g., by dip-coating, spin-coating or drop-casting), cast to get a desired shape (e.g., fibers), or used to produce powders (e.g., nanospheres, microspheres) (**Figure 2.1**).

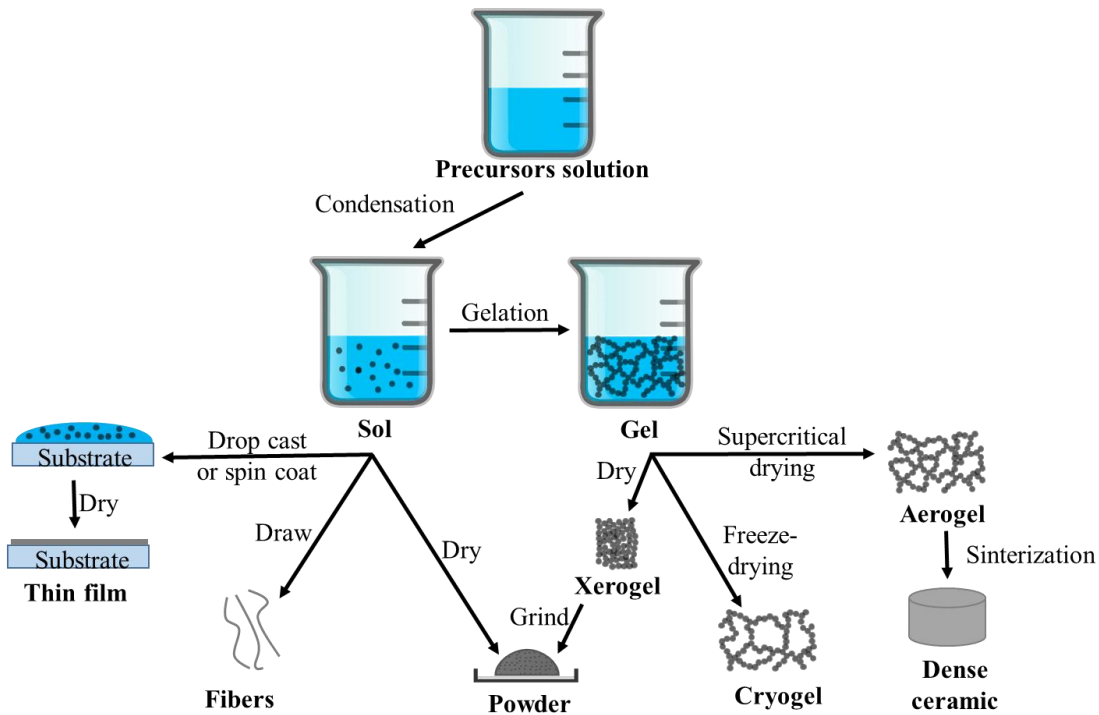


**Figure 2.1.** Sol–gel processing routes to yield different products.

During the formation of the gel, the sol particles aggregate and condense, leading to a continuous increase of the viscosity of the colloidal dispersion. The sol–gel transition occurs when the gel point is reached. At this point the suspension stops “falling” by gravity action and a continuous 3D gel network is formed.

In most cases in which the sol-gel systems form oxide materials, gelation results from the formation of covalent bonds between the sol particles. When other bonds are involved, such as van der Waals forces and hydrogen bonds, the gel formation can be reversible. The gel network structure is mostly dependent of the size and shape of the sol particles.<sup>149,150</sup>

Aging is an optional step after gelation that increases the cohesion between the particles, preventing their breakdown during drying. To age, the gel is covered with solvent and sealed to avoid evaporation. During this process more polycondensation reactions are promoted, creating additional cross-links in the matrix.

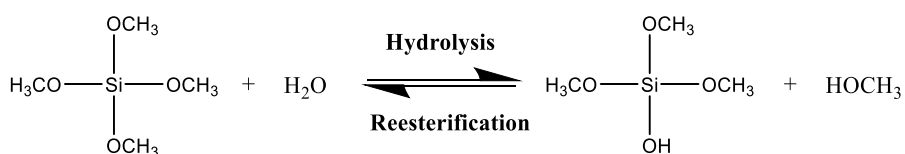
Washing is another optional step of the gel treatment prior to drying, which may be necessary to remove certain by-products. It may imply selecting a solvent that completely dissolves the by-product. This step may require vacuum and sometimes heating.

The treatment (temperature and pressure) adopted to dry the gel dictates the type of monolith (nanostructured solid material) produced: an aerogel, upon drying under

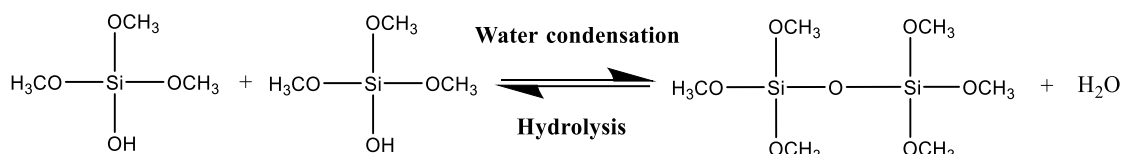
supercritical conditions, a xerogel, upon drying at ambient pressure, and a cryogel, by means of freeze-drying. Dense ceramics and powders can be further obtained by sinterization of aerogels and grinding of xerogels (**Figure 2.1**).<sup>145</sup>

A detailed description of the sol-gel reactions is useful. Any compound that is able to form reactive inorganic surface charges to prevent the coagulation and precipitation can be used as sol-gel precursor. Metal alkoxides have been widely used as precursor compounds. They can form monomers soluble in common organic solvents, particularly alcohols. To illustrate the whole process, let us consider for example tetramethylorthosilicate (TMOS), one of the most common and simple known precursors. The material synthesis starts with a solution containing TMOS and a low-molecular weight organic solvent (e.g., tetrahydrofuran).<sup>149</sup> The alkoxide route can be easily controlled by controlling the hydrolysis (**Figure 2.2A**) and condensation (**Figure 2.2B1** - water condensation, **Figure 2.2B2** - alcohol condensation) reactions through the addition of water (H<sub>2</sub>O) and alcohol (e.g., methanol (CH<sub>3</sub>OH)) to the solution. Water is added to initiate the hydrolysis reactions. The alcohol is added as a homogenizing agent to promote the hydrolysis process due to the immiscibility between the alkoxide and H<sub>2</sub>O.<sup>151</sup> During hydrolysis, (**Figure 2.2A**) a H<sub>2</sub>O molecule will react with a methoxyl group (-OCH<sub>3</sub>) present in TMOS, resulting in the release of one molecule of CH<sub>3</sub>OH and the substitution of the methoxyl group (-OCH<sub>3</sub>) by a hydroxyl group (-OH). The condensation reactions that follow can proceed along two routes: (1) water condensation, in which two -OH groups from different precursor molecules react to release a molecule of H<sub>2</sub>O (**Figure 2.2B1**); (2) alcohol condensation, in which a -OH group from a precursor molecule reacts with a -OCH<sub>3</sub> group from another molecule to release a molecule of CH<sub>3</sub>OH (**Figure 2.2B2**). Both reactions lead to the concomitant formation of siloxane (Si-O-Si) linkages.<sup>148</sup> Complete hydrolysis is only achieved when the stoichiometric molar ratio Si:H<sub>2</sub>O is 4. Below this value partial hydrolysis will occur. Condensation reactions comprise the reaction of silanol (Si-OH) groups to produce Si-O-Si bonds, H<sub>2</sub>O and an alcohol being by-products. Under normal circumstances, condensation can begin within the course of hydrolysis. For instance, particular reaction conditions, such as pH, Si:H<sub>2</sub>O molar ratio, and initial reagents can force condensation to only happen after hydrolysis.<sup>152</sup>

### A - Hydrolysis



### B 1 - Water condensation



### B 2 - Alcohol condensation

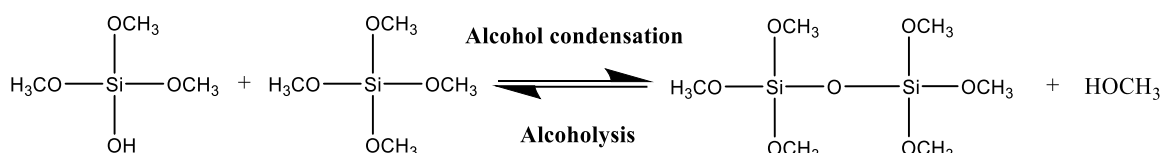


**Figure 2.2.** Schematic representation of the (A) hydrolysis and (B) condensation reactions yielding silica using TMOS as precursor compound.

## *Sol-Gel method*

The sol-gel process is affected by several parameters (e.g., the nature and concentration of the precursor, alcohol and catalyst, the molar ratio of reactants, pH value, temperature, drying and aging conditions) as illustrated below.

### *The precursors*

Two fundamental requirements must be fulfilled by the precursors: being soluble in the reaction media and being sufficiently reactive to contribute to the gel formation. Precursors belonging to the categories of acylates and amines, salts, hydroxides, oxides, complexes, and alkoxides (the most common) can be used.<sup>153</sup>

Even though metal alkoxides of aluminum, titanium or zirconium are a lot more reactive towards H<sub>2</sub>O than alkoxysilanes (Si(OR)<sub>4</sub>, where R is an alkyl group), because of their lower electronegativity and higher Lewis acidity, the latter compounds are the most widely employed. The gentleness of their reaction with H<sub>2</sub>O, sidestepping phase separation, results in good homogeneity. The alkoxysilane concentration and type

interfere in the hydrolysis and condensation reactions, making reactive monomers to be produced at different rates.<sup>154</sup> Evaporation of the precursor's solution, particularly at neutral pH, can happen if a slowly reacting compound, such as an alkoxy silane, is involved.<sup>153</sup> High alkyl networks lead to unreacted monomers which persist in the system until being removed by drying and heating. Branching of the alkyl group and long alkyl chains lead to the decline of the hydrolysis rate.<sup>149</sup> In contrast, alkoxide concentration has, neither effect on the final materials density, nor on the mechanical properties.<sup>154</sup>

#### *Water:TEOS Molar Ratio*

From **Figure 2.2**, it is possible to see how the amount of H<sub>2</sub>O in the sol-gel solution impacts the hydrolysis and condensation kinetics. For the total hydrolysis of Si(OR)<sub>4</sub> precursors under acid catalysis, it is recommended the use a H<sub>2</sub>O:Si ratio of at least 4. A low H<sub>2</sub>O:Si ratio can result in a high content of oligomers and a consequent decrease in the SiO<sub>2</sub> and homogeneity of the final material, as well as in the decrease of the gelation time.<sup>148,153</sup>

#### *pH/electrolytes*

The microstructure of a sol-gel derived material depends on the hydrolysis and condensation reactions that, in turn, can be controlled by the solution's pH. In acid-catalyzed reactions the hydrolysis is favored over condensation. The latter process normally starts at the end of hydrolysis, resulting in dense and transparent solids. In contrast, in base-catalyzed reactions, condensation is faster than hydrolysis, leading to the formation of highly condensed species that can cluster into fine particles prone to precipitating before gelation occurs (**Figure 2.3**).

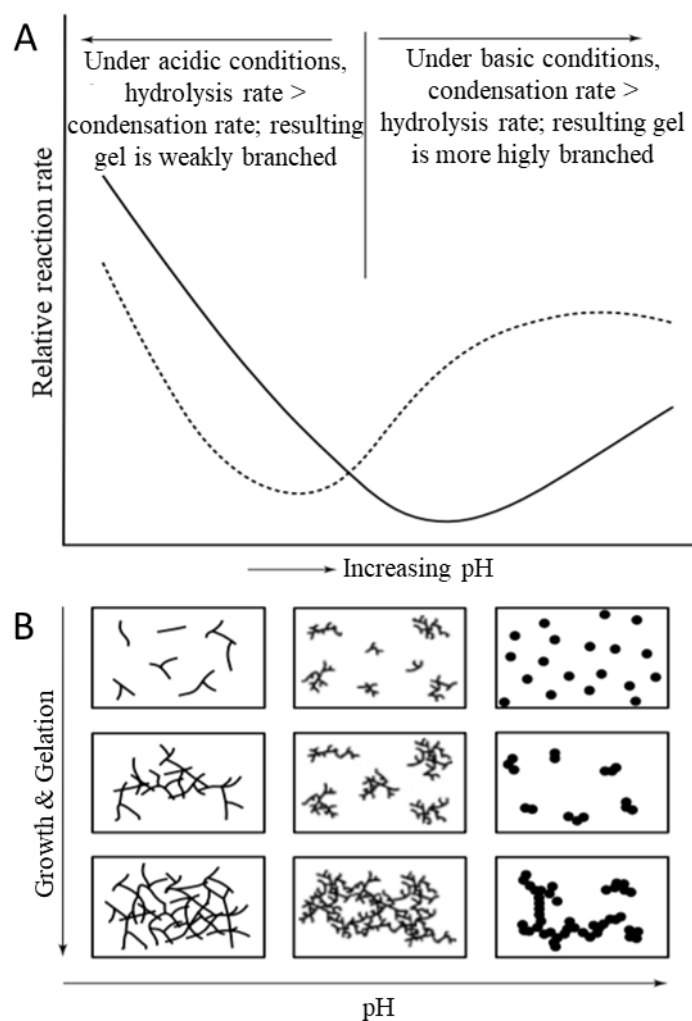


**Figure 2.3.** (A) Hydrolysis and condensation rates of  $\text{Si}(\text{OR})_4$  and (B) structure of the obtained gel, as a function of pH. Adapted from <sup>155</sup>.

Silicon alkoxides usually react slowly with  $\text{H}_2\text{O}$ , but the addition of acid or base speed up the process. For instance, gelation of a TEOS/ethanol solution was reduced from 1000 to 92 h upon addition of hydrochloric acid (HCl).<sup>148</sup> For silicon alkoxides the hydrolysis rate shows a minimum at  $\text{pH} = 7$  and increases exponentially at lower and higher pH values. In contrast, the condensation rate exhibits a minimum at pH around 4.5 and a maximum at pH around 10 (**Figure 2.3**). For a  $\text{pH} < 5$ , hydrolysis is favoured allowing the formation of a huge number of species with reactive Si-OH groups, and condensation is the rate-determining step. On the other hand, at a  $\text{pH} > 5$ , condensation is preferential leading to an instant consumption of hydrolysed species. The hydrolysis is the rate-determining step in this case. The condensation is proportional to the

concentration of  $\text{OH}^-$  ions at medium pH and to the concentration of  $\text{H}^+$  ions for  $\text{pH} < 2$  giving to the silicic acid species positively charged. <sup>149</sup>

Under acid conditions, the oxygen atom in  $\equiv\text{Si}-\text{OR}$  (for hydrolysis) (**Figure 2.4A**) or  $\text{Si}-\text{OH}$  (for condensation) (**Figure 2.5A**) are protonated and  $\text{ROH}$  or  $\text{H}_2\text{O}$  are the exit groups, respectively.

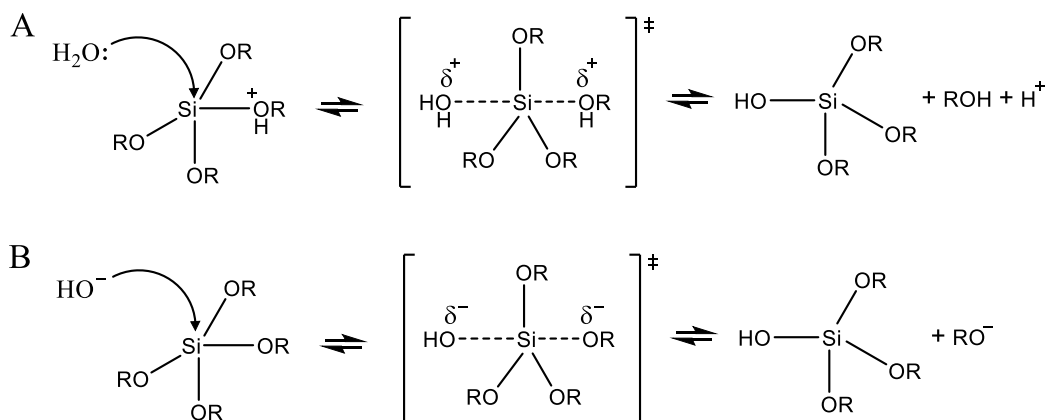


**Figure 2.4.** (A) Acid- and (B) base-catalysed hydrolysis of silicon alkoxides. Adapted from <sup>156</sup>.

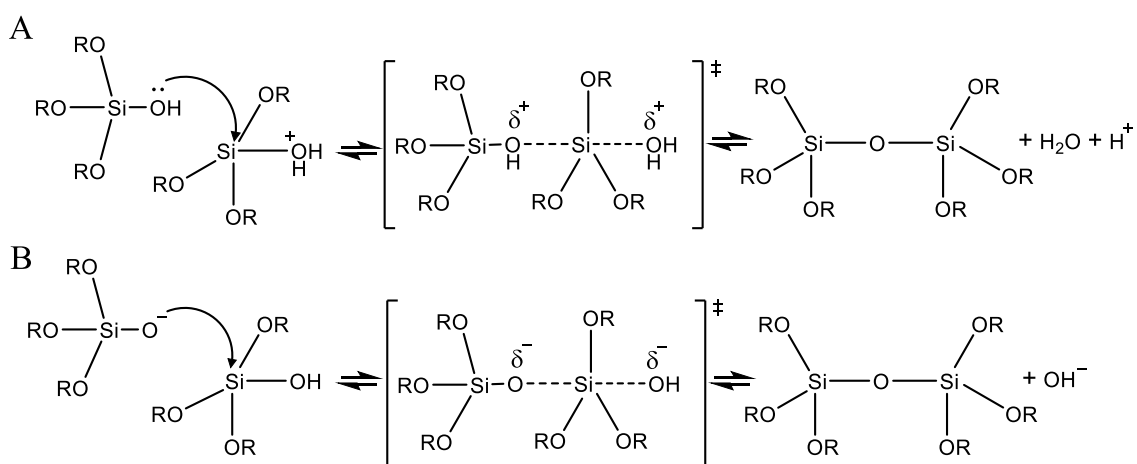


**Figure 2.5.** (A) Acid- and (B) base-catalysed condensation of silicon alkoxides. Adapted from <sup>156</sup>.

Under basic conditions, the reaction proceeds by nucleophilic attack of either an  $\text{OH}^-$  ion in the case of hydrolysis (**Figure 2.4B**) or a  $\equiv\text{Si}-\text{O}^-$  ion in the case of condensation (**Figure 2.5B**). The entering  $\text{OH}^-$  or  $\equiv\text{Si}-\text{O}^-$  groups are formed by deprotonation of  $\text{H}_2\text{O}$  or a  $\equiv\text{Si}-\text{OH}$  group. The  $\text{Si}-\text{O}-\text{Si}$  bonds can be cleaved again by  $\text{OH}^-$  in strongly alkaline conditions.

In the case of the polymerization of aqueous silica (**Figure 2.6**), three pH domains can be observed at  $\text{pH} < 2$ ,  $\text{pH} 2-7$ , and  $\text{pH} > 7$ , where the pH values of 2 and 7 are seen as boundaries. The  $\text{pH} \sim 2$  corresponds approximately to the point of zero charge (PZC) and the isoelectric point (IEP), where the surface charge and the electrophoretic mobility are zero, respectively. At  $\text{pH} \geq 7$ , the silica solubility and dissolution rates are maximum, and the surface charge generates a substantial repulsion, resulting in a growth of particles without aggregation or gelation.<sup>157,158</sup> For a pH below 2, the polymerization rate is proportional to  $\text{H}^+$  concentration. At pH 2-7 it is assumed that the polymerization rate is proportional to  $\text{OH}^-$  concentration.<sup>159</sup> For a pH below 7, the gel time is inversely proportional to the polymerization rate.

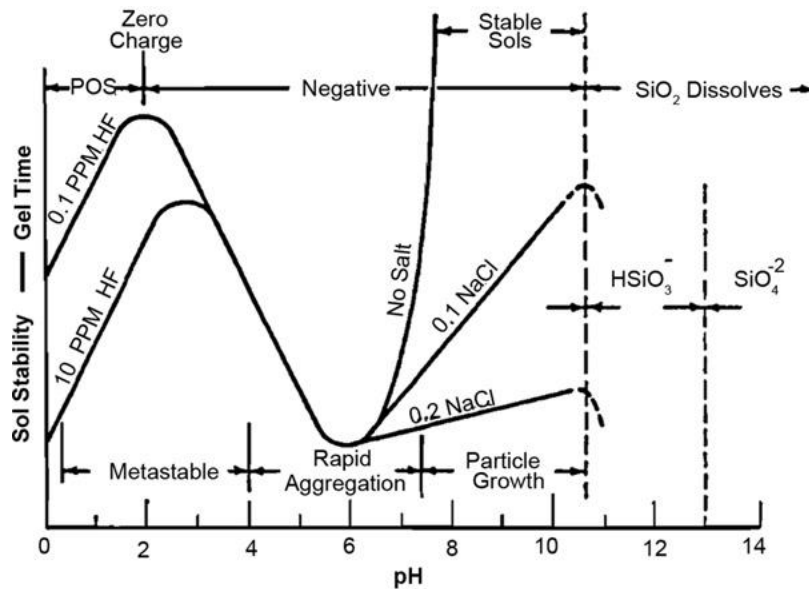


**Figure 2.6.** Effect of pH on the gel time of a colloidal silica-water system.<sup>160</sup>

The particles size increase with the increase of pH given the generation of negative charges through the ionization of the condensed silica. With the increase of the repulsion caused by charges, the particles size increases in order to overcome it, and “particulate” sols are formed at pH 7-10 (**Figures 2.6 and 2.7**).<sup>161</sup> The presence of electrolytes (salts) at slightly alkaline pH (7–10) can effect significantly the polymerization behaviour of a sol-gel reaction. In their absence, the particle repulsion due to negative particle surface prevents polymerization for  $\text{pH} > 7$ , and the colloidal system is stabilized. The addition of electrolytes leads to the formation of cations that cause coagulation, since the attractive forces between the particles remain the same, but the repulsive ones are minimized

because of the compression of the electrical double layer that surrounds the particles (Figures 2.6 and 2.7).<sup>149,162</sup>

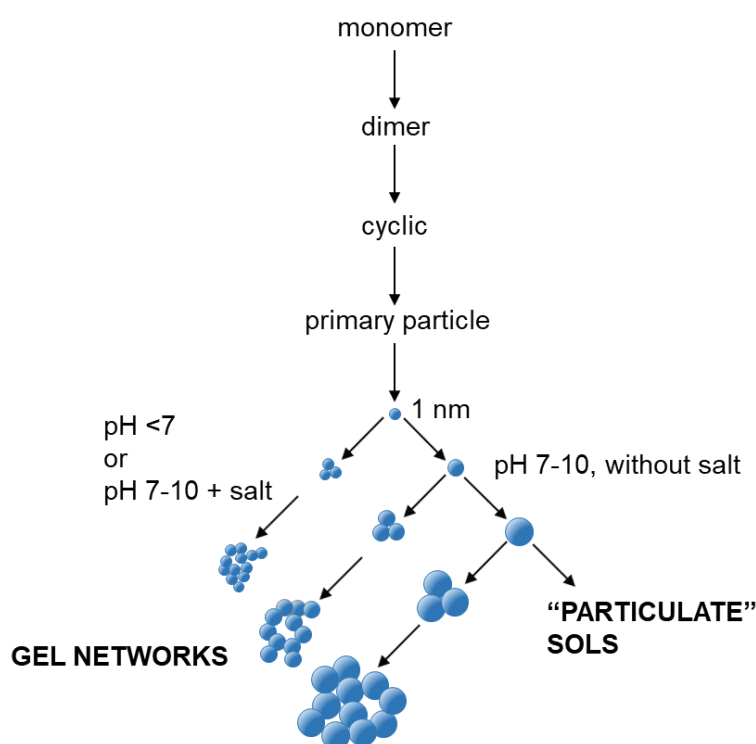


**Figure 2.7.** Polymerization behaviour of silica describing the sol–gel process. In basic solution the particles grow in size and in acidic solution, or in the presence of coagulating salt, particles aggregate into 3D networks and form gels. Adapted from<sup>161</sup>

In general, silica sols have a maximum stability at pH ~ 2 and polymerization increases at pH ~ 6. In the presence of cations (salts), aggregation is favoured over gelling. Thus, special care is needed in the sol–gel processes not to introduce unwanted salt contaminations in the system. The use of acids or bases as catalysts is a source of contamination. In the case of bases, ammonia represents a good alternative as it is not ionic. Acids, on the other hand, always involve the addition of anionic species (counterions) that influence the reaction rates and gelation.<sup>149,157</sup>

The pH is a particularly important parameter to control the final material texture, that influences porosity, gelation time, density, and volume shrinkage during the drying process.<sup>148</sup>

### *Solvents, temperature, aging, and drying*

Usually, a solvent is necessary at the beginning of the process to guarantee a good mixture of the alkoxide-based systems. The selection of the solvent is fundamental. Its

properties (e.g., polarity, viscosity, dipole moment) influence the reaction rates and consequently the final sol–gel structure. For instance, tetrahydrofuran (THF) can be used in the case of mixtures of organotrialkoxysilanes ( $R'Si(OR)_3$ ) and  $H_2O/ROH$  to stabilize polar species carrying Si-OH groups, such as hydroxyalkoxysilanes  $[Si(OR)_x(OH)_y]_n$ , via hydrogen bonds.<sup>149</sup> The drying step implies the loss of  $H_2O$ ,  $ROH$ , and other volatile constituents, leading to gel shrinkage and structure tensions,<sup>163</sup> that can cause cracks in the monolith.<sup>153</sup> Since hydrolysis and condensation are still on-going after gel formation, heating at reasonably high temperatures (100-500 °C) promotes the creation of covalent Si-O-Si bonds and removes the organic species.<sup>154</sup> Aging at room temperature is a slow process, but by increasing the thermal treatment temperature, the porosity is also increased.<sup>148</sup>

### *Organic-inorganic hybrid materials*

One important characteristic of the sol-gel process is the possibility of combining organic and components at the nanometric scale, in nearly any ratio, leading to the formation of organic-inorganic hybrid nanocomposites. The versatility of these materials has attracted tremendous interest in different fields of research, such as chemistry, physics and materials, for the creation of new materials and devices with the best features of both constituents (inorganic and organic).

Hybrid materials are nanocomposites at the molecular scale in which at least one component, organic or inorganic, is present with a nanometer size from a few Å to several tens of nanometers. The resulting properties (e.g. optical, electrical, mechanical, chemical and thermal stability) derive from the strong synergy produced by the hybrid interface and not from the components individually. Hybrid materials may be divided into two classes based on the type of interaction or nature of the chemical bond between organic and inorganic compounds. Class I corresponds to hybrid systems in which the organic and inorganic phases are connected by weak interactions, such as van der Waals, hydrogen bonds or electrostatic interactions (**Figure 2.8A**). Class II hybrids comprise systems in which the organic and inorganic components are linked by covalent or ionic-covalent bonds at the molecular level (**Figure 2.8B**).<sup>46,164</sup>

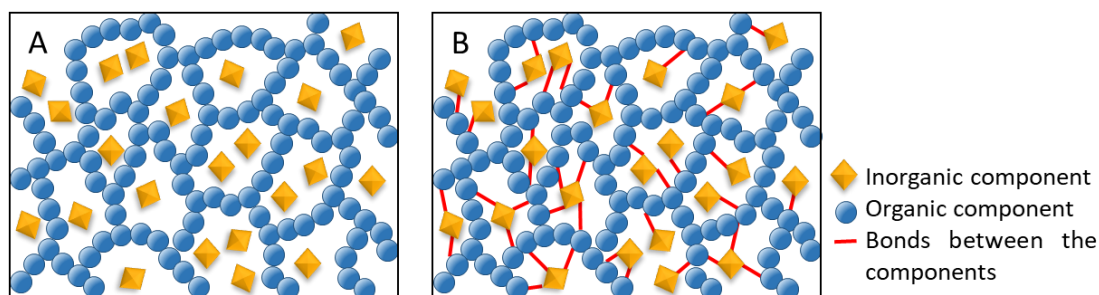


**Figure 2.8.** Hybrids classification based on the type of molecular interaction: (A) class I and (B) class II. Adapted from <sup>165</sup>.

Yet, the classification of these materials is not always an easy task. A classic example are the organic-inorganic hybrid matrices doped with lanthanide-based compounds for optical applications.<sup>102</sup> Even if the lanthanide-based complexes interact with the host hybrid via van der Waals or hydrogen bond forces,<sup>166</sup> the hybrid is composed of strong chemical bonds between the organic and inorganic parts has a significant impact on the general properties and therefore, the material is classified as Class II hybrid.

In the last three decades, a family of Class II hybrid materials, named ureasilis (ureasilicates), consisting of organic poly(oxyethylene) (POE) chains covalently bonded at both ends to an inorganic siliceous skeleton by means of urea cross-links (-NHC-(=O)NH-) has emerged as a one of the best host to boost the optical efficiency of lanthanide complexes..<sup>167-172</sup> The results showed that the  $\text{Ln}^{3+}$  ions can coordinate to the matrix (e.g., through interaction with the oxygen atom of the carbonyl groups of the urea moieties ( $\text{C}=\text{O}) \cdots \text{Eu}^{3+}$ ), resulting in the increase of the emission quantum yield of the final material.<sup>172-175</sup> These materials have found applications in areas, such as LSCs<sup>80,130</sup>, LDS layers<sup>108</sup>, ECDs<sup>176</sup> and coloured displays<sup>177</sup>.

### *Ionic liquids, ionogels and ionosilicas*

As pointed out above, ILs present a myriad of unique properties, which include high thermal stability (usually up to 200-300 °C), non-flammability, high ionic conductivity (around  $10^{-4}$  to  $8 \cdot 10^{-2}$  S  $\text{cm}^{-1}$  at room temperature), and wide electrochemical stability window (around 5.7 V between Pt electrodes<sup>75</sup>) which transform them into very attractive candidates as high-performance “green” electrolytes for advanced solid state electrochemical devices, such as lithium batteries, fuel cells, dye-sensitized solar cells, actuators, and electric double-layer capacitors, among others. Another clear advantage of ILs is that their structure may be designed through a judicious

choice of the cation and/or anion, allowing their properties to be properly tailored for a specific task.<sup>178</sup>

Despite their tremendous potential, the use of ILs as advanced materials remains often a problem because of their characteristic liquid state. Not surprisingly, one of the greatest challenges in this field whenever targeting applications in solid devices consists in the immobilization of the IL without jeopardizing their outstanding properties. One way to achieve this is to impregnate it in a support, where it is used as an adsorbed film. Supported IL catalysts (SILCs) illustrate this approach.<sup>75</sup> SILSCs consist of metal catalytic agents immobilized in IL films that are supported on silica beads, resulting in free-flowing powders that are particularly suited for constant fixed-bed reactors. Another approach relies on the immobilization of ILs in polymer membranes (e.g., polymerization of the IL monomer, cross-linkage of a polymer in the IL, or polymer swelling with the IL) and in silica matrices via sol-gel processing. The latter procedure allows the retention of a higher amount of IL, while ensuring the needed transparency for optical applications.<sup>75,178–180</sup> Therefore, ILs have been used for the preparation of an extensive variety of inorganic and hybrid materials comprising silicas and organosilicas, alloys, metal oxides and salts, open-framework structures, and nanostructured metals.<sup>75</sup> The remaining of this section is focused on two classes of silica-based hybrid materials incorporating ILs: ionogels and ionosilicas.

A ionogel (or ion gel) can be described as a solid-like material where the IL is immobilized by percolation in a 3D network.<sup>75</sup> In the light of this approach, the liquid-like dynamics of the IL is preserved and, for instance, the ionic conductivities may remain identical to those of the pure IL, making these materials ideal for electrochemical devices, such as fuels cells and PV systems.<sup>181</sup> Besides, the ability to easily shape the ionogels as pellets, coatings or rods, is promising for applications in optical and especially electroluminescent devices.<sup>178</sup> Ionogels can be separated into two main groups of gels which differ in the type of internal cross-linking of the 3D network. Physical ionogels are characterized by weak (reversible) cross-links resulting from hydrogen bonds, crystallite junctions, etc., whereas chemical ionogels present cross-links formed via covalent bonds.<sup>75</sup> Physical gels originating from organic gelators or divided solids exhibit poor mechanical properties, as they are obtained as pastes, jellies, or slurries. A way to avoid this problem is to produce chemical ionogels, in which the IL is confined in a covalently interconnected 3D network with superior mechanical resistance. With this purpose, alkoxide precursors can be used to prepare inorganic oxides via the sol-gel process. In

this case the IL will typically affect the structural and textural properties of the inorganic matrix. Another option regards nanocomposite matrices in which the (bio)polymer network is covalently bonded to oxide nanofillers created in situ by the sol–gel process.<sup>75</sup>

It should be noted that the intrinsic properties of ionogels result from both the IL and the constituent forming the 3D network.<sup>75</sup> The nature of the latter can be divided into three categories, depending on the nature of the host matrix: organic (e.g., low molecular weight gelators or polymers, such as poly(oxyethylene) (POE)), inorganic (e.g., oxide nanoparticles, carbon nanotubes or oxide networks formed by sol–gel chemistry, such as silica), and organic–inorganic hybrids (e.g., polymers containing inorganic fillers, such as silsesquioxanes).<sup>181</sup> Another factor that may affect the properties of ionogels is the nanometer scale assembly, since the ILs exert a plasticizing effect. This effect is present when the glass temperature ( $T_g$ ) of the ionogel is higher than that of the pure IL and lower than that of the pure organic polymer. The confinement effect detected in inorganic ionogels on the other side is more specific, since the confinement in the host matrix nanopores can change significantly the physical-chemical properties of the IL.<sup>75</sup> Ionogels that maintain the original properties of the ILs (e.g., ionic conductivity) are desirable. Moreover, the encapsulation of designed molecules showing certain properties, such as luminescence, sensing, catalytic or electroactivity, in the immobilized IL phase opens infinite possibilities of functionalization.<sup>75</sup> Accordingly, transparent silica-based ionogels have been used to produce luminescent materials upon combination with lanthanide complexes.<sup>181</sup> In short the functionalization results from the interaction between the IL and the host matrix, and the polymer tractability, as well the sol–gel versatility in shaping, leads to an easy adaptation of ionogels to an extensive series of devices.<sup>75</sup> These materials have found numerous applications in the energy field (electrolytes for lithium batteries and solar cells), drug release systems, and task-specific solutes.<sup>181</sup>

Ionosilicas (or i-silicas, ISs) are described as siliceous materials comprising covalently bonded ionic groups. Since they present a mixed inorganic/ionic nature, ISs combine the features of silica constituents (polarity, possibility to control the surface properties, high specific surface area, texture, and architectures on the mesoscopic length scale) and ILs (ion selectivity, tuneable hydrophilicity/hydrophobicity, and chemical design). Consequently, ISs present a tremendous potential for the materials' scientist to produce tailor-made solids possessing tuneable physical-chemical and surface properties combined with a high of control in terms of morphologies and architectures. Grafting of a chemical functionality to a solid support is extremely attractive as it avoids leaking, it

enables the reuse of functional solids, and it assists the reactants and catalyst separation.<sup>181</sup> Since ILs are not cheap,<sup>182</sup> this method is appealing as it allows reducing the quantity and reuse of IL, which is beneficial from economic and ecological perspectives.

Different approaches have been adopted for the synthesis of IS-type materials. ISs can be seen as a special case of organosilicas, since the methodologies of synthesis are similar, although the precursors have an ionic nature. Depending on how the organic functional group is linked to the material, two classes of ISs may be identified: (1) Surface-functionalized ISs; and (2) IS hybrid materials.

Surface-functionalized ISs are characterized by the attachment of the organic ionic group via covalent bonds to the silica support surface. These materials can be synthesized through post-synthesis grafting or co-condensation reactions. IS hybrid materials consist in the integration of the organic units in the silica framework and can only be made by hydrolysis/polycondensation reactions with di- or oligosilylated organic precursors.<sup>181</sup>

With respect to surface-functionalized ISs, three cases can be present, where the cation, the anion, or both ions are chemically grafted to the silica surface (**Figure 2.9**).

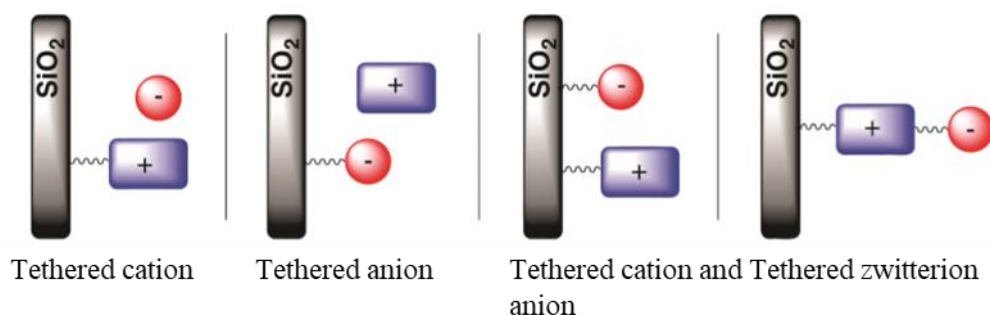


**Figure 2.9.** Different types of surface-functionalized ionosilicas.<sup>181</sup>

The surface-functionalized ISs comprising grafted cations are the most studied cases owing to the cationic precursors' versatility that results from ammonium, imidazolium, phosphonium or pyridinium-based compounds, where the imidazolium-based ISs have an unrivalled place in this field. For the functionalization of the cation, typically a hydrolyzable trialkoxysilyl group is involved. **Figure 2.10** illustrates two different methods of synthesis for a monosilylated imidazolium precursor (3-methyl-1-(3-(triethoxysilyl)propyl)imidazolium halide) (**centre**): post-synthesis grafting (**Figure 2.10A**) and hydrolysis/co-condensation (**Figure 2.10B**).<sup>181</sup>

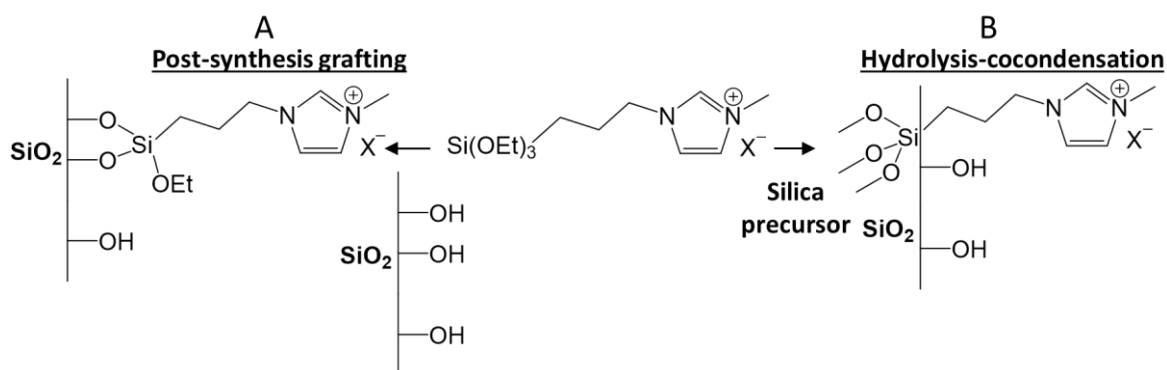


**Figure 2.10.** Synthesis of surface-functionalized ionosilicas via (A) post-synthesis grafting and (B) hydrolysis-cocondensation reactions. Adapted from <sup>181</sup>.

For the production of IS hybrid materials, ionic precursors are used as templates (structure directing agents) for hydrolysis–polycondensation reactions which show the strong contribution of the precursor concerning the formation of structured mesophases, based on ionic precursor–surfactant interactions.<sup>181</sup> For the production of these materials, ionic interactions between the silylated precursor, more specifically the organo-ionic part of the compound, and the anionic structure directing agent (surfactant) are required. In this case, the ionic precursor acts as a molecular component for the formation of the solid phase, as structure directing and structure inducing compound. Since the precursor and surfactant can be modified, a huge diversity of IS mesophases is possible. Another important feature for the hybrid ISs is the steric shielding of the organocationic precursor. This is a critical parameter for the IS mesophases nanostructure, since it governs the ionic interactions concerning the surfactant and precursor. Strong precursor–surfactant interactions are mandatory for the synthesis of nanostructured ionosilica phases and can be overcome by the design of the precursor and soft template.<sup>181</sup>

The grafting of ionic precursors to the surface of silica nanoparticles leads to ionic nanoparticles, which represent another type of materials besides surface-functionalized and hybrid ISs. Archer *et al.*<sup>183</sup> investigated the phase behaviour of these materials, as well as their application as electrolytes in lithium metal batteries.

The main applications of ISs benefit from the diversified ionic inorganic nature of these materials and are placed in the fields of catalysis, separation, and molecular recognition.<sup>181</sup>

## 2.2. Electrochromic windows: working principles

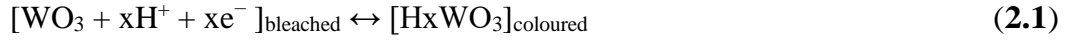
Different mechanisms have been proposed to describe the coloration of EC layers. The most extensively accepted explanation associates the coloration phenomenon to intervalence charge transfer (IVCT), which involves an electron transfer between two metal sites. The optical and electrical features are determined by the energy gap between the valence band and the conduction band of the EC materials. In an ECD the colouration mechanism involves the EC layer and the ion storage (IS) layer. For an EC layer with cathodic electrochromism, the material responds to a direct current electrical field by electrochemical reduction with the simultaneous taking in of charge-neutralizing cations, changing from transparent to a coloured state. Reversing the polarity reverses the colour change. The IS layer supplies the necessary ions for the EC reaction. This layer can also have EC properties thus enhancing colour change.<sup>12</sup> **Figure 2.11** shows a variety of elements that possess cathodic or anodic electrochromism, with highlight to vanadium that exhibits both.

1 H Hydrogen																	2 He Helium
3 Li Lithium	4 Be Beryllium											5 B Boron	6 C Carbon	7 N Nitrogen	8 O Oxygen	9 F Fluorine	10 Ne Neon
11 Na Sodium	12 Mg Magnesium											13 Al Aluminum	14 Si Silicon	15 P Phosphorus	16 S Sulfur	17 Cl Chlorine	18 Ar Argon
19 K Potassium	20 Ca Calcium	21 Sc Scandium	22 Ti Titanium	23 V Vanadium	24 Cr Chromium	25 Mn Manganese	26 Fe Iron	27 Co Cobalt	28 Ni Nickel	29 Cu Copper	30 Zn Zinc	31 Ga Gallium	32 Ge Germanium	33 As Arsenic	34 Se Selenium	35 Br Bromine	36 Kr Krypton
37 Rb Rubidium	38 Sr Strontium	39 Y Yttrium	40 Zr Zirconium	41 Nb Niobium	42 Mo Molybdenum	43 Tc Technetium	44 Ru Ruthenium	45 Rh Rhodium	46 Pd Palladium	47 Ag Silver	48 Cd Cadmium	49 In Indium	50 Sn Tin	51 Sb Antimony	52 Te Tellurium	53 I Iodine	54 Xe Xenon
55 Cs Cesium	56 Ba Barium	57 La Lanthanum	72 Hf Hafnium	73 Ta Tantalum	74 W Tungsten	75 Re Rhenium	76 Os Osmium	77 Ir Iridium	78 Pt Platinum	79 Au Gold	80 Hg Mercury	81 Tl Thallium	82 Pb Lead	83 Bi Bismuth	84 Po Polonium	85 At Astatine	86 Rn Radon
87 Fr Francium	88 Ra Radium	89 Ac Actinium	104 Rf Rutherfordium	105 Db Dubnium	106 Sg Seaborgium	107 Bh Bohrium	108 Hs Hassium	109 Mt Meitnerium	110 Ds Darmstadtium	111 Rg Roentgenium	112 Cn Copernicium	113 Nh Nihonium	114 Fl Flerovium	115 Mc Moscovium	116 Lv Livermorium	117 Ts Tennessine	118 Og Oganesson

**Figure 2.11.** Periodic table of the elements. The coloured boxes refer to the documented transition metals oxides that have cathodic or anodic electrochromism or both.<sup>12</sup>

Standard ECDs comprise as EC1 layer  $\text{WO}_3$ , a cathodic colouring material, and  $\text{NiO}$ , an anodic colouring material, as EC2 layer. In the case of cathodic EC oxides, the optical absorption variation can happen in any intermediate level between a maximum and a minimum. Even if the coloration mechanisms are still not very well comprehended, they are largely associated with charge transference and polaron absorption.<sup>184,185</sup>

For  $\text{WO}_3$  one assumes insertion and extraction of protons (or any other small cation) and electrons in  $\text{WO}_3$  by the simple electrochemical reaction



where the reaction should only be partially to be reversible and the coloured compound should be written  $\text{H}_x\text{WO}_3$  with  $x < 0.5$ .<sup>12,37,186</sup> To better understand the optical properties of ion and electron exchange we can consider that the electronic band structure suitable to oxides consists of octahedral “building blocks”. In this configuration the metal  $d$  levels split into two bands with the conventional notation  $e_g$  and  $t_{2g}$ . The oxygen  $2p$  bands are separated from the split  $d$  bands by an energy gap. Undoped  $\text{WO}_3$ , which has a full  $\text{O}2p$  band and an empty  $d$  band, is transparent given the large band gap.<sup>12,37</sup> The insertion of small ions and associated electrons leads to a partial filling of the  $d$  band and consequent optical absorption. As ions and electrons are inserted, electrons move to tungsten sites, where some of the  $\text{W}^{6+}$  sites turn to  $\text{W}^{5+}$ . If the inserted electrons absorb a photon, it can gain enough energy to be transferred to a neighbouring site. This mechanism between sites  $i$  and  $j$ , termed IVCT, can be written as:<sup>12,13,43</sup>



The effectiveness of this process depends on the transference of an electron from an occupied state to an empty one able to accept it. The EC properties of  $\text{WO}_3$  rely on this mechanism, as colour shifts from transparent to blue during the ions and electrons insertion. If the insertion is too large not only transfers



will happen, but also



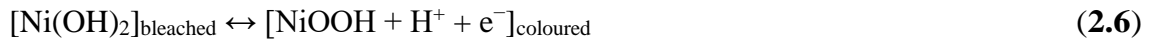
and



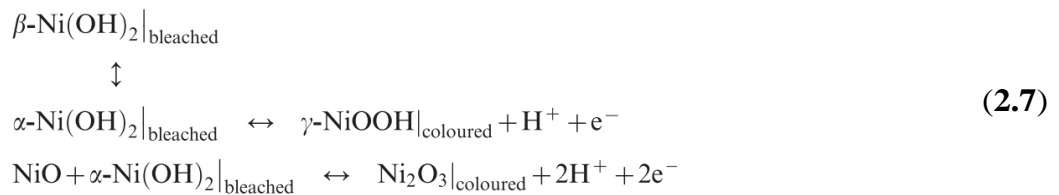
will occur. The process (2.3) appears to prevail over the other.<sup>37</sup>

$\text{NiO}$  films are considered promising candidates as p-type TCOs, with band gap ( $E_g$ ) values around 3.6 - 4.0 eV.  $\text{NiO}$  films with low resistivity ( $1.4 \times 10^{-1} \Omega \text{ cm}$ ) can be achieved by sputtering. The spray pyrolysis method (SPM) represents a very important deposition method for TCO films fabrication, since this is a simple technique, no vacuum is required, and is suitable for large-area coatings. However, the resistivity of doped  $\text{NiO}$

films is about 1  $\Omega$  cm. Undoped NiO has a wide  $E_g$  value and shows low p-type conductivity. The conduction mechanism of NiO films is first and foremost determined by holes created from nickel position, oxygen interstitial atoms, and used dopant. In this case, the NiO has some empty  $t_{2g}$  states that can be filled with the insertion of ions and electrons. Under these conditions the material presents a band gap between the  $e_g$  and  $t_{2g}$  states and transparency is provided if the gap is large enough.<sup>37</sup> Colouration of NiO is based on the transition between light brownish ( $Ni^{2+}$ ) and brown ( $Ni^{3+}$ ).<sup>42,185,187</sup> The electrochemical reaction considering the insertion and extraction of protons and electrons for the Ni-based oxide is



which is expected to only happen on the hydrous grain boundaries. In this case, the bleached state is associated with  $Ni(OH)_2$  and the coloured state is related with  $NiOOH$ .  $Ni(OH)_2$  exists in two forms,  $\alpha$  and  $\beta$ , where the difference depends on water required for stabilization, with  $\beta$  requiring a higher content of water than  $\alpha$ . Subsequently, these phases can be oxidized to the resultant  $\gamma$  and  $\beta$  oxyhydroxides. However, these reactions do not involve NiO, and thus cannot explain its coloration. But, by the extraction of two protons (one that causes a transformation from  $\beta$ - $Ni(OH)_2$  to  $\gamma$ - $NiOOH$ , and the other one that is compensated by the creation of a hole on the  $Ni^{2+}$  in NiO), the superoxide  $Ni_2O_3$  is formed. This reaction is incorporated in the extended Bode scheme (2.7)<sup>185</sup> These reactions are those responsible for the electrochromism in the hydrated Ni-oxide-based materials.<sup>185</sup>



Therefore,  $WO_3$ - and NiO-based ECDs have been extensively studied as a good option because of their complementarity. In the bleached state, both  $WO_3$  and NiO are colourless. In the coloured state  $WO_3$  and NiO turn to blue and brown, respectively, making the ECD present a grayish colour in the coloured state given their colour

combination. **Figure 2.12** summarizes the reactions and  $e^-/H^+$  transport that occurs in a  $WO_3/NiO$ -based ECD.

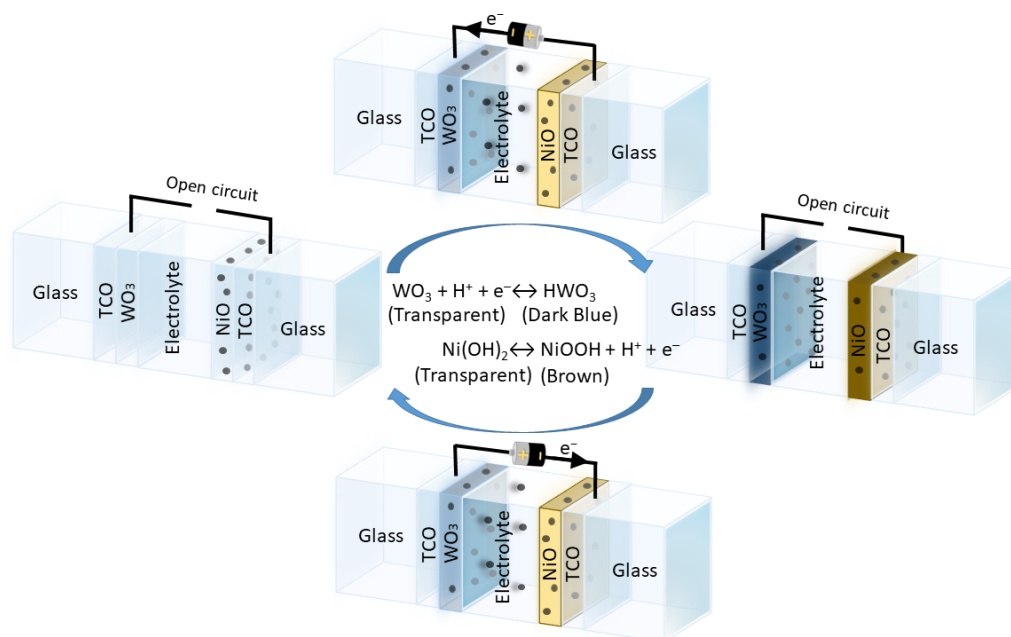


**Figure 2.12.** Schematic representation of an archetypal glass/TCO/ $WO_3$ /electrolyte/NiO/TCO/glass ECD, showing the transport of cations and electrons as a result of applied voltage.

A summary of several parameters of  $WO_3$ - and NiO-based ECDs previously studied is given in **Table 1.1** in terms of device size, applied voltage, switching time, and transmittance in the coloured and bleached states. It is possible to conclude that the combination of  $WO_3$  and NiO in ECDs works for different types of electrolytes, such as hybrid materials,<sup>70,79,83</sup> polymers (e.g. PMMA,<sup>84–87</sup> polysaccharides<sup>88,89</sup>), and ceramics.<sup>90–</sup>

### 2.3. Luminescent solar concentrators and luminescent down-shifting layers: working principles

The rationale behind LDS layers and LSCs is to enhance the PV cell's UV response by down-shifting short wavelength solar radiation to longer wavelengths where the absorption of the solar cell is higher.<sup>17,94,188–191</sup> The converted photons have energy more resonant with the photosensitivity of the PV devices, as illustrated in **Figure 2.13** for distinct types of cells.

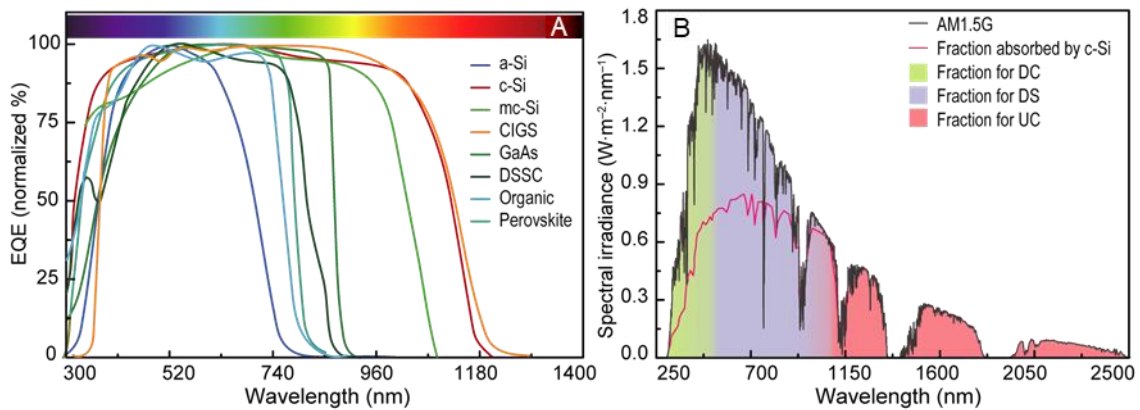


**Figure 2.13.** Spectral converters for PV devices and AM1.5G spectrum. (A) Normalized external quantum efficiency for single-junction PV cells with confirmed terrestrial efficiencies measured under the global AM1.5 spectrum ( $1000 \text{ W} \cdot \text{m}^{-2}$ ) at a cell temperature of  $25^\circ\text{C}$ .<sup>192</sup> (B) AM1.5G solar spectral irradiance spectrum. The shadowed areas represent the fraction available for down-conversion (26 %, up to 550 nm), down-shifting (81 %, up to 1100 nm) and up-conversion (16%, in the 1200-2500 nm range) for a c-Si wafer. The fraction absorbed by c-Si is also indicated.<sup>193</sup> Adapted from <sup>17</sup>.

A LSC comprises an optical waveguide-coated or -embedded material containing emissive centres that by absorbing the sunlight, re-emit photons that are directed by total internal reflection to the PV devices placed at the edges. Moreover, LSCs allow the fabrication of devices with a diversity of shapes, colours, transparency, flexibility, and lightweight that make them attractive from the architectural and design point of view, since they can be incorporated into buildings to create semi-transparent BIPVs, or turn regular objects into electricity generators. Different pathways contribute to the loss of the incident light (**Figure 2.14**).

In the case of the LSCs, optical performance is affected by numerous factors associated with the optical properties of the polymer matrix and emitting centres. Efficient

photoluminescence (PL) emitters for LSC applications need to present some properties: (1) large absorption coefficient and broad absorption overlapping the solar spectrum, (2) large Stokes-shift, (3) high emission quantum yield, (4) high photo/chemical stability, and (5) solubility in the polymer matrix.<sup>194</sup>

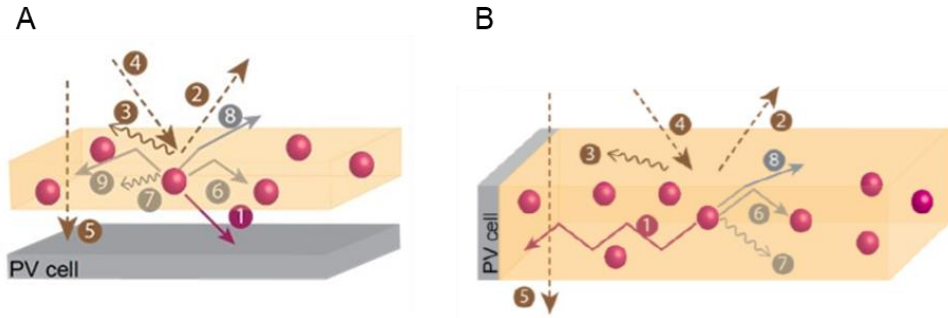


**Figure 2.14.** Operating principles of luminescence spectral conversion in a: (A) LDS device and (B) LSC. The primary processes and losses occurring are: (1) emission from the optically active centre, (2) Fresnel reflections, (3) surface scattering, (4) waveguide attenuation, (5) transmitted radiation, (6) re-absorption by neighbour centres, (7) non-radiative relaxation, (8) emission within the escape cone, (9) radiation lost through the sides. Adapted from <sup>17</sup>

### Performance quantification

The performance of a LDS layer and of a LSC are quantified by the optical conversion efficiency ( $\eta_{opt}$ ), which is a measure of the ratio between the output power at the LSC edges ( $P_{out}$ ) and the incident optical power ( $P_{in}$ ):<sup>195–199</sup>

$$\eta_{opt} = \frac{P_{out}}{P_{in}} \quad (2.8)$$

The  $\eta_{opt}$  can be described by weighting all the losses in the LSC, given by the product of several terms:<sup>198</sup>

$$\eta_{opt} = (1-R) \eta_{abs} \eta_{SA} \eta_{yield} \eta_{Stokes} \eta_{trap} \eta_{tr} \quad (2.9)$$

where:

- $R = (n_f - n_i)^2 / (n_f + n_i)^2$  is the Fresnel reflection coefficient for perpendicular incidence, in which  $n_i$  represents the refractive index of the optically active layer at the incident wavelength ( $\lambda_i$ ).

- $\eta_{abs} = 1 - 10^{-A}$  is the ratio of photons absorbed by the emitting layer to the number of photons falling on it, with A representing the absorbance value at  $\lambda_i$ . For LSCs with a non-planar geometry,  $\eta_{abs}$  is not constant along the device surface and, then, the thickness must be estimated accordingly. For instance, for cylindrical geometry, and perpendicular incidence of sun radiation, the optical absorption path increases from the middle to the surface along the radial direction.
- $\eta_{SA}$  is the self-absorption efficiency, arising from self-absorption of the emitting centres. When the spectral overlap between the excitation and emission spectra of the emitting centres is null,  $\eta_{SA} = 1$ , as in the case of  $\text{Ln}^{3+}$ . If this overlap is not null,  $\eta_{SA} < 1$ , as typically observed for dyes and QDs.
- $\eta_{yield}$  is the emission quantum yield of the optically active centre at  $\lambda_i$ .
- $\eta_{Stokes} = \lambda_i / \lambda_p$  is the Stokes efficiency calculated by the energetic ratio between the average energy of the emitted photons (the emission peak position,  $\lambda_p$ , in energy units) and the incident energy (corresponding to  $\lambda_i$ ).
- $\eta_{trap} = (1 - 1/n_p^2)^{1/2}$  is the trapping efficiency, where  $n_p$  is the refractive index of the emitting medium at  $\lambda_p$ , is defined as the fraction of photons confined within the substrate, i.e., the fraction of photons emitted from the edge versus the photons emitted from the face and edge combined. This term accounts for the emission losses at the surface through a so-called escape cone.
- $\eta_{tr}$  takes into account the transport losses due to matrix absorption and scattering, frequently it is considered that  $\eta_{tr} = 1$ , as the transport and scattering losses are neglected.

## CHAPTER 3

### 3 - LANTHANIDE-BASED IONOSILICAS FOR LUMINESCENT SOLAR CONCENTRATORS AND DOWN-SHIFTING LAYERS

The integration of PV elements in urban environments is gaining visibility due to the current interest in developing energetically sustainable buildings. However, the mismatch between the PV cells absorption and the solar irradiance on Earth is one of the major limitations towards more efficient PV energy conversion. With the goal of overcoming this drawback, new lanthanide-doped surface functionalized ISs designated as 1-butyl-3-[3-(trimethoxysilyl)propyl]imidazolium tetra(2-thenoyltrifluoroacetate) neodymate(III)/europate(III)/terbate(III)/yttrate(III) ([B(TMSP)Im][Ln(tta)<sub>4</sub>], where Ln = Nd<sup>3+</sup>, Eu<sup>3+</sup>, Tb<sup>3+</sup> and Yb<sup>3+</sup>), abbreviated as IS-Ln, were produced and embedded within a poly(methyl methacrylate) (PMMA) matrix. The resulting materials, produced as transparent films, henceforth noted as PMMA-Ln-X (with X=m<sub>IS-Ln</sub>/m<sub>PMMA</sub>), absorb in the UV spectral region and emit in the visible/NIR spectral region. They exhibit large Stokes-shift, enabling the production of transparent coatings with negligible self-absorption. The PMMA-Eu-10 material demonstrated efficient solar radiation harvesting (spectral overlap of  $\sim 9.5 \times 10^{19}$  photons·s<sup>-1</sup>·m<sup>-2</sup>) and conversion (emission quantum yield (*q*)  $\sim 52\%$ ). By controlling the PMMA-Ln-X film thickness during its deposition onto a PV cell surface, the film acted as a LDS or a LSC layer. The overall electrical output of the device resulted in an absolute external quantum efficiency increase of  $\sim 32\%$  for the optimized Eu<sup>3+</sup>-based films in the UV spectral region (compared with the bare PV device, which is among the best values reported so far). In addition, when tested as LSCs, the IS-Eu and IS-Tb layers showed great potential for the fabrication of efficient and environmentally resistant devices, with optical conversion efficiency values of  $\sim 0.27$  and  $\sim 0.34\%$ , respectively.

### 3.1. Introduction

In this chapter, ISs, a subclass of organosilicas situated at the interface of silica hybrid materials and ILs, were developed and studied. In ISs an ionic group is anchored to the silica framework. These hybrid materials, the synthesis and characterization of which were recently reviewed, were proposed as good candidates for organic light emitting diodes (OLEDs) and LSCs.<sup>98,181,200</sup>

Targeting the progress of luminescent materials for the development of LDS layers and LSCs, new ISs were prepared here for the first time. The compounds include a silica matrix covalently bonded to 1-butyl-3-propyl-imidazolium cations via the propyl chain. The positive charge of this pendant group is counterbalanced by  $[\text{Eu}(\text{tta})_4]^-$  ions. The general chemical structure of the new compounds is shown in **Figure 3.1 (top right)**. The lanthanide complex anions were introduced upon exchange of the chloride ion ( $\text{Cl}^-$ ) of the parent compound.<sup>201</sup> The rationale of the materials design strategy is straightforward. Compared to the situation found in neutral  $[\text{Eu}(\text{tta})_3(\text{H}_2\text{O})_2]$  ( $q = 29\%$ <sup>39</sup>), which comprises three  $\text{tta}^-$  ligands, in  $[\text{Eu}(\text{tta})_4]^-$  the presence of an additional  $\text{tta}^-$  ligand adds two extra carbonyl ( $\text{C}=\text{O}$ ) oxygen atoms to the first coordination sphere of the  $\text{Ln}^{3+}$  ion. This change is extremely appealing, helping to further reduce deleterious quenching effects, and thus increase the  $q$  values.

These novel lanthanide-doped ISs (henceforth named IS-Ln) were embedded within PMMA, since this thermoplastic plastic is considered an appropriate choice for the production of flexible luminescent materials with high optical transparency under solar irradiation. PMMA is a low-cost, environmentally friendly, and non-toxic polymer that can accommodate high dopant concentrations before concentration quenching occurs, yielding high optical quality transparent matrices exhibiting no photodegradation.<sup>171,200</sup> Moreover, PMMA presents high resistance to UV radiation exposure and several chemical treatments, and exceptional performance in all-weather conditions,<sup>202</sup> which are critical features when applications in LDS layers and LSCs are envisaged. The combination of PMMA, which typically absorbs in the shorter UV range, with the IS-Ln materials, which absorb at longer UV wavelengths, offers excellent prospects for LDS layers and LSC applications (**Figure 3.1**). Here, PMMA was doped with IS-Ln (where  $\text{Ln} = \text{Nd}^{3+}, \text{Eu}^{3+}, \text{Tb}^{3+}$  and  $\text{Yb}^{3+}$ ) to yield new luminescent materials noted as PMMA-Ln-X (with  $X = m_{\text{IS-Ln}}/m_{\text{PMMA}}$ ). The structural, thermal and optical properties of the as-produced samples were characterized. PMMA-Ln-X films were subsequently tested as

independent LSC devices, and also as a coupled LDS layer/LSC single device. The study of the latter devices was performed by Dr. Ana Rita Frias in the framework of her PhD thesis,<sup>23</sup> and by Dr. Sandra F. H. Correia. In the light of this novel approach, the simultaneous evaluation of the LSC performance of an LDS layer deposited on a PV panel and containing PV cells in the edges was attempted (**Figure 3.1**). An optimized device based on an IS-Eu-based LDS layer deposited onto a Si-based PV cell yielded a maximum absolute EQE increase of ~32%, and a total delivered power increase of ~4%, compared to the bare bottom-mounted PV cell.

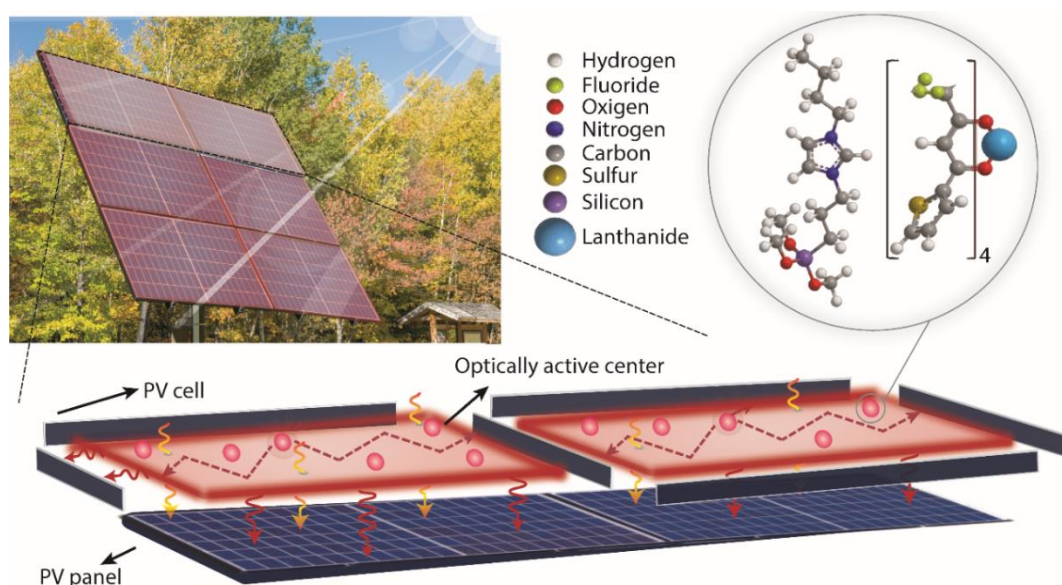


**Figure 3.1.** Schematic representation showing the use of a LDS layer (red colour) acting also as a LSC in combination with PV cells, in which the guided radiation that reaches the edges of the LDS layer is used by edge-mounted PV cells. The inset depicts the chemical composition of the emitting IS-Ln centres.

For LSCs, PMMA-Eu-20 and PMMA-Tb-20 were used to produce two devices in glass substrate aiming smart window applications. The devices showed optical conversion efficiency values of ~0.27 and ~0.34%, and PCE values of  $7.8 \times 10^{-4}$  and  $1.9 \times 10^{-3}$  %, for PMMA-Eu-20 and PMMA-Tb-20 LSCs, respectively.

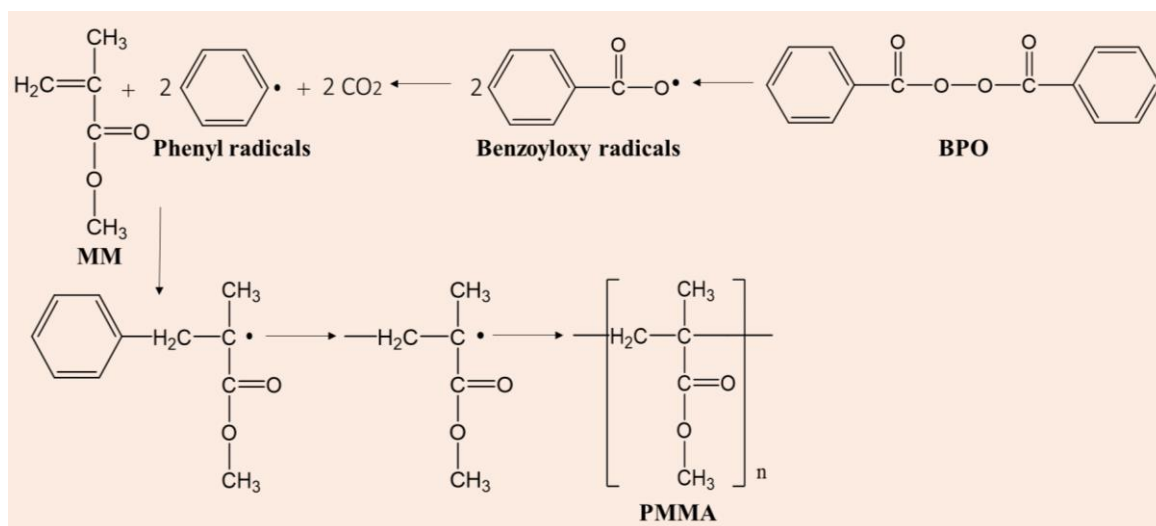
### 3.2.Synthesis

**Materials.** For the syntheses, the chemicals used were N-butylimidazole (BIm, 98%, Sigma-Aldrich), (3-chloropropyl)trimethoxysilane (CPTMS, 97%, Sigma-Aldrich), neodymium(III) chloride hexahydrate ( $\text{NdCl}_3 \cdot 6\text{H}_2\text{O}$ , 99.9%, Sigma-Aldrich),

europium(III) chloride hexahydrate ( $\text{EuCl}_3 \cdot 6\text{H}_2\text{O}$ , 99.99%, Sigma-Aldrich), terbium(III) chloride hexahydrate ( $\text{TbCl}_3 \cdot 6\text{H}_2\text{O}$ , 99.9%, Acros Organics), ytterbium(III) chloride hexahydrate ( $\text{YbCl}_3 \cdot 6\text{H}_2\text{O}$ , 99.9%, Sigma-Aldrich), 2-thenoyltrifluoroacetone (tta) (99%, Sigma-Aldrich), methyl methacrylate (MM) (99%, Acros), benzoyl peroxide (BPO) (97%, Alfa Aesar), anhydrous ethyl acetate (EtOAc, 98.8%, Sigma-Aldrich), ethanol (EtOH, 99.8%, Fisher Chemical), tetrahydrofuran (THF, Sigma-Aldrich), sodium hydroxide (NaOH, Merck), and dichloromethane (DCM, HPLC grade, Fisher Chemical and  $\geq 99.9\%$ , Honeywell Riedel-de Haën). All the chemicals were used as received. Ultrapure water was used in all experiments.

The syntheses of PMMA, IL-Ln ionosilicas and composite films are described in detail as follows and are schematically represented in **Schemes 3.1**, **3.2** and **3.3**, respectively.

**Synthesis of PMMA.** PMMA was prepared by mixing 10 g of MM with 0.06 g of BPO in a glass vial. The mixture was heated at 80-90 °C for 30 min and then transferred to an oven at 40 °C until complete polymerization (**Scheme 3.1**). Once polymerized, PMMA was broken into pieces and a piece was dissolved in THF. The solution was deposited onto a glass surface to produce a film. Its transparency in the visible region is demonstrated in the UV/visible absorption spectrum (**Figure 3.2**).



**Scheme 3.1.** Synthesis of PMMA via free radical addition polymerization.

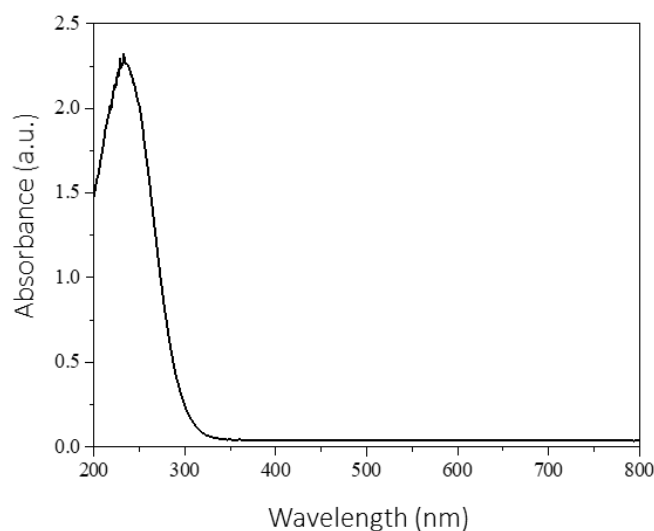
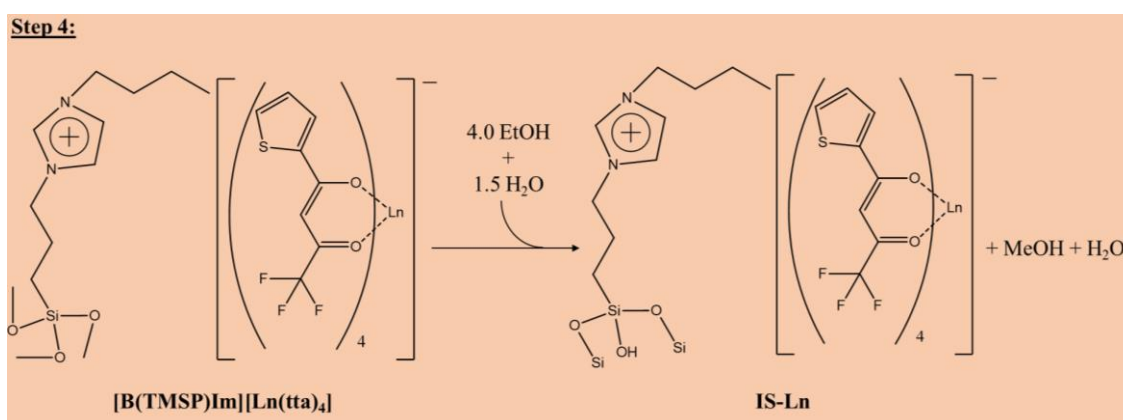
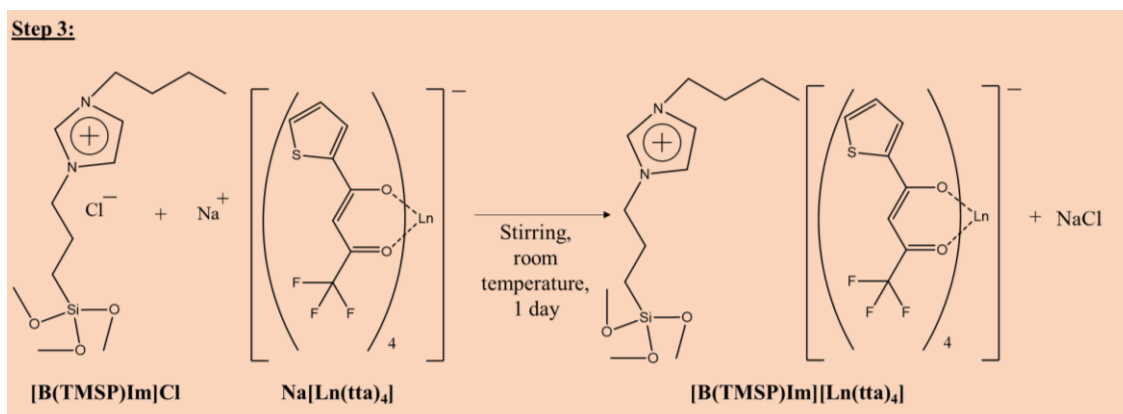
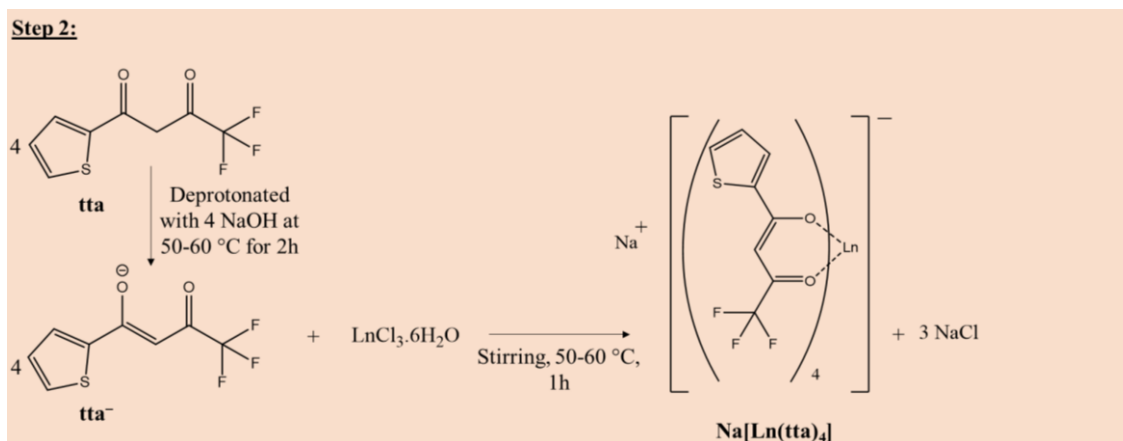
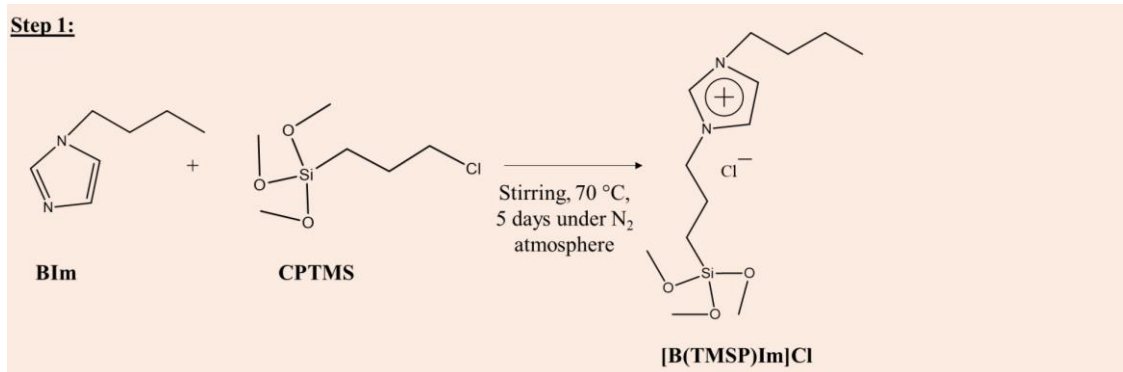


**Figure 3.2.** UV/visible absorption spectrum of PMMA.

*Synthesis of 1-butyl-3-[3-(trimethoxysilyl)propyl]imidazolium chloride ([B(TMSP)Im]Cl).* This compound was formed by mixing BIm with CPTMS (molar ratio BIm:CPTMS = 1:1) (**Scheme 3.2, Step 1**). The mixture was stirred at 70 °C for 5 days under nitrogen atmosphere. The resulting pale-yellow viscous product was washed thrice with anhydrous EtOAc (10 mL). It was then dried under vacuum to remove excess EtOAc and finally stored under vacuum conditions.

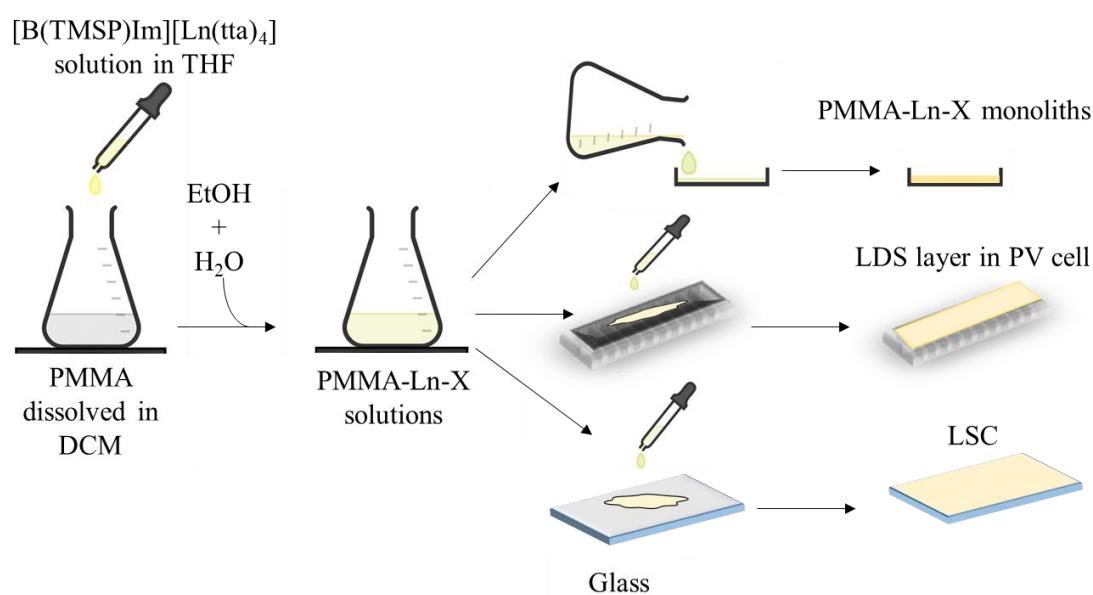
*Synthesis of sodium tetra(2-thenoyltrifluoroacetate) neodymate (III)/europate(III)/terbate(III)/yttrate(III) (Na[Ln(tta)<sub>4</sub>]).* For the preparation of Na[Ln(tta)<sub>4</sub>] salt (Ln = Nd<sup>3+</sup>, Eu<sup>3+</sup>, Tb<sup>3+</sup>, and Yb<sup>3+</sup>), a mass of 0.889 g of tta was dissolved in EtOH and then deprotonated with 0.16 g NaOH at 50-60 °C for 2 h. To this solution 1 equivalent of LnCl<sub>3</sub>·6H<sub>2</sub>O, dissolved in EtOH, was added dropwise (molar ratio tta:NaOH:LnCl<sub>3</sub>·6H<sub>2</sub>O = 4:4:1) (**Scheme 3.2, Step 2**). After keeping the mixtures at 50-60 °C for 1 h, EtOH was evaporated under reduced pressure on a rotary evaporator and the as-produced salts were dried for 3 days at 50 °C. The salts were subsequently dissolved in THF to remove sodium chloride (NaCl) by precipitation and centrifugation (thrice at 3000 r.p.m.). The products were dried in an oven at 50 °C, washed with ultrapure ice water, and dried again in an oven at 50 °C, then dried under vacuum conditions, and finally stored in a desiccator.



**Scheme 3.2.** Syntheses of the IS-Ln ionosilicas.

*Synthesis of 1-butyl-3-[3-(trimethoxysilyl)propyl]imidazolium tetra(2-thenoyltrifluoroacetate) neodymate(III)/europate(III)/terbate(III)/ytterbate(III) ([B(TMSP)Im][Ln(tta)<sub>4</sub>] with Ln = Nd<sup>3+</sup>, Eu<sup>3+</sup>, Tb<sup>3+</sup>, and Yb<sup>3+</sup>) and corresponding ionosilicas (IS-Ln).* To synthesize the [B(TMSP)Im][Ln(tta)<sub>4</sub>] and the IS-Ln compounds, Na[Ln(tta)<sub>4</sub>] was reacted with [B(TMSP)Im]Cl in THF under nitrogen atmosphere (molar ratio Na[Ln(tta)<sub>4</sub>]:[B(TMSP)Im]Cl=1:1) (**Scheme 3.2, Step 3**). NaCl was removed from the solution by precipitation and centrifugation (thrice at 3000 r.p.m.). EtOH and water were then added to this solution (molar ratio [B(TMSP)Im][Ln(tta)<sub>4</sub>]:EtOH:H<sub>2</sub>O=1:4:1.5) to initiate the sol-gel process. The mixture was stirred in a sealed flask for approximately 30 min, cast into a Teflon mold, covered with Parafilm and left in a fume cupboard for 24 h. The mold was subsequently transferred to an oven at 50 °C and the resulting IS-Ln sample, produced as a glassy monolith with a yellowish (Ln = Eu<sup>3+</sup>, Tb<sup>3+</sup>, and Yb<sup>3+</sup>) or blueish (Ln = Nd<sup>3+</sup>) hue, was aged for a period of 4 weeks (**Scheme 3.2, Step 4**). Elemental analyses: **IS-Nd** (NdC<sub>42</sub>H<sub>34</sub>S<sub>4</sub>N<sub>2</sub>O<sub>11</sub>SiF<sub>12</sub>). Calculated: C, 39.68; H, 2.70; N, 2.20; S, 10.09. Found: C, 41.15; H, 3.44; N, 2.23; S, 8.20; **IS-Eu** (EuC<sub>42</sub>H<sub>34</sub>S<sub>4</sub>N<sub>2</sub>O<sub>11</sub>SiF<sub>12</sub>). Calculated: C, 39.44; H, 2.69; N, 2.19; S 10.03. Found: C, 39.04; H, 2.85; N, 2.34; S, 8.04; **IS-Tb** (TbC<sub>42</sub>H<sub>34</sub>S<sub>4</sub>N<sub>2</sub>O<sub>11</sub>SiF<sub>12</sub>). Calculated: C, 39.23; H, 2.67; N, 2.18; S, 9.97. Found: C, 39.04; H, 3.02; N, 2.29; S, 9.38; **IS-Yb** (YbC<sub>42</sub>H<sub>34</sub>S<sub>4</sub>N<sub>2</sub>O<sub>11</sub>SiF<sub>12</sub>). Calculated: C, 38.80; H, 2.64; N, 2.16; S, 9.86. Found: C, 39.96; H, 3.05; N, 2.23; S, 8.31.

*Synthesis of the PMMA-Ln-X films.* For the preparation of the PMMA-Ln-X samples, a THF solution of [B(TMSP)Im][Ln(tta)<sub>4</sub>] was added to a PMMA solution in DCM (**Scheme 3.3**). EtOH and water were added to this solution (molar ratio B(TMSP)Im][Ln(tta)<sub>4</sub>]: EtOH: H<sub>2</sub>O = 1:4:1.5). The mixture was then stirred in a sealed flask for approximately 30 min. PMMA solutions with X=10 and 20% were produced. For the fabrication of the LDS layers, the PMMA-Ln-X materials were deposited onto commercial c-Si PV cells (KXOB22-01X8F, IXYS), hereafter designated as PV-1, by drop-casting of 0.07 mL of the PMMA-Ln-X solution. Then, the devices were placed in a DCM-rich atmosphere, at room temperature, where they remained for 5 h to ensure a slow drying of the layer and thus yield a transparent film. The same procedure was used to deposit the solution in glass to produce LSC.



**Scheme 3.3.** Syntheses of the composite films/LDS layers/LSC (Ln = Nd<sup>3+</sup>, Eu<sup>3+</sup>, Tb<sup>3+</sup> and Yb<sup>3+</sup>, X= 10, 20 % wt).

### 3.3. Results and discussion

#### Structural characterization

Prior the characterization of the final compounds, the chemical structure of the intermediary compounds [B(TMSP)Im]Cl, Na[Ln(tta)<sub>4</sub>] and [B(TMSP)Im][Ln(tta)<sub>4</sub>], and that of IS-Ln were confirmed.

**[B(TMSP)Im]Cl.** The molecular structure of [B(TMSP)Im]Cl (**Figure 3.3A**) and in particular the formation of the N<sup>+</sup>-C link between BIm and CPTMS were deduced from the <sup>1</sup>H and <sup>13</sup>C NMR spectra represented in **Figures 3.3B** and **3.4C**, respectively. The attribution of the corresponding resonances is given in **Table 3.1**.

In the <sup>1</sup>H NMR spectrum, the resonances at 9.30 and 7.85 ppm are associated with the three carbon atoms of the imidazolium ring. The 9.40 peak can be related with a shift of the 9.30 peak caused by hydrogen bonds with residual impurities in the sample.<sup>203</sup> The 4.25 ppm resonance, characteristic of the N<sup>+</sup>-C<sub>propyl</sub> link, confirms the success of the reaction between BIm and CPTMS. The peak at 3.5 ppm confirms that the methoxy (CH<sub>3</sub>O-) groups suffered no major hydrolysis. The 1.85 and 0.55 ppm signals correspond to the hydrogen atoms of the bridging propyl chain between the nitrogen and the silicon atom, and the signals between 1.80, 1.25 and 0.90 ppm correspond to the carbon atoms of the pendant butyl chain. The 4.15 ppm resonance is assigned to the N-C<sub>butyl</sub> link.<sup>204,205</sup>

In the  $^{13}\text{C}$  NMR spectrum the peak at 50.0 ppm indicates the presence of non-hydrolyzed methoxyl ( $\text{CH}_3\text{O}-$ ) groups. The 50.8, 23.2 and 5.3 ppm signals are associated with the carbon atoms of the bridging propyl chain. The peak at 6.6 ppm is tentatively associated with a minor hydrolysis of the compound that may have likely shifted the carbon atom closest to the silicon atom to higher  $\delta$  values,<sup>206</sup> possibly due to presence of water in the solvent. The three remaining signals between 48.5 and 13.2 are due to the carbon atoms of the pendant butyl chain.

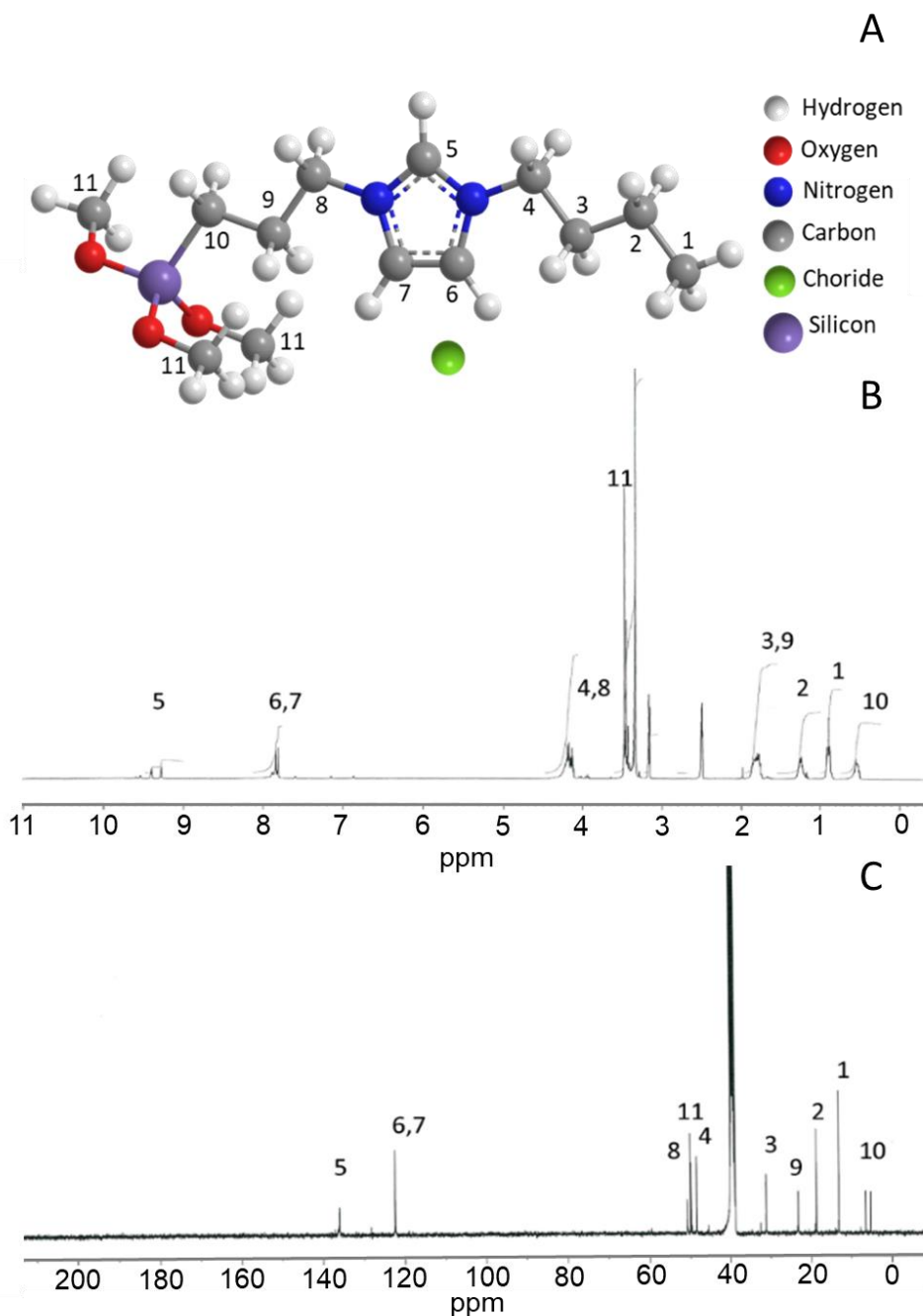


**Figure 3.3.** (A) Schematic representation of the chemical structure, and (B)  $^1\text{H}$  and (C)  $^{13}\text{C}$  NMR spectra (standardized intensity vs chemical shift) of  $[\text{B}(\text{TMSP})\text{Im}]\text{Cl}$ .

**Table 3.1.**  $^1\text{H}$  and  $^{13}\text{C}$  NMR spectroscopic data of  $[\text{B}(\text{TMSP})\text{Im}]\text{Cl}$ . Chemical shifts ( $\delta$ ) in ppm.

NMR	$\delta_{\text{experimental}}$	$\delta_{\text{literature}}^{203,207}$	Attribution
$^1\text{H}$	0.55	0.63	H <sub>10</sub> propyl-Si
	0.90	0.92	H <sub>1</sub> butyl
	1.25	1.27	H <sub>2</sub> butyl
	1.80	1.81	H <sub>3</sub> butyl
	1.85	2.00	H <sub>9</sub> propyl
	3.50	3.56	H <sub>11</sub> methoxyl
	4.15	4.23	H <sub>4</sub> butyl-N <sub>ring</sub>
	4.25	4.35	H <sub>8</sub> propyl-N <sub>ring</sub>
	7.85	7.39	H <sub>6,7</sub> ring
	9.30; 9.40	10.11	H <sub>5</sub> ring
$^{13}\text{C}$	5.3; 6.6	5.9	C <sub>10</sub> propyl
	13.2	13.3	C <sub>1</sub> butyl
	18.7	18.8	C <sub>2</sub> butyl
	23.2	24.1	C <sub>9</sub> propyl
	31.1	31.4	C <sub>3</sub> butyl
	48.5	48.5	C <sub>4</sub> butyl
	50.0	50.7	C <sub>11</sub> methoxyl
	50.8	51.7	C <sub>8</sub> propyl
	122.4	121.9	C <sub>6,7</sub> ring
	136.0	136.5	C <sub>5</sub> ring

To find further support to the NMR results, the FT-IR spectrum of  $[\text{B}(\text{TMSP})\text{Im}]\text{Cl}$  was recorded and analyzed. The spectrum is reproduced in **Figure 3.4**, green line, and the attribution of the vibrational bands is listed in **Table 3.2**.

In the 3200-2800  $\text{cm}^{-1}$  interval most of the bands observed are associated with BIm, except that located at 3106  $\text{cm}^{-1}$  (**Figure 3.4**, black line) which is tentatively assigned to the CH<sub>ring</sub> asymmetric stretching. This band was downshifted to 3044  $\text{cm}^{-1}$  as a result of the formation of N<sup>+</sup>-C link.<sup>208</sup> In the 1550-500  $\text{cm}^{-1}$  spectral region, the formation of  $[\text{B}(\text{TMSP})\text{Im}]\text{Cl}$  (**Figure 3.4**, green line). was confirmed through the absence of the characteristic bands of CPTMS at 1310 and 864  $\text{cm}^{-1}$ <sup>209</sup> (**Figure 3.4**, red line). The bands characteristic of the methoxyl groups of CPTMS remain present, pointing out that this compound did not suffer significant hydrolysis, in agreement with the NMR data.<sup>209</sup> The water bending 1640  $\text{cm}^{-1}$  band is absent in the spectrum. The bands due to the butyl chain suggest that the tg<sup>±</sup>tt conformation is preserved in the compound.<sup>210</sup>

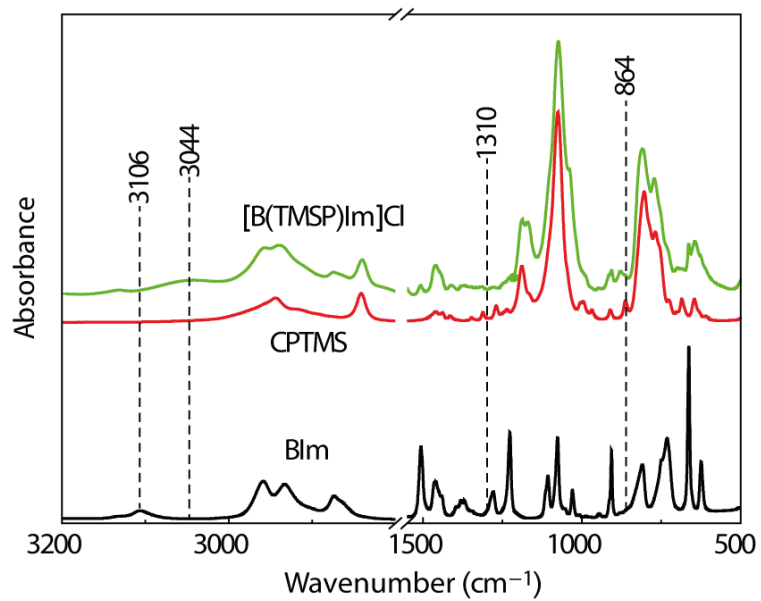


**Figure 3.4.** FT-IR spectra of BIm, CPTMS and [B(TMSP)Im]Cl.

**Table 3.2.** Assignment of the FT-IR vibrational bands of [B(TMSP)Im]Cl.

BIm	CPTMS	[B(TMSP)Im]Cl	BIm <sup>172</sup> /CPTMS <sup>179</sup>	Assignment
3133		3133	3133	CH <sub>ring</sub> symmetric stretch
3106		3044		CH <sub>ring</sub> asymmetric stretch
2959		2959	2959	CH <sub>3</sub> asymmetric stretch (r <sup>-</sup> )
2933		2933	2933	CH <sub>3</sub> symmetric FR (r <sup>+FR</sup> )
2902		2902	2902	CH <sub>2</sub> asymmetric stretch (d <sup>-</sup> )
2874		2874	2874	CH <sub>3</sub> symmetric stretch (r <sup>+</sup> )
2863		2863	2863	CH <sub>2</sub> symmetric stretch (d <sup>+</sup> )
	2840	2840	2840	-Si-OCH <sub>3</sub>
1506		1506	1504; 1508	In plane C-H bending (ring) + CH <sub>2</sub> scissoring; NC anti symmetric stretching + in plane C-H bending (ring)
1460		1458	1461.9	CH <sub>2</sub> scissoring
1393			1397.3	CH <sub>2</sub> twisting + NC anti symmetric stretching
1379, 1370			1369.3; 1383.5	CH <sub>2</sub> wagging + CH <sub>3</sub> umbrella
	1310		1310	-Si-CH <sub>2</sub> CH <sub>2</sub> CH <sub>2</sub> -Cl
1279			1278.7	In plane C-H (C-H) bending (ring)+ CH <sub>2</sub> wagging
1226		1227	1228	In plane C-H bending (ring)+ NC stretching
	1190	1190	1190	-Si-OCH <sub>3</sub>
1106			1111.1	In plane C-H bending (ring)
1076, 1053	1076	1076	1100-1080; 1075.3	In plane C-H (C-H) bending (ring); -Si-OCH <sub>3</sub>
1030		1041	1031	NC <sub>2</sub> scissoring (ring) + CH <sub>2</sub> rocking
946, 907		947	945.4; 903.1	NC <sub>2</sub> scissoring (ring)
	910	908	910	-Si-CH <sub>2</sub> CH <sub>2</sub> CH <sub>2</sub> -Cl
	864		860	-Si-CH <sub>2</sub> CH <sub>2</sub> CH <sub>2</sub> -Cl
810		810	808.9	Out of plane C-H bending (ring)
749- 731		752;731	753.9; 751.8; 730.1; 726.4; 721.5	Out of plane C-H (C-H) bending (ring)
665		665	662.7	Out of plane C-H bending (ring) + NC <sub>2</sub> wagging (ring)
622			623	Out of plane C-H bending (ring) + NC <sub>3</sub> wagging (ring)

*Na[Ln(tta)<sub>4</sub>]*. To conclude about the formation of this compound (**Figure 3.5A**) the FT-IR spectrum of this compound was examined in the 1700-1500 cm<sup>-1</sup> interval (**Figure 3.6**, red line). In this range of wavenumbers, valuable information regarding the changes undergone by the C=O and C=C stretching vibrations of tta upon complexation to the Ln<sup>3+</sup> ions may be retrieved.

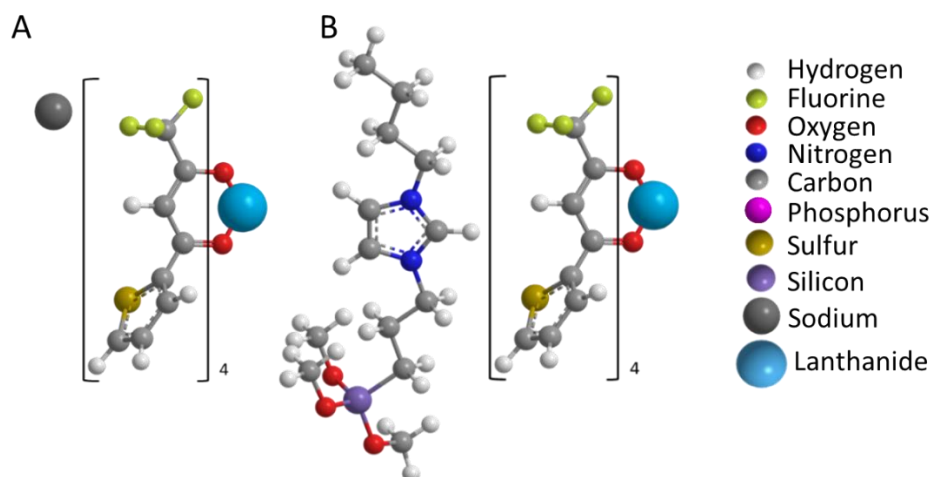


**Figure 3.5.** Schematic representation of the chemical structure of (A)  $\text{Na}[\text{Ln}(\text{tta})_4]$  and (B)  $[\text{B}(\text{TMSP})\text{Im}][\text{Ln}(\text{tta})_4]$ .

The bands corresponding to the C=O and C=C stretching vibrations of the free tta are reported at  $1676$  and  $1632\text{ cm}^{-1}$ , respectively.<sup>211</sup> In the present work these bands were detected at  $1652$  and  $1636\text{ cm}^{-1}$  (**Figure 3.6**, black line). In the  $\text{Na}[\text{Ln}(\text{tta})_4]$  compounds, both bands were downshifted to  $1600$  and  $1535\text{ cm}^{-1}$ , respectively,<sup>211</sup> thus confirming  $\text{tta}^-$  bonding to the  $\text{Ln}^{3+}$  ions. The FT-IR spectrum of  $\text{Na}[\text{Eu}(\text{tta})_4]$  is shown in **Figure 3.6** (red line).

**IS-Eu.** The FT-IR spectrum of this compound (**Figure 3.6**, green line) was analysed to validate its chemical structure. Similarly to the situation found in the FT-IR spectrum of  $\text{Na}[\text{Ln}(\text{tta})_4]$ , the C=O and C=C stretching vibrations of  $\text{tta}^-$  are seen at  $1600$  and  $1535\text{ cm}^{-1}$ , respectively,<sup>211</sup> corroborating the conservation of  $\text{tta}^-$  bonding to the  $\text{Ln}^{3+}$  ions in IS-Ln upon replacement of the  $\text{Na}^+$  ion by the  $[\text{B}(\text{TMSP})\text{Im}]^+$  ion.

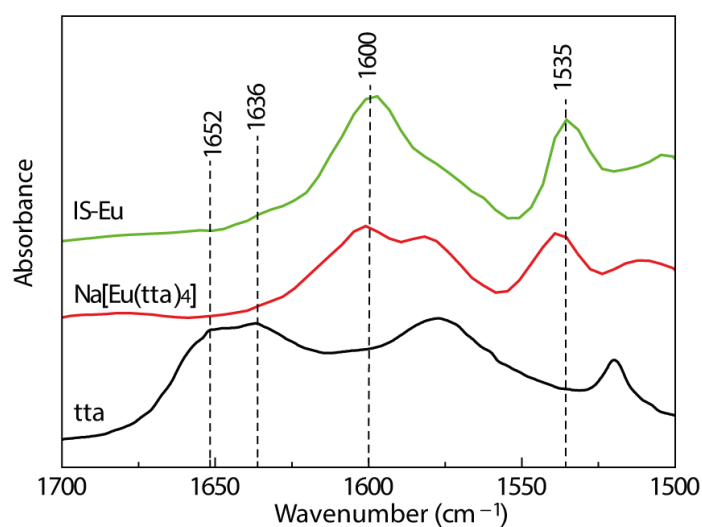


**Figure 3.6.** FT-IR spectra of tta,  $\text{Na}[\text{Eu}(\text{tta})_4]$  and IS-Eu.

**IS-Ln and PMMA-Ln-X.** The structural, morphological, and thermal properties of the IS-Ln and PMMA-Ln-X samples were characterized.

The structure of the materials was examined by means of XRD, POM, TEM, and FT-IR. **Figure 3.7A** (red line) reproduces the XRD pattern of IS-Eu which shows a broad band at  $20.1^\circ$  ascribed to the presence of coherent diffracting domains of the siliceous backbone.<sup>212</sup> The structural unit distance estimated, using the Bragg law (**Equation A.1**), was  $4.4 \text{ \AA}$ . Additionally, a component around  $8.9^\circ$  was also discerned **Figure 3.7A** (red line) being ascribed to in-plane ordering of intra-siloxane domains with a characteristic distance of  $\sim 7 \text{ \AA}$ .<sup>213</sup> The presence of the low-intensity band at  $4.2^\circ$  (unit distance  $\sim 21 \text{ \AA}$ ) (**Figure 3.7A**, red line) may be interpreted with the help of the POM and TEM images of IS-Eu. The thin superimposed platelets and the submicrometer birefringence evidenced by POM (**Figure 3.7B**) reveal the anisotropic nature of the sample. The well-ordered structures observed in several regions of the TEM image (**Figure 3.7C**) indicate the occurrence of a lamellar organization in IS-Eu. The latter phenomenon was also observed for layered silicates displaying a bilayer arrangement in which 1-butylimidazolium chloride groups, bonded to the siliceous network via propyl chains, were found to be partially interdigitated.<sup>201,214–216</sup> The length of the pendant butylimidazolium-based group (from the terminal carbon atom of the butyl chain to the Si atom; **Figure 3.3A**) was estimated to be  $\sim 14 \text{ \AA}$ , assuming an all-*trans* conformation for the butyl chain.<sup>215</sup> This leads us to conclude that the  $4.2^\circ$  peak corresponds to the 1<sup>st</sup> order of a lamellar bilayer arrangement. It is noteworthy that in IS-Eu the characteristic distance is  $21 \text{ \AA}$  ( $< 2 \times 14 \text{ \AA}$ ), suggesting more interpenetration of the pendant chains than that found in Takahashi's silicate.<sup>215</sup> The absence of the higher orders of the  $4.2^\circ$  peak reveals that this lamellar organization has a low degree of order, probably because of the bulkiness of the complex anion.

Upon incorporation into PMMA ( $X=10$ ), the IS-Eu-related diffraction pattern was completely overlapped by that characteristic of PMMA (**Figure 3.7A**, light blue line).<sup>217,218</sup> However, for the more concentrated samples PMMA-Ln-20 this effect is less evident (**Figure 3.7A**).

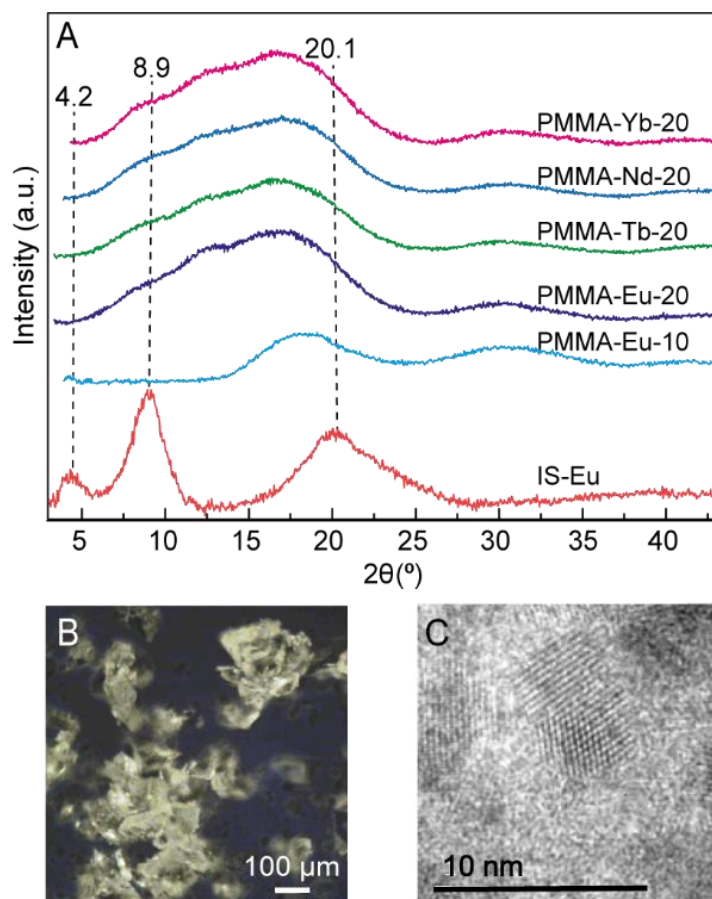


**Figure 3.7.** (A) XRD diffraction patterns of IS-Eu, PMMA-Eu-10 and PMMA-Ln-20 (Ln = Nd<sup>3+</sup>, Eu<sup>3+</sup>, Tb<sup>3+</sup> and Yb<sup>3+</sup>); (B) POM (crossed polarizers), and (C) TEM images of IS-Eu.

As the PMMA macromolecule contains in its composition a C=O group in the pendant chain, it was essential to determine if at least a proportion of these groups bonded to the Ln<sup>3+</sup> ions in the composite materials.<sup>219</sup> To elucidate the IS-Ln ... PMMA interaction, the ATR/FT-IR spectra of the PMMA-Ln-X samples were examined (**Figure 3.8**). The fact that the broad and prominent band due to the stretching vibration of the acrylate C=O group of PMMA at 1722 cm<sup>-1</sup> (**Figure 3.8**, black line) remained unshifted in the FT-IR spectra of PMMA-Eu-10 (**Figure 3.8**, brown line), PMMA-Nd-20 (**Figure 3.8**, blue line), PMMA-Tb-20 (**Figure 3.8**, green line), and PMMA-Yb-20 (**Figure 3.8**, pink line) provided conclusive evidence that the C=O groups of PMMA did not interact with the Ln<sup>3+</sup> ions in any of these samples.<sup>41</sup> However, the FT-IR data revealed additional information. The inspection of the C=O stretching band of the tta<sup>-</sup>-ligands in these spectra was particularly useful. While IS-Eu produced a band centred at approximately 1600 cm<sup>-1</sup> (**Figure 3.6**, green line, and **Figure 3.8**, red line), the intensity maximum of

this mode was shifted to  $1610\text{ cm}^{-1}$  upon incorporation of IS-Eu into the PMMA matrix (**Figure 3.8**, brown line), thus pointing out that the local chemical environment around the  $\text{Ln}^{3+}$  ions changed slightly, suggesting a slight weakening of the  $\text{Eu}^{3+}\text{-O}=\text{C}(\text{tta}^-)$  bonding. The same effect occurred for the other IS-Ln.<sup>219</sup> These results are not surprising considering steric hindrance effects arising from the interaction between the bulky  $\text{tta}^-$  ligands and the PMMA chains which comprise bulky acrylate groups.

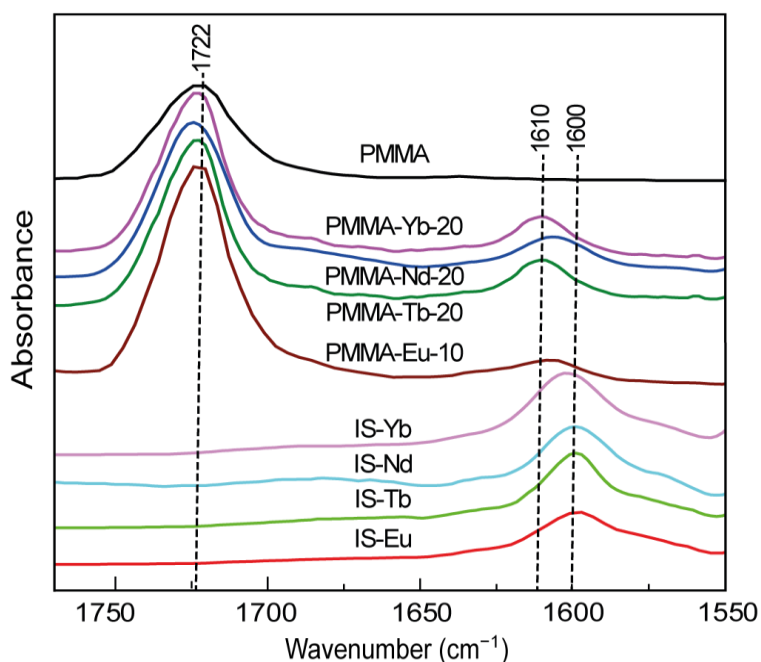


**Figure 3.8.** ATR/FT-IR spectra of PMMA, IS-Ln, PMMA-Eu-10 and PMMA-Ln-20 (Ln =  $\text{Nd}^{3+}$ ,  $\text{Tb}^{3+}$  and  $\text{Yb}^{3+}$ ).

The morphology of the PMMA-Ln-X samples was studied by SEM, EDS mapping, and POM. While the SEM image of PMMA-Eu-10 (**Figure 3.9A**) shows that this composite exhibits a homogeneous texture, the corresponding EDS mapping images demonstrate that all the components are homogeneously distributed. The same results were observed for the other samples (not shown).

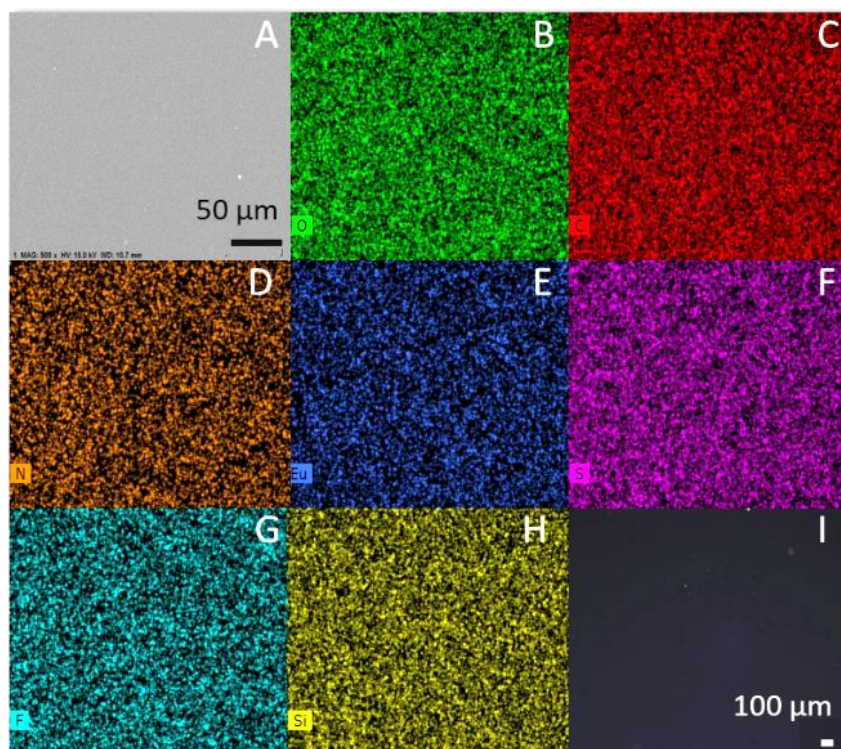


**Figure 3.9.** (A) SEM, (B-H) EDS mapping (oxygen – green, carbon – red, nitrogen – orange, europium – dark blue, sulfur – purple, fluorine – cyanide, silicon – yellow) and (I) POM images of PMMA-Eu-10.

The thermal behaviour of the IS-Ln and PMMA-Ln-X samples was studied by TGA and DSC.

The TGA curve of the IS-Yb sample (**Figure 3.10**, blue line) shows a loss of 1% from 23 to 140 °C probably due to the release of adsorbed water.<sup>78</sup> Analysis of the DTGA data (**Figure 3.10**, red line) in the 140-800 °C range reveals three main decomposition stages with maximum mass loss rates occurring at 232, 333 and 616 °C, related with the thermal decomposition of the  $tta^-$  ligands,<sup>220,221</sup> of the cation organic moieties,<sup>220</sup> and possibly of the Si-O-Si skeleton structure,<sup>220,221</sup> respectively. These losses represent a total of 78 % which is in good agreement with the theoretical value (79 %). At 800 °C the remaining mass is associated with pure silica ( $SiO_2$ )<sup>222</sup> and lanthanide oxide ( $Ln_2O_3$ ).<sup>220,223</sup> This analysis confirm the presence of four  $tta^-$  ligands in the anion and the lack of  $H_2O$  molecules in IS-Yb.

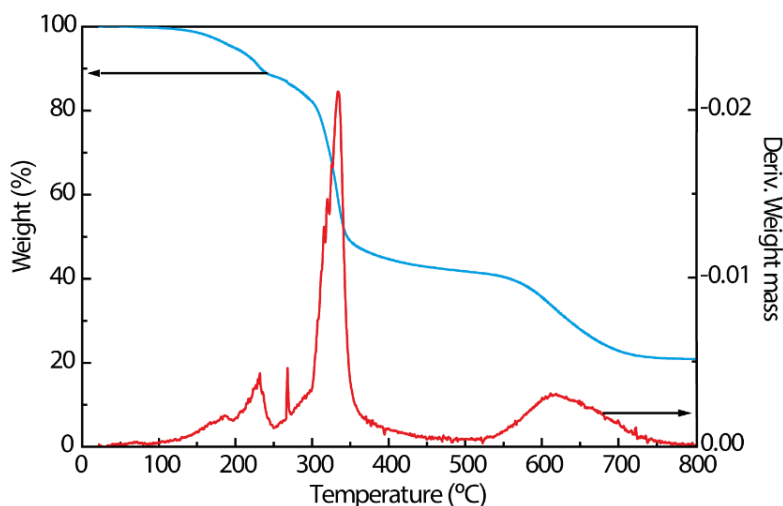


**Figure 3.10.** TGA (light blue line) and DTGA (red line) curves of IS-Yb.

The DSC curve of PMMA (**Figure 3.11**, black line) displays a  $T_g$  value of about 68 °C, indicating that the PMMA sample is essentially isotactic.<sup>217</sup> The IS-Eu material gave rise to a broad, asymmetric endothermic peak centred at 70 °C with onset at 56 °C (**Figure 3.11**, red line, and inset). This reversible thermal event (**Figure 3.12**) is tentatively associated with two effects: the order-disorder transition of the pendant organic groups located in the interlamellar space, and the reversible thermotropic *gauche/trans* transition of the butyl group of the imidazolium ring.<sup>224</sup> This reversible effect is very attractive for applications in optical devices.<sup>225</sup> The PMMA-Eu-10 composite exhibited a thermal behaviour identical to that of PMMA, indicating that no alteration in the PMMA chains arrangement resulted upon IS-Eu incorporation.

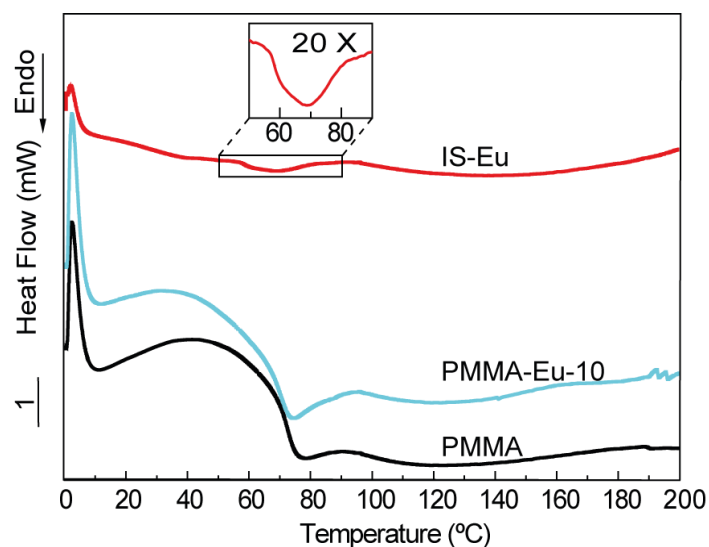


**Figure 3.11.** DSC curves of PMMA, IS-Eu and PMMA-Eu-10.

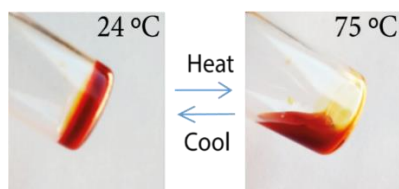


**Figure 3.12.** Reversible thermal transition of IS-Eu.

The water static contact angle ( $\theta$ ) of the IS-Ln and composite samples were determined to get insight into the wettability behaviour. PMMA is hydrophilic, with a  $\theta$  value of  $\sim 69 \pm 2^\circ$  (**Figure 3.13**), in agreement with the reported value,<sup>226</sup> and the IS-Ln samples are hydrophobic ( $\sim 128 \pm 7 < \theta < \sim 141 \pm 4$ ). **Figure 3.13** shows that all the PMMA-Ln-X films, except PMMA-Yb-X ( $\theta = \sim 100 \pm 2^\circ$ ), also display hydrophilic behaviour.

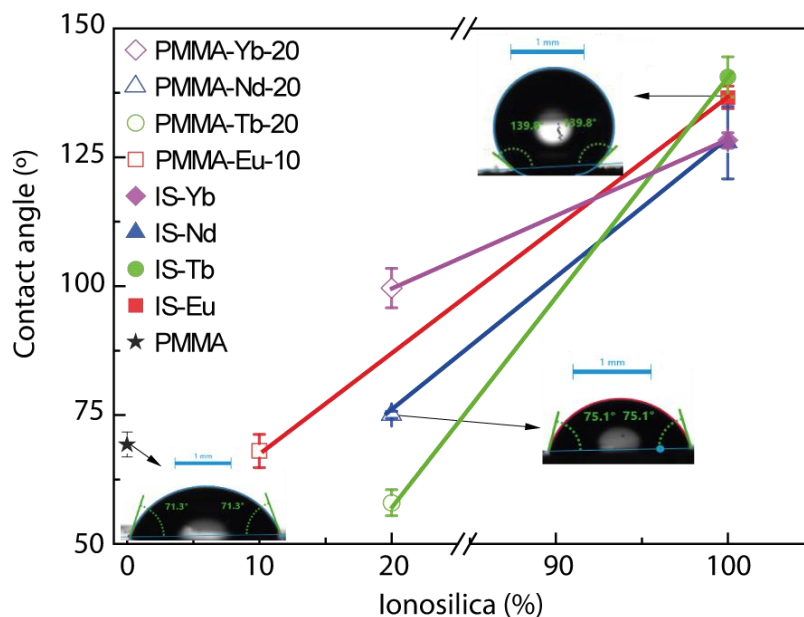


**Figure 3.13.** Water static contact angles of PMMA, IS-Ln, and PMMA-Ln-X.

### Optical properties

**Figure 3.14A** shows the room temperature emission spectra of the PMMA-Ln coatings excited at the wavelength that maximizes the emission intensity. The emission spectra are dominated by the lines ascribed to the  $\text{Tb}^{3+}$  ( $^5\text{D}_4 \rightarrow ^7\text{F}_{6-3}$ ),  $\text{Eu}^{3+}$  ( $^5\text{D}_0 \rightarrow ^7\text{F}_{0-4}$ ),  $\text{Yb}^{3+}$  ( $^2\text{F}_{5/2} \rightarrow ^2\text{F}_{7/2}$ ) and  $\text{Nd}^{3+}$  ( $^4\text{F}_{3/2} \rightarrow ^4\text{I}_{11/2}$ ) transitions. Independently of the selected

excitation wavelength (270-380 nm), no sign of the PMMA intrinsic emission could be observed, which readily suggests efficient PMMA-to-ligand/Ln<sup>3+</sup> energy transfer.<sup>227</sup>

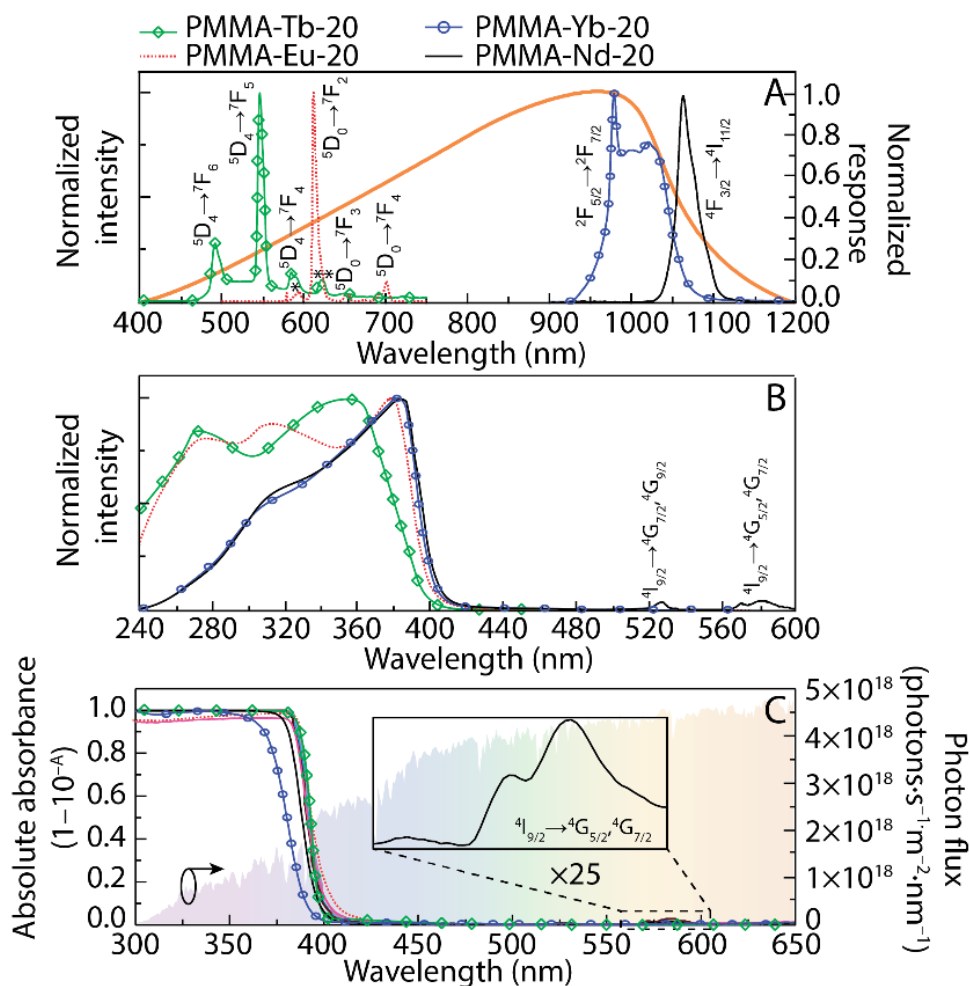


**Figure 3.14.** (A) Si absorption spectrum and emission spectra excited at 360-380 nm. The \* and \*\* assign the superimposition between the Eu<sup>3+</sup>  $^5D_0 \rightarrow ^7F_{0-1}$ / $^5D_0 \rightarrow ^7F_2$  and the Tb<sup>3+</sup>  $^5D_4 \rightarrow ^7F_4$ / $^5D_4 \rightarrow ^7F_3$  transitions, respectively. (B) Excitation spectra monitored at 545 nm/612 nm/978 nm/1062 nm for PMMA-Tb/Eu/Yb/Nd-20. (C) Absorption spectra; the inset shows a magnification of the Nd<sup>3+</sup> related  $^4I_{9/2} \rightarrow ^4G_{5/2}$ ,  $^4G_{7/2}$  transition.

The excitation spectra were selectively monitored, **Figure 3.14B**. In the case of PMMA-Eu, the spectra show three main components peaking at 275, 320 and 380 nm. The low intensity of the intra-4f<sup>6</sup> lines indicates that the Eu<sup>3+</sup> excited states in PMMA are populated via ligand-sensitization. The 320 and 380 nm components resemble those already observed for isolated Eu(tta)<sub>3</sub>(H<sub>2</sub>O)<sub>2</sub><sup>171</sup> and for organic-inorganic hybrids incorporating Eu(tta)<sub>3</sub>(H<sub>2</sub>O)<sub>2</sub> and Eu(tta)<sub>3</sub>(phen) (phen=1,10-phenantroline), being

ascribed to the  $\pi-\pi^*$  electronic transition of the organic ligands.<sup>228</sup> Apart from changes in the relative intensity, the UV-visible absorption spectrum reveals the same components detected in the excitation spectra, **Figure 3.14B** and **Figure 3.14C**. The emission decay curves were monitored under UV excitation (360-380 nm) revealing a single exponential behaviour (**Figure 3.15**). From the best data fit, the lifetime values were estimated (**Table 3.3**). The increase of the lifetime values as the temperature decreases suggests the presence of thermally activated non-radiative channels, as detailed below. The absolute emission quantum yield ( $q$ ) values were measured as a function of the excitation wavelength (270-385 nm for PMMA-Eu-10/20, PMMA-Tb-10/20, PMMA-Yb-10/20 samples, and 808 nm for PMMA-Nd-10/20), in which the maximum values were found for excitation wavelengths in the UV spectral region depending on the material (**Table 3.3**) and for PMMA-Nd-10/20 the  $q$  was higher when excited at 808 nm. The lower  $q$  values found for the NIR emitting films (Nd<sup>3+</sup>, Yb<sup>3+</sup>) suggest the stronger contribution of the organic ligands for the non-radiative transition probability, with respect to that found in the visible-emitting (Eu<sup>3+</sup>, Tb<sup>3+</sup>) materials.<sup>229,230</sup>

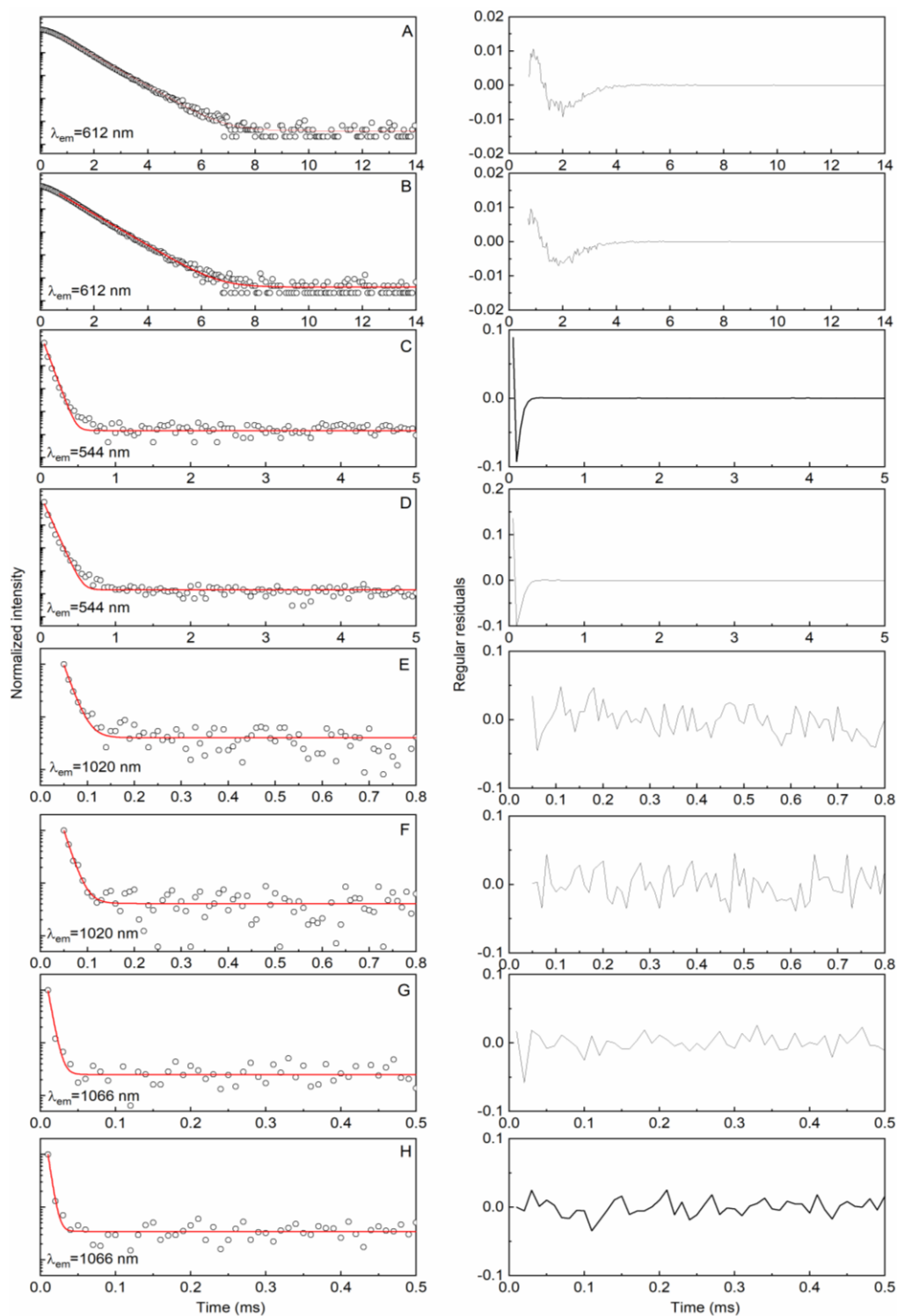


**Figure 3.15.** Room temperature emission decay curves for (A) PMMA-Eu-10, (B) PMMA-Eu-20, (C) PMMA-Tb-10, (D) PMMA-Tb-20, (E) PMMA-Yb-10, (F) PMMA-Yb-20, (G) PMMA-Nd-10 and (H) PMMA-Nd-20 excited at 380 nm and monitored at 612 nm (Eu), 544 nm (Tb), 1062 nm (Nd) and 978 nm (Yb). The solid lines represent the best fit ( $r^2 > 0.97$ ) using a single exponential function. The respective residual plots are shown on the right-hand side.

These values although lower than those previously reported for PMMA doped with  $\text{Eu}(\text{tta})_3(\text{phen})$ , with  $q=0.73\pm 0.06$ ,<sup>231</sup> and  $[\text{Eu}(\text{hfac})_3(\text{DPEPO})]$  (hfac=hexafluoroacetylacetonate and DPEPO=bis(2-(diphenylphosphino)phenyl)ether oxide, with values of  $q=0.85\pm 0.09$ ,<sup>232</sup> are similar to that of a composite material consisting of PMMA and the ionic liquid 1-hexyl-3-methylimidazolium bis(trifluoromethylsulfonyl)-imide with  $\text{Eu}(\text{tta})_3(\text{phen})$ , which presented  $q=0.46$ .<sup>233</sup>

**Table 3.3.** Emission lifetime values, integral overlap ( $O$ ,  $\times 10^{19}$  photons $\cdot\text{s}^{-1}\cdot\text{m}^{-2}$ ), absolute emission quantum yield ( $q$ ), molar extinction coefficient ( $\varepsilon$ ,  $\times 10^3$   $\text{M}^{-1}\cdot\text{cm}^{-1}$ ) and brightness ( $B$ ,  $\text{M}^{-1}\cdot\text{cm}^{-1}$ ) of PMMA-Ln-X.

	$\tau$ (ms)	$O$	$\varepsilon$	$q^{a,b}$	$B$
PMMA-Tb-10	0.060 $\pm$ 0.001	8.1	3.6 (360 nm)	0.006	21.6
PMMA-Tb-20	0.061 $\pm$ 0.001	8.4	1.6 (360 nm)	0.008	12.8
PMMA-Eu-10	0.655 $\pm$ 0.001	8.7	2.0 (375 nm)	0.517	1.0 $\times 10^3$
PMMA-Eu-20	0.640 $\pm$ 0.001	9.5	1.1 (368 nm)	0.473	5.2 $\times 10^2$
PMMA-Yb-10	0.017 $\pm$ 0.001	7.9	-	<0.001	-
PMMA-Yb-20	0.015 $\pm$ 0.001	8.7	2.2 (335 nm)	<0.001	-
PMMA-Nd-10	0.005 $\pm$ 0.001	8.2	-	0.001	-
PMMA-Nd-20	0.004 $\pm$ 0.001	10.0	4.0 (335 nm)	0.001	4.0

<sup>a</sup> $q$  values excited at 360 nm for PMMA-Tb-10/20, 380 nm for PMMA-Eu-10/20, 385 nm for PMMA-Yb-10/20 and 808 nm for PMMA-Nd-10/20 (power density of 531.88  $\text{W}\cdot\text{cm}^{-2}$ ). <sup>b</sup> The absolute emission quantum yield error is 10%.

Comparing the photoluminescence characterization data of the isolated IS and of the IS incorporated into the PMMA host, no significant changes were verified. For the illustrative case of IS-Eu and PMMA-Eu-10, the low-temperature emission spectra in **Figure 3.16A** present no variation in the energy, fwhm, relative intensity and number of emission components of the  $^5\text{D}_0 \rightarrow ^7\text{F}_{0-4}$ . The same happens for the excitation spectra (**Figure 3.17**), showing the same components in both cases, indicating that there are no modifications in the first coordination sphere. The emission decay curves measured at low and room temperature and estimated lifetime values (**Figure 3.16B** and **3.18**, and **Table 3.4**) of the mentioned samples corroborate the data from structural

characterization, which pointed out that there is no chemical interaction between PMMA and IS-Ln. Nevertheless, the structural arrangement of the IS-Ln in the PMMA matrix may induce some suppression of non-radiative mechanisms, which is indicated by an increase in the emission lifetime values for the PMMA-Eu-10 comparing with that of solely IS-Ln. Moreover, it is possible to notice a rise time of  $\sim 100 \mu\text{s}$  in the emission decay curve of the PMMA-Eu-10, which may be due to the cross-relaxation of the  $^5\text{D}_1$  excited state.

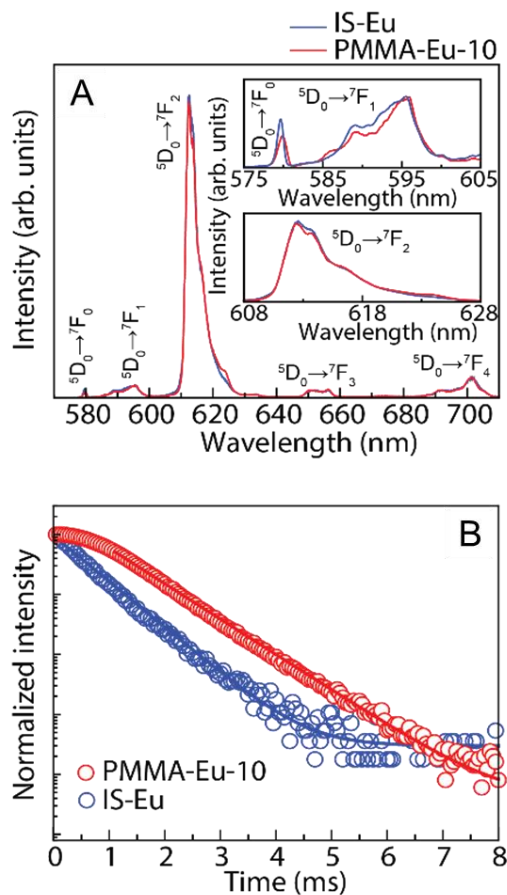


**Figure 3.16.** (A) Low temperature (12 K) emission spectra excited at 385 nm; the insets show a magnification of the  $^5\text{D}_0 \rightarrow ^7\text{F}_0$ ,  $^5\text{D}_0 \rightarrow ^7\text{F}_1$  and  $^5\text{D}_0 \rightarrow ^7\text{F}_2$  transitions and (B) low temperature (12 K) emission decay curves excited at 385 nm and monitored at 612 nm for PMMA-Eu-10 and IS-Eu.

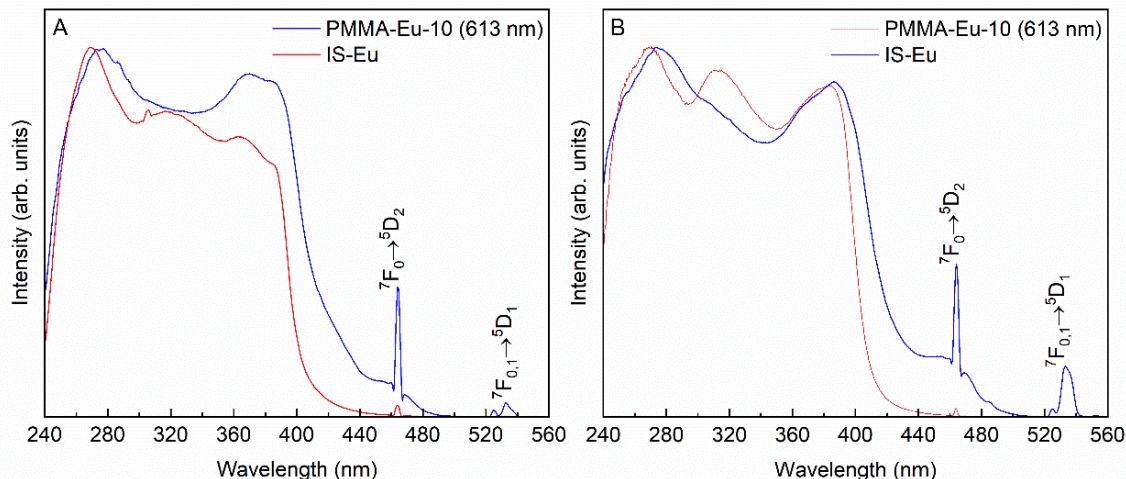


**Figure 3.17.** (A) Low temperature (12 K) and (B) room temperature excitation spectra of the IS-Eu and of PMMA-Eu-10 and of PMMA-Eu-10 monitored at 613 nm.

The lifetime dependence on the temperature may be further rationalized as follows. The experimental transition probability may be expressed as  $\tau_{exp}^{-1} = k_r + k_{nr}$ , where  $k_r$  is the radiative recombination probability and  $k_{nr}$  represents the non-radiative recombination probability. Since at low temperature (12 K),  $\tau_{exp}^{-1} \sim k_r$  the analogous values found for IS-Eu and PMMA-Eu-10 are in good agreement with the maintenance of the  $\text{Ln}^{3+}$ -first coordination sphere after PMMA incorporation. Nonetheless, as the temperature is raised, the  $\tau_{exp}^{-1}$  is larger for PMMA-Eu-10, indicating a suppression of  $k_{nr}$  due to the presence of PMMA.

**Table 3.4.** Emission lifetime values at low (12 K) and room temperature for IS-Eu and PMMA-Eu-10 excited at 365 and 385 nm, respectively, and monitored at 612 nm.

Sample	$\tau$ (ms)	
	12 K	300 K
IS-Eu	0.569±0.004	0.487±0.005
PMMA-Eu-10	0.576±0.005	0.510±0.005

The light harvesting ability of the optically active materials is of primary importance when seeking for PV related applications.<sup>141</sup> So, in order to maximize the performance of LSCs, it is relevant to quantify the overlap integral between the materials absorbance and the sunlight available for PV conversion, given by **Equation (3.1)**.<sup>234</sup>

$$O = \int_{\lambda_1}^{\lambda_2} \Phi_{AM1.5G}(\lambda) \times (1 - 10^{-A(\lambda)}) d\lambda \quad (3.1)$$

where  $\lambda_1$  (300 nm) and  $\lambda_2$  (800 nm) are the limits of the spectral overlap between the absorption spectrum of each sample and the AM1.5G spectrum,  $\Phi_{AM1.5G}$  is the AM1.5G photon flux and  $A$  is the absorbance of the PMMA-Ln samples.

The spectral overlap is illustrated in **Figure 3.14C**, for which the calculated  $O$  values indicate a potential to absorb  $\sim 2\%$  of the solar photon flux<sup>235</sup> on the surface of the Earth ( $4.3 \times 10^{21}$  photons $\cdot$ s<sup>-1</sup> $\cdot$ m<sup>-2</sup>) for all the coatings. To complement the quantification of the light harvesting ability, the molar extinction coefficient ( $\varepsilon$ , M<sup>-1</sup> $\cdot$ cm<sup>-1</sup>) was estimated (**Table 3.3**).

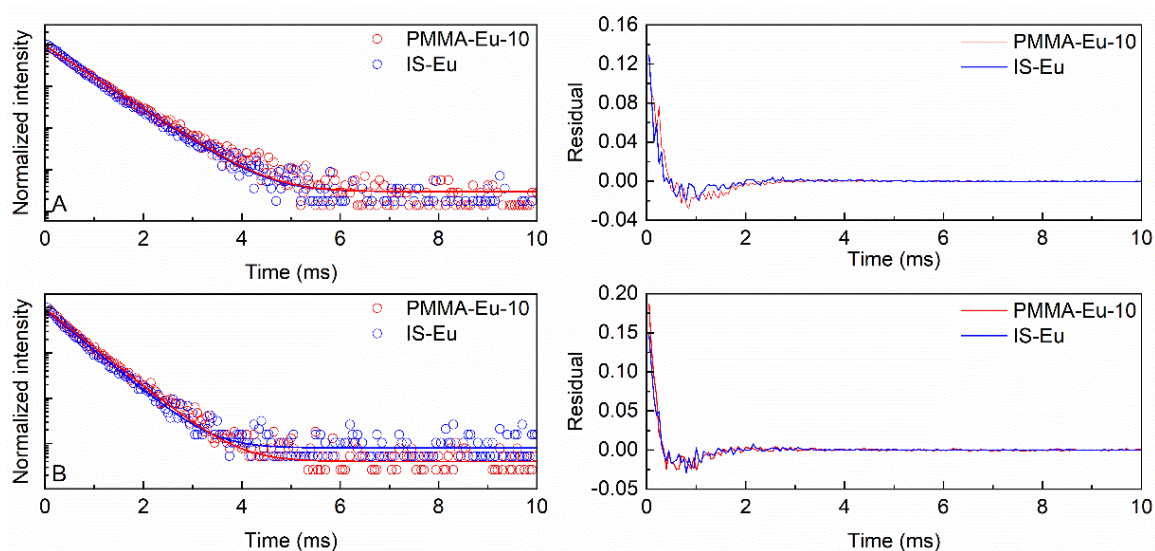


**Figure 3.18.** (A) Low temperature (12 K) and (B) room temperature emission decay curves of IS-Eu and PMMA-Eu-10 excited at 385 nm and monitored at 612 nm. The respective residual plots are shown on the right-hand side.

Brightness defined as  $B = \varepsilon \times q$  is a measure of the light emission efficiency and light harvesting ability, allowing the contribution of both parameters to be compared across distinct samples. The larger  $B$  value is governed by the larger  $q$  values of PMMA-Eu-10/20. Taking into account the optical properties, namely the largest integral overlap and brightness values, PMMA-Eu-10 is the coating with highest potential for PV applications both as LDS layers and LSC.

To see the PMMA-Ln-X true potential in real applications, LDS layers and LSC were made using these materials.

## Luminescent down-shifting layers

The use of LDS layers on PV cells may have a beneficial two-fold effect on the enhancement of their performance: (1) reducing the surface reflectance, and (2) increasing the EQE in the absorption range of the LDS layer through UV-downshifting of the collected radiation. As an example, is presented here the results for the PMMA-Eu-10 layer with  $1.71\pm 0.12\ \mu\text{m}$  that was deposited onto the top surface of PV-1 **Figure. 3.19A**.

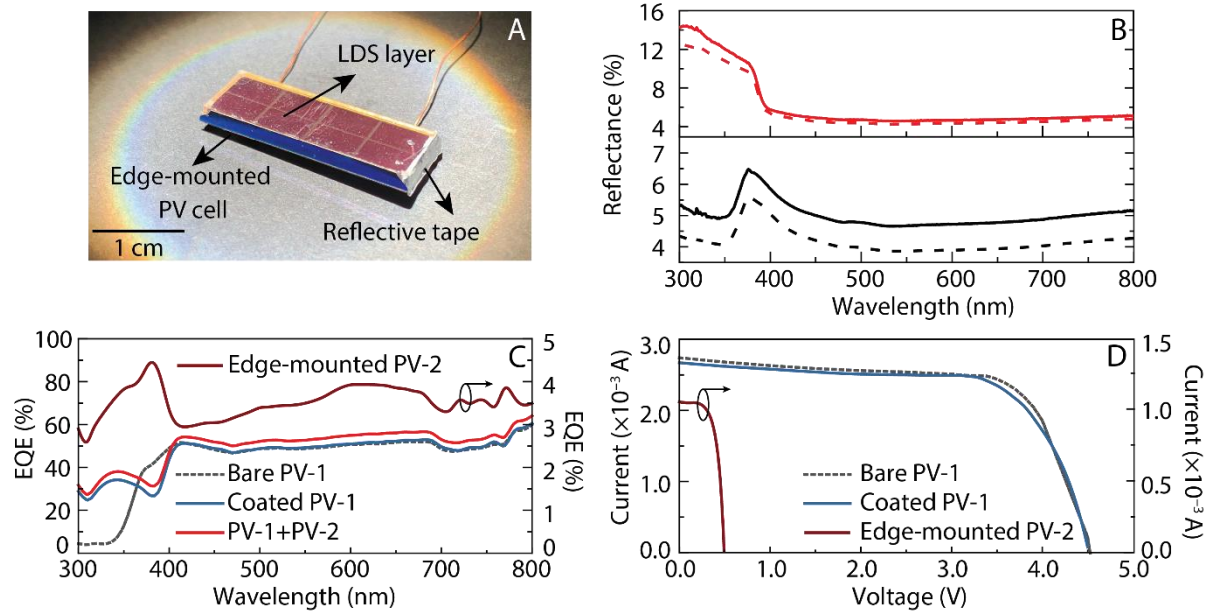


**Figure 3.19.** (A) Photograph of the prototype of the combined LDS layer and LSC device under AM1.5G radiation. (B) Total (solid line) and diffuse (dashed line) reflectance of (top) PMMA-Eu-10/20 and (bottom) average curves for different bare PV cells. (C) EQE curves of the bare PV cell, coated PV-1, edge-mounted PV-2 and the curve showing the contribution of both PV devices. (D) V-I curves of the bare PV cell, coated PV-1 and edge-mounted PV-2.

The influence of depositing one LDS layer onto the top of a PV cell surface will affect the reflectance of the latter and consequently the absorption ability of the PV device. **Figure. 3.19B** shows the total and diffuse reflectance for representative LDS layers and the average reflectance curves obtained for the bare PV cells. It is noticeable that the total reflectance of the bare PV cells is always higher than the diffuse one.

As shown in **Figure. 3.19C**, an increase in the EQE (calculated through **Equation (3.2)**), is noticeable in the UV/blue region between 300 and 360 nm, which is the spectral

range where Si PV cells have lower performance and, also, corresponds to the absorption region of the LDS layer (PMMA-Eu-10).

$$EQE = \frac{I_{sc} h c}{P_{in} e \lambda} \quad (3.2)$$

where,  $I_{sc}$  is the generated short-circuit current,  $h$  is the Planck's constant,  $c$  is the speed of light,  $P_{in}$  is the power of the incident beam and  $e$  is the charge of the electron.

Between 300 and 360 nm, an absolute increase of ~28%, equivalent to a gain of ~6, can be observed (for 340 nm incident radiation). Although a slight decrease in the EQE of the coated PV-1 can be observed compared to the bare PV-1 between 365 and 400 nm, the overall performance of the coated PV-1 is ~5% higher than the case for the bare PV cell. Moreover, by adding the edge-mounted PV-2 to the system, a further improvement in the performance of the PV system may be obtained. In this case, the EQE curve of the edge-mounted PV cell resembles the excitation/absorption spectra of the LDS layer, proving an effective guidance of converted radiation. Taking into account the contribution of both PV-1 and PV-2 cells, an absolute increase in the EQE of 32%, equivalent to a gain of ~7, may be observed (for 340 nm incident radiation). In this case, the overall performance of the system increased ~13% relatively to the bare PV-1, showing the effectiveness of this combined approach of LDS layers and LSCs. The V-I curves of the PV cell with and without the LDS layers were also measured. **Figure 3.19D** demonstrates that adding the LDS layer to the PV-1 device yielded no significant differences in the electrical output. Nevertheless, considering the electrical power delivered by the edge-mounted PV-2 device, the total delivered power may increase ~4%.

The results found for the PMMA-Eu-10 films are very promising and among the highest values reported for absolute EQE increase of PV cells coated with LDS layers in the UV spectral region, being of the same order of magnitude of the highest values reported for  $\text{Ln}^{3+}$ -based LDS layers<sup>110,121</sup> **Table 3.5**. The only exception to this trend is the case of a LDS layer based on the  $\text{Eu}(\text{tta})_3 \cdot (\text{H}_2\text{O})_2$  complex with 4,5-bis(pinene)-2,2'-bipyridine ligand dispersed in poly(vinyl acetate) (PVA), which yielded an absolute EQE increase of ~50%.<sup>100</sup>

**Table 3.5.** Absolute EQE increase in the UV spectral region for Ln<sup>3+</sup>-based LDS layers for c-Si and dye-sensitized solar cells (DSSCs).

Optically active layer	PV device	EQE increase (%)
PMMA-Eu-10 <sup>this work</sup>		32
[Eu(tta) <sub>3</sub> (tppo) <sub>2</sub> ]/EVA <sup>110</sup>		19
Eu(tta) <sub>3</sub> (phen)/EVA <sup>110</sup>		17
[EuL <sub>3</sub> ]/EVA <sup>110</sup>		15
[TbL <sub>3</sub> ]/EVA <sup>110</sup>		15
[Eu(tta) <sub>3</sub> bpbpy]/PVA <sup>100</sup>	c-Si	50
[Eu(tfc) <sub>3</sub> : EABP] 1:1/EVA <sup>115</sup>		5
[Eu(tfc) <sub>3</sub> /Eu(dbm) <sub>3</sub> phen]/PVA <sup>116</sup>		5
Ba <sub>2</sub> SiO <sub>4</sub> :Eu <sup>2+ 117</sup>		3
SiO <sub>2</sub> /Ba <sub>2</sub> SiO <sub>4</sub> :Eu <sup>2+ 118</sup>		3
LaVO <sub>4</sub> /Dy <sup>3+ 123</sup>		2
EuD <sub>4</sub> TEA <sup>121</sup>	DSSC	25

EVA = ethylene-vinyl acetate; PVA = polyvinyl acetate; tppo = triphenylphosphine oxide; phen = 1,10-phenanthroline; L = triazole-pyridine-bistetrazolate; bpbpy = 4,5-bis(pinene)-2,2'-bipyridine; Eu(tfc)<sub>3</sub> = tris[3-(trifluoromethylhydroxymethylene)-d-camphorate]europium(III); EABP = 4,40-bis(diethylamino)benzophenone; dbm = dibenzoylmethane; EuD<sub>4</sub>TEA = europium tetrakis dibenzoylmethide triethylammonium; DSSC = dye-sensitized solar cell.

### Luminescent solar concentrators

The PMMA-Ln-X were also used to fabricate LSCs. From the analysis of the emission and excitation spectra, large ligands-induced Stokes-shift of ~10000 cm<sup>-1</sup> for PMMA-Tb-20 and PMMA-Eu-20 are found, as desirable for LSCs applications. Thus, a layer of each one of the materials was deposited on top of a glass substrate. (**Figure 3.20** and **Table 3.6**).

**Table 3.6.** Thickness of the active layer of the LSCs deposited on glass.

Sample	Thickness (μm)
PMMA-Tb-20	10.70±0.05
PMMA-Eu-20	5.10±0.09

The light emitted at the surface of the PMMA-Tb-20 and PMMA-Eu-20-based LSCs are guided and concentrated towards the substrate edges (**Figures 3.21** and **3.22**).

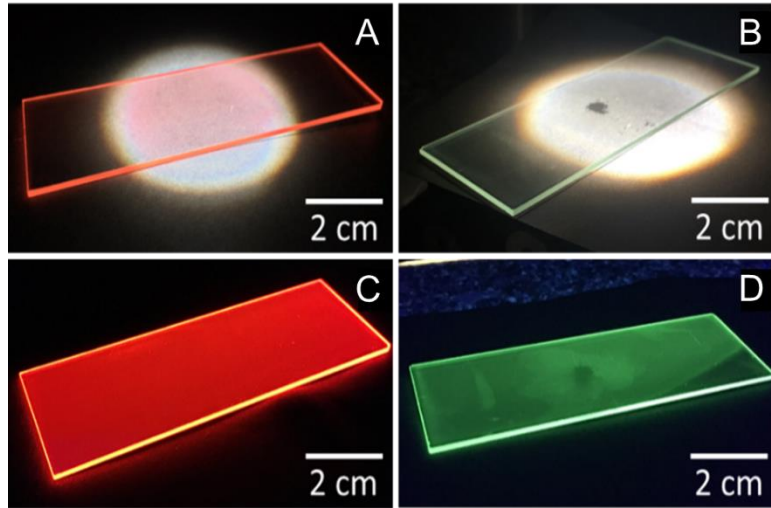


**Figure 3.20.** Photographs of the LSCs based on (A,C) PMMA-Eu-20 and (B,D) PMMA-Tb-20 under AM1.5G (top) and UV radiation at 365 nm (bottom).

As presented in **Figure 3.20**, light emission and guidance to the edges occurs both under AM1.5G and UV radiation, **Figure 3.21**. The performance of the LSCs was quantified by the estimation of  $\eta_{opt}$  through **Equation (3.3)**, yielding values of  $\eta_{opt} \sim 0.27\%$  and  $\sim 0.34\%$  for the LSCs based on PMMA-Tb-20 and PMMA-Eu-20, respectively (**Table 3.7**).

$$\eta_{opt} = \frac{I_{SC}^L V_0^L A_e \eta_{solar}}{I_{SC} V_0 A_s \eta_{PV}} \quad (3.3)$$

where  $I_{SC}^L$  and  $V_0^L$  are the short-circuit current and the open-circuit voltage of the PV device when coupled to the LSC ( $I_{SC}$  and  $V_0$  are the corresponding values of the PV device exposed directly to the solar radiation),  $\eta_{solar}$  is the efficiency of the PV device relatively to the total solar spectrum and  $\eta_{PV}$  is the efficiency of the PV device at the LSC emission spectral range.

**Table 3.7.** Quantification of parameters expressed in **Equation (3.3)** for  $\eta_{opt}$  calculation.

	$I_{SC}^L$ (A)	$V_0^L$ (V)	$I_{SC}$ (A)	$V_0$ (V)	$A_e$ (m <sup>2</sup> )	$A_s$ (m <sup>2</sup> )	$\eta_{solar}$	$\eta_{PV}$
PMMA-Tb-20	$4.1 \times 10^{-6}$	1.69	$4.0 \times 10^{-5}$	3.5	$2 \times 10^{-5}$	$7 \times 10^{-4}$	57.6	30.2
PMMA-Eu-20	$2.4 \times 10^{-5}$	0.72	$1.0 \times 10^{-4}$	1.9				44.2

We note that in some works, the authors used a distinct expression to calculate  $\eta_{opt}$ , considering only the ratio between  $I_{SC}$  and  $I_{SC}^L$ , yielding to overestimated results.<sup>95,236,237</sup> Nevertheless, to enable a comparison with the literature, we calculate  $\eta_{opt}$  using such expression, yielding  $\eta_{opt}$  values of 0.29% and 0.68% for PMMA-Tb-20 and PMMA-Eu-20, respectively. In addition, the effective contribution of the LSCs on the generation of electric current was evaluated by calculating the *PCE* values, through **Equation (3.4)**, yielding values of  $7.8 \times 10^{-4}$  % and  $1.9 \times 10^{-3}$  % for PMMA-Tb-20 and PMMA-Eu-20 LSCs, respectively.

$$PCE = \frac{P_{out}^{el}}{P_{in}} \frac{I_{SC}^L V_0^L}{A_S \int_{\lambda_1}^{\lambda_2} I_{AM1.5G}(\lambda) d\lambda} \times FF \quad (3.4)$$

where  $P_{out}^{el}$  and  $FF = 0.75$  are the PV device output electrical power and fill factor, respectively.

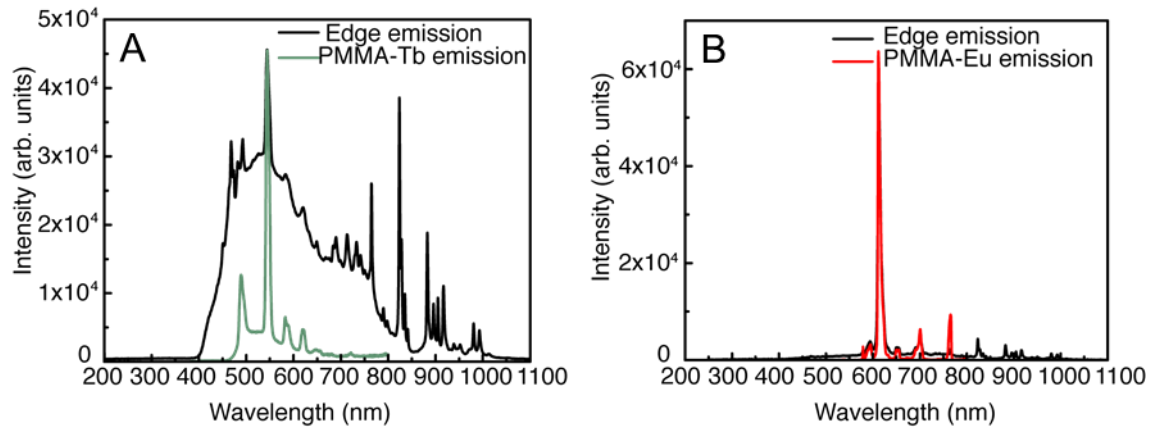


**Figure 3.21.** Emission of the LSCs collected at the edges of the LSCs based on (A) PMMA-Tb-20 and (B) PMMA-Eu-20. The emission spectra at the edges of the LSCs spectra were acquired using a spectrometer OceanOptics Maya 2000 Pro coupled with an optical fiber under AM1.5G radiation.

### 3.4. Conclusions

Herein, new  $\text{Ln}^{3+}$ -doped surface functionalized ISs embedded in PMMA were successfully produced and characterized structurally, thermally and optically. The resultant optically active films absorb the UV component of the solar irradiance on Earth (300-400 nm) and convert it to emission in the visible-NIR spectral regions (crystalline-silicon PV cells maximum absorption). These materials were used as combined LDS layers and LSC into a single device by using edge-mounted PV cells to take advantage of the guided radiation in the LDS layers, increasing the electrical output of the system. The PV cell presented an absolute increase in the EQE of  $\sim 32\%$  between 300-360 nm relatively to the bare PV cell, which unequivocally proves the applicability of this novel approach.

## 4 - DI-UREASILS FOR ELECTROCHROMIC DEVICES

In this chapter, a new design concept for EC smart windows, easy to implement at the industrial level, is introduced. It enables simultaneous control of visible and NIR solar radiation, thus contributing to reduce heating and cooling loads especially in buildings located in areas experiencing wide daily temperature ranges. The EC device comprises a-IZO, a visible/NIR-transparent TCO layer, and a sol-gel protonic ionic liquid (PIL)-doped di-ureasil electrolyte displaying high transparency and high proton conductivity. The device offers three voltage-operated modes: bright hot (+3.0 V: transmittances of 70/83% at 555/1000 nm), semi-bright warm (-2.0 V: transmittances of 37/35% at 555/1000 nm), and dark cold (-2.5 V: transmittances of 6/4% at 555/1000 nm). Its main figures of merit are: high switching efficiency (transmittance variations of 64/79% at 555/1000 nm), high optical density modulation (1.1/1.3 at 555/1000 nm), high optical contrast ratio in the visible region (lightness variation of  $\approx 43$ ), good cycling stability, exceptionally high coloration efficiency ( $-12538/-14818 \text{ cm}^2 \text{ C}^{-1}$  and  $+2901/+3428 \text{ cm}^2 \text{ C}^{-1}$  at 555/1000 nm), good optical memory (transmittance variation loss of only 24% more than 4 months after coloration), and unique self-healing ability following mechanical stress.

#### 4.1. Introduction

In conventional ECDs, when a voltage is applied, solar radiation in the visible and NIR spectral regions are blocked in the dark mode.<sup>238</sup> The fine control of the NIR region of the solar spectrum is, however, of the utmost interest for energy-saving applications, since more than 50% of the solar energy lies in the NIR region. The NIR blocking function in the bleached state is a basic requisite for energy-efficient buildings located in hot-climate regions. In contrast, in the case of buildings situated in cold-climate countries, a NIR admitting function is sought in the transparent mode. The efficient integration of visible and NIR blocking/admission functions in a single smart window is of high relevance for energy saving purposes. To date, very few works have explored this topic. Relying on plasmonics, Milliron *et al.*<sup>239</sup> used ITO nanocrystals (which can either block or allow NIR light to pass through), and a niobium oxide (NbOx) glass (able to transition between a transparent state and another one that blocks visible light) to fabricate dual-

band smart windows with selective and independent control of visible and NIR radiations by varying the applied voltage over a range of 2.5 V. Further developments led to three-mode smart windows displaying a bright mode (visible and NIR admitted), cool mode (visible admitted and NIR blocked), and dark mode (visible and NIR blocked).<sup>238</sup> Xu *et al.*<sup>240</sup> combined WO<sub>3</sub> with plasmonic gold (Au) nanostructures to propose a sterile smart window able to adjust optical transmission and photothermal conversion of visible and NIR lights. Recently, in an attempt to overcome several issues associated with the use of monovalent cations as insertion ions in ECDs, Zhang *et al.*<sup>241</sup> proposed an Al<sup>3+</sup> intercalation/deintercalation-enabled dual-band EC smart window exhibiting efficient and independent control of visible and NIR light transmittance, and impressive overall performance. Another very interesting approach was introduced more recently by Barawi *et al.*<sup>39</sup> based on the attractive spectro-electrochemical features of vanadium-modified titanium oxide (VTO) colloidal nanocrystals. These authors combined an active electrode layer of VTO, which selectively operates in the visible region, with a nanocrystalline WO<sub>3</sub> layer, which selectively operates in the NIR, and in the NIR plus visible regions, to produce an ECD switchable across four distinct optical modes (fully transparent, visible blocked, NIR blocked, and visible plus NIR blocked) upon application of low voltages.

In this chapter the use of a conducting oxide electrode transparent in the visible and NIR regions is proposed for the first time for the fabrication of a dynamic solar control window with simultaneous adjustment of visible and NIR radiation. The as-prepared ECD is endowed with a voltage-actuated three-mode operation: a bright hot mode (visible and NIR admitted) (**Figure 4.1A**), a semi-bright warm mode (visible and NIR semi-blocked) (**Figure 4.1B**), and a dark cold mode (visible and NIR blocked) (**Figure 4.1C**). This device is particularly well suited for the windows of buildings located in areas combining high elevation, dry air, and frequency of strong cold fronts, which experience wide daily temperature ranges (e.g., Texas and Oklahoma Panhandles, USA<sup>242</sup>). The rational underlying strategy for the new TCO/a-WO<sub>3</sub>/IC/c-NiO/TCO ECD has been to include: (1) a-IZO, with visible and NIR transmittance higher than ITO due to the lower carrier concentration and higher charge mobility,<sup>58,243–245</sup> as TCO; (2) a quasi-anhydrous ormolyte (organically modified silicate electrolyte) film, with high proton conductivity and high transparency, as IC. The chosen ormolyte is composed a homemade N-butylimidazolium trifluoromethanesulfonate ([BIm][TfO]) PIL (**Figure 4.2A**) and a sol–gel derived di-urea cross-linked poly(oxyethylene) (POE)/siloxane hybrid host matrix (di-ureasil)<sup>169</sup> (**Figure 4.2B**). For the sake of simplicity, this ormolyte

system will be henceforth designated as DUPIL<sub>x</sub>, where x represents the ratio, in %, of the mass of [BIm][TfO] per mass of POE. The DUPIL<sub>60</sub> material was chosen, since it presents the highest ionic conductivity ( $6.3 \times 10^{-5}$ ,  $1.9 \times 10^{-3}$ , and  $3.7 \times 10^{-3}$  S cm<sup>-1</sup> at 21, 99, and 140 °C, respectively).

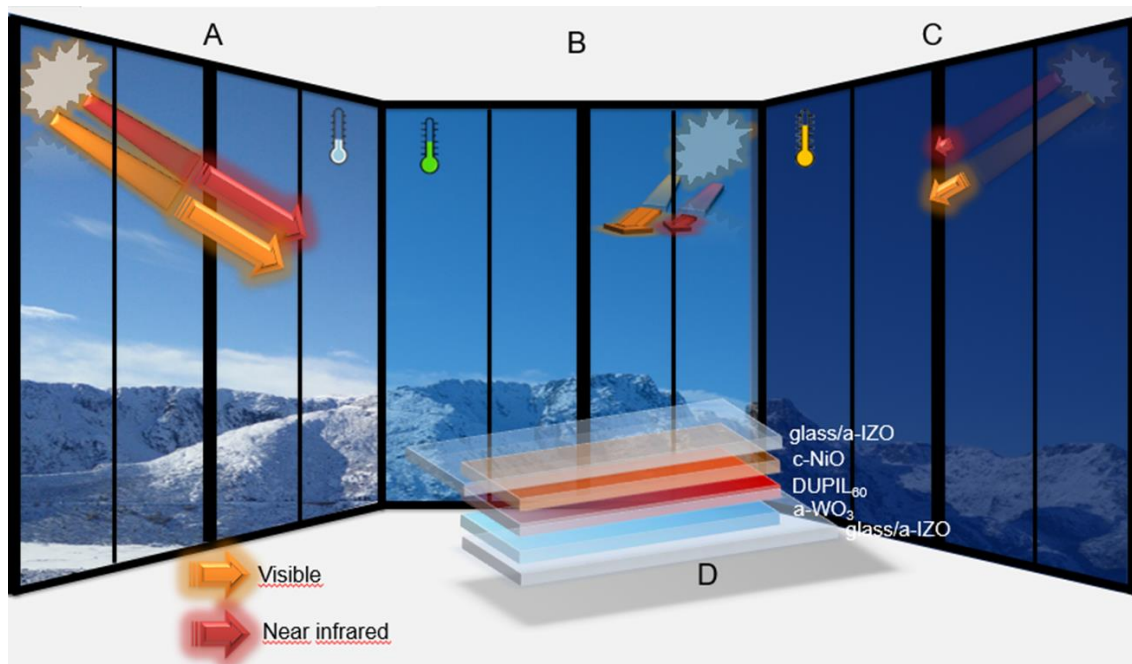


**Figure 4.1.** Schematic representation of the three-mode modulation of a smart window based on the voltage-actuated a-IZO/a-WO<sub>3</sub>/DUPIL<sub>60</sub>/c-NiO/a-IZO ECD: (A) bright hot mode (0.0 V), (B) semi-bright warm mode (-2.0 V), (C) dark cold mode (-2.5 V), (D) configuration of the ECD.

## 4.2.Synthesis

**Materials.** The chemicals used in this work were trifluoromethanesulfonic acid (HTfO, Fluka, p.a.), N-butylimidazole (BIm, 98%, Aldrich), dichloromethane (CH<sub>2</sub>Cl<sub>2</sub>, Fluka, p.a.), O,O'-Bis(2-aminopropyl) polypropylene glycol-blockpolyethylene glycol-block-polypropylene glycol 1.900 (Jeffamine ED-2001®, average molecular weight 2001 g mol<sup>-1</sup>, Fluka), 3-isocyanatepropyltriethoxysilane (ICPTES, 95%, Aldrich), tetrahydrofuran (THF, Merck), ethanol (EtOH, Panreac, p.a.) were used as received. Ultrapure water was used in all experiments.

**Synthesis of [BIm][TfO] (Figure 4.2A).** The synthesis was performed according to the procedure reported by Cardoso *et al.*<sup>69</sup> BIm was dissolved in CH<sub>2</sub>Cl<sub>2</sub> and cooled in an ice bath, and then reacted with HTfO, which was added dropwise in a molar ratio 1.6

BIm: 1 HTfO. The reaction mixture was allowed to warm to room temperature slowly. After being stirred continuously for two days, CH<sub>2</sub>Cl<sub>2</sub> was evaporated. The resultant viscous yellow oil was washed with diethyl ether and ethyl acetate 6 times, and then dried in dynamic vacuum at room temperature for 72 h.

**Synthesis of the [BIm][TfO]-doped ormolytes.** The synthesis of the [BIm][TfO]-doped ormolytes<sup>69,169</sup> detailed in **Table 4.1**, involved reacting a POE-based Jeffamine ED-2001® diamine with ICPTES to yield the di-urea (-NH(C=O)NH-) bridged hybrid molecule. This precursor was subsequently hydrolysed. The condensation reactions that followed induced the growth of the siloxane network. In the first stage of the synthesis of the di-ureasil precursor a mass of the diamine (**Table 4.1**) was dissolved in 10 mL of THF by stirring. A volume of ICPTES (**Table 4.1**) was added to this solution in a fume cupboard. The flask was then sealed and the solution stirred for about 12 h at a moderate reaction temperature (40 °C). The grafting process was infrared-monitored: as the reaction progressed, the intensity of the very strong and sharp absorption band located at about 2274 cm<sup>-1</sup>, attributed to the vibration of the -Si(CH<sub>2</sub>)<sub>3</sub>NCO group, progressively decreased, while that of bands produced by urea groups increased. A urea bridged organic/inorganic hybrid sol, designated as diureapropyltriethoxysilane (d-UPTES(2000)), **Figure 4.2B**, was obtained. In the second stage of the synthesis, a mixture of ethanol and high purity distilled water (molar proportion of 1 ICPTES:4 EtOH:1.5 H<sub>2</sub>O), and an appropriate mass of [BIm][TfO] were then added to the d-UPTES(2000) solution. The mixture was stirred in a sealed flask for approximately 30 min.

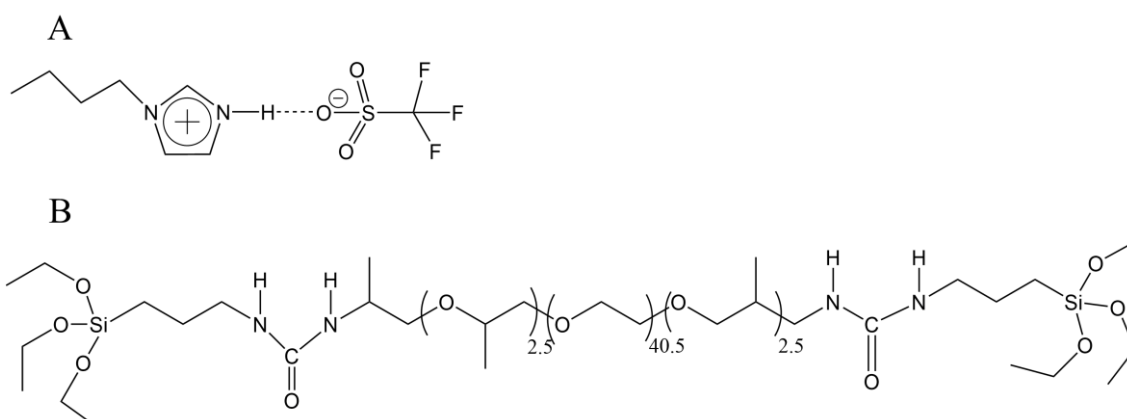


**Figure 4.2.** Molecular structures of the (A) [BIm][TfO] PIL and (B) of the non-hydrolyzed d-UPTES(2000) precursor (a+c = 2.5 and b = 40.5).

**Table 4.1.** Synthesis procedure of the DUPIL<sub>x</sub> ormolytes.

x	m <sub>Jeff ED-2001</sub> (g)	m <sub>POE</sub> (g)	V <sub>ICPTES</sub> (mL)	V <sub>EtOH</sub> (mL)	V <sub>H2O*</sub> (μL)	m <sub>PIL</sub> (g)	n <sub>PIL</sub> (mol)	n <sub>H2O**</sub> (mol)	x'***	Si/PIL (molar)
40	1.027	0.916	0.254	0.239	28	0.366	1.28×10 <sup>-3</sup>	8.13×10 <sup>-4</sup>	38	0.80
50	1.026	0.915	0.254	0.239	28	0.458	1.60×10 <sup>-3</sup>	1.02×10 <sup>-3</sup>	48	0.64
60	1.008	0.899	0.249	0.235	27	0.539	1.89×10 <sup>-3</sup>	1.20×10 <sup>-3</sup>	58	0.53

x = m<sub>PIL</sub>/m<sub>POE</sub> (w/w %);

\* Added water

\*\* Adsorbed water by the PIL

\*\*\* x' = m<sub>PIL</sub>/m<sub>POE</sub> (w/w %) with m<sub>PIL</sub> corrected after subtracting the mass of adsorbed water.

A small volume of the resulting solution was used for the assembly of the ECD and the remaining volume was cast into a Teflon mold, which was covered with Parafilm, left in a fume cupboard for 24 h, and finally transferred to an oven at 40 °C where it remained for 4 weeks. The as-produced ormolyte was obtained as a transparent and flexible monolith with a transmittance of about 60% (**Figure 4.3**).

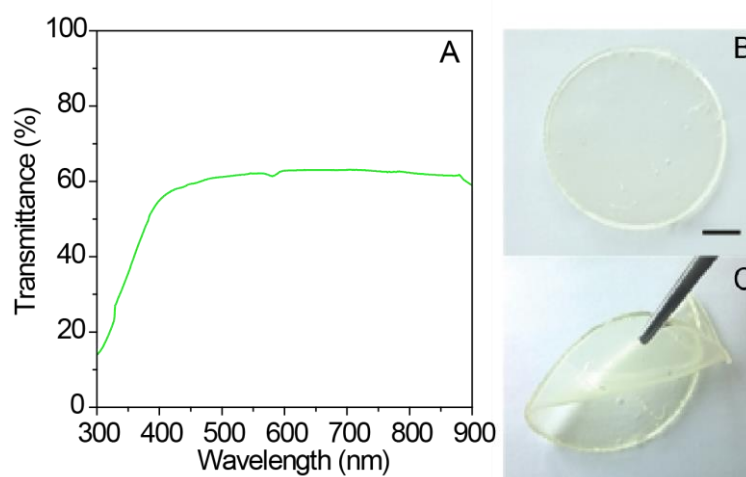


**Figure 4.3.** (A) Ultraviolet (UV)-vis spectrum of the DUPIL<sub>60</sub> ormolyte after being washed with water. (B, C). Photographs of the monolith highlighting its transparency and flexibility (scale bar corresponds to 1 cm).

### ECD assembly

The active and non-active layers of the ECD where prepared and characterized, as described as follows. The active EC layers of the device (a-WO<sub>3</sub> and c-NiO) were deposited by sputtering and e-beam evaporation, respectively, on glass. The a-IZO thin films (resistivity of  $7.97 \times 10^{-4}$  W cm, mobility of  $52.1 \text{ cm}^2 \text{ V}^{-1} \text{ s}^{-1}$  and carrier concentration of  $1.50 \times 10^{20} \text{ cm}^{-3}$ ) were deposited by sputtering, in a homemade system,

from In<sub>2</sub>O<sub>3</sub>/ZnO 89.3/10.7 wt%, 99.99%, 3" diameter x 6 mm thick (Super Conductive Materials). The sputtering was carried out at room temperature keeping the deposition pressure (argon and oxygen) constant to a value of 0.13 Pa. The distance between the substrate and the target was 10 cm, and the radio frequency (r.f.) power was 100 W. a-WO<sub>3</sub> was produced in a Pfeiffer Vacuum Classic 500 system using 3" diameter ceramic target from Plasmaterials, at an argon and oxygen atmosphere (oxygen partial pressure of 0.2 Pa) and a deposition pressure of 1.0 Pa, under a r.f. power of 200 W, achieving a thickness of 300 nm. A polycrystalline NiO (i.e., c-NiO) thin film was deposited by e-beam evaporation in a homemade system, from NiO commercial pellets random pieces 3-6 mm (99.99%, Super Conductive Materials), with an initial chamber pressure of  $7 \times 10^{-4}$  Pa and growth rate of 6 nm min<sup>-1</sup>, reaching a thickness of 300 nm. AFM images of the a-IZO, a-WO<sub>3</sub>, and c-NiO layers were recorded in an AFM CSI Nano-Observer equipment (Scientec) in tapping mode using a super sharp Si HQ:NSC19/FORTA probe with a frequency resonance of 60 kHz and a spring constant of 0.3 N m<sup>-1</sup>. Flattening and elimination of line noise tools and a Lowpass filter provided by the Gwyddion 2.38 software were used to improve the quality of the images.

For the ECD, a prototype square-shaped with  $2.2 \times 2.2$  cm<sup>2</sup> active area was assembled under atmospheric conditions using the optimized formulation (DUPIL<sub>60</sub>) (**Figure 4.1D**). A small volume of the ormolyte sol was cast onto the surface of a-WO<sub>3</sub>/a-IZO sputtered coated glass plate. After solvent evaporation, a c-NiO/a-IZO-sputtered coated glass plate was placed on the top of it so that the two coatings faced each other. Free space was left on one side of the glass plates to ensure the electrical contacts. The assembled system was then pressed together and left in rest prior to the electro-optical analyses.

### 4.3. Results and discussion

#### Ormolytes structural characterization

In an attempt to choose the proper IC from the DUPIL<sub>x</sub> family of ormolytes, the samples were characterized by XRD, DSC, SEM/EDS and complex impedance spectroscopy. The XRD patterns of the DUPIL<sub>x</sub> ormolytes with x = 40, 50 and 60 (**Figure 4.4A**) exhibited a prominent broad Gaussian-shaped band at  $q'$  (where  $q' = 4\pi\sin\theta/\lambda$ , where  $2\theta$  is the scattering angle and  $\lambda$  is the wavelength) values of ca. 14.2, 14.9 and 14.7

$\text{nm}^{-1}$  respectively, attributed to ordering within the siliceous domains.<sup>212</sup> The corresponding characteristic distances  $d$  (where  $d = 2\pi/q$ ) are 0.44, 0.42 and 0.43 nm, respectively. In addition, DUPIL<sub>40</sub> produced another band at  $5.8 \text{ nm}^{-1}$  (1.08 nm) and DUPIL<sub>60</sub> yielded two shoulders at about 4.7 and  $8.8 \text{ nm}^{-1}$  (1.34 and 0.71 nm, respectively),<sup>246</sup> which are tentatively ascribed to intra-siloxane domains.<sup>213</sup>

In the DSC curves, the endothermic peaks detected at 21 and 35 °C for  $x = 40$  and at 41 °C for  $x = 50$  (**Figure 4.4B**) are associated with the fusion of the POE chains.<sup>172</sup> The absence of the characteristic peaks of crystalline POE chains of d-U(2000) in the XRD patterns of these two samples (**Figure 4.4A**) suggests that both peaks are probably masked by the broad band. The origin of the thermal event centred at 155 °C (**Figure 4.4B**) for  $x = 60$  is unknown. The very broad endotherm around 100 °C detected in the case of the samples with  $x = 40$  and 50 (**Figure 4.4B**) is probably due to the release of entrapped solvents (THF, water or ethanol).

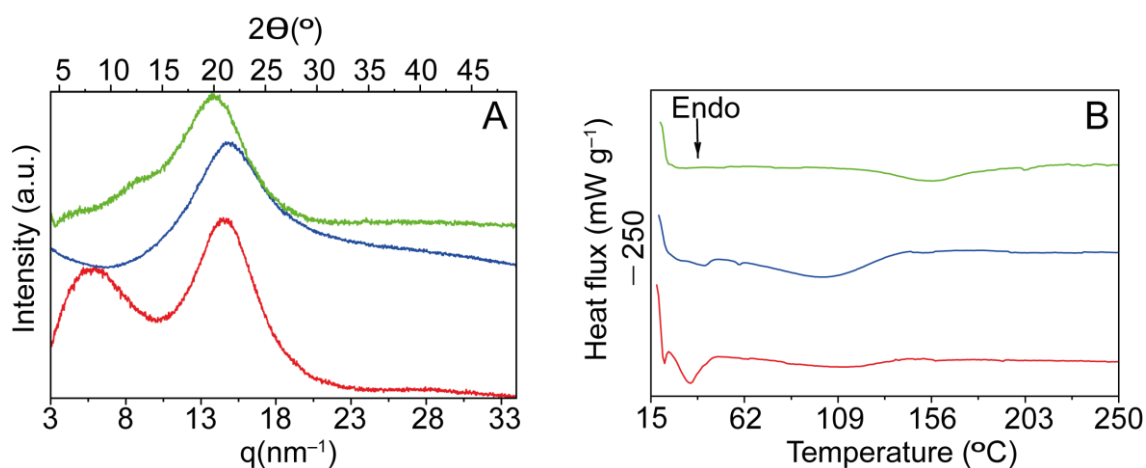


**Figure 4.4.** (A) XRD patterns and (B) DSC curves of the DUPIL<sub>x</sub> ormolytes with  $x = 40$  (red line), 50 (blue line) and 60 (green line).

The crucial role of SEM analysis in the identification of released PIL at the surface of the DUPIL<sub>x</sub> ormolyte films was emphasized earlier.<sup>69</sup> The SEM image of the PIL-rich sample with  $x = 60$  revealed the formation of circular micro-objects with a diameter around 1400  $\mu\text{m}$  which closely resemble the spherulites typically observed in semi-crystalline POE-containing PEs (**Figure 4.5A(a)**). The EDS data demonstrate that these micro-objects are mainly composed of carbon and oxygen atoms and a small amount of nitrogen atoms, while lacking silicon atoms (**Figure 4.5A(b), 4.5A(c), 4.5A(e), 4.5A(f)** and **4.6**). Moreover, these EDS mapping images confirm a homogeneous distribution of the fluorine and sulfur atoms of the anions (**Figures 4.5A(d)** and **4.5A(g)**, respectively,

and **Figure 4.6**). These results support that at the surface of this material a fraction of the PIL interacted with the POE chains and the urea cross-links. The anisotropic nature of the micro-objects is beautifully evidenced by POM under crossed polarizers (**Figure 4.5A(h)**). To remove the PIL from the surface of the three ormolytes, these were immersed in ultrapure water for 20 s, dried with a soft tissue, and kept in an oven at 80 °C for 48 h. The SEM images of **Figures 4.5B(a)-(g)** and the POM image of **Figure 4.5A(h)**, recorded under crossed polarizers, confirm the complete elimination of the POE/PIL/urea cross-links micro-objects from the surface of the DUPIL<sub>60</sub> ormolyte.

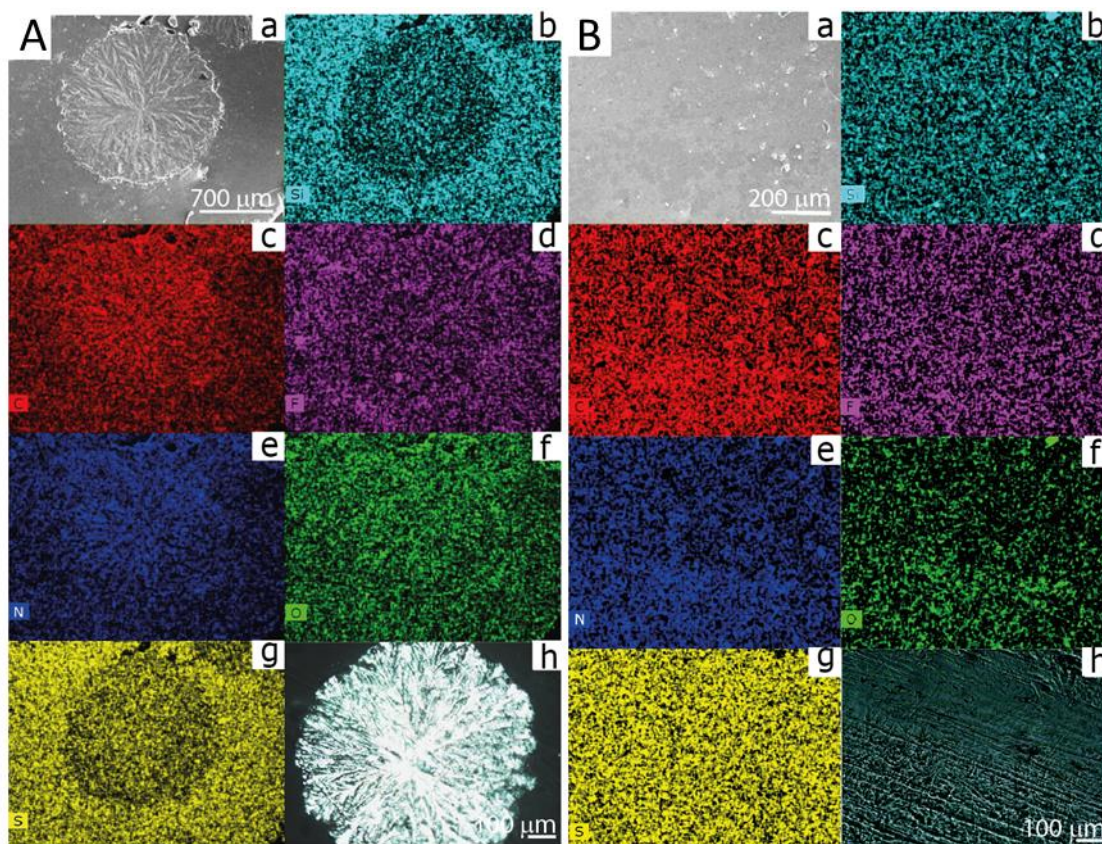


**Figure 4.5.** (a) SEM, EDS mapping ((b) silicon, (c) carbon, (d) fluorine, (e) nitrogen, (f) oxygen, and (g) sulphur) and (h) POM images of the DUPIL<sub>60</sub> ormolyte (A) as-prepared and (B) washed with water.

Element	Wt(%)	Element	Wt(%)
Si	0.45 ± 0.10	Si	2.25 ± 0.25
C	50.64 ± 12.37	C	45.41 ± 11.46
N	5.56 ± 2.63	N	7.27 ± 3.06
O	36.61 ± 9.36	O	29.99 ± 7.99
F	4.28 ± 1.66	F	9.25 ± 2.89
S	2.46 ± 0.24	S	5.84 ± 0.48

**Figure 4.6.** EDS data for the as-prepared DUPIL<sub>60</sub> ormolyte.

**Figure 4.7** demonstrates that the ionic conductivity of the ormolytes with  $x = 40$ , 50 and 60 is higher than that reported for samples with  $x = 10$  and 30<sup>69</sup> in the whole range of temperatures (**Table 4.2**). The trend observed confirms that the progressive increase of PIL concentration led to an improvement of the ionic transport. This finding indicates that the PIL affects the dipolar and ionic component of the polymer due to the ionic character of the PIL itself, and the presence of ion-dipole interactions. All the samples revealed a non-linear variation of the ionic conductivity with temperature which is a typical behaviour for disordered electrolytes, well described by the Vogel-Tammann-Fulcher (VTF) equation.

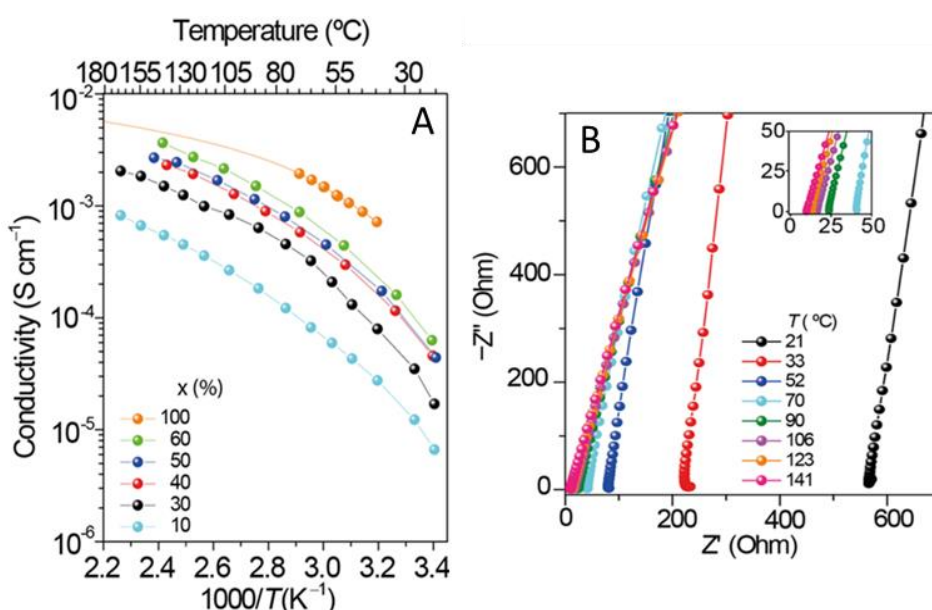


**Figure 4.7.** (A) Ionic conductivity of the DUPIIL<sub>x</sub> ormolytes. The lines drawn are just guides for the eyes. (B) Nyquist plot for the DUPIIL<sub>60</sub> ormolyte at different temperatures. The lines drawn are just guides for the eyes.

The ionic conductivities of the DUPIIL<sub>x</sub> ormolytes with  $x = 50$  and 60 are not significantly different over the whole range of temperatures examined (the most concentrated sample is only slightly more conducting) leading us to speculate that  $x = 60$  is presumably the threshold PIL concentration that yields the highest ionic conductivity values ( $6.3 \times 10^{-5}$ ,  $2.2 \times 10^{-3}$  and  $3.7 \times 10^{-3}$  S cm<sup>-1</sup> at 21, 106 and 140 °C, respectively). (**Figure 4.7** and **Table 4.2**). The amorphous DUPIIL<sub>60</sub> material was therefore the sample chosen for the ECD assembly.

The reason for the enhanced ionic conductivity of the electrolytes doped with [BIm][TfO] with respect to those doped with [EIm][TfO]<sup>71</sup> is presumably associated with the fact that, while larger cations lead to lower cation mobility, longer alkyl side chains grafted onto the imidazolium ions increase the short-range repulsive interactions among the ions and destroy charge organization. This would lead to a weak interaction among the POE chains promoting the separation of ion transport from polymer chain motion, which is a temperature-dependent process, and an increase of charge carriers (mobile protons).<sup>247–249</sup>

**Table 4.2.** Ionic conductivity of the DUPIL<sub>x</sub> ormolytes.

PIL	x (%)	Ionic conductivity (S cm <sup>-1</sup> )			Ref.
		Temperature (°C)			
		21	99	140	
[EIm][TfO]	0 <sup>a</sup>	3.0×10 <sup>-9</sup>	4.4×10 <sup>-8</sup>	-	71
	5	2.7×10 <sup>-6</sup>	5.2×10 <sup>-5</sup>	-	
	10	7.5×10 <sup>-7</sup>	7.0×10 <sup>-6</sup>	-	
	30	7.4×10 <sup>-6</sup>	1.1×10 <sup>-4</sup>	-	
	40	1.4×10 <sup>-5</sup>	5.2×10 <sup>-4</sup>	-	
	50	7.8×10 <sup>-5</sup>	1.4×10 <sup>-3</sup>	2.8×10 <sup>-3</sup>	
	60	4.6×10 <sup>-5</sup>	1.4×10 <sup>-3</sup>	-	
100 <sup>b</sup>	5.0×10 <sup>-3</sup>	3.0×10 <sup>-2</sup>	5.0×10 <sup>-2</sup>	250	
[BIm][TfO]	5	4.0×10 <sup>-6</sup>	6.3×10 <sup>-5</sup>	1.2×10 <sup>-4</sup>	69
	10 <sup>c</sup>	6.6×10 <sup>-6</sup>	2.6×10 <sup>-4</sup>	5.5×10 <sup>-4</sup>	
	30 <sup>c</sup>	1.7×10 <sup>-5</sup>	7.0×10 <sup>-4</sup>	1.5×10 <sup>-3</sup>	
	40 <sup>c</sup>	4.6×10 <sup>-5</sup>	1.3×10 <sup>-3</sup>	2.4×10 <sup>-3</sup>	This work
	50 <sup>c</sup>	5.1×10 <sup>-5</sup>	1.4×10 <sup>-3</sup>	2.6×10 <sup>-3</sup>	
	60 <sup>c</sup>	6.3×10 <sup>-5</sup>	1.9×10 <sup>-3</sup>	3.7×10 <sup>-3</sup>	
100 <sup>b</sup>	-	3.1×10 <sup>-3 d</sup>	4.6×10 <sup>-3 d</sup>	69	

<sup>a</sup>Non-doped d-U(2000) hybrid host; <sup>b</sup>Pure PIL; <sup>c</sup>Washed samples; <sup>d</sup>Values tentatively obtained through extrapolation assuming a B-Spline function.

## ECD optical properties

At this stage, several technical parameters were employed to characterize the performance of the a-IZO/a-WO<sub>3</sub>/DUPIL<sub>60</sub>/c-NiO/a-IZO ECD: the switching speed (time  $\tau$  required for the colouring/bleaching process), the switching efficiency (optical contrast measured by the transmittance change  $\Delta T = T_{\text{bleached}} - T_{\text{coloured}}$ , in %, at a given wavelength), the optical density (optical modulation measured by  $\Delta OD = -\log(T_{\text{coloured}}/T_{\text{bleached}})$ ), the coloration efficiency (CE =  $\Delta OD/\Delta Q$ , where Q is the inserted/desinserted charge density) and the 1976 Commission Internationale d'Éclairage (CIE) L\*a\*b\* colour coordinates (L\* is the lightness (0 = black, 100 = diffuse white), a\* is a red–green balance (+a\* = red and r

The typical response time of the ECD was fast ( $\tau \approx 50$  s). The as-prepared ECD exhibited a light yellowish hue (L\* = 79.4, a\* = -1.50 and b\* = 11.3) (**Figure 4.8** (brown triangle)) and T values of 67% and 80% at 555 and 1000 nm, respectively (**Table 4.3**).

**Table 4.3.** Electro-optical parameters of the a-IZO/WO<sub>3</sub>/DUPIL<sub>60</sub>/NiO/a-IZO ECD. T values are given in %.

$\lambda$ (nm)	$T_{\text{as-prepared}}$		$T_{\text{coloured}}$			$T_{\text{coloured}}$				$CE_{\text{in}}$ $CE_{\text{out}}$	
	0.0 V	+3.0 V	-2.0 V	$\Delta T$	$\Delta OD$	-2.5 V	$\Delta T$	$\Delta(OD)$	(cm <sup>2</sup> C <sup>-1</sup> )		
555	67	70	37 <sup>a)</sup>	33 <sup>a)</sup>	0.28 <sup>a)</sup>	11 <sup>a)</sup>	6 <sup>b)</sup>	64 <sup>b)</sup>	1.1 <sup>b)</sup>	-12538	+2901
1000	80	83	35 <sup>a)</sup>	48 <sup>a)</sup>	0.38 <sup>a)</sup>	9 <sup>a)</sup>	4 <sup>b)</sup>	79 <sup>b)</sup>	1.3 <sup>b)</sup>	-14818	+3428

<sup>a)</sup>after CV cycling; <sup>b)</sup>after CV plus CA cycling.

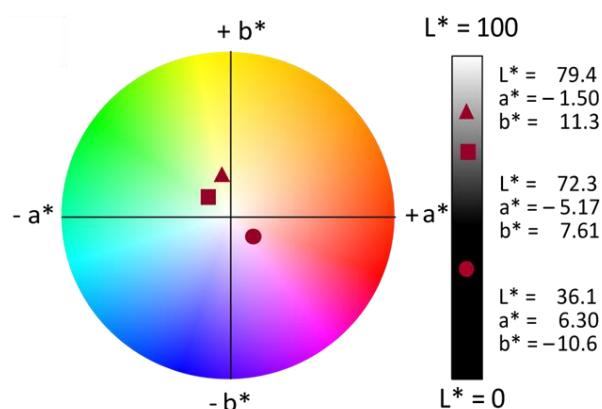


**Figure 4.8.** CIE 1976 L\*a\*b\* colour diagram of the ECD: as-deposited state (brown triangle), coloured state at -2.5 V after CA cycling (brown circle), and end of optical memory test (brown square).

The device was subsequently bleached by applying +3.0 V during 250 s and the T values increased to 70% and 83%, respectively (**Figure 4.1A**, **Figure 4.9** (left, purple line) and **Table 4.3**). At this point, the ECD was transparent (photograph in **Figure 4.9**). The ECD was then submitted to six CV cycles. The scanning was performed at  $50 \text{ mV s}^{-1}$  from the initial voltage of 0.0 to +3.0 V (bleaching), then to  $-2.5 \text{ V}$  (colouring), and finally it was reversed again to 0.0 V. In the 6<sup>th</sup> CV curve, a broad, non-resolved anodic peak, centred at  $\approx 0.5 \text{ V}$ , was evident (**Figure 4.10**).

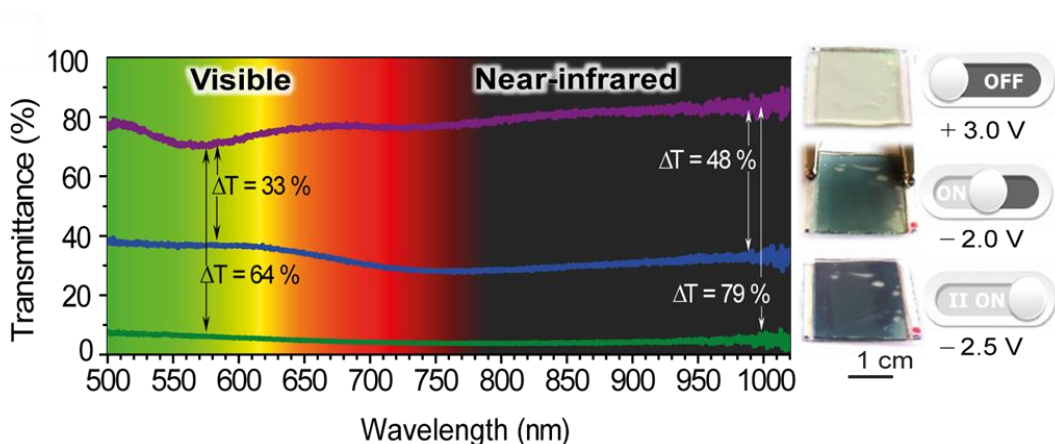


**Figure 4.9.** Left: Transmission spectra of the a-IZO/a-WO<sub>3</sub>/DUPIL<sub>60</sub>/c-NiO/a-IZO ECD in the bleached state (purple line) and in the coloured states upon application of  $-2.0 \text{ V}$  (blue line) and  $-2.5 \text{ V}$  (green line). Right: Photographs of the ECD at variable voltages.

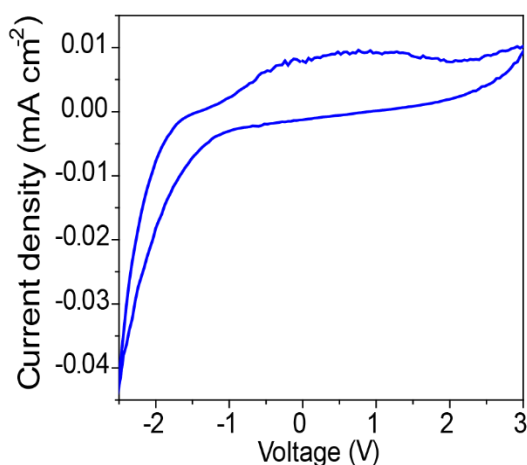


**Figure 4.10.** Cyclic voltamogram of the a-IZO/a-WO<sub>3</sub>/DUPIL<sub>60</sub>/c-NiO/a-IZO ECD (6<sup>th</sup> cycle, scan rate  $50 \text{ mV s}^{-1}$ )

After CV cycling, a voltage of  $-2.0 \text{ V}$  was applied for 250 s (**Figure 4.1B**). This led to a reduction of the T values to 37% and 35% at 555 and 1000 nm, respectively (**Figure 4.9** (left, blue line), and **Table 4.3**). At this stage, the ECD displayed a light blue

colour (photograph in **Figure 4.9** (right)). Upon application of  $-2.5$  V for 250 s (**Figure 4.1C**), the transmittance was further reduced to 11% and 9% at 555 and 1000 nm, respectively (**Figure 4.9** (left, green line) and **Table 4.3**), and the colour of the ECD became dark blue (photograph in **Figure 4.9** (right)).

We note that the application of a voltage window lower than that indicated (i.e.,  $<2.0$  V) did not produce any colour change. After recording the visible-NIR spectrum and reconnecting the electrodes for the CA tests, the two plates of the ECD were split apart (mechanical stress). Anyhow the ECD was successfully reassembled and the CA analysis was performed subsequently by applying  $\pm 2.5$  V steps for 30 cycles (100 s per colouring/bleaching cycle) (Inset of **Figure 4.11**). After concluding that the ECD had self-healed, 500 additional cycles were performed. **Figure 4.11** reveals that, although the charge density remained very low during the first 200 cycles, it was enhanced significantly in the following cycles. It is also clear that, unlike in other ITO-based similar ECDs,<sup>251</sup> the cathodic charge densities are markedly lower than the anodic ones, indicating that the charge needed to induce the switch to the coloured mode was unusually low.

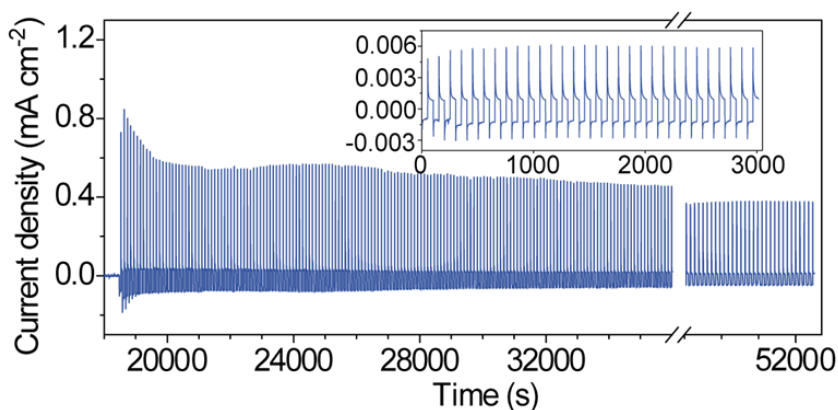


**Figure 4.11.** Variation of the current density with voltage steps of  $\pm 2.5$  V at every 50 s after 500 cycles. Inset: preliminary 30 cycles under the same conditions right after mechanical stress.

At the end of the CA measurements, a voltage of  $-2.5$  V was applied to the ECD and the visible-NIR spectrum was recorded. **Figure 4.9** (left, green line) and **Table 4.3** demonstrate that CA cycling improved the switching efficiency, pushing the T values down to 6% and 4% at 555 and 1000 nm, respectively. At this stage, the ECD exhibited

a dark blue colour ( $L^* = 36.1$ ,  $a^* = 6.30$ , and  $b^* = -10.6$  (**Figure 4.8** (brown circle) and photograph of **Figure 4.9** (right)). With respect to the as-prepared state, this coloured state corresponded to an optical contrast ratio  $\Delta L^*$  of  $\approx 43$  ( $79.4 \rightarrow 36.1$ ). This value is higher than that reported for ECDs incorporating EC polymers that have the full colour palette neutral state and also attain highly transmissive states upon switching<sup>252</sup> ( $\Delta L^*$  of 33 ( $85 \rightarrow 52$ )), but lower than those found for the first neutral-state black polymeric electrochrome ( $\Delta L^*$  of 53 ( $72 \rightarrow 19$ ))<sup>253</sup> and for a genuine highly transparent to truly black ECD based on an ambipolar system of polyamides and viologen<sup>254</sup> ( $\Delta L^*$  of 81 ( $87.5 \rightarrow 6.5$ )).

**Figure 4.12** shows the CE values as a function of  $Q$  for selected bleaching and colouring cycles. Colossal CE values are observed both at 555 and 1000 nm, especially during charging ( $-12\ 538$  and  $-14\ 818\ \text{cm}^2\ \text{C}^{-1}$ , respectively, assuming  $\Delta\text{OD}$  values of 1.1 and 1.3, respectively (**Table 4.3**)). These results point out that a very large optical modulation occurred at a very small charge insertion. Similar observations can be made with respect to the CE values deduced for bleaching (**Table 4.3**).

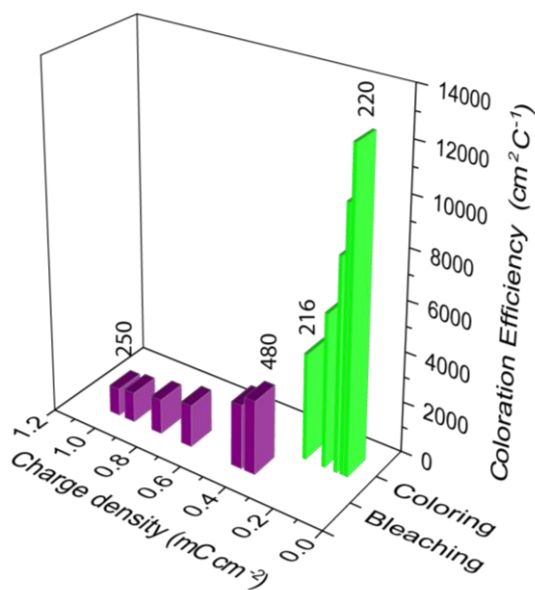


**Figure 4.12.** Coloration efficiency of the bleaching and coloration states at 555 nm as a function of charge density at different cycles.

The open-circuit memory of the ECDs was monitored during a period of 134 days after polarization at  $-2.5$  V. **Figure 4.13** proves that the performance of the device is exceptionally good, since a loss of the T value of only 24% occurred after this long period of time. In parallel, a shift to  $L^* = 72.3$ ,  $a^* = -5.17$ , and  $b^* = 7.61$  resulted (**Figure 4.8** (brown square)).

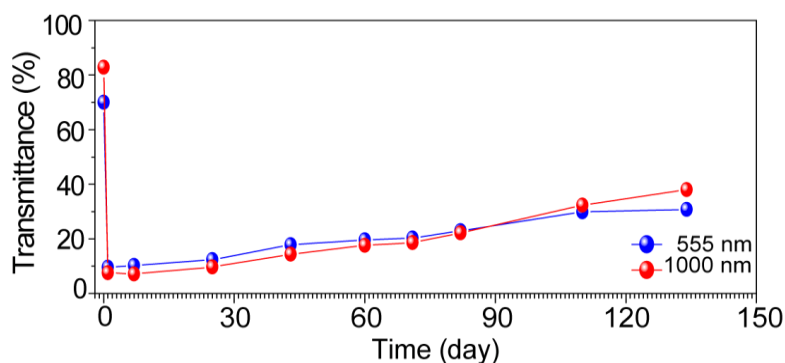


**Figure 4.13.** Optical memory test of the a-IZO/a-WO<sub>3</sub>/DUPIL<sub>60</sub>/c-NiO/a-IZO ECD.

The huge difference between the cathodic and anodic kinetics, the unusually high CE values (greater for the cathodic process), and the remarkable optical memory (slow bleaching under open circuit) of the ECD may be tentatively correlated with interfacial issues intimately associated with the structure/morphology of the TCO material and of the active electrodes. In fact, as the IZO and WO<sub>3</sub> layers used were both amorphous and exhibited low average roughness values (0.29 and 0.15 nm, respectively) (**Figures 4.14A, 4.14B** and **Figures 4.14C, 4.14D**, respectively), the electric field which hit the a-IZO/a-WO<sub>3</sub> plate upon application of the voltage was spread in a much more uniform way than in the case of the a-IZO/c-NiO plate. This happened because NiO was polycrystalline and had a less homogenous surface topography (average roughness of 0.41 nm) (**Figures 4.14E, 4.14F**). As a consequence, the cathodic process (reduction, accompanied by ion intercalation) was facilitated and a very high optical contrast was achieved at low load. In contrast, a higher load was required for the anodic process (oxidation, together with ion deinsertion) to occur.

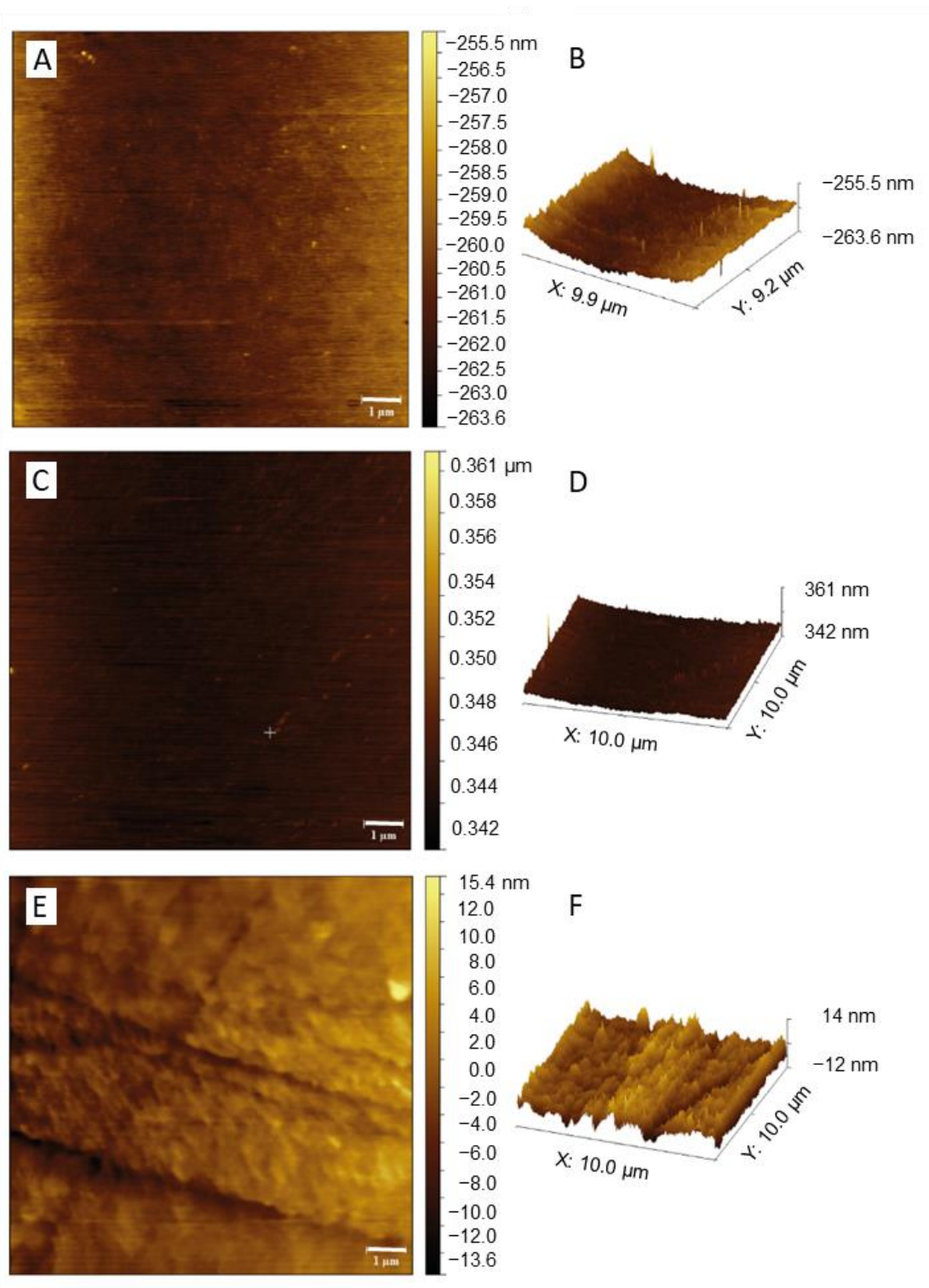


**Figure 4.14.** AFM images of the surfaces of (A,B) a-IZO (a-IZO glass plate), (C,D) a-WO<sub>3</sub> (a-WO<sub>3</sub>/a-IZO glass plate) and (E,F) c-NiO (c-NiO/a-IZO glass plate).

#### 4.4. Conclusions

In this chapter it was demonstrated that the combined use of a-IZO, a conducting oxide transparent in the visible and NIR spectral regions, and of the DUPIL<sub>60</sub> ormolyte, obtained by sol-gel chemistry, allowed producing an ECD with high visible and NIR transparency, and voltage-actuated dual coloration tuning, enabling three-mode operation (bright hot, semi-bright warm, and dark cold). The ECD delivered a number of extraordinary features, in particular high switching efficiency, high optical modulation, good cycling stability and coloration efficiency values during bleaching and especially coloration, excellent optical memory, and unusual self-healing ability following mechanical stress. These advantages made this ECD energy efficient and thus extremely attractive for applications in smart windows of buildings located in continental climatic regions where large temperature range variations often take place in a single day. For the buildings' occupants, such easily operated dynamic windows will provide substantial comfort. Ideally, this new concept can be applied straightaway by any smart EC window producer company. Indeed, the replacement of ITO by conducting oxides transparent in the visible and NIR spectral regions is straightforward to implement, since it does not imply, either additional costs, or changes in the current processing technology regardless of the nature of the system (rigid glass-made or flexible polymer-made). The impact of the present concept on the building sector can be potentially huge within a short period of time. The use of other such oxides opens a myriad of excellent prospects for the area of EC smart windows.

## 5 - LUMINESCENT PMMA-BASED SOLID ELECTROLYTE MEMBRANES FOR SMART WINDOWS AIMING ENERGY-EFFICIENT BUILDINGS

In the present chapter the technological potential of the PMMA-based composites doped with the Ln-doped ISs discussed in **Chapter 3** is extended to the field of electrochromic smart windows. Here, these materials were successfully employed as electrolytes in ECDs with foreseen application in the future ZEBs. Seeking to impart to these devices a fine control of the sunlight (visible radiation) and heat gain (NIR radiation), these electrolytes comprised, apart from PMMA, a mixture of IS-Eu-1+IS-Nd-19 plus the commercial IL 1-butyl-3-methylimidazolium hexafluorophosphate ([BMIm][PF<sub>6</sub>]) with  $X' = m[\text{BMIm}][\text{PF}_6]/m_{\text{PMMA}}$ . An optimized electrolyte sample was used in an ECD with configuration glass/a-IZO/a-WO<sub>3</sub>/(PMMA/IS-Eu-1/IS-Nd-19/[BMIm][PF<sub>6</sub>]-X')/c-NiO/a-IZO/glass with  $X' = 55$ . The device demonstrated fast switching speed (> 50 s) and high transparency in the visible and NIR spectral regions ( $T = 79/96/89\%$  at 555/1000/1500 nm in the as-prepared state). Upon application of  $\pm 2.5$  V for 200 cycles, the  $T_{\text{bleached}}/T_{\text{coloured}}$  values were 44/28, 46/26, 39/20 and 27/9 % at 555, 1000, 1500 and 1650 nm, respectively. The device performance increased with cycling. The  $CE_{\text{in}}/CE_{\text{out}}$  values calculated at the 200<sup>th</sup> cycle at 555, 1000, 1500 and 1650 nm were:  $-302/+181$ ,  $-381/+228$ ,  $-446/+267$  and  $-734/+440$  cm<sup>2</sup> C<sup>-1</sup>. The results obtained in this chapter confirm that the PMMA/IS-Eu-1/IS-Nd-19/[BMIm][PF<sub>6</sub>]-X' composite materials are of interest for the construction of sustainable energy-efficient integrated devices. These transparent luminescent materials lend themselves to simultaneous application as ECD electrolyte, and LDS and LSC layers (**Chapter 3**) of windows containing edge-mounted PV cells. This design would guarantee in a single device system energy harvesting, energy generation, and energy management ability.

### 5.1. Introduction

The potential of joining transparency, energy harvesting, energy generation, and energy management in a single device provides a huge niche market with potential applications in several areas, in particular glazing in buildings.<sup>255</sup> In this context, smart PV windows (SPWs) have emerged as an encouraging green technology on account of their ability to assimilate in a single device energy harvesting, electrical power output,

energy management, energy saving, and privacy protection. SPWs can exert a major impact as an architectural element to reduce building energy consumption (air conditioning, ventilation and heating), and increase the occupant's visual and thermal comfort.<sup>256,257</sup> In the light of the SPW concept, different materials were developed. Lin *et al*<sup>257</sup> demonstrated the use of a thermochromic solar cell for SPWs applications. These authors used an inorganic halide perovskite (caesium lead iodide/bromide) undergoing thermally-driven, moisture-mediated reversible transitions between a transparent non-perovskite phase ( $T_{\text{visible}} = 81.7\%$ ) with low power output, and an intensely coloured perovskite phase ( $T_{\text{visible}} = 35.4\%$ ) with high power output. The device displayed tuneable colours, transparency, an efficiency up to 7%, a phase transition at 105 °C, and excellent cycling stability with no colour reduction or performance degradation. Xia *et al*<sup>256</sup> produced high-efficiency and reliable SPWs by coupling multiresponsive liquid crystal/polymer composite (LCPC) films and semi-transparent perovskite solar cells (ST-PSCs), in which LCPC films were applied for transparency control of SPWs. These offered multiple working modes with exceptional electrical power output, energy saving, and privacy protection performances. Wheeler *et al*<sup>258</sup> produced a PV device with a switchable absorber layer with dynamic sunlight response. Under illumination, photothermal heating switched metal halide perovskite-methylamine complex absorber layer from a transparent state ( $T_{\text{visible}} = 68\%$ ) to an absorbing, PV coloured state ( $T_{\text{visible}} < 3\%$ ) due to methylamine separation. After cooling, the methylamine complex was reformed and the absorber layer became transparent again.

Herein, induced by the good performance of the PMMA-Ln-X materials as LDS and LSC layers demonstrated in **Chapter 3**, and by the encouraging results obtained in **Chapter 4**, and aiming the development of SPWs composed of integrated LSC/LDS/PV/ECD devices, we further tested their potential as IC (electrolyte) of ECDs (**Figure 5.1A**).

In the ECDs assembled the TCO, EC1 and EC2 layers were the same as those used in **Chapter 4** (i.e., a-IZO, a-WO<sub>3</sub>, and c-NiO, respectively). The a-WO<sub>3</sub> layer featured the UN Sustainable Development Goal 11 symbol (**Figures 5.1A, 5.1C and 5.1D**). The IC was a PMMA-based composite doped with a IS-Eu-1+IS-Nd-19 mixture, and [BMIm][PF<sub>6</sub>] (55% wt. with respect to PMMA). As demonstrated in **Chapter 3**, layers produced by the dispersion of IS-Eu and IS-Nd in PMMA are attractive, since they emit in the visible-to-NIR spectral region. The purpose of the addition of [BMIm][PF<sub>6</sub>] to the above mixture was to decrease the viscosity and increase the ionic conductivity of

the IC layer, and, as a consequence, improve the ECD operation. The device was noted as ECD@PISIL, where P, IS and IL stand for polymer, ionosilica and ionic liquid, respectively.

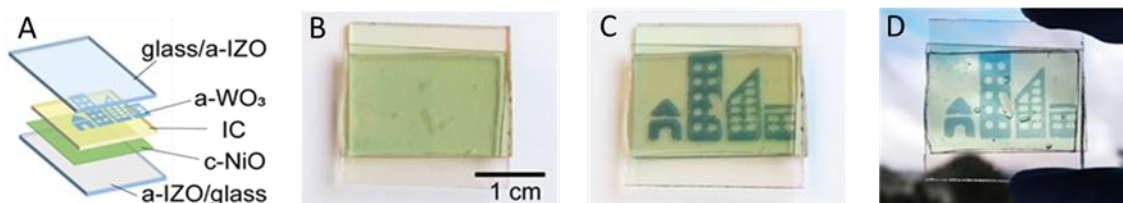


**Figure 5.1.** Archetypal ECD@PISIL tested. (A) Schematic representation, where IC is PMMA/IS-Eu-1/IS-Nd-19/[BMIm][PF<sub>6</sub>]-55; (B) as-prepared; (C) coloured state at  $-2.5$  V against a white background; (D) coloured state at  $-2.5$  V against an outside environment background.

## 5.2.Synthesis

**Materials.** N-butylimidazole (BIm, 98%, Sigma-Aldrich), (3-chloropropyl)trimethoxysilane (CPTMS, 97%, Sigma-Aldrich), neodymium(III) chloride hexahydrate (NdCl<sub>3</sub>.6H<sub>2</sub>O, 99.9%, Sigma-Aldrich), europium(III) chloride hexahydrate (EuCl<sub>3</sub>.6H<sub>2</sub>O, 99.99%, Sigma-Aldrich), 2-thenoyltrifluoroacetone (tta, 99%, Sigma-Aldrich), methyl methacrylate (MM) (99%, Acros), benzoyl peroxide (BPO, 97%, Alfa Aesar), anhydrous ethyl acetate (EtOAc, 98.8%, Sigma-Aldrich), ethanol (EtOH, 99.8%, Fisher Chemical), tetrahydrofuran (THF, Sigma-Aldrich), sodium hydroxide (NaOH, Merck), 1-butyl-3-methylimidazolium hexafluorophosphate ([BMIm][PF<sub>6</sub>], 98+%, Alfa Aesar), and dichloromethane (DCM, HPLC grade, Fisher Chemical) were used as received. Ultrapure water was used in all experiments.

**Synthesis of the IS-Eu-1 and IS-Nd-19 ionosilica mixture.** The IS-Eu-1/IS-Nd-19 mixture was prepared according to the procedure reported in **Chapter 3**. It primarily involved mixing the precursor compounds [B(TMSP)Im][Eu(tta)<sub>4</sub>] with [B(TMSP)Im][Nd(tta)<sub>4</sub>] in the appropriated ratio.

**Synthesis of the PMMA/IS-Eu-1/IS-Nd-19/[BMIm][PF<sub>6</sub>] composite.** The preparation of the PMMA/IS-Eu-1/IS-Nd-19/[BMIm][PF<sub>6</sub>]-based material was carried out as follows: a mass of 1 g of MM was mixed with 0.006 g of BPO in 6 vials. The

mixture was heated at 80-90 °C for 25 min. A THF solution of the IS mixture was then added to each vial (20% wt. IS-Eu-1/IS-Nd-19 with respect to MM). The 6 mixtures were then doped with increasing concentrations of [BMIm][PF<sub>6</sub>] (X = 25, 35, 45, 55, 65, and 75 %, where  $X = m_{[\text{BMIm}][\text{PF}_6]}/m_{\text{PMMA}}$ ) and subsequently transferred to an oven at 50 °C until complete polymerization. The resulting samples, represented by the notation PMMA/IS-Eu-1/IS-Nd-19/[BMIm][PF<sub>6</sub>]-X, were characterized by ATR/FT-IR, DSC, and complex impedance spectroscopy. Elemental analysis of PMMA/IS-Eu-1/IS-Nd-19/[BMIm][PF<sub>6</sub>]-55. Calculated: Eu, 0.066; Nd, 1.190. Found: Eu, 0.085; Nd, 1.700.

### ECD assembly

The active layers of the ECD device (a-WO<sub>3</sub> and c-NiO) were deposited by sputtering and e-beam evaporation, respectively, onto an a-IZO-coated glass previously deposited by sputtering. The a-WO<sub>3</sub> layer was produced in an argon and oxygen atmosphere (oxygen partial pressure of 0.2 Pa) using a deposition pressure of 1.0 Pa, under an r.f. power of 200 W in a Pfeiffer Vacuum Classic 500 system using 3 diameter ceramic target from Plasmaterials, yielding a thickness of 300 nm. A polycrystalline NiO (c-NiO) film with a 300 nm thickness was obtained from NiO commercial random pellets pieces 3-6 mm (99.99%, Super Conductive Materials), and deposited by e-beam evaporation in a homemade system, with an initial chamber pressure of  $7 \times 10^{-4}$  Pa and growth rate of 6 nm min<sup>-1</sup>. The a-IZO thin films (resistivity of  $7.97 \times 10^{-4}$  Ω cm, mobility of 52.1 cm<sup>2</sup> V<sup>-1</sup> s<sup>-1</sup>, and carrier concentration of  $1.50 \times 10^{20}$  cm<sup>-3</sup>) were deposited by sputtering, in a homemade system, from In<sub>2</sub>O<sub>3</sub>/ZnO 89.3/10.7 wt%, 99.99%, 3 in. diameter × 6 mm thick (Super Conductive Materials). The sputtering process was carried out at a constant 0.13 Pa value (argon and oxygen) and room temperature. The substrate and target were apart by 10 cm and the r.f. power was 100 W. AFM images of the a-IZO, a-WO<sub>3</sub>, and c-NiO layers were recorded in an AFM CSI Nano-Observer equipment (Scientec) in tapping mode using a super sharp Si HQ:NSC19/FORTA probe with a frequency resonance of 60 kHz and a spring constant of 0.3 N m<sup>-1</sup>.

In this work, two ECDs were tested: ECD@PISIL, comprising the PMMA/IS-Eu-1/IS-Nd-19/[BMIm][PF<sub>6</sub>]-55 monolith as IC, and ECD@IS, in which the IC was exclusively the IS-Eu-1/IS-Nd-19 mixture.

The prototype ECD@PISIL with  $2.5 \times 2$  cm<sup>2</sup> active area, was assembled under atmospheric conditions. A piece of PMMA/IS-Eu-1/IS-Nd-19/[BMIm][PF<sub>6</sub>]-55 film with

the dimensions of the ECDs and with a thickness of  $0.9 \text{ mm} \pm 0.1 \text{ mm}$  was cut out of the monolith and sandwiched between a- $\text{WO}_3$ /a-IZO-coated glass. A c-NiO/a-IZO-coated glass plate so that the two EC coatings (i.e., a- $\text{WO}_3$  and c-NiO) faced each other. Free space was left on one side of the glass plates to ensure the electrical contacts. The assembled system was then pressed together prior to the electro-optical analyses.

ECD@IS, with  $2.6 \times 1.8 \text{ cm}^2$  active area, was assembled using a similar procedure. This mixture had to be first heated at  $50 \text{ }^\circ\text{C}$  and then it was cast onto the surface of the a- $\text{WO}_3$ /a-IZO-coated glass with the help of a micropipette.

### 5.3. Results and discussion

#### Monoliths structural characterization

The monolith samples were first characterized to determine the optimal electrolyte material for ECD assembly.

To elucidate the interaction between PMMA and [BMIm][PF<sub>6</sub>] the samples were studied by ATR/FT-IR spectroscopy (**Figure 5.2**). Analysis of the ATR/FT-IR spectra revealed that the stretching vibration band of the C=O group of PMMA at  $1724 \text{ cm}^{-1}$  (**Figure 5.2B**, black line) remained unshifted in the case of the doped samples (PMMA/IS-Eu-1/IS-Nd-19/[BMIm][PF<sub>6</sub>]-X) (**Figure 5.2B**, coloured lines) indicating no interaction between PMMA and [BMIm][PF<sub>6</sub>]. The interaction between PMMA and IS-Ln was discussed in **Chapter 3 (Figure 3.8)** and the same conclusion was reached.

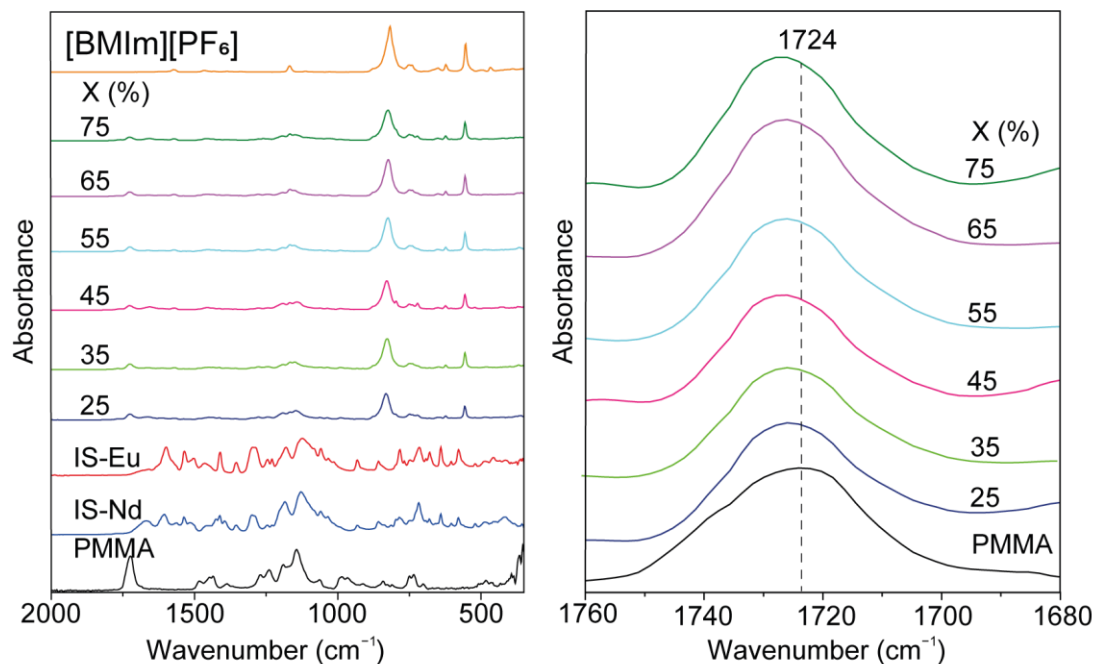


**Figure 5.2.** ATR/FT-IR spectra of PMMA, IS-Eu, IS-Nd and PMMA/IS-Eu-1/IS-Nd-19/[BMIm][PF<sub>6</sub>]-X monoliths in the (A) 2000-400 cm<sup>-1</sup> and (B) 1760-1680 cm<sup>-1</sup>.

The DSC curves of the PMMA/IS-Eu-1/IS-Nd-19/[BMIm][PF<sub>6</sub>]-X monoliths (**Figure 5.3**) exhibit an exothermic peak with onset temperature around 155 °C associated with the beginning of thermal degradation. In these DSC thermograms it was not possible to detect the  $T_g$  depression over the whole range of temperatures considered. Scott *et al.*<sup>259</sup> demonstrated the increasing plasticizing effect exerted by [BMIm][PF<sub>6</sub>] on the PMMA matrix. An almost linear decrease of  $T_g$  with the increase of [BMIm][PF<sub>6</sub>] concentration between 0-50 wt% was reported. A remarkable  $T_g$  decrease of approximately 40 °C occurred at 50 wt% from an initial  $T_g$  value around 120 °C. Moreover, Zhao *et al.*<sup>260</sup> prepared PMMA/MWCNT nanocomposites (where MWCNT is multiwall carbon nanotube) doped with [BMIm][PF<sub>6</sub>] and found that this IL was able to act as multifunctional agent, specifically reducing drastically the  $T_g$  value of the PMMA matrix, thus acting as an efficient plasticizer and increasing in parallel the electrical conductivity of the nanocomposites prepared.<sup>261</sup>

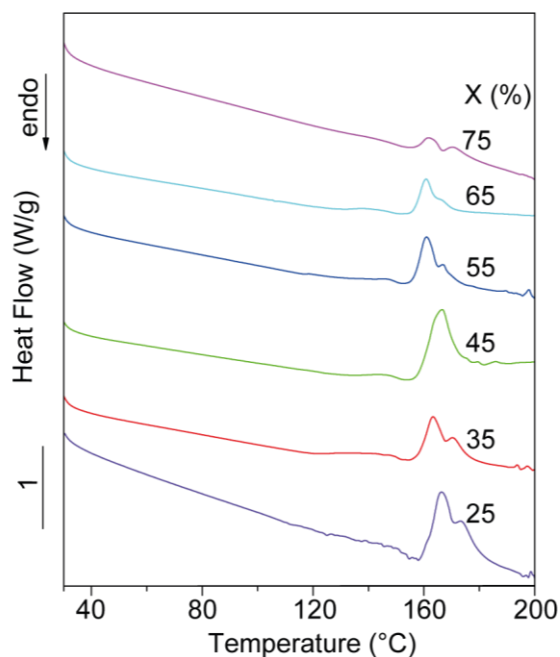


**Figure 5.3.** DSC curves of the PMMA/IS-Eu-1/IS-Nd-19/[BMIm][PF<sub>6</sub>]-X monoliths.

As expected, the ionic conductivity of the doped samples was found to be much higher than that of pure PMMA (around  $8.57 \times 10^{-13} \text{ S cm}^{-1}$  at room temperature<sup>262</sup>) and lower than that of [BMIm][PF<sub>6</sub>], reaching its maximum for  $X = 55$  (**Figure 5.4**, blue line and symbols). The temperature dependence of the ionic conductivity of IS-Eu (**Figure 5.4**, black line and symbols) exhibits an abrupt change around 40-70 °C which leads to a conductivity increase of about two orders of magnitude. This dramatic slope change must be associated with the thermal event observed in the DSC curve in the same temperature interval (**Figure 3.11**, red line). The latter event was tentatively attributed to two effects: the order-disorder transition caused by the pendant organic groups placed in the interlamellar space of IS-Eu, and the reversible thermotropic *gauche/trans* transition of the butyl group in the imidazolium ring of [BMIm][PF<sub>6</sub>].<sup>224</sup> The ionic conductivity of the PMMA/IS-Eu-1/IS-Nd-19/[BMIm][PF<sub>6</sub>]-X electrolytes is governed by the [BMIm][PF<sub>6</sub>] concentration, but the effect is less marked in the most concentrated samples. The sample with  $X = 55$  was selected for the ECD tests, because it combined high ionic conductivity at lower doping concentration ( $2.13 \times 10^{-4}$  and  $8.76 \times 10^{-4} \text{ S.cm}^{-1}$  at room temperature and 44 °C, respectively). The temperature dependent ionic conductivity plot exhibits a nonlinear behaviour that is typically described by the VTF relation.<sup>263</sup>

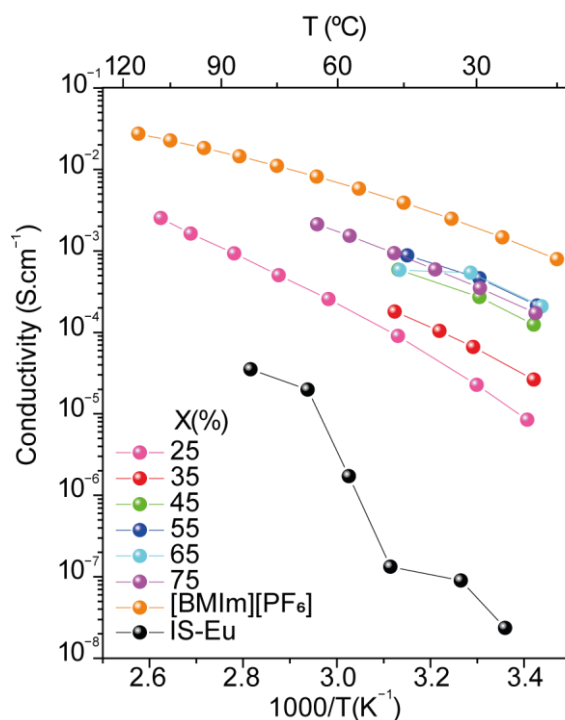


**Figure 5.4.** Temperature dependence of the ionic conductivity of IS-Eu, [BMIm][PF<sub>6</sub>] and PMMA/IS-Eu-1/IS-Nd-19/[BMIm][PF<sub>6</sub>]-X electrolytes. [BMIm][PF<sub>6</sub>] data from <sup>262</sup>.

### Optical properties

The photoluminescent properties of PMMA/IS-Eu-1/IS-Nd-19/[BMIm][PF<sub>6</sub>]-55 were also studied. As pointed out in **Chapter 3**, this material presents the dual contribution arising from the Eu<sup>3+</sup> (<sup>5</sup>D<sub>0</sub>→<sup>7</sup>F<sub>0-4</sub>) and Nd<sup>3+</sup> (<sup>4</sup>F<sub>3/2</sub>→<sup>4</sup>I<sub>11/2,13/2</sub>) intra-4f transitions, as it is revealed in the room temperature emission spectrum excited at 360 nm ranges from the visible to the NIR spectral range (**Figure 5.5**). No sign of the PMMA intrinsic emission could be observed regardless of the selected excitation wavelength (330-385 nm), indicating efficient PMMA-to-ligand/Ln<sup>3+</sup> energy transfer.<sup>227</sup> The excitation spectra displayed in **Figure 5.5B** were monitored selectively for each Ln<sup>3+</sup> centre. The spectrum monitored at the Eu<sup>3+</sup> emission (<sup>5</sup>D<sub>0</sub>→<sup>7</sup>F<sub>2</sub> transition) shows two main components peaking at 330 and 385 nm. The low intensity of the intra-4f<sup>6</sup> lines indicates that the Eu<sup>3+</sup> excited states in PMMA are populated via ligand-sensitization. The 330 and 385 nm components resemble those already observed for isolated Eu(tta)<sub>3</sub>(H<sub>2</sub>O)<sub>2</sub><sup>171</sup> and for organic-inorganic hybrids incorporating Eu(tta)<sub>3</sub>(H<sub>2</sub>O)<sub>2</sub> and Eu(tta)<sub>3</sub>(phen) (phen=1,10-phenantroline), being ascribed to the π-π\* electronic

transition of the organic ligands.<sup>228</sup> In the case of the spectrum monitored at the Nd<sup>3+</sup> emission (<sup>4</sup>F<sub>3/2</sub>→<sup>4</sup>I<sub>11/2</sub> transition), a main band peaking at 375 nm and characteristic of excitation transitions of Nd<sup>3+</sup> is evident. We note that the materials are transparent absorbing mainly the UV component of the sunlight, as illustrated in **Figure 5.5B**.

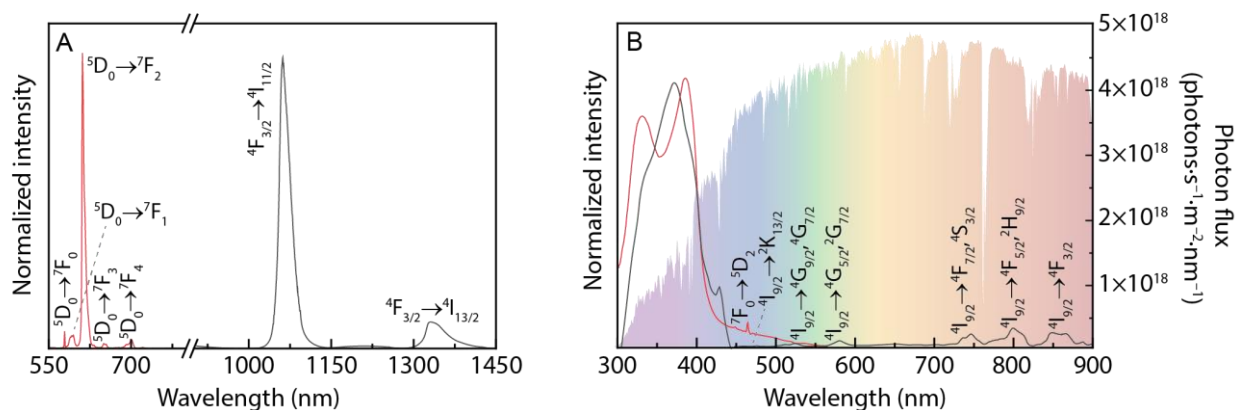


**Figure 5.5.** (A) Emission spectrum excited at 360 nm and (B) excitation spectra monitored at 612 nm (red line) and 1056 nm (black line) for the PMMA/IS-Eu-1/IS-Nd-19/[BMIm][PF<sub>6</sub>]-55. The shadowed area represents the AM1.5G photon flux (right y axis).

## ECDs

The as-prepared ECD@PISIL (**Figure 5.1B**) exhibited T values of ca. 79, 96, 89 and 77 % at 555, 1000, 1500 and 1650 nm, respectively (**Table 5.1**, **Figure 5.6A**, red line) and a light greenish hue ( $L^* = 59.66$ ,  $a^* = -4.62$  and  $b^* = 2.46$ ) (**Figure 5.7A**, white circle). The absorption peaks observed in **Figure 5.6A** from  $\pm 500$ -800 nm are tentatively associated with the energy levels of Nd<sup>3+</sup> ion.<sup>264</sup>

**Table 5.1.** Electro-optical parameters of ECD@ PISIL and ECD@IS. T values are given in %.

$\lambda$ [nm]	T <sub>as-prepared</sub>	T <sub>bleached</sub> a)	T <sub>coloured</sub> a)	$\Delta T$ a)	$\Delta OD$ a)	T <sub>bleached</sub> b)	T <sub>coloured</sub> b)	$\Delta T$ b)	$\Delta OD$ b)	CE <sub>in</sub> b)	CE <sub>out</sub> b)	
	0.0 V	2.5 V	-2.5 V			2.5 V	-2.5 V			(cm <sup>2</sup> C <sup>-1</sup> )		
ECD@PISIL	555	79	44	34	10	0.11	44	28	16	0.20	-302	181
	1000	96	46	32	14	0.16	46	26	20	0.25	-381	228
	1500	89	39	26	13	0.18	39	20	19	0.29	-446	267
	1650	77	27	13	14	0.32	27	9	18	0.48	-734	440
ECD@IS	0.0 V	2.0 V	-2.0 V			2.0 V	-2.0 V					
	555	75	69	67	2	0.01	44	41	3	0.03	-201	152
	1000	83	68	67	1	0.01	36	34	2	0.02	-162	123
	1500	80	63	62	2	0.01	32	31	1	0.01	-90	68
	1650	76	61	59	2	0.01	29	28	1	0.01	-100	75

a) After 1<sup>st</sup> series of cycling. See text for details.

b) After 3<sup>rd</sup> series of cycling (200 CA cycles/50 CA cycles)

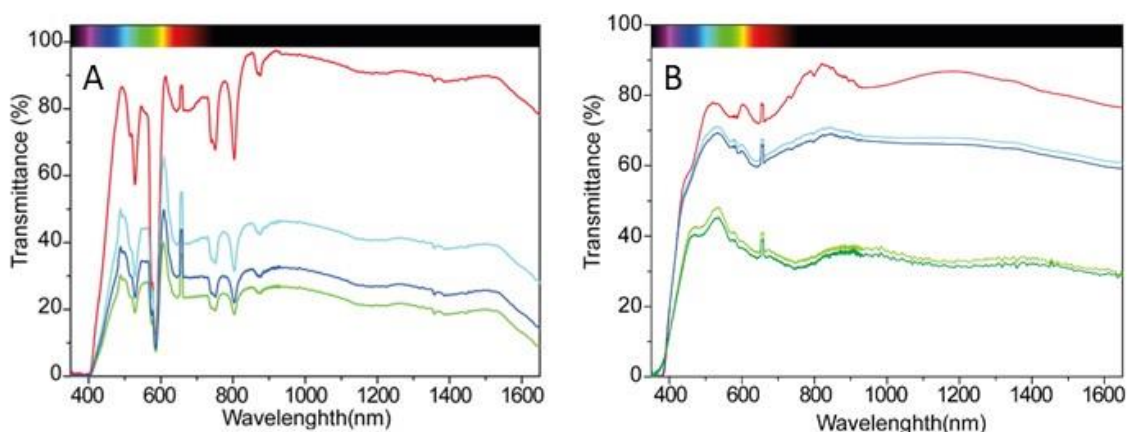


**Figure 5.6.** Visible-NIR spectra of the ECDs: (A) ECD@PISIL in the as-prepared state (red line), bleached state (light blue line), coloured state after 10 CA cycles ( $\pm 2.5$  V) (dark blue line); and coloured state after 200 CA cycles ( $\pm 2.5$  V) (green line). (B) ECD@IS in the as-prepared state (red line), bleached state (light blue line), coloured state upon application of  $-2.0$  V (dark blue line), bleached state after 50 CA cycles ( $\pm 2.0$  V) (light green line), and coloured state after 50 CA cycles (dark green line).

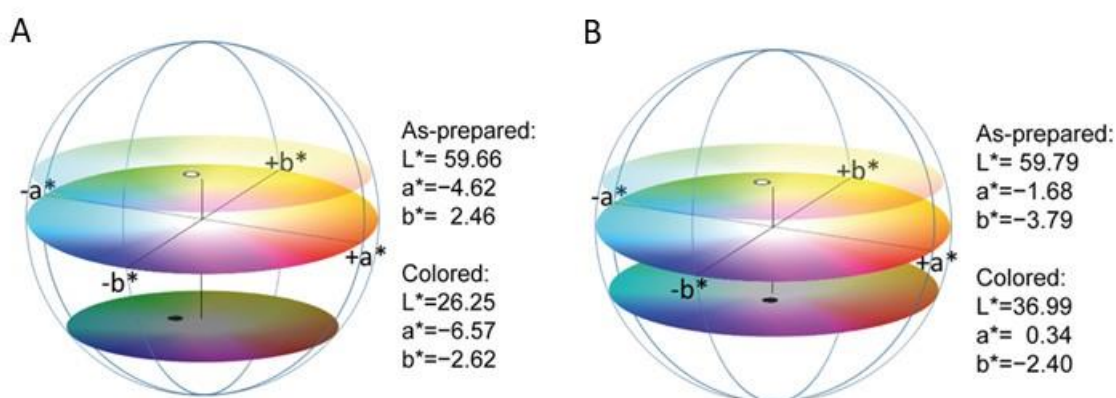


**Figure 5.7.** CIE 1976  $L^*a^*b^*$  colour diagram of the ECDs. (A) ECD@PISIL: as-deposited state (white circle), and coloured state at  $-2.5$  V after 200 CA cycles (black circle); (B) ECD@IS: as-deposited state (white circle), coloured state at  $-2.0$  V after 50 CA cycles (black circle).

The ECD@PISIL was subject to three series of cycling procedures. Cycling series 1 comprised the application of: (1) 10 CV cycles ( $\pm 1.0$  V, 50 mV/s) followed by a CA cycle (0.0 V, 200 s;  $-1.0$  V, 200 s;  $+1.0$  V, 200 s), (2) 10 CV cycles ( $\pm 1.5$  V, 50 mV/s) followed by a CA cycle (0.0 V, 200 s;  $-1.5$  V, 200 s;  $+1.5$  V, 200 s), (3) 10 CV cycles ( $\pm 2.0$  V, 50 mV/s) followed by a CA cycle (0.0 V, 200 s;  $-2.0$  V, 200 s;  $+2.0$  V, 200 s), (4) 10 CV cycles ( $\pm 2.5$  V, 50 mV/s). The T values were then recorded for  $+2.5/-2.5$  V,

being 44/34 %, 46/32 %, 39/26 % and 27/13 % at 555, 1000, 1500 and 1650 nm, respectively (**Figure 5.6A**, light blue/dark blue lines, and **Table 5.1**). **Figures 5.1C** and **5.1D** show the coloured ECD@PISIL against a white background, and as a window frame, respectively. Cycling series 2 included 1 CA cycle (0.0 V, 200 s; - 2.5 V, 200 s; 2.5 V, 200 s), 2 CA cycles ( $\pm 3.0$  V, 200 s), 12 CA cycles ( $\pm 2.5$  V, 50 s) and 4 CA ( $\pm 2.5$  V, 30 s). Cycling series 3 involved 200 CA cycles ( $\pm 2.5$  V, 50 s). As a result, a decline in the T values to 28, 26, 20 and 9 % at 555, 1000, 1500 and 1650 nm, respectively, occurred (**Figure 5.6A**, green line and **Table 5.1**).

The study of the ECD@PISIL over 200 bleaching/colouring CA cycles ( $\pm 2.5$  V at every 50 s) (**Figure 5.8A**) demonstrated the excellent cycling stability of the device. As expected, after this CA treatment the T values for the coloured state decreased considerably with respect to those measured in the first cycles (**Table 5.1**). Accordingly, the  $\Delta OD$  values were markedly enhanced (**Table 5.1**). The  $CE_{in}/CE_{out}$  values calculated at the 200<sup>th</sup> cycle at 555, 1000, 1500 and 1650 nm were  $-302/+181$ ,  $-381/+228$ ,  $-446/+267$ , and  $-734/+440$   $cm^2 C^{-1}$ , respectively. These CE values are considerably lower than those obtained with the ECD proposed in **Chapter 4** which included the sol-gel derived DUPIL<sub>60</sub> electrolyte, but are significantly higher (more than 10 times) than those reported, for instance, for an ECD incorporating another sol-gel derived electrolyte, poly( $\epsilon$ -caprolactone) (PCL(530))/siloxane hybrid doped with potassium triflate ( $KCF_3SO_3$ ) and the Eu(btfac)<sub>3</sub>phen complex (where btfac is 4,4,4-trifluoro-1-phenyl-2,4-butanedionate and phen is 1,10-phenantroline) ( $CE_{in}$  of  $-23$   $cm^2 C^{-1}$ ).<sup>79</sup>

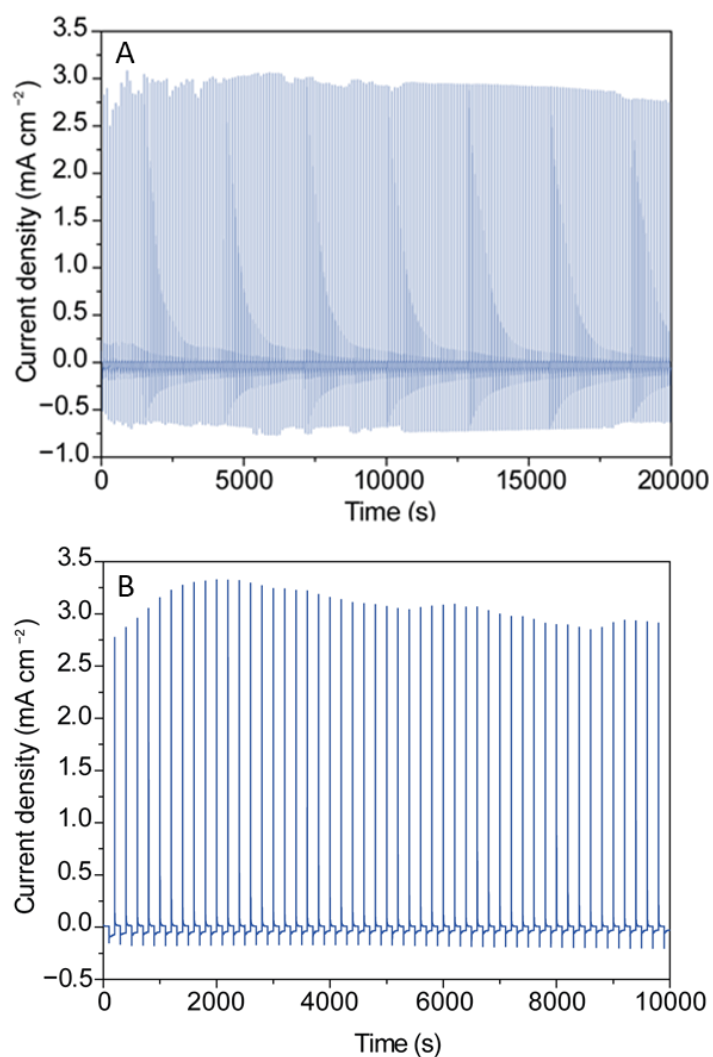


**Figure 5.8.** Variation of the current density of the devices: (A) ECD@PISIL (voltage steps of  $\pm 2.5$  V at every 50 s after 200 cycles) and (B) ECD@IS (voltage steps of  $\pm 2.0$  V at every 100 s) after 50 cycles.

**Figure 5.8.** also allows inferring a huge difference between the cathodic and anodic current densities, which is corroborated by the fact that the T values of the bleached state (**Figure 5.6A**, light blue line) did not coincide with that of the as-prepared state (**Figure 5.6A**, red line). In **Chapter 4** the same situation, although less marked, was detected in an ECD including the same TCO material (a-IZO) and the same active electrodes (a-WO<sub>3</sub> and c-NiO). This effect was associated with the structure/morphology of the a-IZO, a-WO<sub>3</sub>, and c-NiO layers. The first two materials are amorphous and displayed low average roughness values, whereas c-NiO is polycrystalline and exhibited a less homogenous surface topography. As a consequence, the cathodic process was facilitated over the anodic process, and thus less charge was needed to trigger the optical effect (coloration). In the case of ECD@PISIL, the crystalline regions detected in the

electrolyte presumably slowed down the disinsertion process. However, considering that the electrolyte PMMA/IS-Eu-1/IS-Nd-19/[BMIm][PF<sub>6</sub>]-55 exhibits higher room temperature ionic conductivity ( $2.13 \times 10^{-4} \text{ S.cm}^{-1}$ ) than DUPIL<sub>60</sub> ( $6.3 \times 10^{-5} \text{ S cm}^{-1}$ ), **Figure 4.7**, the inefficient bleaching observed in ECD@PISIL is probably associated with the nature of the charge carriers. In fact, while in DUPIL<sub>60</sub>, the species responsible for ion conduction are small protons, in the case of PMMA/IS-Eu-1/IS-Nd-19/[BMIm][PF<sub>6</sub>]-55 the charge carriers are presumably the bulky PF<sub>6</sub><sup>-</sup> anions.

For comparison purposes, the ECD@IS was also tested. The as-prepared device, lacking both PMMA and IL, exhibited T values of 75, 83, 80 and 76% at 555, 1000, 1500 and 1650 nm, respectively (**Table 5.1, Figure 5.6B**, red line), and a light blueish hue ( $L^* = 59.79$ ,  $a^* = -1.68$  and  $b^* = -3.79$ ) (**Figure 5.7B**, white circle). The ECD@IS was first subject to 10 CA cycles ( $\pm 2 \text{ V}$ , 100s). As a consequence, the T values recorded for the bleached (**Figure 5.6B**, light blue) and coloured (**Figure 5.6B**, dark blue) states decreased. When the ECD@IS was subsequently submitted to 50 CA cycles ( $\pm 2 \text{ V}$ , 100s) (**Figure 5.6B**), the T values of the bleached/coloured states dropped to 44 /41%, 36/34%, 32/31% and 29/28% at 555, 1000, 1500 and 1650 nm, respectively (**Table 5.1, Figure 5.6B**, light green/dark green lines), and a dark blue colour ( $L^* = 36.99$ ,  $a^* = 0.34$  and  $b^* = -2.40$ ) (**Figures 5.7B**, black circle) resulted. **Figure 5.8B** illustrates again the dramatic difference in terms of current density required for charge and discharge. The calculated  $\Delta OD$  values are rather small (**Table 5.1**). The  $CE_{in}/CE_{out}$  values calculated at the 50<sup>th</sup> cycle at 555, 1000, 1500 and 1650 nm were  $-201/+152$ ,  $-162/+123$ ,  $-90/+68$ , and  $-100/+75 \text{ cm}^2 \text{ C}^{-1}$ , respectively (**Table 5.1**), thus, as expected, considerable lower than those observed for ECD@PISIL, demonstrating the beneficial effect resulting from the use of an electrolyte sample with higher conductivity.

#### 5.4. Conclusions

Two ECDs (ECD@PISIL and ECD@IS) for smart windows were produced that allow the simultaneous control of the incident visible and NIR solar radiation, and exhibit emission in the visible/NIR, thus increasing in parallel the aesthetics of the window and heat gain. The two ECDs differ in the electrolyte formulation. In both devices the host matrix is PMMA doped with a mixture of the ionosilicas IS-Eu and IS-Nd. In the case of ECD@PISIL, the electrolyte contains in addition [BMIm][PF<sub>6</sub>]. ECD@PISIL represents a better option than ECD@IS. The former device exhibited several attractive features, such as fast switching speed, good cycling stability, and high  $CE_{in}/CE_{out}$  values at 555,

1000, 1500 and 1650 nm ( $-302/+181$ ,  $-381/+228$ ,  $-446/+267$  and  $-734/+440$   $\text{cm}^2 \text{C}^{-1}$ ) after 200 CA cycles. Its bleaching efficiency is, however, poor, probably due to the bulkiness of the electrolyte charge carriers (very likely the  $\text{PF}_6^-$  anions) which affects negatively the disinsertion process.

The operation of the ECD@PILSIL comprising PMMA/IS-Eu-1/IS-Nd-19/[BMIm][PF<sub>6</sub>]-55 is the proof of concept that this material or similar materials with enhanced performance can be used simultaneously as ECD electrolyte, and LDS and LSC layers in smart windows.

The encouraging results obtained clearly justify further improvement of the electrolytes to enhance the electro-optical features of the ECD@PISIL. Given the results obtained in **Chapter 4**, changing the [BMIm][PF<sub>6</sub>] IL by the [BIm][TfO] PIL would be the first choice. Another option could be the synthesis via sol-gel chemistry of other host matrices through the co-condensation of appropriate precursors, such as 3-(trimethoxysilyl)propyl methacrylate (TMSPMA) and/or d-UPTES(2000) (cf. **Chapter 4**) with [B(TMSP)Im][Ln(tta)<sub>4</sub>] (cf. **Chapter 3**). This approach could be obviously extended to other organic/inorganic hybrids (e.g., d-U(600),<sup>265</sup> d-U(900),<sup>60,171</sup> t-U(5000),<sup>234</sup> etc.) to impart simultaneously transparency and flexibility.

## 6 - GENERAL CONCLUSIONS AND PERSPECTIVES

In this section, the main results presented and discussed throughout the different chapters of this thesis are summarized. The main objectives were achieved. Here, new Ln<sup>3+</sup>-doped surface functionalized ISs embedded in a transparent and flexible matrix (PMMA) were successfully produced and characterized. These materials were tested as LDS layers/LSCs and when doped with an IL, they played the role of electrolytes in ECD devices with emission in the visible and NIR spectral regions.

The general conclusion of this thesis is that Nd<sup>3+</sup>-, Eu<sup>3+</sup>-, Tb<sup>3+</sup>- and Yd<sup>3+</sup>- based ISs prepared by the sol-gel method provide a sustainable and viable approach towards ECD, LSC and LDS layers. Several materials science and materials engineering challenges were addressed over the course of this work to produce optical materials that absorb mostly in the UV spectral region (300-400 nm) and emit in the visible-NIR spectral regions. The structural, thermal and optical features of the films were characterized. The PMMA doped with Eu<sup>3+</sup>, Tb<sup>3+</sup>-based ISs produced exhibit encouraging results as LDS layers/LSCs since they present high optical efficiency. This is especially true in the case of the Eu<sup>3+</sup>-based material due to its high absolute emission quantum yield. Additionally, these materials allowed the combination of LDS layers and LSC into a single device by using edge-mounted PV cells to take advantage of the guided radiation in the LDS layers, increasing the electrical output of the system. An absolute increase in the EQE of ~32% between 300-360 nm was observed for the PV cell when compared to the bare PV cell, showing the effectivity of this new approach. These materials revealed appealing for LSCs, as transparent PV windows for urban integration of light harvesting devices, for future ZEBs and environment-resistant devices presenting lower toxicity when compared with QDs technology. Yet to make this technology competitive, additional improvements, such as excitation deviation towards the blue and quantum yield increase are needed in order to increase  $\eta_{opt}$  and the PCE values.

Here, we also verified that the combined use of a-IZO, a conducting oxide transparent in the visible and NIR spectral regions, and an organic-inorganic hybrid (d-U(2000), obtained by sol-gel chemistry) doped with an IL ([BIm][TfO]), allowed the production of an ECD with high visible and NIR transparency, and voltage-actuated dual coloration tuning, enabling three-mode operation (bright hot, semi-bright warm, and dark

cold). The ECD delivered a number of extraordinary features, in particular high switching efficiency, high optical modulation, good cycling stability and coloration efficiency values during bleaching and especially coloration, excellent optical memory, and unusual self-healing ability following mechanical stress. These properties make this ECD a good approach for smart windows requests in buildings located in continental climatic regions, characterized by large temperature range variations in a single day.

At last, we demonstrated the potential of the PMMA-based composites doped with the ISs in ECDs. A PMMA-based system doped with  $\text{Eu}^{3+}$ - and  $\text{Nd}^{3+}$ -based ISs plus the commercial IL [BMIm][PF<sub>6</sub>] was successfully employed as electrolyte in ECD anticipating application in ZEBs. The ECD, named ECD@PISIL, allowed to control simultaneously the incident solar visible and NIR radiation and also the radiation emitted (visible/NIR). The ECD demonstrated fast switching speed (> 50 s), high transparency in the visible and NIR spectral regions, and good stability over 200 cycles. Besides, the electrolyte exhibited emission in the visible and NIR regions of the spectra, correspondent to the emissions of IS-Eu and IS-Nd, respectively. The results obtained confirm the potential of this new approach for the construction of sustainable energy-efficient integrated devices since these transparent luminescent materials could work simultaneously as ECD/LSC/LDS layer for windows containing edge-mounted PV cells. With this technology, a multifunctional device comprising energy harvesting, energy generation, and energy management ability can be created. This study represents, obviously, the proof of concept and further studies are needed to demonstrate its overall performance.

New prospects of future work should involve the synthesis of efficient visible/NIR-emitting IS-Ln with a better matching to the c-Si bandgap. That should involve the increase of absolute emission quantum yield, especially in the case of IS-Nd and IS-Yb that could be achieved by using more suitable ligands for these lanthanides, as an alternative to  $\text{tta}^-$ . Similarly, other lanthanide ions, such as  $\text{Tm}^{3+}$  and  $\text{Er}^{3+}$ , should be tested to obtain different emission in the visible/NIR region of the spectra. In addition, the use of other organic-inorganic hybrids to host the IS-Ln offering transparency and flexibility should be considered. The self-healing feature found in the DUPIL<sub>60</sub> electrolyte is extremely appealing for a smart window, allowing to increase its durability.

Future work for ECD/LSC should also comprise the performance evaluation of the device in function of the layer's thickness in order to see how the parameters varies such conductivity, visible/NIR emission, colour efficiency, switching time.

## Appendix A – Structural and optical characterization

All the samples were characterized after the synthesis.

### *X-ray diffraction*

XRD patterns were recorded in the  $2\theta$  range spanning from 3 to 50 ° by using a PANalytical Empyrean diffractometer system under exposure of  $\text{CuK}\alpha$  radiation (1.54 Å) at room temperature. The spacing between planes in the atomic lattice ( $d$ ) was calculated using the Bragg's Law.

The spacing between planes in the atomic lattice ( $d$ ) is calculated using the Bragg's Law equation:

$$n\lambda = 2 d \sin\theta \quad (\text{A.1})$$

where  $n$  is an integer,  $\lambda$  is the X-ray wavelength and  $\theta$  is the diffraction angle in degrees.

The mean size of the ordered crystalline ( $D$ ) domains can be determined using the Debye-Scherrer equation.

$$D = \frac{K\lambda}{\beta \cos\theta} \quad (\text{A.2})$$

where  $K$  is the Scherrer constant (0.9),  $\beta$  is the fwhm(full-width-at-half-maximum) of the X-ray peak in radians,  $\lambda$  is the X-ray wavelength and  $\theta$  is the Bragg angle.

### *Fourier transform infrared spectroscopy*

Fourier transform infrared spectroscopy (FT-IR) is a widely technique used for the identification of functional groups in a material by irradiating the latter with IR radiation. For that, the material must be composed of IR active molecules that present a dipole moment ( $\text{H}_2\text{O}$ ,  $\text{SO}_2$ ,  $\text{NH}_3$ ). Symmetrical molecules (e.g.  $\text{H}_2$  and  $\text{O}_2$ ) do not absorb IR radiation, since they have zero dipole moment. Infrared (IR) spectroscopy consist in the measure of the IR radiation that was absorbed by each bond present in the molecule. The result is obtained as a spectrum designated as % transmittance (or absorbance) versus wavenumber ( $\text{cm}^{-1}$ ). It is important to note that since each bond owns a distinct natural vibrational frequency, a specific radiation (frequency) will be absorbed by a specific bond in a molecule. Even more, this specific radiation absorption is not affected by other bond.

So, IR spectroscopy stands as a powerful technique that delivers fingerprint information about the sample chemical composition and permits the measure of all sorts of samples: solids, liquids, and gases.

The IR region of the electromagnetic spectrum can be separated into three regions: near-IR (14000– 4000  $\text{cm}^{-1}$ ), mid-IR (4000–400  $\text{cm}^{-1}$ ), and far-IR (400–40  $\text{cm}^{-1}$ ). The mid-IR is the furthestmost region used for analysis since all molecules have primary molecular vibrations and specific absorbance frequencies in this range. As the sample is submitted to the IR radiation, particular wavelengths interact with the chemical bonds of the molecules present in the material to endure vibrations as contracting, stretching, and bending.

Spectral peaks are obtained as a consequence of the absorption of bond vibrational energy causing an association between IR band positions and the molecule chemical structures. The IR spectrum is obtained by calculating the background intensity ( $I_0$ ) and  $I$ , the sample intensity in the spectrum (**Equations A.3** and **A.4**). Besides qualitative information is also possible to obtain quantitative information. It is via a mathematical function named Fourier transform (FT) that the interferogram (intensity versus time spectrum) collected by the FT-IR equipment is converted into a IR spectrum (intensity versus frequency spectrum).<sup>266,267</sup>

**Table A.1.** Range in wavenumber ( $\text{cm}^{-1}$ ) of various functional groups.<sup>266</sup>

Range ( $\text{cm}^{-1}$ )	Functional group
3200–3550	O-H stretching
2500–3000	Carboxylic O-H
3300–3500	N-H stretch, primary amine gives two, secondary one, while tertiary amine gives no peak
3500–3500	O=C-N-H stretch
2260–2220	Nitrile (CN)
2950–2850	C-H stretch
3010–3100	=C-H stretch
1620–1680	C=C stretch
1740–1690	Aldehyde C=O
1750–1680	Ketone C=O
1750–1735	Ester C=O
1780–1710	Carboxylic acid C=O
1690–1630	Amide C=O
2800–2700	Aldehyde C-H stretch

For Chapter 3, the FT-IR spectra of the reagent compounds were acquired at room temperature using a Bruker IFS-66V Fourier transform spectrometer. The spectra were collected over the 4000–400  $\text{cm}^{-1}$  range by averaging at least 150 scans at a resolution of 2  $\text{cm}^{-1}$ . Solid samples (2 mg) were finely ground, mixed with approximately 175 mg of dried potassium bromide (Acros, spectroscopic grade) and pressed into pellets. Prior to recording the spectra, the discs were kept under vacuum at room temperature for several days in order to reduce the levels of adsorbed water. Liquid samples were recorded using NaCl cells. Attenuated Total Reflection (ATR)/FT-IR spectroscopy. ATR/FT-IR spectra were performed in IRAffinity-1S Fourier Transform Infrared Spectrophotometer Shimadzu with an ATR module and the LabSolutions IR 2.13 software. The spectra were recorded in the 4000-400  $\text{cm}^{-1}$  wavenumber range with 8  $\text{cm}^{-1}$  resolution and an average of 126 scans per sample.

For Chapter 5, the ATR/FT-IR spectra of the PMMA, IS-Eu, IS-Nd and PMMA/IS-Eu-1/IS-Nd-19/BMImPF<sub>6</sub>-X materials were performed in a Bruker Tensor 27 with a Specac Golden Gate (Diamond) ATR and the Opus 6.5 software. The spectra were recorded in the 4000-350  $\text{cm}^{-1}$  wavenumber range with 4  $\text{cm}^{-1}$  resolutions and an average of 256 scans per sample.

### *Absorption spectroscopy*

To calculate the absorbance (A) the following relation is used:

$$A = \log\left(\frac{I_0}{I}\right) \quad (\text{A.3})$$

where  $I_0$  is the incident intensity and  $I$  is the transmitted intensity by the material, respectively.

The Beer's law related the absorbance with the concentration of the species ( $c$ )

$$A = \epsilon lc \quad (\text{A.4})$$

where  $\epsilon$  is the molar absorptivity,  $l$  the path length and  $c$  the sample concentration.<sup>266,267</sup>

The UV/visible absorption spectra were recorded using a Lambda 950 dual-beam spectrometer (Perkin-Elmer). The molar extinction coefficient was calculated using Beer Lambert law, and the molar brightness ( $B$ )

$$B = \varepsilon \times q \quad (\text{A.5})$$

were calculated for the highest absorption wavelength.

### *Thermogravimetric Analysis*

Thermogravimetric Analysis (TGA) measurements were performed with a TGA-50 Shimadzu. A mass of 10.99 mg was placed in platinum cans. Each sample was heated from 22 to 800 °C at 10 °C·min<sup>-1</sup>. The purge gas used in all experiments was high purity nitrogen supplied at a constant 20 mL·min<sup>-1</sup> flow rate.

### *Differential Scanning Calorimetry (DSC)*

In Chapter 3 the differential Scanning Calorimetry (DSC) measurements were performed with a Perkin Elmer Diamond DSC. A mass of 4-5 mg was placed in 60 µL stainless steel cans. Each sample was heated from 0 to 200 °C at 10 °C·min<sup>-1</sup>. The purge gas used in all experiments was high purity nitrogen supplied at a constant 2 mL·min<sup>-1</sup> flow rate.

In Chapter 4 the DSC curves of the electrolytes were obtained with a DSC 204 Netzsch equipment. A mass of 7-10 mg was placed in a 40 µL aluminium pan and stored in a desiccator over P<sub>2</sub>O<sub>5</sub> for 1 week at room temperature under vacuum. After the drying treatment, the can was hermetically sealed and the thermogram was recorded. Each electrolyte sample was heated from 20-30 to 300 °C at 10 °C min<sup>-1</sup>. The purge gas was high purity nitrogen supplied at a constant 25 mL min<sup>-1</sup> flow rate.

In Chapter 5 the DSC database was recorded using a DSC Mettler Toledo 822/e equipment (Schwarzenbach, Switzerland), where the samples were placed in a 40 µL perforated aluminium pan. The samples were heated from 30 to 200 °C at 10 °C·min<sup>-1</sup> under a flowing argon atmosphere.

### *Scanning electronic microscopy (SEM)/Energy Dispersive X-ray spectroscopy (EDS)*

Scanning electronic microscopy (SEM) images were obtained at 20 kV on a Hitachi S-3400N type II microscope equipped with a Bruker x-flash 5010 at high vacuum. The samples were coated with gold. Elemental mapping analysis on microscopic sections of selected electrolytes were performed by Energy Dispersive X-ray spectroscopy (EDS). The acquisition time for satisfactory resolution and noise performance was 1-5 min.

### *Transmission Electron Microscopy (TEM)*

Transmission Electron Microscopy (TEM) micrographs were obtained using the Hitachi H9000 in microscope operating at 300 kV. The sample was dissolved in THF. Then one drop of this solution was put directly onto a 400 mesh copper grid coated with a carbon film.

### *Elemental analysis*

CHNS analysis was performed with a TruSpec 630-200-200 CNHS Analyser with an accuracy of 1% for each element.

### *Nuclear Magnetic Resonance (<sup>1</sup>H and <sup>13</sup>C)*

<sup>1</sup>H and <sup>13</sup>C NMR spectra were obtained using a Bruker ARX400 400 MHz spectrometer with DMSO as solvent. Chemical shifts ( $\delta$ ) are reported in parts per million (ppm) relative to tetramethylsilane (TMS) and splitting multiplicities are described as s = singlet; t = triplet; or m = multiplet.

### *Polarized optical microscopy (POM)*

Polarized optical microscopy (POM) images of the Eu-IS were recorded using an OPTIKA B-600POL microscope equipped with an 8 megapixel digital photo camera. The images were analysed using with the OPTIKA VISION PRO software.

### *Static Contact Angle*

Contact angles ( $\theta$ ) were measured at room temperature with ultra-pure distilled water using a Contact Angle OCAH 200 (DataPhysics Instruments) and SCRA-20 software. The samples were analysed as pellets. The volume of the liquid droplets was kept constant at 2  $\mu$ L. The  $\theta$  values were measured at three different spots and the results reported correspond to the average value of the three measurements. The error analysis of the data was implemented by arithmetic mean of the root mean square error.

### *Conductivity*

The ionic conductivity of the ormolytes was determined by complex impedance measurements. An ormolyte disk was placed between two 10 mm diameter ion blocking gold electrodes (Goodfellow, >99.9 %). The electrode/ormolyte/electrode assembly was secured in a suitable constant-volume support, which was installed in a Buchi TO 51 tube oven. A calibrated type K thermocouple, placed close to the ormolyte disk, was used to measure the sample temperature with a precision of about  $\pm 0.2$  °C and samples were characterized over a temperature range of between 20 and 170 °C. Bulk conductivities of the samples were obtained during heating cycles using the complex plane impedance technique (Autolab PGSTAT-12 (Eco Chemie)) over a frequency range of 65 kHz to 0.5 Hz. The electrolyte behaviour was found to be almost ideal and bulk conductivities were extracted in the conventional manner from impedance data by using an equivalent circuit composed of  $R_b$  in parallel with  $C_g$ , where  $R_b$  is the electrical resistance of the electrolyte and  $C_g$  is its geometric capacity. The circuit element corresponding to the blocking electrode interface was simulated by a series  $C_{dl}$  element, where  $C_{dl}$  is the double layer capacity.

### *Photoluminescence spectroscopy*

The term 'luminescence' was introduced for the first time by Wiedemann in 1888 and can be described as the emission of light by a material after the absorption of energy. Luminescence can have different excitation sources (e.g. X-rays and electromagnetic radiations) given origin to different categories usually designated by a prefix. In the photoluminescence case, the source are photons.

The efficiency of the luminescence can be rationalised based on the quantum efficiency, which may be expressed based on radiative and non-radiative processes. Whereas the radiative decay results in the emission of a photon, in a nonradiative process the excitation energy is lost (thermal radiation). In this simple case, the emission decays exponentially with a constant time:

$$\tau = \frac{1}{k_r + k_{nr}} \quad (\text{A.6})$$

where  $\tau$  is the emission lifetime. The quantum efficiency ( $\eta_{PL}$ ) is then can be obtained by:

$$\eta_{PL} = \frac{k_r}{k_r + k_{nr}} = \frac{\tau}{\tau_R} \quad (\text{A.7})$$

where,  $\tau_R = 1/k_r$  is the radiative lifetime.<sup>18</sup>

The absolute emission quantum yield ( $q$ ), defined as the ratio between the number of emitted photons to the number of absorbed ones:<sup>268</sup>

$$q = \frac{\# \text{ of emitted photons}}{\# \text{ of absorbed photons}} \quad (\text{A.8})$$

To experimentally determine  $q$ , special equipment is required (e.g. integrating spheres and scattering agents for system calibration).

## Appendix B – ECD characterization

The evaluation of an ECD is essential and must be done in a way to compare performances and, for that, different parameters must be taken into account. The switching time is one of the important parameters. Switching time or response time is defined as the time required to pass from the bleached to the coloured states. Depending on the ECD size, it can take from seconds to minutes and is also related to the applied voltage, thickness and ionic conductivity of the electrolyte, and ion diffusion, thickness and morphology of the EC layers.

The open circuit memory is defined as the capacity of a ECD to maintain the optical properties after the application of voltage. The longer the time when no voltage is applied, the better is the ECD in terms of this parameter. In addition, lifetime is a fundamental factor to allow the device to be commercially and economically available. The cycling life correspond to the number of cycles that an ECD can hold. Here, the reversibility of redox reaction interferes majorly since if the reactions are not balanced, the ECD performance is damaged. Some other parameters condition the ECD performance, such as structure and technique of films preparation, dimensions and type of ion conducting material.<sup>12</sup>

The transmittance change ( $\Delta T$ ) can be quantified as the difference between the transmittance measured at the bleached ( $T_b$ ) and coloured ( $T_c$ ) states, for a wavelength ( $\lambda$ )

$$\Delta T(\lambda) = T_b - T_c \quad (\text{B.1})$$

The ECD can suffer deterioration through the cycling process or as a result of high voltage application. The contrast ratio (CR) (**Equation B.2**) quantifies the colour change intensity, and is defined as the ratio between the transmittance in the bleached state ( $T_b$ ) and coloured state ( $T_c$ ).

$$CR(\lambda) = \frac{T_b}{T_c}(\lambda) \quad (\text{B.2})$$

The optical density (OD) (**Equation B.3**) is obtained from the logarithmic ratio between the transmittance ( $T$ ) in the bleached state and the coloured state of the ECD for a given wavelength:

$$\Delta OD(\lambda) = \log_{10} \left( \frac{T_b}{T_c} \right) (\lambda) \quad (\text{B.3})$$

The coloration efficiency (CE) (**Equation B.4**) is defined as the ratio of the change in OD ( $\Delta OD$ ) to inserted/extracted charge per unit area (Q) for a given wavelength

$$CE(\lambda) = \frac{\Delta OD(\lambda)}{Q} \quad (\text{B.4})$$

High coloration efficiency means that a large optical modulation is achieved with a small amount of inserted/extracted charge. In conclusion, several parameters must be taken into account for an ECD to work properly. In **Table B.1**, the parameters values requested for ECDs are shown.

**Table B.1** Requirements for ECDs.<sup>40,269</sup>

Parameters	Values
Bleached state solar/visible transmittance	$\leq 70\text{-}50\%$
Coloured state solar/visible transmittance	$\leq 20\text{-}10\%$
Switching voltage	$\leq 5 \text{ V}$
Switching time	$\leq 10 \text{ s to } 5 \text{ min}$
Open circuit memory	2-24 h
Cycling life	25 000-50 000 cycle / 20-30 year
Operating temperature	-30 to 90°C

In **Chapter 4**, the optical transmittance of the ECD was measured in the 400–1020 nm range using a DH Mini, UV–vis–NIR Lightsource Ocean Optics. The cyclic voltammetry (CV) and chronoamperometry (CA) tests were carried out using an Autolab 302 N model potentiostat/galvanostat. In the setup used for measurements, the a-WO<sub>3</sub>/a-IZO substrate played the role of working electrode, the electrolyte acted as a reservoir of ions for insertion, and the c-NiO/a-IZO substrate acted as counter and reference electrodes. The cathodic and anodic charge densities were determined through integration of the CA curves during the colouring and bleaching processes, respectively. The Commission Internationale d'Éclairage (CIE) 1976 L\*a\*b\* colour space ECD coordinates were obtained with a Chroma Meter CR-300 Minolta (Osaka, Japan). The L\*, a\*, and b\* parameters (L\* is the lightness, a\* represents the green–red component, and b\* represents the blue–yellow component) were calculated from the average values obtained from three measurements with a standard deviation below 2%.

In **Chapter 5**, the ECDs optical transmittance was measured in the 350–1650 nm range using a DH Mini, UV–vis–NIR Lightsource Ocean Optics and deuterium and halogen lamps. The CA tests were carried out using a Gamry potentiostat/galvanostat ZRA 11107. In the setup used for measurements, the a-WO<sub>3</sub>/a-IZO substrate played the role of working electrode, the electrolyte acted as a reservoir of ions for insertion, and the c-NiO/a-IZO substrate acted as counter and reference electrodes. The cathodic and anodic charge densities were obtained through the CA curves integration during the colouring and bleaching processes, respectively and CV was performed at a scan rate of 50 mV s<sup>-1</sup>.

The CIE 1976 L\*a\*b\* colour space ECD coordinates were obtained in the same device, where L\*, a\*, and b\* parameters were calculated from the average values obtained from three independent measurements in different places of the window.

## Appendix C – List of publications

1. M. A. Cardoso, H. M. R. Gonçalves, R. F. P. Pereira, M. M. Silva, S. Pereira, E. Fortunato, M. T. Gonçalves, A. J. M. Valente, R.A.S. Ferreira, V. de Zea Bermudez, Solar spectral management with electrochromic devices including PMMA films doped with lanthanide-doped ionosilicas, *paper in preparation*
2. M. A. Cardoso, S. F. H. Correia, A. R. Frias, H. M. R. Gonçalves, R. F. P. Pereira, S. C. Nunes, M. Armand, P. S. André, V. de Zea Bermudez, R.A.S. Ferreira, Solar spectral conversion based on plastic films of lanthanide-doped ionosilicas for photovoltaics: down-shifting layers and luminescent solar concentrators, *Journal of Rare Earths*, 38(5) (2020) 531
3. A. R. Frias, M. A. Cardoso, A. R. N. Bastos, S. F. H. Correia, P. S. André, L. D. Carlos, V. de Zea Bermudez, R. A. S. Ferreira, Transparent luminescent solar concentrators using Ln<sup>3+</sup>-based ionosilicas towards photovoltaic windows, *Energies*, 12(3) (2019) 451
4. M. A. Cardoso, R. F. P. Pereira, S. Pereira, H. Gonçalves, M. M. Silva, L. D. Carlos, S. C. Nunes, E. Fortunato, R. A. S. Ferreira, R. Rego, V. de Zea Bermudez, Three-mode modulation electrochromic device with high energy efficiency for windows of buildings located in continental climatic regions, *Adv. Sustainable Syst.* 3 (3) (2019) 1800115
5. R. P. Pereira, S. C. Nunes, G. Toquer, M. A. Cardoso, A. J. M. Valente, M. M. Silva, L. D. Carlos, R. A. S. Ferreira, V. de Zea Bermudez, Novel highly luminescent amine-functionalized bridged silsesquioxanes, *Frontiers in Chemistry - Inorganic Chemistry*, 5(131) (2018)
6. M. Fernandes, M. A. Cardoso, L. C. Rodrigues, M. M. Silva, R. A. S. Ferreira, L. D. Carlos, S.C. Nunes, V. de Zea Bermudez, d-Poly(epsilon-caprolactone)(530)/siloxane biohybrid films doped with protic ionic liquids, *Journal of Electroanalytical Chemistry*, 799 (2017) 249

## REFERENCES

- 1 C. G. Granqvist, M. A. Arvizu, Bayrak Pehlivan, H. Y. Qu, R. T. Wen and G. A. Niklasson, *Electrochim. Acta*, 2018, **259**, 1170–1182.
- 2 *World Energy Assessment Report: Energy and the Challenge of Sustainability*, United Nations, New York (USA), 2000.
- 3 World Energy Outlook (2018); International Energy Agency (2018).
- 4 L. Belussi, B. Barozzi, A. Bellazzi, L. Danza, A. Devitofrancesco, C. Fanciulli, M. Ghellere, G. Guazzi, I. Meroni, F. Salamone, F. Scamoni and C. Scrosati, *J. Build. Eng.*, 2019, **25**, 100772.
- 5 *Transition to Sustainable Buildings*, OECD/IEA, Paris, France, 2013.
- 6 C. G. Granqvist, *Mater. Today Proc.*, 2016, **3**, S2–S11.
- 7 2010 Energy Performance of Buildings Directive (EPBD), <https://eur-lex.europa.eu/eli/dir/2010/31/oj>, (accessed 10 February 2020).
- 8 2012 Energy Efficiency Directive, <https://eur-lex.europa.eu/legal-content/EN/TXT/?uri=celex%3A32012L0027>, (accessed 10 February 2020).
- 9 Directive (UE) 2018/844, [https://eur-lex.europa.eu/legal-content/EN/TXT/?uri=uriserv%3AOJ.L\\_.2018.156.01.0075.01.ENG](https://eur-lex.europa.eu/legal-content/EN/TXT/?uri=uriserv%3AOJ.L_.2018.156.01.0075.01.ENG), (accessed 10 February 2020).
- 10 Sustainable Development Goals, <https://sustainabledevelopment.un.org/?menu=1300>, (accessed 10 February 2020).
- 11 B. P. Jelle, A. Hynd, A. Gustavsen, D. Arasteh, H. Goudey and R. Hart, *Sol. Energy Mater. Sol. Cells*, 2012, **96**, 1–28.
- 12 R. J. Mortimer, D. R. Rosseinsky and P. M. S. Monk, *Electrochromic Materials and Devices*, Wiley-VCH Verlag GmbH & Co. KGaA, Weinheim, Germany, 2013.
- 13 R. T. Wen, M. A. Arvizu, G. A. Niklasson and C. G. Granqvist, *Surf. Coatings Technol.*, 2016, **290**, 135–139.
- 14 C. G. Granqvist and G. A. Niklasson, *Sol. Energy Mater. Sol. Cells*, 2018, **180**, 213–226.
- 15 H. Khandelwal, A. P. H. J. Schenning and M. G. Debije, *Adv. Energy Mater.*, , DOI:10.1002/aenm.201602209.
- 16 *Solar Generation 6: Solar Photovoltaic Electricity Empowering the World*, 2011.

- 17 R. A. S. Ferreira, S. F. H. Correia, A. Monguzzi, X. Liu and F. Meinardi, *Mater. Today*, 2020, **33**, 105–121.
- 18 X. Huang, S. Han, W. Huang and X. Liu, *Chem. Soc. Rev.*, 2013, **42**, 173–201.
- 19 M. G. Debije and V. A. Rajkumar, *Sol. Energy*, 2015, **122**, 334–340.
- 20 W. H. Weber and J. Lambe, *Appl. Opt.*, 1976, **15**, 2299–2300.
- 21 R. Reisfeld and S. Neuman, *Nature*, 1978, **274**, 144–145.
- 22 F. Meinardi, F. Bruni and S. Brovelli, *Nat. Rev. Mater.*, 2017, **2**, 17072.
- 23 A. R. Frias, University of Aveiro, 2019.
- 24 Glass to Power, <https://www.glasstopower.com/>, (accessed 19 December 2020).
- 25 UbiQD - Ubiquitous Quantum Dots, <https://ubiqd.com/>, (accessed 19 December 2020).
- 26 N. C. Davy, M. Sezen-Edmonds, J. Gao, X. Lin, A. Liu, N. Yao, A. Kahn and Y.-L. Loo, *Nat. Energy*, 2017, **2**, 17104.
- 27 D. J. Milliron, *Nat. Energy*, 2017, **2**, 17116.
- 28 V. K. Thakur, G. Ding, J. Ma, P. S. Lee and X. Lu, *Adv. Mater.*, 2012, **24**, 4071–4096.
- 29 Y. Alesanco, A. Viñuales, J. Rodriguez and R. Tena-Zaera, *Materials (Basel)*, 2018, **11**, 1–27.
- 30 H. Fang, P. Zheng, R. Ma, C. Xu, G. Yang, Q. Wang and H. Wang, *Mater. Horizons*, 2018, **5**, 1000–1007.
- 31 P. Yang, P. Sun and W. Mai, *Mater. Today*, 2016, **19**, 394–402.
- 32 R. Jedinák, *Adv. Mater. Res.*, 2013, **855**, 39–42.
- 33 N. Aste, J. Compostella and M. Mazzon, *Energy Procedia*, 2012, **30**, 404–413.
- 34 M. Casini, *Renew. Energy*, 2018, **119**, 923–934.
- 35 C. G. Granqvist, *Thin Solid Films*, 2016, **614**, 90–96.
- 36 R. T. Wen, M. A. Arvizu, G. A. Niklasson and C. G. Granqvist, *Surf. Coatings Technol.*, 2016, **290**, 135–139.
- 37 B. S. Geoffrey and C. G. Granqvist, *GREEN NANOTECHNOLOGY: Solutions for Sustainability and Energy in the Built Environment*, Taylor and Francis Group, 2011.
- 38 R. Sullivan, E. S. Lee, K. Papamichael, M. Rubin and S. E. Selkowitz, in *Optical Materials Technology for Energy Efficiency and Solar Energy Conversion XIII*, 1994, vol. 2255, pp. 443–455.
- 39 M. Barawi, G. Veramonti, M. Epifani, R. Giannuzzi, T. Sibillano, C. Giannini, A.

- Rougier and M. Manca, *J. Mater. Chem. A*, 2018, **6**, 10201–10205.
- 40 R. Baetens, B. P. Jelle and A. Gustavsen, *Sol. Energy Mater. Sol. Cells*, 2010, **94**, 87–105.
- 41 C. M. Lampert, A. Agrawal, C. Baertlien and J. Nagai, *Sol. Energy Mater. Sol. Cells*, 1999, **56**, 449–463.
- 42 J. Livage and D. Ganguli, *Sol. Energy Mater. Sol. Cells*, 2001, **68**, 365–381.
- 43 R. J. Mortimer, *Annu. Rev. Mater. Res.*, 2011, **41**, 241–268.
- 44 B. Orel, U. Opara Krašovec, U. Lavrenčič Štangar and P. Judeinstein, *J. Sol-Gel Sci. Technol.*, 1998, **11**, 87–104.
- 45 M. A. Macêdo and M. A. Aegerter, *J. Sol-Gel Sci. Technol.*, 1994, **2**, 667–671.
- 46 C. Sanchez, P. Belleville, M. Popall and L. Nicole, *Chem. Soc. Rev.*, 2011, **40**, 696.
- 47 W. R. Lian, Y. C. Huang, Y. A. Liao, K. L. Wang, L. J. Li, C. Y. Su, D. J. Liaw, K. R. Lee and J. Y. Lai, *Macromolecules*, 2011, **44**, 9550–9555.
- 48 C. Ma, M. Taya and C. Xu, *Electrochim. Acta*, 2008, **54**, 598–605.
- 49 A. Califórnia, A. S. Silva, J. Gonçalves, A. Branco, C. Pinheiro and C. Costa, *Sol. Energy Mater. Sol. Cells*, 2016, **153**, 61–67.
- 50 C. G. Granqvist, *Switchable glazing technology for eco-efficient construction*, 2013.
- 51 B. Deng, P. C. Hsu, G. Chen, B. N. Chandrashekar, L. Liao, Z. Ayitimuda, J. Wu, Y. Guo, L. Lin, Y. Zhou, M. Aisijiang, Q. Xie, Y. Cui, Z. Liu and H. Peng, *Nano Lett.*, 2015, **15**, 4206–4213.
- 52 C. J. Tang, J. M. Ye, Y. T. Yang and J. L. He, *Opt. Mater. (Amst.)*, 2016, **55**, 83–89.
- 53 C. M. White, D. T. Gillaspie, E. Whitney, S. H. Lee and A. C. Dillon, *Thin Solid Films*, 2009, **517**, 3596–3599.
- 54 D. Mecerreyes, R. Marcilla, E. Ochoteco, H. Grande, J. A. Pomposo, R. Vergaz and J. M. Sánchez Pena, *Electrochim. Acta*, 2004, **49**, 3555–3559.
- 55 A. A. Argun, A. Cirpan and J. R. Reynolds, *Adv. Mater.*, 2003, **15**, 1338–1341.
- 56 Z. D. Marks, D. Glugla, J. T. Friedlein, S. E. Shaheen, R. R. McLeod, M. Y. Kahook and D. P. Nair, *Org. Electron. physics, Mater. Appl.*, 2016, **37**, 271–279.
- 57 N. Sarmadian, R. Saniz, B. Partoens and D. Lamoen, *Sci. Rep.*, 2016, **6**, 1–9.
- 58 G. Gonçalves, P. Barquinha, L. Raniero, R. Martins and E. Fortunato, *Thin Solid Films*, 2008, **516**, 1374–1376.

- 59 L. Znaidi, *Mater. Sci. Eng. B Solid-State Mater. Adv. Technol.*, 2010, **174**, 18–30.
- 60 P. Barbosa, L. Rodrigues, M. Silva, M. Smith, A. Gonçalves and E. Fortunato, *J. Mater. Chem.*, 2010, **20**, 723–730.
- 61 L. Yue, J. Ma, J. Zhang, J. Zhao, S. Dong, Z. Liu, G. Cui and L. Chen, *Energy Storage Mater.*, 2016, **5**, 139–164.
- 62 P. M. S. Monk, R. J. Mortimer and D. R. Rosseinsky, *Electrochromism : fundamentals and applications*, 1995.
- 63 M. B. Armand, J. M. Chabagno and M. J. Duclot, *Fast Ion Transp. Solids*.
- 64 F. M. Gray, *Solid Polymer Electrolytes: Fundamentals and Technological Applications*, VCH, 1991.
- 65 P. C. Barbosa, M. M. Silva, M. J. Smith, A. Gonçalves and E. Fortunato, *Electrochim. Acta*, 2007, **52**, 2938–2943.
- 66 P. M. Beaujuge and J. R. Reynolds, 2010, 268–320.
- 67 C. H. Yang, L. R. Huang, Y. K. Chih and S. L. Chung, *J. Phys. Chem. C*, 2007, **111**, 3786–3794.
- 68 H. J. Byker, *Electrochim. Acta*, 2001, **46**, 2015–2022.
- 69 M. A. Cardoso, R. Leones, L. C. Rodrigues, M. Fernandes, F. L. Figueiredo, S. C. Nunes, M. M. Silva and V. deZeaBermudez, *ChemElectroChem*, 2016, **3**, 783–789.
- 70 M. A. Cardoso, R. F. P. Pereira, S. Pereira, H. Gonçalves, M. M. Silva, L. D. Carlos, S. C. Nunes, E. Fortunato, R. A. S. Ferreira, R. Rego and V. de Zea Bermudez, *Adv. Sustain. Syst.*, 2019, **3**, 1970007.
- 71 M. A. Cardoso, M. Fernandes, L. C. Rodrigues, R. Leones, M. M. Silva and V. De Zea Bermudez, *Electrochim. Acta*, 2014, **147**, 288–293.
- 72 Y. Charbouillot, D. Ravaine, M. Armand and C. Poinignon, *J. Non. Cryst. Solids*, 1988, **103**, 325–330.
- 73 P. Judeinstein, J. Livage, A. Zarudiansky and R. Rose, *Solid State Ionics*, 1988, **28**, 1722–1725.
- 74 D. Kéomany, C. Poinignon and D. Deroo, *Sol. Energy Mater. Sol. Cells*, 1994, **33**, 429–441.
- 75 J. Le Bideau, L. Viau and A. Vioux, *Chem. Soc. Rev.*, 2011, **40**, 907–925.
- 76 R. D. Rogers and K. R. Seddon, *Science (80-. )*, 2003, **302**, 792–793.
- 77 H. Ohno, *Electrochemical aspects of ionic liquids*, Wiley-Interscience, 2005.
- 78 M. Fernandes, V. Freitas, S. Pereira, R. Leones, M. Silva, L. Carlos, E.

- Fortunato, R. A. S. Ferreira, R. Rego and V. de Zea Bermudez, *Energies*, 2018, **11**, 3513.
- 79 M. Fernandes, A. M. P. Botas, R. Leones, S. Pereira, M. M. Silva, R. S. Ferreira, L. D. Carlos, E. Fortunato, R. Rego and V. de Zea Bermudez, *ECS Trans.*, 2014, **61**, 213–225.
- 80 S. F. H. Correia, P. P. Lima, E. Pecoraro, S. J. L. Ribeiro, P. S. André, R. A. S. Ferreira and L. D. Carlos, *Prog. Photovoltaics Res. Appl.*, 2016, **24**, 1178–1193.
- 81 M. Fernandes, S. S. Nobre, L. C. Rodrigues, A. Gonçalves, R. Rego, M. C. Oliveira, R. A. S. Ferreira, E. Fortunato, M. M. Silva, L. D. Carlos and V. D. Z. Bermudez, *ACS Appl. Mater. Interfaces*, 2011, **3**, 2953–2965.
- 82 M. Fernandes, V. T. Freitas, S. Pereira, E. Fortunato, R. A. S. Ferreira, L. D. Carlos, R. Rego and V. De Zea Bermudez, *Sol. Energy Mater. Sol. Cells*, 2014, **123**, 203–210.
- 83 A. Pennisi, F. Simone, G. Barletta, G. Di Marco and M. Lanza, *Electrochim. Acta*, 1999, **44**, 3237–3243.
- 84 R. Lechner and L. K. Thomas, *Sol. Energy Mater. Sol. Cells*, 1998, **54**, 139–146.
- 85 C. G. Granqvist, E. Avendaño and A. Azens, *Thin Solid Films*, 2003, **442**, 201–211.
- 86 W. Chen, C. Zhu, L. Guo, M. Y. Yan, L. Wu, B. Zhu, C. Qi, S. Liu, H. Zhang and Y. Peng, *J. Mater. Chem. C*, 2019, **7**, 3744–3750.
- 87 W. Cheng, M. Moreno-Gonzalez, K. Hu, C. Krzyszkowski, D. J. Dvorak, D. M. Weekes, B. Tam and C. P. Berlinguette, *iScience*, 2018, **10**, 80–86.
- 88 S. C. Nunes, S. M. Saraiva, R. F. P. Pereira, S. Pereira, M. M. Silva, L. D. Carlos, E. Fortunato, R. A. S. Ferreira, R. Rego and V. De Zea Bermudez, *ACS Appl. Energy Mater.*, 2019, **2**, 1951–1960.
- 89 R. Ramadan, H. Kamal, H. M. Hashem and K. Abdel-Hady, *Sol. Energy Mater. Sol. Cells*, 2014, **127**, 147–156.
- 90 D. Dong, W. Wang, A. Rougier, G. Dong, M. Da Rocha, L. Presmanes, K. Zrikem, G. Song, X. Diao and A. Barnabé, *Nanoscale*, 2018, **10**, 16521–16530.
- 91 L. Kullman, A. Azens, G. Vaivars and C. . Granqvist, *Sol. Energy*, 2000, **68**, 517–522.
- 92 A. Azens, *Solid State Ionics*, 1998, **113–115**, 449–456.
- 93 F. Meinardi, S. Ehrenberg, L. Dharmo, F. Carulli, M. Mauri, F. Bruni, R. Simonutti, U. Kortshagen and S. Brovelli, *Nat. Photonics*, 2017, **11**, 177–185.

- 94 E. Klampaftis, D. Ross, K. R. McIntosh and B. S. Richards, *Sol. Energy Mater. Sol. Cells*, 2009, **93**, 1182–1194.
- 95 Y. Zhou, D. Benetti, Z. Fan, H. Zhao, D. Ma, A. O. Govorov, A. Vomiero and F. Rosei, *Adv. Energy Mater.*, 2016, **6**, 1501913.
- 96 E. Klampaftis, M. Congiu, N. Robertson and B. S. Richards, *IEEE J. Photovoltaics*, 2011, **1**, 29–36.
- 97 M. J. Currie, J. K. Mapel, T. D. Heidel, S. Goffri and M. A. Baldo, *Science (80-. )*, 2008, **321**, 226–228.
- 98 A. Frias, M. Cardoso, A. Bastos, S. Correia, P. André, L. Carlos, V. de Zea Bermudez and R. Ferreira, *Energies*, 2019, **12**, 451.
- 99 S. F. H. Correia, A. R. Frias, L. Fu, R. Rondão, E. Pecoraro, S. J. L. Ribeiro, P. S. André, R. A. S. Ferreira and L. D. Carlos, *Adv. Sustain. Syst.*, 2018, **2**, 1800002.
- 100 J. Liu, K. Wang, W. Zheng, W. Huang, C.-H. Li and X.-Z. You, *Prog. Photovoltaics Res. Appl.*, 2013, **21**, 668–675.
- 101 X. Yang, J. Chen, S. Zheng and C. Chen, *J. Rare Earths*, 2020, **38**, 1158–1164.
- 102 L. D. Carlos, R. A. S. Ferreira, V. De Zea Bermudez and S. J. L. Ribeiro, *Adv. Mater.*, 2009, **21**, 509–534.
- 103 P. Moraitis, R. E. I. Schropp and W. G. J. H. M. van Sark, *Opt. Mater. (Amst.)*, 2018, **84**, 636–645.
- 104 F. Meinardi, A. Colombo, K. A. Velizhanin, R. Simonutti, M. Lorenzon, L. Beverina, R. Viswanatha, V. I. Klimov and S. Brovelli, *Nat. Photonics*, 2014, **8**, 392–399.
- 105 B. Zhang, P. Zhao, L. J. Wilson, J. Subbiah, H. Yang, P. Mulvaney, D. J. Jones, K. P. Ghiggino and W. W. H. Wong, *ACS Energy Lett.*, 2019, **4**, 1839–1844.
- 106 F. Meinardi, H. McDaniel, F. Carulli, A. Colombo, K. A. Velizhanin, N. S. Makarov, R. Simonutti, V. I. Klimov and S. Brovelli, *Nat. Nanotechnol.*, 2015, **10**, 878–885.
- 107 D. Yang, H. Liang, Y. Liu, M. Hou, L. Kan, Y. Yang and Z. Zang, *Dalt. Trans.*, 2020, **49**, 4725–4731.
- 108 S. F. H. Correia, A. R. N. Bastos, L. Fu, L. D. Carlos and P. S. André, Rute A. S. Ferreira, *Opto-Electronic Adv.*, 2019, **2**, 19000601–19000608.
- 109 D. Alonso-Álvarez, D. Ross, E. Klampaftis, K. R. McIntosh, S. Jia, P. Storiz, T. Stolz and B. S. Richards, *Prog. Photovoltaics Res. Appl.*, 2015, **23**, 479–497.
- 110 T. Fix, A. Nonat, D. Imbert, S. Di Pietro, M. Mazzanti, A. Slaoui and L. J.

- Charbonnière, *Prog. Photovoltaics Res. Appl.*, 2016, **24**, 1251–1260.
- 111 W. J. Ho, S. K. Feng, J. J. Liu, Y. C. Yang and C. H. Ho, *Appl. Surf. Sci.*, 2018, **439**, 868–875.
- 112 W. J. Ho, B. J. You, J. J. Liu, W. Bin Bai, H. J. Syu and C. F. Lin, *Materials (Basel)*, , DOI:10.3390/ma11050845.
- 113 W. J. Ho, Y. J. Deng, J. J. Liu, S. K. Feng and J. C. Lin, *Materials (Basel)*, , DOI:10.3390/ma10010021.
- 114 W. J. Ho, Y. T. Shen, J. J. Liu, B. J. You and C. H. Ho, *Nanomaterials*, , DOI:10.3390/nano7100340.
- 115 A. Le Donne, M. Dilda, M. Crippa, M. Acciarri and S. Binetti, *Opt. Mater. (Amst)*, 2011, **33**, 1012–1014.
- 116 A. Le Donne, M. Acciarri, D. Narducci, S. Marchionna and S. Binetti, *Prog. Photovoltaics Res. Appl.*, 2009, **17**, 519–525.
- 117 W. Bin Hung, J. Y. Chen, K. W. Sung and T. M. Chen, *J. Ceram. Process. Res.*, 2014, **15**, 157–161.
- 118 J.-Y. Chen, C. K. Huang, W. B. Hung, K. W. Sun and T. M. Chen, *Sol. Energy Mater. Sol. Cells*, 2014, **120**, 168–174.
- 119 W.-B. Hung and T.-M. Chen, *Sol. Energy Mater. Sol. Cells*, 2015, **133**, 39–47.
- 120 P. Song, C. Zhang and P. Zhu, *J. Alloys Compd.*, 2016, **661**, 14–19.
- 121 G. Griffini, F. Bella, F. Nisic, C. Dragonetti, D. Roberto, M. Levi, R. Bongiovanni and S. Turri, *Adv. Energy Mater.*, 2015, **5**, 1401312.
- 122 Z. Hosseini, W.-K. Huang, C.-M. Tsai, T.-M. Chen, N. Taghavinia and E. W.-G. Diau, *ACS Appl. Mater. Interfaces*, 2013, **5**, 5397–5402.
- 123 J. Liu, Q. Yao and Y. Li, *Appl. Phys. Lett.*, 2006, **88**, 173119.
- 124 N. Chander, A. F. Khan, P. S. Chandrasekhar, E. Thouti, S. K. Swami, V. Dutta and V. K. Komarala, *Appl. Phys. Lett.*, , DOI:10.1063/1.4891181.
- 125 X. Hou, T. Xuan, H. Sun, X. Chen, H. Li and L. Pan, *Sol. Energy Mater. Sol. Cells*, 2016, **149**, 121–127.
- 126 V. T. Freitas, L. S. Fu, A. M. Cojocariu, X. Cattoen, J. R. Bartlett, R. Le Parc, J. L. Bantignies, M. W. C. Man, P. S. Andre, R. A. S. Ferreira and L. D. Carlos, *ACS Appl. Mater. Interfaces*, 2015, **7**, 8770–8778.
- 127 V. Misra and H. Mishra, *J. Chem. Phys.*, 2008, **128**, 244701.
- 128 J. Graffion, X. Cattoën, M. Wong Chi Man, V. R. Fernandes, P. S. André, R. A. S. Ferreira and L. D. Carlos, *Chem. Mater.*, 2011, **23**, 4773–4782.

- 129 J. Graffion, A. M. Cojocariu, X. Cattoën, R. A. S. Ferreira, V. R. Fernandes, P. S. André, L. D. Carlos, M. Wong Chi Man and J. R. Bartlett, *J. Mater. Chem.*, 2012, **22**, 13279–13285.
- 130 M. M. Nolasco, P. M. Vaz, V. T. Freitas, P. P. Lima, P. S. André, R. A. S. Ferreira, P. D. Vaz, P. Ribeiro-Claro and L. D. Carlos, *J. Mater. Chem. A*, 2013, **1**, 7339–7350.
- 131 F. Meinardi, A. Colombo, K. A. Velizhanin, R. Simonutti, M. Lorenzon, L. Beverina, R. Viswanatha, V. I. Klimov and S. Brovelli, *Nat. Photonics*, 2014, **8**, 392–399.
- 132 J. L. Banal, J. M. White, K. P. Ghiggino and W. W. H. Wong, *Sci. Rep.*, 2015, **4**, 4635.
- 133 S. F. H. Correia, V. de Zea Bermudez, S. J. L. Ribeiro, P. S. André, R. A. S. Ferreira and L. D. Carlos, *J. Mater. Chem. A*, 2014, **2**, 5580–5596.
- 134 V. Kataria and D. S. Mehta, *J. Rare Earths*, DOI:10.1016/j.jre.2020.09.021.
- 135 X. Wang, T. Wang, X. Tian, L. Wang, W. Wu, Y. Luo and Q. Zhang, *Sol. Energy*, 2011, **85**, 2179–2184.
- 136 T. Wang, J. Zhang, W. Ma, Y. Luo, L. Wang, Z. Hu, W. Wu, X. Wang, G. Zou and Q. Zhang, *Sol. Energy*, 2011, **85**, 2571–2579.
- 137 R. Rondão, A. R. Frias, S. F. H. Correia, L. Fu, V. De Zea Bermudez, P. S. André, R. A. S. Ferreira and L. D. Carlos, *ACS Appl. Mater. Interfaces*, 2017, **9**, 12540–12546.
- 138 A. R. Frias, E. Pecoraro, S. F. H. Correia, L. M. G. Minas, A. R. Bastos, S. García-Revilla, R. Balda, S. J. L. Ribeiro, P. S. André, L. D. Carlos and R. A. S. Ferreira, *J. Mater. Chem. A*, 2018, **6**, 8712–8723.
- 139 A. R. Frias, S. F. H. Correia, M. Martins, S. P. M. Ventura, E. Pecoraro, S. J. L. Ribeiro, P. S. André, R. A. S. Ferreira, J. A. P. Coutinho and L. D. Carlos, *Adv. Sustain. Syst.*, 2019, **3**, 1800134.
- 140 J. L. Banal, J. M. White, T. W. Lam, A. W. Blakers, K. P. Ghiggino and W. W. H. Wong, *Adv. Energy Mater.*, 2015, **5**, 1500818.
- 141 R. Reisfeld, D. Shamrakov and C. Jorgensen, *Sol. Energy Mater. Sol. Cells*, 1994, **33**, 417–427.
- 142 Y. Zhao and R. R. Lunt, *Adv. Energy Mater.*, 2013, **3**, 1143–1148.
- 143 B. V. G. Mohan, K. Muniasamy, S. Karaznov, A. Robson Benjamin and V. Veerapandy, *Mater. Today Proc.*, 2020, **33**, 2503–2511.

- 144 G. Griffini, M. Levi and S. Turri, *Sol. Energy Mater. Sol. Cells*, 2013, **118**, 36–42.
- 145 D. Levy and M. Zayat, *The Sol-Gel Handbook*, Wiley-VCH Verlag GmbH & Co. KGaA, 2015.
- 146 J. Livage, in *Sol-Gel Technologies for Glass Producers and Users*, Springer Science+Business Media New, New York, 2004, pp. 1–2.
- 147 Y. Dimitriev, Y. Ivanova and R. Iordanova, *J Univ Chem Technol Metall.*, 2008, **43**, 181–192.
- 148 C. A. Milea, C. Bogatu and A. Duta, *Eng. Sci.*, 2011, **4(53)**, 59–66.
- 149 U. Schubert, in *The Sol-Gel Handbook*, Wiley-VCH Verlag GmbH & Co. KGaA, Weinheim, Germany, 2015, pp. 1–28.
- 150 S. Esposito, *Materials (Basel)*, 2019, **12**, 668.
- 151 M. N. Rahaman, *Ceramic Processing and Sintering*, CRC Press, 2017.
- 152 J. E. Mark, 1989, pp. 47–68.
- 153 H. K. Schmidt, E. Geiter, M. Mennig, H. Krug, C. Becker and R. P. Winkler, *J. Sol-Gel Sci. Technol.*, 1998, **13**, 397–404.
- 154 C. J. Barbé, D. J. Cassidy, G. Triani, B. A. Latella, D. R. G. Mitchell, K. S. Finnie, K. Short, J. R. Bartlett, J. L. Woolfrey and G. A. Collins, *Thin Solid Films*, 2005, **488**, 153–159.
- 155 M. V. Landau, in *Handbook of Heterogeneous Catalysis*, 2008, pp. 119–160.
- 156 A. E. Danks, S. R. Hall and Z. Schnepp, *Mater. Horizons*, 2016, **3**, 91–112.
- 157 C. J. Brinker and G. W. Scherer, *Sol-Gel Science: The Physics and Chemistry of Sol-Gel Processing*, 2013.
- 158 F. Branda, in *Advances in Nanocomposites - Synthesis, Characterization and Industrial Applications*, InTech, 2011.
- 159 H. E. Bergna and W. O. Roberts, *Colloid. Silica Fundam. Appl.*, 2005, 1–897.
- 160 M. Nouri-Khezrabad, M. A. L. Braulio, V. C. Pandolfelli, F. Golestani-Fard and H. R. Rezaie, *Ceram. Int.*, 2013, **39**, 3479–3497.
- 161 M. Jokinen, E. Györvary and J. B. Rosenholm, *Colloids Surfaces A Physicochem. Eng. Asp.*, 1998, **141**, 205–216.
- 162 E. J. T. Stefurak, D. R. Lowe, D. Zentner and W. W. Fischer, *Bull. Geol. Soc. Am.*, 2015, **127**, 1090–1107.
- 163 J. Estella, J. C. Echeverría, M. Laguna and J. J. Garrido, *Microporous Mesoporous Mater.*, 2007, **102**, 274–282.

- 164 S. H. Mir, L. A. Nagahara, T. Thundat, P. Mokarian-Tabari, H. Furukawa and A. Khosla, *J. Electrochem. Soc.*, 2018, **165**, B3137–B3156.
- 165 G. Kickelbick and Editor, *Hybrid Materials: Synthesis, Characterization, and Applications*, 2007.
- 166 J. Feng and H. Zhang, *Chem. Soc. Rev.*, 2013, **42**, 387–410.
- 167 V. T. Freitas, P. P. Lima, R. A. S. Ferreira, E. Pecoraro, M. Fernandes, V. De Zea Bermudez and L. D. Carlos, *J. Sol-Gel Sci. Technol.*, 2013, **65**, 83–92.
- 168 S. C. Nunes, V. De Zea Bermudez, M. M. Silva, M. J. Smith, D. Ostrovskii, R. A. Sá Ferreira, L. D. Carlos, J. Rocha, A. Goncalves and E. Fortunato, *J. Mater. Chem.*, 2007, **17**, 4239–4248.
- 169 V. de Zea Bermudez, L. D. Carlos and L. Alcácer, *Chem. Mater.*, 1999, **11**, 569–580.
- 170 V. T. Freitas, P. P. Lima, R. A. S. Ferreira, L. D. Carlos, E. Pecoraro, S. J. L. Ribeiro and V. De Zea Bermudez, *J. Sol-Gel Sci. Technol.*, 2014, **70**, 227–235.
- 171 M. Fernandes, V. de Zea Bermudez, R. A. Sá Ferreira, L. D. Carlos and N. V. Martins, *J. Lumin.*, 2008, **128**, 205–212.
- 172 V. De Zea Bermudez, L. D. Carlos, M. C. Duarte, M. M. Silva, C. J. R. Silva, M. J. Smith, M. Assunção and L. Alcácer, *J. Alloys Compd.*, 1998, **275–277**, 21–26.
- 173 V. de Zea Bermudez, R. A. Sá Ferreira, L. D. Carlos, C. Molina, K. Dahmouche and S. J. L. Ribeiro, *J. Phys. Chem. B*, 2001, **105**, 3378–3386.
- 174 L. D. Carlos, Y. Messaddeq, H. F. Brito, R. A. Sá Ferreira, V. De Zea Bermudez and S. J. L. Ribeiro, *Adv. Mater.*, 2000, **12**, 594–598.
- 175 R. A. Sá Ferreira, L. D. Carlos, R. R. Gonçalves, S. J. L. Ribeiro and V. de Zea Bermudez, *Chem. Mater.*, 2001, **13**, 2991–2998.
- 176 M. Hajzeri, L. S. Perše, M. Koželj, B. Orel and A. Šurca Vuk, *Sol. Energy Mater. Sol. Cells*, 2015, **139**, 51–64.
- 177 L. . Carlos, R. . Sá Ferreira, I. Orion, V. de Zea Bermudez and J. Rocha, *J. Lumin.*, 2000, **87–89**, 702–705.
- 178 K. Lunstroot, K. Driesen, P. Nockemann, C. Görrler-Walrand, K. Binnemans, S. Bellayer, J. Le Bideau and A. Vioux, *Chem. Mater.*, 2006, **18**, 5711–5715.
- 179 K. Lunstroot, K. Driesen, P. Nockemann, K. Van Hecke, L. Van Meervelt, C. Görrler-Walrand, K. Binnemans, S. Bellayer, L. Viau, J. Le Bideau and A. Vioux, *J. Chem. Soc. Dalton Trans.*, 2009, 298–306.
- 180 C. P. Mehnert, *Chem. - A Eur. J.*, 2005, **11**, 50–56.

- 181 P. Hesemann, L. Viau and A. Vioux, in *The Sol-Gel Handbook*, Wiley-VCH Verlag GmbH & Co. KGaA, Weinheim, Germany, 2015, vol. 2, pp. 487–518.
- 182 R. Ciriminna, P. Hesemann, J. J. E. Moreau, M. Carraro, S. Campestrini and M. Pagliaro, *Chem. - A Eur. J.*, 2006, **12**, 5220–5224.
- 183 S. S. Moganty, S. Srivastava, Y. Lu, J. L. Schaefer, S. A. Rizvi and L. A. Archer, *Chem. Mater.*, 2012, **24**, 1386–1392.
- 184 C. G. Granqvist, in *Electrochromic Materials and Devices*, 2015.
- 185 G. A. Niklasson and C. G. Granqvist, *J. Mater. Chem.*, 2007, **17**, 127–156.
- 186 S. Darmawi, S. Burkhardt, T. Leichtweiss, D. A. Weber, S. Wenzel, J. Janek, M. T. Elm and P. J. Klar, *Phys. Chem. Chem. Phys.*, 2015, **17**, 15903–15911.
- 187 S. Pereira, A. Gonçalves, N. Correia, J. Pinto, L. Pereira, R. Martins and E. Fortunato, *Sol. Energy Mater. Sol. Cells*, 2014, **120**, 109–115.
- 188 H. J. Hovel, R. T. Hodgson and J. M. Woodal, *Sol. Energy Mater.*, 1979, **2**, 19–29.
- 189 C. Strümpel, M. McCann, G. Beaucarne, V. Arkhipov, A. Slaoui, V. Švrček, C. del Cañizo and I. Tobias, *Sol. Energy Mater. Sol. Cells*, 2007, **91**, 238–249.
- 190 K. R. McIntosh, G. Lau, J. N. Cotsell, K. Hanton, D. L. Bätzner, F. Bettiol and B. S. Richards, *Prog. Photovoltaics Res. Appl.*, 2009, **17**, 191–197.
- 191 R. Rothmund, S. Kreuzer, T. Umundum, G. Meinhardt, T. Fromherz and W. Jantsch, *Energy Procedia*, 2011, **10**, 83–87.
- 192 M. A. Green, E. D. Dunlop, D. H. Levi, J. Hohl-Ebinger, M. Yoshita and A. W. Y. Ho-Baillie, *Prog. Photovoltaics Res. Appl.*, 2019, **27**, 565–575.
- 193 B. S. Richards, *Sol. Energy Mater. Sol. Cells*, 2006, **90**, 2329–2337.
- 194 Y. Zhou, H. Zhao, D. Ma and F. Rosei, *Chem. Soc. Rev.*, 2018, **47**, 5866–5890.
- 195 A. F. Mansour, H. M. A. Killa, S. Abd El-Wanees and M. Y. El-Sayed, *Polym. Test.*, 2005, **24**, 519–525.
- 196 F. Purcell-Milton and Y. K. Gun'ko, *J. Mater. Chem.*, 2012, **22**, 16687.
- 197 G. Maggioni, A. Campagnaro, S. Carturan and A. Quaranta, *Sol. Energy Mater. Sol. Cells*, 2013, **108**, 27–37.
- 198 T. Dienel, C. Bauer, I. Dolamic and D. Brühwiler, *Sol. Energy*, 2010, **84**, 1366–1369.
- 199 M. D. Hughes, C. Maher, D.-A. Borca-Tasciuc, D. Polanco and D. Kaminski, *Renew. Energy*, 2013, **52**, 266–272.
- 200 Z. Fan, Y. Wang, Z. Xue, L. Zhang, Y. Chen and S. Zhang, *J. Sol-Gel Sci.*

- Technol.*, 2014, **72**, 328–333.
- 201 F. Zhou, T. Wang, Z. Li and Y. Wang, *Luminescence*, 2015, **30**, 1303–1307.
- 202 M. Zettl, O. Mayer, E. Klampaftis and B. S. Richards, *Energy Technol.*, 2017, **5**, 1037–1044.
- 203 S. C. Nunes, G. Toquer, M. A. Cardoso, A. Mayoral, R. A. S. Ferreira, L. D. Carlos, P. Ferreira, P. Almeida, X. Cattoën, M. Wong Chi Man and V. de Zea Bermudez, *ChemistrySelect*, 2017, **2**, 432–442.
- 204 M. Litschauer and M. A. Neouze, *J. Mater. Chem.*, 2008, **18**, 640–646.
- 205 N. Gonsior, F. Mohr and H. Ritter, *Beilstein J. Org. Chem.*, 2012, **8**, 390–397.
- 206 F. De Buyl and A. Kretschmer, *J. Adhes.*, 2008, **84**, 125–142.
- 207 M. T. L. Casford and P. B. Davies, *Langmuir*, 2012, **28**, 10741–10748.
- 208 K. Hanke, M. Kaufmann, G. Schwaab, M. Havenith, C. T. Wolke, O. Gorlova, M. A. Johnson, B. P. Kar, W. Sander and E. Sanchez-Garcia, *Phys. Chem. Chem. Phys.*, 2015, **17**, 8518–8529.
- 209 P. J. Launer and B. Arkles, in *Silicon Compounds: Silanes and Silicones*, eds. B. Arkles and G. L. Larson, Gelest, Inc, Morrisville, PA, 3rd Editio., 2013, pp. 175–178.
- 210 N. Ramanathan, K. Sundararajan and K. Sankaran, *Spectrochim. Acta - Part A Mol. Biomol. Spectrosc.*, 2015, **139**, 75–85.
- 211 Z. Abbas, S. Dasari and A. K. Patra, *RSC Adv.*, 2017, **7**, 44272–44281.
- 212 L. D. Carlos, V. de Zea Bermudez, R. A. Sá Ferreira, L. Marques and M. Assunção, *Chem. Mater.*, 1999, **11**, 581–588.
- 213 L. Fu, R. A. Sá Ferreira, N. J. O. Silva, L. D. Carlos, V. De Zea Bermudez and J. Rocha, *Chem. Mater.*, 2004, **16**, 1507–1516.
- 214 D. Sangian, Y. Ide, Y. Bando, A. E. Rowan and Y. Yamauchi, *Small*, 2018, **14**, 1–14.
- 215 N. Takahashi, H. Hata and K. Kuroda, *Chem. Mater.*, 2010, **22**, 3340–3348.
- 216 N. Takahashi, H. Hata and K. Kuroda, *Chem. Mater.*, 2011, **23**, 266–273.
- 217 A. Singhal, K. A. Dubey, Y. K. Bhardwaj, D. Jain, S. Choudhury and A. K. Tyagi, *RSC Adv.*, 2013, **3**, 20913.
- 218 H. Wang, Y. Wang, L. Zhang and H. Li, *RSC Adv.*, 2013, **3**, 8535.
- 219 J. A. Kai, M. C. F. C. Felinto, L. A. O. Nunes, O. L. Malta and H. F. Brito, *J. Mater. Chem.*, 2011, **21**, 3796–3802.
- 220 J. Xu, Y. Zhang, H. Chen, W. Liu and Y. Tang, *Dalt. Trans.*, 2014, **43**, 7903–

- 7910.
- 221 L. Sun, Y. Liu, S. Dang, Z. Wang, J. Liu, J. Fu and L. Shi, *New J. Chem.*, 2016, **40**, 209–216.
- 222 R. Bouchal, I. Miletto, U. D. Thach, B. Prelot, G. Berlier and P. Hesemann, *New J. Chem.*, 2016, **40**, 7620–7626.
- 223 L. De Almeida, S. Grandjean, N. Vigier and F. Patisson, *Eur. J. Inorg. Chem.*, 2012, **2012**, 4986–4999.
- 224 A. Efimova, G. Hubrig and P. Schmidt, *Thermochim. Acta*, 2013, **573**, 162–169.
- 225 Q. Ru, Y. Wang, W. Zhang, X. Yu and H. Li, *Eur. J. Inorg. Chem.*, 2013, **1**, 2342–2349.
- 226 S. Kirchhecker, S. Tröger-Müller, S. Bake, M. Antonietti, A. Taubert and D. Esposito, *Green Chem.*, 2015, **17**, 4151–4156.
- 227 P. P. Lima, S. S. Nobre, R. O. Freire, S. A. Júnior, R. A. Sá Ferreira, U. Pischel, O. L. Malta and L. D. Carlos, *J. Phys. Chem. C*, 2007, **111**, 17627–17634.
- 228 M. Fernandes, V. de Zea Bermudez, R. A. S. Ferreira, L. D. Carlos, A. Charas, J. Morgado, M. M. Silva and M. J. Smith, *Chem. Mater.*, 2007, **19**, 3892–3901.
- 229 C. Sanchez, F. Ribot and B. Lebeau, *J. Mater. Chem.*, 1999, **9**, 35–44.
- 230 M. C. Gonçalves, N. J. O. Silva, V. de Zea Bermudez, R. A. Sá Ferreira, L. D. Carlos, K. Dahmouche, C. V. Santilli, D. Ostrovskii, I. C. Correia Vilela and A. F. Craievich, *J. Phys. Chem. B*, 2005, **109**, 20093–20104.
- 231 J. Garcia-Torres, P. Bosch-Jimenez, E. Torralba-Calleja, M. Kennedy, H. Ahmed, J. Doran, D. Gutierrez-Tauste, L. Bautista and M. Della Pirriera, *J. Photochem. Photobiol. A Chem.*, 2014, **275**, 103–113.
- 232 O. Moudam, B. C. Rowan, M. Alamiry, P. Richardson, B. S. Richards, A. C. Jones and N. Robertson, *Chem. Commun.*, 2009, 6649–6651.
- 233 K. Lunstroot, K. Driesen, P. Nockemann, L. Viau, P. H. Mutin, A. Vioux and K. Binnemans, *Phys. Chem. Chem. Phys.*, 2010, **12**, 1879–1885.
- 234 R. Rondão, A. R. Frias, S. F. H. Correia, L. Fu, V. de Zea Bermudez, P. S. André, R. A. S. Ferreira and L. D. Carlos, *ACS Appl. Mater. Interfaces*, 2017, **9**, 12540–12546.
- 235 J.-C. G. Bünzli and A.-S. Chauvin, in *Handbook on the Physics and Chemistry of Rare-Earths*, eds. J.-C. G. Bünzli and V. K. Pecharsky, Elsevier B. V., Amsterdam, 2014, vol. 44, pp. 169–281.
- 236 G. V. Shcherbatyuk, R. H. H. Inman, C. Wang, R. Winston and S. Ghosh, *Appl.*

- Phys. Lett.*, 2010, **96**, 191901.
- 237 R. H. Inman, G. V. Shcherbatyuk, D. Medvedko, A. Gopinathan and S. Ghosh, *Opt. Express*, 2011, **19**, 24308–24313.
- 238 A. Kraft and M. Rottmann, *Sol. Energy Mater. Sol. Cells*, 2009, **93**, 2088–2092.
- 239 A. Llordés, G. Garcia, J. Gazquez and D. J. Milliron, *Nature*, 2013, **500**, 323–326.
- 240 J. Xu, Y. Zhang, T. T. Zhai, Z. Kuang, J. Li, Y. Wang, Z. Gao, Y. Y. Song and X. H. Xia, *ACS Nano*, 2018, **12**, 6895–6903.
- 241 S. Zhang, S. Cao, T. Zhang, A. Fisher and J. Y. Lee, *Energy Environ. Sci.*, 2018, **11**, 2884–2892.
- 242 National Weather Services, Extreme Temperature Ranges, <http://weather.gov/ama/50ranges>, (accessed 1 July 2018).
- 243 S. Parthiban, V. Gokulakrishnan, K. Ramamurthi, E. Elangovan, R. Martins, E. Fortunato and R. Ganesan, *Sol. Energy Mater. Sol. Cells*, 2009, **93**, 92–97.
- 244 S. Calnan and A. N. Tiwari, *Thin Solid Films*, 2010, **518**, 1839–1849.
- 245 S. Pereira, A. Gonçalves, N. Correia, J. Pinto, L. Pereira, R. Martins and E. Fortunato, *Sol. Energy Mater. Sol. Cells*, 2014, **120**, 109–115.
- 246 S. C. Nunes, V. de Zea Bermudez, M. M. Silva, M. J. Smith, E. Morales, R. A. Sá Ferreira, L. D. Carlos and J. Rocha, *Solid State Sci.*, 2006, **8**, 1484–1491.
- 247 C. M. Burba, J. Janzen, E. D. Butson and G. L. Coltrain, *J. Phys. Chem. B*, 2013, **117**, 8814–8820.
- 248 C. M. Burba and R. Frech, *J. Chem. Phys.*, , DOI:10.1063/1.3571458.
- 249 J. Jiang, D. Gao, Z. Li and G. Su, *React. Funct. Polym.*, 2006, **66**, 1141–1148.
- 250 J. Schauer, A. Sikora, M. Plíšková, J. Mališ, P. Mazúr, M. Paidar and K. Bouzek, *J. Memb. Sci.*, 2011, **367**, 332–339.
- 251 M. Fernandes, R. Leones, A. M. S. Costa, M. M. Silva, S. Pereira, J. F. Mano, E. Fortunato, R. Rego and V. De Zea Bermudez, *Electrochim. Acta*, 2015, **161**, 226–235.
- 252 A. L. Dyer, E. J. Thompson and J. R. Reynolds, *ACS Appl. Mater. Interfaces*, 2011, **3**, 1787–1795.
- 253 P. M. Beaujuge, S. Ellinger and J. R. Reynolds, *Nat. Mater.*, 2008, **7**, 795–799.
- 254 H.-S. Liu, B.-C. Pan, D.-C. Huang, Y.-R. Kung, C.-M. Leu and G.-S. Liou, *NPG Asia Mater.*, 2017, **9**, e388–e388.
- 255 A. A. F. Husain, W. Z. W. Hasan, S. Shafie, M. N. Hamidon and S. S. Pandey,

- Renew. Sustain. Energy Rev.*, 2018, **94**, 779–791.
- 256 Y. Xia, X. Liang, Y. Jiang, S. Wang, Y. Qi, Y. Liu, L. Yu, H. Yang and X. Zhao, *Adv. Energy Mater.*, 2019, **9**, 1900720.
- 257 J. Lin, M. Lai, L. Dou, C. S. Kley, H. Chen, F. Peng, J. Sun, D. Lu, S. A. Hawks, C. Xie, F. Cui, A. P. Alivisatos, D. T. Limmer and P. Yang, *Nat. Mater.*, 2018, **17**, 261–267.
- 258 L. M. Wheeler, D. T. Moore, R. Ihly, N. J. Stanton, E. M. Miller, R. C. Tenent, J. L. Blackburn and N. R. Neale, *Nat. Commun.*, 2017, **8**, 1722.
- 259 M. P. Scott, C. S. Brazel, M. G. Benton, J. W. Mays, J. D. Holbrey and R. D. Rogers, *Chem. Commun.*, 2002, **2**, 1370–1371.
- 260 L. Zhao, Y. Li, X. Cao, J. You and W. Dong, *Nanotechnology*, 2012, **23**, 255702.
- 261 A. A. Shamsuri and R. Daik, *Rev. Adv. Mater. Sci.*, 2015, **40**, 45–59.
- 262 O. Zech, A. Stoppa, R. Buchner and W. Kunz, *J. Chem. Eng. Data*, 2010, **55**, 1774–1778.
- 263 X. H. Flora, M. Ulaganathan, R. S. Babu and S. Rajendran, *Ionics (Kiel)*, 2012, **18**, 731–736.
- 264 E. Ceci-Ginistrelli, C. Smith, D. Pugliese, J. Lousteau, N. G. Boetti, W. A. Clarkson, F. Poletti and D. Milanese, *J. Alloys Compd.*, 2017, **722**, 599–605.
- 265 M. Fernandes, R. Leones, S. Pereira, A. M. S. Costa, J. F. Mano, M. M. Silva, E. Fortunato, V. de Zea Bermudez and R. Rego, *Electrochim. Acta*, 2017, **232**, 484–494.
- 266 S. K. Sharma, D. S. Verma, L. U. Khan, S. Kumar and S. B. Khan, *Handbook of Materials Characterization*, .
- 267 C. Techniques, .
- 268 S. Fery-Forgues and D. Lavabre, *J. Chem. Educ.*, 1999, **76**, 1260.
- 269 A. Piccolo and F. Simone, *J. Build. Eng.*, 2015, **3**, 94–103.